NOVEL STRUCTURAL AND FUNCTIONAL IMAGING IN CEREBRAL ARTERIOVENOUS MALFORMATIONS

Joan Patricia Grieve MBBS

St George's Hospital Medical School, London.

Research conducted at:
The National Hospital for Neurology and Neurosurgery,
Queen Square, London WC1N 3BG,
and submitted for the degree of
Doctor of Medicine at the University of London.

May 2004

Address:
25 Kelso Place,
London W8 5QG.

ProQuest LLC
789 East Eisenhower Parkway
P.O. Box 1346
Ann Arbor, MI 48106-1346

ABSTRACT

Clarification of the angio-architecture and haemodynamic effects of cerebral arteriovenous malformations (AVMs) using non-invasive imaging may advance our knowledge and understanding of their natural history, resulting in improvements in the management of patients with these lesions.

The aims of the work in this dissertation was to investigate the haemodynamic effects of AVMs and to determine whether newer non-invasive imaging techniques allow an accurate enough assessment of the angio-architecture of AVMs to be able to replace conventional digital subtraction angiography (DSA) in some clinical situations. The hypotheses were:

1. Non-invasive structural imaging techniques, such as CT angiography (CTA) and MR angiography (MRA), provide adequate structural and volumetric information to replace the more invasive technique of DSA.
2. MR perfusion imaging is able to demonstrate the alteration of cerebral haemodynamics by AVMs.
6 Rapid frame rate DSA (RFRDSA) provides useful quantitative data on the blood flow within cerebral AVMs.

In this work CT and MR angiography (CTA and MRA) were compared with conventional digital subtraction angiography (DSA). Twenty patients were examined with CTA and ten with MRA. Both techniques were able to detect most of the important angio-architectural features, but were not as accurate as DSA as decision-making tools, in particular because temporal resolution and nidus definition were poor. The use of gadolinium enhancement during MRA improved the visualisation of both nidus and draining veins.

The nidal volume of ten AVMs was calculated from DSA and three magnetic resonance (MR) sequences. With biplanar DSA, an ellipsoid volume was calculated using orthogonal projections. MR images showed potential but were difficult to interpret due to varied appearances of flowing blood and, on gadolinium-enhanced MRA, the enhancement of abnormal brain.

The cerebral haemodynamics of fifteen patients with AVMs were examined with contrast bolus tracking. This semi-quantitative technique was able to demonstrate consistent differences in cerebral blood flow and volume, mean transit time and time to minimum signal intensity in brain distant from the AVM. Changes in the perinidal regions were dominated by the presence of draining veins.

A vascular phantom was calibrated to allow calculation of flow rates from rapid frame rate DSA. The technique for quantifying flow was assessed in five patients and compared with values measured by transcranial doppler. It was not possible to calculate accurately flow and velocity for AVM feeding vessels.

These imaging modalities allowed improved appreciation of the structure and haemodynamic effects of cerebral AVMs but further development is needed before they will be of use as reliable clinical tools.

Key Words: cerebral arteriovenous malformation, CT angiography, MR angiography, rapid frame rate DSA, contrast bolus tracking.

CONTENTS

Title....1
Abstract....2
Contents....4
List of Tables....10
List of Figures....11
Acknowledgements....14
List of Abbreviations....15

PART 1 – INTRODUCTION

Chapter 1 - Aims of the work in this dissertation....20
1.1 Hypothesis....20
1.2 Non-invasive structural imaging....21
1.3 Perfusion imaging....21
1.4 Haemodynamic imaging....21

Chapter 2 - Introduction....22
2.1 The clinical significance of arteriovenous malformations....22
2.1.1 Epidemiology....23
2.1.2 Presentation....23
2.1.2.1 Haemorrhage....24
2.1.2.2 Seizures....25
2.1.2.3 Neurological deficit....26
2.1.2.4 Other presenting symptoms....26
2.1.3 Natural history....27
2.2 Pathological Considerations....28
2.2.1 Pathogenesis....28
2.2.2 Elements of an AVM....30
2.2.2.1 Nidus....30
2.2.2.2 Arterial feeders....32
2.2.2.3 Venous drainage....33
2.2.2.4 Sinuses....33
2.2.3 Association of aneurysm and AVM....34
2.3 Classification of AVMs....37
2.3.1 Topographical analysis....37
2.3.2 Spetzler classification....38

2.4 Haemodynamics 39
2.4.1 Cerebral blood flow 39
2.4.1.1 Neuronal Control 40
2.4.1.2 Chemical mediators 40
2.4.2 Regulation of cerebral blood flow 41
2.4.2.1 Autoregulation 41
2.4.2.2 Chemoregulation/metabolic coupling of cerebral blood flow 41
2.4.2.3 Effects of Carbon Dioxide 42
2.4.3 Flow Dynamics within AVMs 42
2.4.3.1 Feeding artery and draining vein pressures 42
2.4.3.2 'Steal' phenomenon 43
2.4.4 Haemodynamic changes associated with treatment 47
2.4.4.1 Normal perfusion pressure breakthrough 47
2.5 Risk factors for haemorrhage 50
2.5.1 Patient factors 50
2.5.1.1 Gender 50
2.5.1.2 Age 51
2.5.1.3 Presentation 51
2.5.2 AVM factors 51
2.5.2.1 Site of AVM 51
2.5.2.2 Size of AVM 52
2.5.3 Angiographic features 53
2.5.3.1 AVM nidus 53
2.5.3.2 Arterial supply 53
2.5.3.3 Venous drainage 54
2.5.3.4 Associated aneurysms 55
2.5.3.5 Combined risk factors 55
2.6 Investigation 56
2.6.1 Plain Xrays 56
2.6.2 CT scan 57
2.6.3 Digital subtraction angiography 57
2.6.4 Magnetic Resonance Imaging 62
2.6.4.1 MR Angiography 64
2.7 Conclusion 67

PART 2 - STRUCTURAL IMAGING

Chapter 3 - CT Angiography 70
3.1 Introduction 70
3.1.1 Basic principles 70
3.1.2 Post processing 71

3.1.3 Clinical applications 75
3.1.3.1 CTA of intracranial aneurysms 75
3.1.3.2 CTA of intracranial AVMs 76
3.2 Methods 77
3.2.1 Patients 77
3.2.2 Imaging 77
3.2.3 Processing 80
3.2.4 Image analysis 81
3.2.5 Statistical analysis 82
3.3 Results 84
3.3.1 Patient baseline characteristics 84
3.3.2 CTA analysis 84
3.3.3 Kappa Values 88
3.4 Discussion 88
3.4.1 Interobserver variability 91
3.4.2 Comparison of imaging techniques 95
3.4.2.1 CTA and DSA of all AVMs 95
3.4.2.2 CTA and DSA of small AVMs 97
3.5 Conclusion 100

Chapter 4 - MR Angiography 103
4.1 Introduction 103
4.2 Methods 104
4.2.1 Patients 104
4.2.2 Imaging 105
4.2.2.1 3D TOF sequences 105
4.2.2.2 Contrast-enhanced gradient-echo sequences 105
4.2.3 Post processing 106
4.2.4 Image analysis 106
4.2.5 Statistical analysis 106
4.3 Results 107
4.3.1 Patient baseline characteristics 107
4.3.2 MRA analysis 107
4.3.3 Kappa values 107
4.3.3.1 Pre and post-contrast 3D TOF 107
4.3.3.2 'Arterial' phase contrast-enhanced gradient-echo MRAs 111
4.3.3.3 'Venous' phase contrast-enhanced gradient-echo MRAs .111
4.4 Discussion 111
4.4.1 Interobserver variability 112
4.4.2 Comparison of imaging techniques 113
4.5 Conclusion 114

Chapter 5 - Volumetric analysis of AVM nidus using MRI 119
5.1 Introduction 119
5.2 Methods 120
5.2.1 Patients 120
5.2.2 Imaging 120
5.2.2.1 3D TOF sequences 121
5.2.2.2 FSE sequences 121
5.2.3 Post processing 121
5.2.4 Image analysis 122
5.2.4.1 MRI 122
5.2.4.2 DSA 122
5.2.5 Statistical analysis 124
5.3 Results 124
5.3.1 Patient baseline characteristics 124
5.3.2 AVM nidus volumes 124
5.3.2.1 Intersequence variability 124
5.3.2.2 Interobserver variability 131
5.4 Discussion 135
5.4.1 Intersequence variability 135
5.4.2 Interobserver variability 136
5.5 Conclusion 142

PART 3 - PERFUSION IMAGING

Chapter 6 - Perfusion imaging using MRI 144
6.1 Introduction 144
6.1.1 Kety method for measuring cerebral blood flow 144
6.1.2 Clinical methods of measuring cerebral blood flow 145
6.1.2.1 Xenon CT 145
6.1.2.2 Cerebral blood flow ^{133} Xenon 146
6.1.2.3 Nuclear Medicine 147
6.1.3 MR perfusion 148
6.1.3.1 Determination of regional cerebral blood flow 149
6.1.3.2 Determination of regional cerebral blood volume 150
6.1.3.3 Determination of mean transit time 151
6.2 Methods 151
6.2.1 Patients 151
6.2.2 Imaging 151
6.2.3 Post processing 152
6.2.4 Statistical analysis 154

6.3 Results 154
6.3.1 Patient baseline characteristics 154
6.3.2 Haemodynamic parameters 154
6.3.2.1 White and grey matter 162
6.3.2.2 Nidus versus contralateral nidus equivalent 163
6.3.2.3 Perinidal region 163
6.4 Discussion 164
6.4.1 Limitations of Contrast Bolus Tracking MRI 164
6.4.2 White and grey matter 166
6.4.3 Nidus 166
6.4.4 Perinidus 167
6.5 Conclusion 169

PART 4 - HAEMODYNAMIC IMAGING

Chapter 7 - Digital Subtraction Angiography 172
7.1 Introduction 172
7.2 Phantom studies 174
7.2.1 Method 174
7.2.1.1 Post processing 177
7.2.1.2 Statistical analysis 178
7.2.2 Results 178
7.2.2.1 Terminology 178
7.2.2.2 Calibration of the model 179
7.2.2.3 Reproducibility of the model 180
7.2.2.4 Angle from the horizontal 182
7.2.2.5 Frame rate, injection rate, field of view, table height, source-image distance and patient-source distance 183
7.2.2.6 Reproducibility and accuracy of angiography machine 183
7.2.3 Conclusion 184

7.3 Patient studies 184
7.3.1 Methods 185
7.3.1.1 Patients 185
7.3.1.2 Imaging 185
7.3.1.3 Post processing 186
7.3.1.4 Statistical analysis 188
7.3.2 Results 188
7.3.2.1 Patient baseline characteristics 188
7.3.2.2 Transcranial Doppler findings 188
7.3.2.3 Time-density curves and calculated velocities 191
7.3.2.4 Comparison of Transcranial Doppler measurements and measured velocities from time-density curves 193
7.3.3 Discussion 194
7.3.3.1 Sources of error 195
7.3.4 Conclusion 198

PART 5 - CONCLUSIONS

Chapter 8 - Conclusions and future studies 201
8.1 Structural Imaging 201
8.1.1 CT and MR angiography 201
8.1.2 MR nidal volumes 204
8.2 Perfusion imaging 205
8.3 Haemodynamic imaging 206
8.4 Conclusion 207

Bibliography 208

Appendices 220
Appendix 1 221
A1.1 Statement of originality 221
A1.2 Collaboration and assistance 221
A1.3 Ethical considerations 222
A1.4 Publications 222
Appendix 2 – Data from Chapter 3 223
Appendix 3 – Data from Chapter 4 242
Appendix 4 – Data from Chapter 6 264
Appendix 5 – Data from Chapter 7 268

LIST OF TABLES

Table 2.1 Topography of intracranial AVMs 37
Table 2.2 Determination of AVM Spetzler grade 39

Table 3.1 Value of kappa and strength of agreement 83
Table 3.2 Pattern of venous drainage on SSD images reported by two radiologists 83
Table 3.3 Demographic data of all patients undergoing CTA 85
Table 3.4 Kappa values for interobserver variability and comparison of imaging techniques for CTA images 89

Table 4.1 Demographic data of all patients undergoing pre- and post-contrast 3D TOF and contrast-enhanced gradient-echo MRA 108
Table 4.2 Kappa values for interobserver variability and comparison of imaging techniques for MRA images 109

Table 5.1 Demographic data of all patients undergoing MR volumetric studies 125
Table 5.2 Mean nidal volume for all investigations 126
Table 5.3 Limits of agreement for all three MR sequences 130
Table 5.4 Mean volume for all observers 132
Table 5.5 Results of two way ANOVA for 3D FSE 133
Table 5.6 Results of two way ANOVA for pre-contrast 3D TOF 134
Table 5.7 Results of two way ANOVA for post-contrast 3D TOF 134

Table 6.1 Demographic data of all patients undergoing MR perfusion studies 155
Table 6.2 Results of haemodynamic parameter comparisons 162

Table 7.1 Demographic data of patients undergoing RFRDSA 189
Table 7.2 Velocities determined by transcranial doppler of all five patients undergoing RFRDSA 190
Table 7.3 MCA and ICA velocities and flows in all patients calculated from RFRDSA 192

LIST OF FIGURES

Figure 2.1 Pre- and post contrast CT scan of a left occipital AVM 58
Figure 2.2 Arterial and venous phases of an AVM on DSA 60
Figure 2.3 Axial T2 FSE image of a left occipital AVM with obvious flow voids 63

Figure 3.1 Segmented SSD image showing vessels, embolisation material and ventriculo-peritoneal shunt using multiple threshold levels and a coloured display.....72
Figure 3.2 Segmented SSD image showing vessels and bone using multiple threshold levels and a coloured display.....72
Figure 3.3 MIP and SSD images of the same AVM.....74
Figure 3.4 A sample threshold graph of CTA acquisition showing average Hounsfield unit values for ROI 78
Figure 3.5 Reference slice showing ROI over cavernous sinus to detect arrival of contrast bolus.....79
Figure 3.6 DSA with corresponding SSD images of an anterior communicating artery aneurysm and venous pouches associated with an AVM 92
Figure 3.7 Embolisation material as seen on DSA, CT axial source data, MIP and SSD images of the same patient 94
Figure 3.8 Arterial and venous phases of an AVM on DSA with a corresponding MIP image 96
Figure 3.9 MIP images of a large and small-sized AVM 98
Figure 3.10 Coronal reformat from axial source data allowing appreciation of intranidal structure and features.....101

Figure 4.1 DSA, CEMRA and pre- and post-contrast 3D TOF images of a small parietal AVM.....115
Figure 4.2 Pre- and post-contrast 3D TOF images of an AVM only visualised well post-contrast because of slow flow in the draining veins 116
Figure 4.3 Visualisation of a draining vein on DSA and pre- and post-contrast 3D TOF.....117

Figure 5.1 DSA of AVM showing three orthogonal measurements of the nidus for use in ellipsoid approximation of nidal volumes 123
Figure 5.2 Graph showing average DSA volumes against volumes by all three MR sequences, together with the line of identity.....126

Figure 5.3 Graph showing the average nidus volume by DSA and MR against the difference in nidal volume 127
Figure 5.4 Graph showing the average log nidus volume by DSA and MR against the difference in log nidus volume by the same two techniques 128
Figure 5.5 Limits of agreement for 3D FSE, pre- and post-contrast TOF....129
Figure 5.6 Observer 3 traces demonstrating intersequence variability on T2 FSE and pre- and post-contrast 3D TOF images 138
Figure 5.7 The problem with enhancing gliotic tissue 139
Figure 5.8 Freehand traces of observers 1 to 3 demonstrating interobserver variability on post-contrast 3D TOF images 140
Figure 5.9 The difficulty with draining veins 141

Figure 6.1 Tracer Kinetics 150
Figure 6.2 A sample arterial time-signal intensity curve....153
Figure 6.3 Regions of interest defined for each slice for each patient....153
Figure 6.4 Cerebral blood flow in all 15 patients 158
Figure 6.5 Cerebral blood volume in all 15 patients....159
Figure 6.6 Mean transit time in all 15 patients 160
Figure 6.7 Time to minimum in all 15 patients 161
Figure 6.8 Schematic demonstration of haemodynamic parameters from the signal intensity – time curve....165
Figure 6.9 Mean transit time colour map for patient 12 with corresponding EPI image 168

Figure 7.1 Unsubtracted DSA image of the vascular phantom 175
Figure 7.2 Subtracted DSA image of the vascular phantom demonstrating the air bubble....175
Figure 7.3 Diagram showing arrangement of phantom as the angle from the horizontal is increased....176
Figure 7.4 Time density curve from DSA showing two dips as the air bubble passes the proximal and distal ROIs....178
Figure 7.5 Graph showing the relationship between true reported and measured flow rates from DSA at 30 frames sec^{-1} 179
Figure 7.6 Graph showing the 95% confidence and prediction intervals for reported and measured flow rates at 30 frames sec^{-1}....181
Figure 7.7 Graph showing the effect of angle from the horizontal on adjusted measured flow rate....182
Figure 7.8 Magnified example of a DSA image with placement of ROIs for generation of time-density curve 187
Figure 7.9 Time-density curve of the right ICA injection of patient 2....191

Figure 7.10 Time-density curve of left MCA injection of patient 5 showing a poor bolus injection 192
Figure 7.11 Graph showing comparison MCA and ICA velocities measured by TCD with those calculated from RFRDSA and their accompanying regression lines..... 193

ACKNOWLEDGEMENTS

First and foremost, I thank Dr Rolf Jäger and Mr Neil Kitchen for their encouragement, help and supervision during the course of my research. I am also especially grateful to Liz Moore, who was a constant source of advice, technical knowledge and stimulating discussion.

In addition, I thank Katharine Briggs, David McManus and Julia Whybrow for performing the vast majority of scans, Drs Mike Bynevelt, Panos Nikolopoulos, Phil Rich, Wendy Taylor and Adam Waldman for their help in analysing the images, Wendy Fowler for meeting my numerous requests for time on the Toshiba angiogram machine and restoration of data and to all those at The National Hospital for Neurology and Neurosurgery, too numerous to mention by name, who have helped in some way.

I gratefully acknowledge Anthony and the late Meg Household who, through the Ethel Household Fellowship, allowed me to carry out this work.

Finally, I thank the patients who took part in these studies, and hope that ultimately they are rewarded by improvements in their management.

LIST OF ABBREVIATIONS

AIF	Arterial input function
ANOVA	Analysis of variance
AP	Antero-posterior
AVM	Arteriovenous malformation
A_x	Arterial concentration of substance x
C_a	Tracer concentration in arterial blood
C_b	Tracer concentration in post arterial blood
C_t	Net tracer concentration in tissue
CBF	Cerebral blood flow
CBT	Contrast bolus tracking
CBV	Cerebral blood volume
CEMRA	Contrast-enhanced magnetic resonance angiography
CI	Confidence interval
cm	centimetres
$CMRO_2$	Cerebral metabolic rate of oxygen
CPP	Cerebral perfusion pressure
CT	Computerised tomography
CTA	Computerised tomography angiography
DSA	Digital subtraction angiography
DVP	Draining vein pressure
DXT	Radiosurgery
EPI	Echo-planar imaging
ECD	Ethyl cysteine dimer

f	Perfusion
f_m	Measured flow rate
f_p	Predicted flow rate
f_t	True reported pump flow rate
F	Fluorine
FAP	Feeding artery pressure
FDG	Fluoro-2-deoxy-D-glucose
FOV	Field of view
FSE	Fast spin-echo
g	grams
Gd-DOTA	Gadolinium gadoteric acid
H_f	Haematocrit factor
HMPAO	Hexamethylpropyleneamine oxime
HU	Hounsfield unit
I	Iodine
ICA	Internal carotid artery
ICH	Intracerebral haemorrhage
IMP	I-d, I-N-isoproyl-p-iodoamphetamine
In	Indium
IVH	Intraventricular haemorrhage
MCA	Middle cerebral artery
MCV	Middle cerebral vein
min	minutes
MIP	Maximum intensity projection
ml	millilitres

mm	millimetres
MR	Magnetic resonance
MRA	Magnetic resonance angiography
MRI	Magnetic resonance imaging
msec	milliseconds
mSv	millisieverts
MTT	Mean transit time
NEX	Number of signal averages
O	Oxygen
OEF	Oxygen extraction fraction
PC	Phase contrast
PET	Positron emission tomography
PID	Patient-image distance
PSD	Patient-source distance
$\mathbf{Q_x}$	Amount of substance x removed from the blood per unit time
rCBF	Relative cerebral blood flow
rCBV	Relative cerebral blood volume
RFRDSA	Rapid frame rate digital subtraction angiography
ROI	Region of interest
SAH	Subarachnoid haemorrhage
sec	seconds
SID	Source-image distance
SPECT	Single Photon Emission Computed Tomography
SSD	Surface-shaded display
SSS	Superior sagittal sinus

T_0	Time to contrast arrival
T1	Longitudinal relaxation time
T2	Transverse relaxation time
T2*	Gradient echo relaxation time
T_{1a}	T_1 of arterial blood
Tc	Technetium
TCD	Transcranial doppler
TE	Time to echo
TIA	Transient ischaemic attack
TOF	Time of flight
TR	Time to recovery
TTM	Time to minimum contrast concentration
v	Velocity
V_x	Venous concentration of substance x
Xe	Xenon
°C	Degrees centigrade
λ	Blood-brain partition coefficient
$\Re$	Residue function
$\otimes$	Convolution operation
ρ	Density of brain

PART 1

INTRODUCTION

Chapter 1

AIMS OF THE WORK IN THIS DISSERTATION

The current management of patients with arteriovenous malformations (AVMs) is often unsatisfactory. One important reason for this is that their natural history and effect on cerebral haemodynamics are poorly understood. In addition, there is often a requirement for repeated cerebral angiography. These procedures are invasive, have associated risks, in particular that of stroke, and currently require inpatient admission. In a pathology that most commonly affects young adults, this has major implications for the patients, their families and society as a whole. Clarification of haemodynamic effects and advances in non-invasive imaging techniques may not only improve our knowledge and understanding of the natural history of AVMs, but may also allow advances in their management.

1.1 Hypothesis

The aims of the work in this dissertation was to investigate the haemodynamic effects of AVMs and to determine whether newer non-invasive imaging techniques allow an accurate enough assessment of the angio-architecture of AVMs to be able to replace conventional digital subtraction angiography (DSA) in some clinical situations. The hypotheses were:

1. Non-invasive structural imaging techniques, such as CT angiography (CTA) and MR angiography (MRA), provide adequate structural and volumetric information to replace the more invasive technique of DSA.
2. MR perfusion imaging is able to demonstrate the alteration of cerebral haemodynamics by AVMs.

3. Rapid frame rate DSA (RFRDSA) provides useful quantitative data on the blood flow within cerebral AVMs.

1.2 Non-invasive structural imaging

The non-invasive structural imaging studies began with a prospective comparison of both CTA and MRA with DSA in patients with cerebral AVMs. The third study compared nidus volume measurements, traditionally determined from DSA, with those estimated from three different magnetic resonance (MR) sequences. This is of particular importance in those patients treated by stereotactic radiosurgery.

1.3 Perfusion imaging

The effects of AVMs on local cerebral perfusion and blood flow were investigated using bolus-tracking technique. Bolus tracking exploits the T2* shortening effects of gadolinium.

1.4 Haemodynamic imaging

The use of RFRDSA at 30 frames sec^{-1} was first validated using a vascular phantom. This technique was then used in a small group of patients to determine the accuracy of flow and velocity measured using RFRDSA and compared with those found on transcranial doppler (TCD).

Chapter 2

INTRODUCTION

2.1 The clinical significance of arteriovenous malformations

Cerebral vascular malformations (CVMs) are inborn errors of vascular morphogenesis, resulting in the formation of abnormal arterial, venous or capillary channels with or without a shunt. CVMs may be classified into several types on the basis of their angiographic and MR image characteristics (Yasargil, 1987; Valavanis, 1996). The primary differentiating feature in CVMs is the presence or absence of shunting within the lesion. Shunting occurs only when a direct communication exists between arterial and venous channels. Angiographically, shunting is characterised by early opacification of draining veins, resulting in decreased arteriovenous transit time. Various degrees of dilatation of the involved arteries and veins may be seen because of increased flow through these low resistance channels (Dembo, 1982). These arteriovenous communications are of two types: fistulous and plexiform. In the fistulous type, an arterial channel empties directly into a venous channel. AVMs make up the plexiform type, where one or several arterial channels feed a vascular conglomerate of multiple arteriovenous communications from which one or multiple venous channels emerge as draining veins. The plexiform vascular conglomerate associated with arteriovenous shunting is called the nidus and may contain one or more direct arteriovenous fistulae, with tangled arteries, venous sinusoid spaces and veins communicating directly without an interposed capillary network (Stein and Wolpert, 1980). Oxygenated blood is shunted directly into the venous system.

AVMs were first recognised by ancient Egyptians in 1500 BC, but it was in 1863 that Virchow (Virchow, 1863) first described the pathological appearances of an intracranial AVM. The first clinical diagnosis has been attributed to Steinheil in 1895 (Steinheil, 1895). Early attempts at operative intervention were unsuccessful, however their diagnosis and treatment was revolutionised by the introduction of cerebral angiography by Moniz in 1927 (Moniz, 1934).

CVMs without evidence of arteriovenous shunting arise from postarteriolar vascular channels and involve either capillaries or veins. This group is made up of capillary telangiectasia, developmental venous anomalies and cavernous malformations.

2.1.1 Epidemiology

Large autopsy studies have shown a prevalence of AVMs of 0.14 - 0.5%, making them seven to ten times less common than intracranial aneurysms (Perret and Nishioka, 1966b; Wilkins, 1985; Stein and Kader, 1992). There is an expected annual incidence of one brain AVM per 100 000 population, of which only 0.006% are multiple (Perret and Nishioka, 1966b; Stein and Wolpert, 1980). Gender distribution is almost equal, although there may be a slight male preponderance, with no genetic predisposition (Perret and Nishioka, 1966b; Michelson, 1979; Parkinson and Bachers, 1980; Crawford, 1986b; Ondra, 1990).

2.1.2 Presentation

Most individuals develop symptoms prior to the age of 40 years with a mean age at presentation of 33.7 years (Perret and Nishioka, 1966b; Michelson, 1979; Parkinson and Bachers, 1980; Dembo, 1982; Luessenhop and Rosa, 1984; Crawford, 1986b; Ondra, 1990; Stein and Kader, 1992). This is in contrast to intracranial aneurysms when only a quarter of patients present by the age of 40 (Perret and Nishioka, 1966b). Fifteen percent of patients however will remain asymptomatic (Brown, 1996). In the first two decades, particularly during period of

brain growth, many lesions show progressive growth and haemodynamic changes with increasing deleterious effects (Luessenhop and Rosa, 1984).

2.1.2.1 Haemorrhage

Sixty to 70% of individuals with AVMs present with haemorrhage at a peak age of 25 - 40 years (Perret and Nishioka, 1966b; Drake, 1979; Crawford, 1986a; Ondra, 1990; Guterman, 1993; Heros, 1993; Turjman, 1995; Brown, 1996). These figures may under-represent the true incidence of haemorrhage as clinically silent haemorrhage is diagnosed at surgery in as many as 10% of patients when haemosiderin staining is seen surrounding the lesion (Stein and Wolpert, 1980). It has been postulated that episodes of acute headache, seizures or other acute neurological symptoms may also represent haemorrhage.

Rupture of AVMs is responsible for 10% of all intracranial haemorrhages and is, after aneurysmal subarachnoid haemorrhage (SAH), the second most frequent cause of an intracerebral bleed from a vascular abnormality (Pott, 1992). Haemorrhage is largely intraparenchymal, although extension into the ventricular system and associated SAH are both common. Of haemorrhages caused by AVMs 30% are SAH, 23% parenchymal, 16% intraventricular haemorrhage (IVH) and 31% combined (Hartmann, 1998).

The mean annual risk of haemorrhage is 2 - 4%, with an associated combined annual mortality and morbidity of 2.7% (Wilkins, 1985; Brown, 1988; Itoyama, 1989; Ondra, 1990; Stein and Kader, 1992; Pollock, 1996a). Brown *et al.* (Brown, 1988) observed that annual haemorrhage rates actually appear to increase over time from 1.3% risk in the first year after diagnosis to 2.2% risk at 15 years, whilst others have found that the risk remains constant or even diminishes with time, regardless of presenting symptom (Itoyama, 1989; Ondra, 1990). The mean time from presentation in any form to haemorrhage is 7.7 years (Ondra, 1990).

Most studies have shown that the risk of repeated haemorrhage increases to 6% in the first year after the initial bleed, thereafter returning to the pre-haemorrhage

risk (Graf, 1983; Wilkins, 1985; Itoyama, 1989). There is an overall rebleed rate of 23 - 35% at a mean of 3.6 years after the presenting haemorrhage (Perret and Nishioka, 1966b; Itoyama, 1989; Brown, 1996; Pollock, 1996a).

2.1.2.2 Seizures

Seizures are the second most common presenting symptom. Twenty to 30% of individuals present initially with seizures, however by the time the diagnosis has been made, as many as half will have had fits (Perret and Nishioka, 1966b; Crawford, 1986a; Crawford, 1986b; Itoyama, 1989; Ondra, 1990; Stein and Kader, 1992; Turjman, 1995; Brown, 1996). The younger the patient at diagnosis the more likely they are to develop epilepsy: patients aged 10 - 19 years have an 82% 20 year risk, whilst those aged 50 have a less than 2% 20 year risk of developing seizures (Crawford, 1986b).

Seizures are a common presenting symptom, particularly if the lesion involves the cortical surface. For this reason, it is commonly large AVMs that cause epilepsy as they are more likely to involve cortex (Crawford, 1986b). Other risk factors for developing seizures include involvement of the temporal lobe, previous haemorrhage and previous intracranial surgery (Crawford, 1986b). Frontal AVMs most commonly present with generalised seizures, whilst the majority of parietal AVMs present with focal motor seizures (45%) (Perret and Nishioka, 1966b). Posterior fossa and basal ganglia lesions rarely cause epilepsy (Crawford, 1986b). Seizures may be a sign of acute haemorrhage or epileptogenic effect of parenchymal iron deposits.

With treatment of the lesion, improved seizure control can be achieved although many still require anticonvulsants. Control of seizures tends to be better following surgery, but useful improvement can be seen with embolisation (complete or partial) (Michelson, 1979). The longer the duration of symptoms prior to treatment, the less likely is improvement after AVM obliteration.

2.1.2.3 Neurological deficit

Non-haemorrhagic focal neurological symptoms in AVM patients are infrequent and appear to be dependent upon the location of the AVM. Most commonly it is lesions within the middle cerebral artery (MCA) distribution that cause neurological deficit. Large basal ganglia lesions may present with slowly progressive dementia, hemiparesis or visual field defect, whilst occasionally brainstem AVMs produce motor or sensory deficit with or without cranial nerve involvement. Symptoms may be permanent, transient or progressive (Michelson, 1979). Non-progressive focal neurological deficit is seen in 7.2% of individuals (stable 4.6%, reversible 2.6%) whilst progressive deficit is seen in only 1.3% (Crawford, 1986a; Crawford, 1986b; Mast, 1995).

The cause of neurological deficit remains uncertain: recurrent haemorrhages, multiple microinfarcts, decreased perfusion because of arterial stenoses, venous hypertension, or 'steal' have all been proposed as possible aetiological mechanisms.

2.1.2.4 Other presenting symptoms

Patients with AVMs often complain of headaches although, as a primary symptom, they are unusual. Pain tends to be well localised, unilateral and throbbing and is often difficult to distinguish from other types of vascular headache (Dembo, 1982). Headache occurs more frequently in AVMs that have a significant dural or pial component and despite treatment of the lesion it often persists (Stein and Kader, 1992; Valavanis, 1996). Cranial bruits are present in 25% of cases and are again especially common with dural AVMs.

Patients may rarely present with raised intracranial pressure, or more commonly, symptoms of localised mass effect such as trigeminal neuralgia. Paediatric patients with large AVMs or vein of Galen aneurysms can present with obstructive hydrocephalus or, if there is significant shunting thorough the lesion, cardiac failure.

2.1.3 Natural history

Knowledge of the natural history of a disease process is a prerequisite for evaluating the influence of any treatment modality on the course of that disease. This is especially true when the risks of therapy may be profound. Recently it has become difficult to identify large groups of untreated patients with AVMs in which to study natural history because of the availability of various treatments. In attempting to elucidate the natural history of AVMs, it is clear that there is a tendency to include patients with more complex lesions in the analyses of untreated patients because the more straightforward lesions are more likely to have been treated.

In their prospective study, Ondra *et al.* (Ondra, 1990) found the annual rate of mortality was 1% and that of severe morbidity 1.7%, these rates being constant over the course of the study. Eighty-five percent of the patients who bled, corresponding to 34% of the patient population of the study, either died or suffered severe morbidity during the 24 years of the study. Other studies have had similar findings (Michelson, 1979; Brown, 1988). Each haemorrhage has an associated 10 - 13% mortality and 30% serious morbidity (Perret and Nishioka, 1966b; Graf, 1983; Heros, 1993). There is a higher incidence of neurological deficits with an intracerebral haemorrhage (ICH) (90.2%) than SAH (56.8%) and the younger the patient, the better the prognosis (Graf, 1983; Itoyama, 1989).

Several authors have demonstrated a worsening mortality and morbidity with repeat haemorrhages (Wilkins, 1985; Brown, 1996; Hartmann, 1998). In one study, the 30 day mortality after the first haemorrhage was 17.6%, but increased dramatically after the second haemorrhage to 50% (Brown, 1996). Overall mortality from the first haemorrhage is 10%, 13% from the second haemorrhage and 20% from subsequent haemorrhages (Wilkins, 1985). Other studies have found no correlation between the number of haemorrhages and outcome although agree that prognosis is worse in those who have bled when compared with those who have not (Itoyama, 1989).

Death from all causes in patients with AVMs is 29% at 20 years and 18% at 10 years, of which 15% are directly attributable to the AVM (Michelson, 1979; Crawford, 1986a). The risk of death does not appear to be dependent on the mode of presentation, size or depth of the AVM, although patients with parietal lobe AVMs have a lower risk of death at 20 years (Crawford, 1986a; Ondra, 1990). Of those who do not die in the first two decades following presentation, 33% will have had no further symptoms, 22% will be in a fair condition and 29% will be disabled (Michelson, 1979).

2.2 Pathological Considerations

2.2.1 Pathogenesis

AVMs are presumed to be congenital in origin. This is supported by the following observations: there is no growth by neoplasia; there is generally no history of trauma, stroke, or other potential cause of a vascular fistula; they cannot be produced experimentally; they rarely become symptomatic after the sixth decade of life; they appear to develop by displacing the maturing brain to its margins and preserving neurological function (Stein and Kader, 1992). That AVMs occur in association with genetic disorders, for example Sturge–Weber, Wyburn-Mason, ataxia telangiectasia and Osler-Weber-Rendu syndromes has also been used as evidence that they are developmental lesions.

The pathogenesis of AVMs is generally attributed to maldevelopment of the cerebral vascular system during the 40 to 80 mm length stage of human embryogenesis, when there is division of vessels into primitive arteries, capillaries and veins (Stein and Wolpert, 1980; Dembo, 1982; Mullan, 1996). However, the underlying anomaly ultimately responsible for the vascular malformation still remains a matter of controversy. Between the 7^{th} week and the end of the first trimester, the primitive penetrating vessels of the brain exist as an anastomotic

plexus that undergoes a continuous remodelling process characterised by the addition and elimination of vascular connections. In 1928, Dandy (Dandy, 1928) postulated that retention of primordial arteriovenous connections from the fetal intracranial vasculature could result in the development of AVMs. Subsequent theories of the causes of AVMs have focused on the persistence of an arteriovenous connection from the fetal intracranial vasculature with the failed development of an intervening capillary network. It has been suggested that a primary maldevelopment of primordial capillaries could result in the disturbed formation of local arteries and veins and that such a dysplastic vascular plexus could account for the spectrum of lesions encountered. Yasargil (Yasargil, 1987) suggests that persistence of the embryonal plexus will lead to a pure plexiform type containing vessels without direct arteriovenous fistulae. A gradual but incomplete destruction of the embryonal plexus will result in a mixed type of malformation, composed of both plexiform connections and direct arteriovenous fistulae; gradual but complete destruction of the plexiform parts will ultimately result in a pure direct arteriovenous fistula

Alternatively, some have postulated that the primary abnormality lies within a disturbed venous drainage system, particularly in view of the venous abnormalities often associated with AVMs (Yasargil, 1987; Mullan, 1996; Nussbaum, 1998). AVMs frequently incorporate evidence of an early failure in venous maturation, such as absence of middle cerebral vein (MCV) or a recognisable connection between it and the cavernous sinus or an AVM exit channel running in an abnormal direction to that found in adult morphology. This suggests that AVMs are already in place before the MCV connects to the cavernous sinus immediately after birth. On closer examination, persistence of a well-recognised earlier venous pathway can often be demonstrated (Mullan, 1996). However, should an arteriovenous fistulous communication take place, the increased flow through the venous side would prohibit the venous regression, which normally occurs as more definitive channels take over.

On the arterial side, the multitude and lack of functional architecture of arteries terminating within the AVM might suggest that they belong to a relatively primitive penetrating vessel. However, these could appear much later under the influence of an appropriate vasogenic hormone (Mullan, 1996). Interestingly, at a microscopic level, veins of AVMs tend to retain their embryonic character, whilst arteries appear to undergo normal developmental maturation (Deshpande and Vidyasagar, 1980; Nussbaum, 1998).

There is evidence that up to a half of these lesions increase in size with time, with increasing enlargement and tortuosity of feeding arteries and draining veins (Drake, 1979; Michelson, 1979; Stein and Wolpert, 1980; Crowell, 1985). This tendency to enlarge is dependent upon the age at which the initial diagnosis was made: the younger the patient at the time of angiography, the more marked the growth. With enlargement, they often progress from a low flow to high flow lesions. It may be that haemodynamic disturbances such as venous outflow obstruction open previous arteriovenous connections, causing a pulse synchronous expansion of abnormal feeding vessels or a gradual dilatation of vessels by haemodynamic stresses (Wakabayashi, 1991; Nussbaum, 1998). Other hypotheses include a local increase in angiogenic factors due to chronically raised intraluminal pressure or indirectly from decreased tissue perfusion with resultant tissue hypoxia (Nussbaum, 1998). Alternatively, haemorrhage from venous overload may be the stimulus for angiogenesis (Nussbaum, 1998).

2.2.2 Elements of an AVM

2.2.2.1 Nidus

The nidus represents the area of arteriovenous shunting within the AVM, and although often difficult to identify precisely, is probably best regarded as that part of the AVM which is interposed between the recognisable feeding arteries and larger terminal draining veins. The nidus of the AVM is composed of a conglomerate of

vascular loops, whose precise origin remains a source of controversy. Some feel they represent abnormal vascular channels, others that they are embryonic veins or normal veins arterialised by high blood flow and pressure.

Microscopically, vascular channels range from well-differentiated arteries and veins to thick-walled, hyalinised channels. In the arteries, the normal lamination of elastica and muscularis is altered with segmental dilatation (Crowell, 1985). They show medial hypertrophy, endothelial thickening with hyaline change and thrombosis and secondary degeneration with fibrosis and atheroma may occur (Stein and Wolpert, 1980). These changes may be caused by mechanical stresses induced by long-standing high flow and may cause an increased risk of stagnation and retrograde thrombosis of former arterial feeders with treatment of the AVM (al-Rodhan, 1993). Calcification of vessels is present in a significant number of lesions and may be prominent (McCormick, 1966; Michelson, 1979; Dembo, 1982). The veins usually have thickened collagenous walls and appear arterialised yet the increased cellularity in their walls depends on proliferation of fibroblasts, not of smooth muscle cells. The abnormal dilated feeding arteries, draining veins and angiomatous nidus are often located primarily in white matter.

AVMs can broadly be divided into two main categories: those with a single nidus (with all the vascular channels somehow interrelated) and those with more than one nidus in which there are adjacent but individually separated components of the malformation. Most AVMs exhibit a defined compact nidus with clearly discernible boundaries and identifiable arterial inlet and venous outlet. In fewer than 10% of cases, the nidus appears as a diffuse, irregular vascular area without clear delineation of the arterial entry zone or the venous exit zone. The nidus may be composed of a single or multiple vascular compartments, where a compartment is defined as an intranidal vascular unit, characterised by one or more feeding arteries, arteriovenous shunting and a unique draining vein. These compartments within the AVM nidus are not rigid well-defined anatomical units but haemodynamic units that may communicate.

Degeneration of parenchyma around and within the malformation is almost constant, with no intervening brain tissue usually being found between vascular loops of the malformation except in cases of a loosely arranged AVM nidus (McCormick, 1966). Any cerebral tissue remaining in the interstices is generally gliotic and considered non-functional, with haemosiderin pigmentation and foci of calcification (Stein and Wolpert, 1980; Kalimo, 1997). This has also been confirmed using functional MRI (Schlosser, 1997).

2.2.2.2 Arterial feeders

Recognition of the type, number and associated angioarchitectural features of feeding arteries is very important in understanding the structure of the AVM and for planning treatment.

Cerebral arteries may be related to a malformation in one of three ways: as a terminal feeding artery, a transit (partially participating) feeding artery or as an artery 'en-passage' (non-participating) non-feeding artery.

Terminal feeding arteries may arise as far proximal as the anterior, middle and posterior cerebral arteries or as far distal as the fourth or fifth branching of these vessels. This type of feeder ends directly in the nidus but, before doing so, gives off branches to normal brain. They may be markedly dilated and tortuous, but often decrease in calibre following treatment of the AVM. Embolisation performed through a terminal feeder is safe, provided the catheter tip is positioned within the distal segment of the artery. The risk of ischaemic complications associated with embolisation relates to brain parenchyma proximal to the AVM. Such complications are caused by reflux of the embolic agent into more proximal segments and inadvertent occlusion of normal branches.

Transit arteries with participation are usually enlarged and seem to enter the malformation. They give off side branches, which feed the AVM but then continue on to supply normal brain beyond. These must be traced to the point where the branches enter the malformation before definitive ligation or embolisation is

undertaken. Arteries 'en passage' are not enlarged but are running in the vicinity of the AVM and often appear to be part of the lesion.

2.2.2.3 Venous drainage

Draining veins are usually divided into superficial groups, which drain into the sagittal, sphenoparietal, cavernous, transverse and sigmoid sinuses, and deep groups which pass to the subependymal collecting system and subsequently into the internal cerebral veins, basal vein of Rosenthal, internal occipital vein, into the vein of Galen and hence into the straight sinus and torcular or petrosal sinuses.

In most cases drainage seems to follow the expected cortical or subcortical vein in the area, but at times unusual routes of drainage are noted, reflecting either pre-existing embryonic channels or perhaps normal small transcerebral venous systems. Unexpected venous drainage most probably represents a secondary event following thrombosis of the anatomically expected draining vein and therefore corresponds to the development of venous collateral circulation, which distributes the increased venous pressure from the AVM into normal veins. Extensive venous collateralisation decreases the risk of rupture and prevents the development of neurological symptoms. Depending on the location of the AVM, collateral rerouting may occur by way of ipsilateral, contralateral or transcerebral veins.

Failure of the venous collateral circulation to compensate for the venous hypertension results in the formation of a focal venous ectasia or varix proximally and the development of acute or progressive, transient or permanent clinical symptoms. Such venous ectasias or varices are vulnerable to rupture and their angiographic demonstration indicates an increased risk of haemorrhage.

2.2.2.4 Sinuses

Sinuses may also be altered by the presence of an AVM, particularly large high flow lesions. Flow directions may be abnormal owing to increased pressure of the arterial input of the AVM being reflected in the venous drainage, or to

anomalous construction of the sinuses themselves. There may be agenesis or obliteration of the sigmoid, transverse, straight and even sagittal sinuses. With sinus obliteration (in cases of callosal, parathalamic, occipital or cerebellar AVMs) embryonic connections, which normally involute, may persist. For example, there is frequently a communication between the vein of Galen and the superior sagittal sinus (SSS) when the straight sinus is occluded.

Viñuela *et al.* (Viñuela, 1985) found angiographic evidence of major venous wall irregularities or stenoses of the galenic system in 14 cases and occlusion of the deep venous system in seven cases of a total of 53 patients with AVMs. Numerous venous collaterals through medullary and cortical regional veins were noted and there was a late drainage through the basal vein of Rosenthal in all cases. They suggested that the abnormal haemodynamic patterns produced by the drainage from AVMs into the vein of Galen and straight sinus might lead to a high incidence of venous occlusion and stenosis. This might, in turn, lead to the higher than expected incidence of intracranial haemorrhage in deep-seated AVMs, which tend to have such drainage patterns. Yasargil encountered frequent anomalies of the sinuses including agenesis and stenosis or occlusion, particularly of the straight, transverse and sigmoid sinuses (Yasargil, 1987). This was mostly observed with large parietal, occipital and posterior fossa AVMs, as well as in AVMs with a significant fistulous component. If the normal dural sinuses were absent, the veins often coursed towards primitive embryonic channels and even out to the skull and scalp. As with any high-pressure intracranial fistula, flow may be reversed in the veins and reflux back through the sinuses. Impaired venous outlets in such cases often resulted in a reflux into the internal cerebral vein as well as reversal and redistribution of venous flow.

2.2.3 Association of aneurysm and AVM

The overall incidence of arterial aneurysms associated with AVMs has been reported as between 10 and 20%, 75% of which are on major feeding arteries

(Michelson, 1979; Miyasaka, 1982; Crawford, 1986a; Brown, 1988; Lasjaunias, 1988; Duong, 1998; Hartmann, 1998). In those presenting with haemorrhage, the incidence of associated aneurysms increases to as much as 58% (Perret and Nishioka, 1966b; Lasjaunias, 1988; Turjman, 1995). Their prevalence increases with age and they are found in 8% of individuals with AVMs aged less than 25 years, 24% of those aged 25 - 50 years and in 37% of those aged greater than 50 years (Miyasaka, 1982; Lasjaunias, 1988).

Three hypotheses exist to explain the high occurrence of aneurysms in association with AVMs: firstly, that the development of the aneurysm is secondary to increased blood flow to AVM; secondly, that both aneurysm and AVM are congenital blood vessel abnormalities that develop simultaneously; thirdly, that their existence is merely co-incidental (Wilkins, 1985). Miyasaka *et al.* (Miyasaka, 1982) reviewed the angiograms of 132 consecutive patients with AVMs and found 43 aneurysms in 22 patients (16.7%). They found that aneurysms were more likely to occur in those patients with larger AVMs. They suggested that as the prevalence of AVMs in a large autopsied series of patients with cerebral aneurysms was not significantly higher than in a control group without aneurysms, that the same developmental defect was unlikely to be responsible for both lesions. Similarly the theory of coincidental association was thought to be unlikely. The distribution of aneurysms and infundibula on major feeding vessels to the AVMs, remote from the Circle of Willis, was such that they concluded that haemodynamic changes in the arteries supplying the malformation must have had some role in the aetiology of concurrent aneurysms.

Aneurysms associated with AVMs fall into three broad categories: those found on the enlarged arterial feeders, but in locations in which aneurysms are often found to arise spontaneously (proximal, related) (35 - 57%); those occurring on feeding vessels in the vicinity of an AVM but at locations in which it is unusual to find aneurysms arising in the absence of an AVM (distal, related) (20%); and finally those which arise at locations seemingly unrelated to the AVM (unrelated) (24 –

43%) (Perret and Nishioka, 1966b; Lasjaunias, 1988). Distal related aneurysms may be extranidal or intranidal.

Management of combined lesions can be difficult. Most authors suggest treatment of the symptomatic lesion first with up to two thirds of aneurysms showing regression with obliteration of the AVM, rendering further treatment unnecessary (Lasjaunias, 1988; Cunha e Sa, 1992; Stein and Kader, 1992). Aneurysms, which do not regress, may be treated as any other unruptured aneurysm after excision of the AVM. When bleeding occurs in the setting of an associated aneurysm and AVM, it is usually the aneurysm that has ruptured, although the site of extravasated blood on CT remains the most accurate way of confirming the source of bleeding prior to treatment (Drake, 1979; Crowell, 1985). Lasjaunias *et al.* suggest that the presence of aneurysms indicates the most high flow feeders and therefore allows targeted endovascular treatment (Lasjaunias, 1988).

Aneurysms often have a thinner and weaker wall than other arterial elements of the AVM. As they are exposed to nearly the same arterial pressures as the arterial components of the AVM, they represent the most likely site of rupture following intra-arterial pressure rises, particularly if sudden. Following embolisation of a nidus compartment, a sudden increase in intraarterial pressure involving the non-occluded vessels supplying the remaining AVM may occur, predisposing unprotected aneurysms to rupture. Therefore, embolisation of AVMs should be first performed through feeding arteries either carrying proximal related aneurysms or supplying compartments containing extra or intranidal aneurysms. In addition, venous hypertension, which occurs with stenosis or obstruction of the venous drainage may lead to aneurysmal rupture.

2.3 Classification of AVMs

As ever more sophisticated means of studying AVMs have developed, systems of classification have diversified from the early descriptive terms based purely on morphological observation.

2.3.1 Topographical analysis

Topographic location of an AVM can be classified by combining information obtained from DSA with that from structural imaging in the form of MRI or CT (Berenstein and Lasjaunias, 1992). A summary of this classification is seen in Table 2.1.

Table 2.1: Topography of intracranial AVMs

	Cortical arteries	Perforating arteries	Choroidal arteries	Deep veins	Superficial veins
Cortical	+	-	-	-	+
Cortico-subcortical	+	-	-	- ‡	+
Cortico-ventricular	+	+ *	+ *	+	+
Cortico-callosal	+	-	+ *	+	+
Deep-seated	+ §	+	-	+	+ ‡
Choroid plexus	-	+ *	+	+	+ ‡

from Berenstein (Berenstein and Lasjaunias, 1992)
‡ Can be recruited via transcerebral veins
§ Insular and cerebellar
* Subependymal arterial anastomosis or branches can be seen

Cortical AVMs are exclusively fed by cortical arteries and drain into superficial veins. Cortico-subcortical lesions recruit cortical arteries and drain into superficial veins but may also drain into the deep venous system if the transcerebral venous system is patent. In both cortical and cortico-subcortical lesions, some regions of the cortex drain to deeply located veins that should not be considered as a

part of the true deep venous system. Such vessels include the medial veins of the temporal lobe and the basal vein, the veins of the cerebellar vermis, and the precentral vein.

Cortico-ventricular lesions correspond to the classical pyramidal shaped malformation, reaching the ventricular wall at their apex. Feeding arteries are both perforating and cortical. Draining veins are also deeply and superficially located. Cortico-callosal lesions belong to the cortico-ventricular group as they have the same venous characteristics, however they do not recruit perforating arteries, but are supplied by the cortical arterial network and choroidal arteries.

Deep-seated lesions can be located supra- or infratentorially in the depth of the brain. Their niduses involve the deep nuclei and the long fibre tracts with their arterial and venous connections. They recruit exclusively perforating arteries and drain into the deep venous system. They may use transcerebral veins if patent, either as a direct venous outlet or as a collateral pathway.

Choroid plexus AVMs are fed primarily by choroidal arteries and subependymal arterial feeders arising from the Circle of Willis. Drainage is via ventricular veins, with occasional recruitment of transcerebral veins when patent.

This form of classification is similar to that described by Yasargil who categorised AVMs according to their anatomical location (Yasargil, 1987).

2.3.2 Spetzler classification

Spetzler and Martin (Spetzler and Martin, 1986) proposed a grading system for AVMs in 1986 on the basis that, in making a recommendation for treatment of a patient with an AVM, it was important to estimate the risk of surgery for that patient. A simple, broadly applicable grading system designed to predict the risk of morbidity and mortality associated with surgical treatment of a specific AVM was proposed. The lesion is graded on size, pattern of venous drainage and eloquence of adjacent parenchyma with a total of six grades (Table 2.2). Points for each of these features are added together to give the grade of the AVM from grade I to V. They

also included a grade VI for those extremely large diffuse AVMs involving critical structures. These lesions were felt to fall into a separate 'inoperable' category. Retrospective application of the grading scheme to their series of surgically excised AVMs demonstrated its correlation with the incidence of post-operative neurological complications.

Table 2.2: Determination of AVM Spetzler grade

Graded Feature	Points Assigned
Size of AVM	
small (< 3cm)	1
medium (3-6cm)	2
large (> 6cm)	3
Eloquence of adjacent brain	
non-eloquent	0
eloquent	1
Pattern of venous drainage	
superficial only	0
deep	1

from Spetzler (Spetzler and Martin, 1986)

2.4 Haemodynamics

2.4.1 Cerebral blood flow

Normal cerebral blood flow (CBF) ranges from 36 to 82 ml $100g^{-1}$ min^{-1} in normal subjects, 80% is distributed to the cerebral cortex and 20% to the white matter. This represents a cerebral perfusion volume of approximately 750 ml min^{-1}, equivalent to 15% of the resting cardiac output. The brain accounts for about 20%

of the body's total oxygen consumption. CBF values of greater than 170 ml $100g^{-1}$ min^{-1} have been found in patients with cerebral AVMs (Deutsch, 1983).

Regardless of the fluid flowing through a vessel, the smaller the calibre and greater the length, the greater the resistance to flow. Flow is inversely related to resistance and directly proportional to the pressure gradient along the vessel. Vessels in parallel will have less resistance than vessels in series; an AVM must be considered as a combination of these.

Blood vessels are able to distend and contract, which can greatly affect the volume and rate of blood flow through them. As these vessels are not rigid, they require a certain amount of pressure within them to remain patent. In arterioles and larger vessels, the pressure required for distension is also highly dependent upon muscular tone. As veins contain a smaller amount of muscular and elastic tissue, they are more readily distensible but tend to collapse when intraluminal pressure is low. The expansibility of veins allows them to hold a large capacity of blood.

2.4.1.1 Neuronal Control

The cerebral vasculature has a rich extrinsic innervation from the autonomic nervous system, but this supply is to pial vessels only. The extrinsic sympathetic supply is derived from the superior cervical ganglion. The parasympathetic fibres (which originate in the brainstem nuclei) travel via the facial nerve through the sphenopalatine ganglion and thence to the perivascular neural plexus. Despite its extensive input, the functional significance of extrinsic autonomic regulation of CBF remains unclear. The cerebral vasculature also receives input from the intrinsic neural regulatory systems originating in the brainstem. Experimental electrical stimulation of these areas results in a significant increase in CBF.

2.4.1.2 Chemical mediators

The precise chemical mechanisms by which vascular smooth muscle tone is determined remain unknown. Modulators of cerebral vascular tone are thought to

include the vasodilators acetylcholine, adenosine, calcitonin gene-related peptide, vasoactive intestinal peptide, substance P and nitric oxide and the vasoconstrictors neuropeptide Y and endothelin 1.

2.4.2 Regulation of cerebral blood flow

CBF is normally tightly controlled by two major mechanisms: autoregulation and chemoregulation/metabolic coupling. It is also affected by a variety of other mediators, in particular arterial partial pressure of carbon dioxide.

2.4.2.1 Autoregulation

Autoregulation is the process by which CBF remains at a relatively constant level despite variations in cerebral perfusion pressure (CPP), where :

CPP = systemic arterial blood pressure - intracranial pressure

Vascular tone in resistance vessels is determined by transmural pressure, an increase in which produces vasoconstriction and a reduction in flow, and *vice versa.* Blood flow to the brain can be constantly maintained between a systemic arterial blood pressure of approximately 50 to 180mmHg. Resistance vessels are maximally vasodilated at a CPP of 40mmHg; vasoconstriction is maximal at a CPP of 180mmHg. Beyond these limits, CBF changes in direct proportion to the systemic blood pressure.

2.4.2.2 Chemoregulation/metabolic coupling of cerebral blood flow

Local CBF is determined by cerebral metabolism. The oxygen consumption of human brain (cerebral metabolic rate for oxygen, $CMRO_2$) is usually fairly stable, in the range 3.0 – 3.8 ml $100g^{-1}$ min^{-1}. The coupling of cerebral metabolism with CBF is referred to as chemoregulation/metabolic coupling. Brain $CMRO_2$ is significantly influenced by temperature with a 5% reduction in $CMRO_2$ with every 1°C drop in temperature.

2.4.2.3 Effects of Carbon Dioxide

Hypercapnia increases cerebrovascular resistance, which in turn decreases CBF and cerebral vascular volume; hypocapnia has the opposite effect. This CBF response is mediated by changes in extracellular hydrogen ion concentration.

2.4.3 Flow Dynamics within AVMs

A more thorough knowledge of basic circulatory mechanisms and their control within AVMs and the surrounding parenchyma is essential if their treatment is to become more effective and safer. Haemodynamics in draining veins appears to play a particularly important role in the stability of AVMs and it is therefore important to establish the range of values of normal cerebral vein velocities and the range of flow velocities of draining veins of AVMs; knowledge of both could, for example, provide points of reference that may help determine the elimination of arteriovenous shunting and the restoration of normal haemodynamics in the cerebral venous system as endpoints for endovascular intervention.

However, detailed and accurate haemodynamic characterisation of an AVM nidus is currently not possible in practice because of the usual angioarchitectural complexity of cerebral AVMs (particularly in those referred for embolisation), the fragile nature and small size of vessels within the nidus that renders them inaccessible to safe microcatheterisation and the limitations of current imaging modalities that are unable to clearly resolve individual vascular components of the nidus. Therefore, in assessing the haemodynamic consequences of the presence of an AVM, the acquisition of flow and pressure information from AVM arterial feeders and draining veins is a feasible alternative to haemodynamic data obtained directly from the nidus of the AVM (Murayama, 1998).

2.4.3.1 Feeding artery and draining vein pressures

Most studies demonstrate a reduction in feeding artery pressure (FAP) to 40 – 50% of systemic arterial pressure (Nornes and Grip, 1980; Handa, 1993; Kader

and Young, 1996). It appears that the intra-arterial pressure decreases with distance along the arterial tree, although pressure drops are particularly exaggerated at major branch points. The fall in pressure is proportional to the number and length (greater than 8cm from the Circle of Willis in particular) of feeding arteries (Nornes and Grip, 1980). This may be in part related to the AVM size, since FAP is inversely proportional to AVM size (Spetzler, 1992).

The magnitude of flow through a fistula is inversely proportional to the resistance across it. Therefore, FAP should be lower in large high-flow lesions. By measuring blood velocity in arterial feeders, TCD may provide an estimation of flow thorough an AVM. TCD velocities in the parent vessels of feeding arteries to the AVM have been found to correlate with lesion size (Fleischer, 1993; Kader, 1994). In addition, Fleischer *et al.* (Fleischer, 1993) confirmed a significant inverse correlation between FAP and parent vessel peak velocity.

The pressure within draining veins, however, is increased compared with normal cerebral veins (Nornes and Grip, 1980; Young, 1994). FAP and superficial draining vein pressure (DVP) appear to have a parallel relationship, in that higher arterial pressure is associated with higher venous pressure (Young, 1994). This suggests that the nidus allows some transmission of arterial pressure to the draining vein. Contrary to this however, is the observation that increases in systemic pressure do not influence DVP (Young, 1994; Kader and Young, 1996). It may be that the nidus does not behave simply as a passive conduit for pressure transmission, but that there is a pressure buffering effect by the feeding arteries (Kader and Young, 1996). In addition the transnidal pressure drop or net CPP gradient is inversely correlated with AVM size (Young, 1994).

2.4.3.2 'Steal' phenomenon

Shunting of blood through an AVM is exclusively pressure-dependent, in contrast to flow through normal vasculature of the central nervous system in which flow is autoregulated. If an AVM causes a 'sump' effect on the surrounding

cerebral tissue, there is no physiological mechanism that enables redistribution of flow. As a consequence, the perfusion pressure to the surrounding brain is reduced with an associated decrease in relative CBF (rCBF) (Deruty, 1996). It has been suggested that this may be responsible for certain neurological deficits, defined as 'steal'. This concept is the subject of considerable controversy.

There have been reports of angiographic evidence of 'steal' with poor filling of adjacent vessels (Norlen, 1949; Feindel, 1971; Leblanc and Little, 1990; Sorimachi, 1995). Removal of the AVM allows normal filling of these vessels on angiography. There also appears to be poor activity demonstrated by functional MRI immediately adjacent to the AVM. It has been suggested that this gives weight to the argument proposing that 'steal' exists and that blood is being diverted away from normal tissue by a sump effect of the AVM (Beltramello, 1996). Okabe *et al.* (Okabe, 1983) studied rCBF before and after AVM excision, comparing the classical method of scintillation detection of radioactive xenon with stable xenon CT. Compared with age-matched controls, rCBF values in patients were significantly reduced in areas adjacent to the AVM in both grey and white matter. Hemispheric flows were also significantly reduced compared to normal controls for grey matter throughout, with a significantly reduced rCBF in the ipsilateral hemisphere compared with the contralateral hemisphere. These differences were not seen in white matter. After successful surgical removal of the AVM, mean rCBF returned to normal in both grey and white matter and areas adjacent to the AVM and the contralateral hemisphere. Okabe's finding that the grey matter was subject to the greatest degree of vascular 'steal' might be expected, as grey matter receives a greater proportion of blood than does white matter.

Cerebral autoregulation maintains CBF relatively constant over a wide range of perfusion pressures and above the threshold for ischaemia. The lower limit of autoregulation in humans is normally approximately 50mmHg (Kader and Young, 1996). However, more than half of all AVM patients have a distal pressure of less than 40mmHg, significantly below the lower limit of autoregulation (Kader and

Young, 1996). Even increasing systemic mean arterial pressure by 25mmHg with phenylephrine fails to increase CBF in these hypotensive vascular territories (Young, 1994; Kader and Young, 1996). This suggests that chronic hypotension does not necessarily result in impaired autoregulation or vasomotor paralysis with loss of ability to vasoconstrict in order to prevent acute increases in perfusion pressure. Instead it appears to adaptively displace the lower limit of autoregulation in affected vascular territories by a shift of the autoregulatory curve to the left. In other words, the pressure at which the resistance vessels of the brain become maximally dilated and therefore CBF begins to change in a passive fashion with increases in arterial pressure is reset to a lower level (Hacein-Bey, 1995; Kader and Young, 1996). This is supported by the fact that, although perfusion deficits can appear after vasodilatation, secondary to hypercapnia obtained by acetazolamide administration, it appears to occur at a much lower pressure than is commonly thought to be the lower limit of autoregulation (Hacein-Bey, 1995). The mechanism by which this occurs is not known. AVMs may therefore induce cerebral hypotension, most probably related to high bulk flow through the conductance vessels that supply the low resistance AVM nidus. However, these hypotensive areas often seem to have normal vasoreactivity and are able to function normally with CBF reset to a slightly lower level (Takeuchi, 1987; Kader and Young, 1996).

There are numerous reports of deficits or CBF reductions which are partially or completely resolved with AVM obliteration, although there have been no studies which relate alterations of CBF to specific vascular patterns or pressure changes (Leblanc and Little, 1990; Tanaka, 1993). It would be expected that a severely hypotensive arterial territory should have a compensatory increase in cerebral blood volume (CBV) compared to normal. Although global CBV does appear to be elevated, there is no evidence of a large regional change in CBV corresponding to a decrease in arterial pressure, (Tyler, 1989; Fink, 1992; Kader and Young, 1996). Previous positron emission tomography (PET) and single photon emission CT (SPECT) studies have demonstrated that there is no such increase in CBV in the

regions surrounding the AVM (Takeuchi, 1987; Fink, 1992). In addition, there is no compensatory increase in oxygen or glucose extraction fraction, implying that CBF in the perinidal regions of the AVM, although low, is far above any critical level (Fink, 1992). Kader (Kader and Young, 1996) suggested that rather than demonstrating 'steal', these changes may represent nothing more than the gliotic area often seen around the AVM nidus.

Another possible cause for this coupled reduction in CBF and CBV is a phenomenon similar to the functional disruption in areas remote from strokes termed 'diaschisis', a transient event in which a reduction of rCBF is seen in uninvolved areas distant from an acute stroke (Homan, 1986; Tyler, 1989; Meyer, 1991; Tanaka, 1993; Kader and Young, 1996; Yamada, 1999). Patterns of distant diaschisis in the thalamus, brainstem and contralateral cerebellum have been seen in AVM patients (Homan, 1986; Tyler, 1989; Tanaka, 1993). This suggests some remote anatomical or functional neural derangement unrelated to the haemodynamic effects of the arteriovenous shunt. Although the mechanism and significance of diaschisis remain controversial, it is thought that, following acute localised lesions of the central nervous system (arising from any cause), there is a loss of afferent and efferent axons in one area, causing cell body loss or decreased cell body activity in remote cortical or subcortical regions owing to loss of association fibres between the two areas (Tarr, 1990; Meyer, 1991). MRI studies suggest that the neuronal mass within the hypotensive area may be reduced (Tanaka, 1993) and Iizuka *et al.* (Iizuka, 1990) described widespread neuronal degeneration in the thalamus by retrograde degeneration after MCA occlusion in a rat model.

Other possible explanations for focal neurological symptoms previously attributed to 'steal' include focal seizures, previous haemorrhage, venous hypertension or mass effect, with only a minority being due to haemodynamic failure as result of arterial hypotension. Some authors suggest that all of these mechanisms may have a role to play in the neurological symptoms and haemodynamic alterations

associated with AVMs, but that in individual patients, one particular mechanism may predominate (Tarr, 1990).

2.4.4 Haemodynamic changes associated with treatment

Changes associated with treatment can be monitored and can be useful in assessing progress in the obliteration of the fistula. Post-operatively, there is an increase in arterial pressure in feeders with an increase in stump pressure of approximately 50% on pre-occlusive levels with an associated drop in venous pressure (Nornes and Grip, 1980; Hassler and Steinmetz, 1987; Handa, 1993). The ratio of systemic arterial blood pressure to FAP increases by about 20% to approximately 60 – 70% of normal systemic arterial pressure, this ratio normally being 90% (Handa, 1993). This results in an acute rise in the arteriovenous pressure gradient and normalisation of perfusion pressure (Nornes and Grip, 1980; Kader and Young, 1996; Murayama, 1998).

Transvenous assessment of flow velocity may be more useful than transarterial assessment of pressure in the haemodynamic evaluation of arteriovenous shunting during embolisation. Convergence of peak systolic and end-diastolic draining vein velocities to differences below 10 cm sec^{-1} are associated with complete embolisation. This is unlike the changes observed in FAP after embolisation in which the pressure rises are parallel to the pressure values measured before embolisation (Murayama, 1998).

2.4.4.1 Normal perfusion pressure breakthrough

Complications, including both oedema and haemorrhage, may follow the eradication of an AVM. This occurs rarely in 2 – 4% of individuals and is most commonly seen in large high-flow AVMs with numerous large calibre feeding arteries (Spetzler, 1978; Morgan, 1993; Kader and Young, 1996; Young, 1996). The normal perfusion pressure breakthrough theory was proposed by Spetzler (Spetzler, 1978) in 1978 to account for and describe the onset of acute cerebral

swelling and haemorrhage following excision of large AVMs. Spetzler suggested that, in the presence of a large AVM, the nidus offers no resistance, resulting in intracranial steal and relative ischaemia of the surrounding hemisphere. This leads to vasomotor paralysis and loss of autoregulation in the surrounding vessels, which remain maximally dilated. After occlusion, flow is redirected to the surrounding hemisphere as it returns to normal perfusion pressure. Nornes *et al.* (Nornes and Grip, 1980) demonstrated an immediate rise in stump pressure in arterial feeders following a test occlusion. By correcting for a decrease in venous pressure following occlusion, the rise in the CBF of surrounding parenchyma becomes even more dramatic. Unable to autoregulate, the paralysed vessels do not constrict in response to the increased perfusion pressure and oedema and haemorrhage result. Barnett *et al.* (Barnett, 1987) found that the two patients in their series who developed normal perfusion pressure breakthrough following surgery had low local cortical blood flow and disturbed carbon dioxide reactivity before AVM excision with a marked increase in local cortical blood flow after excision. Batjer *et al.* (Batjer, 1988) also confirmed that these complications were seen most commonly in patients who had a significantly depressed hemispheric CBF before treatment which increased dramatically following embolisation compared with the unaffected group. Nornes *et al.* (Nornes and Grip, 1980) noted that, in their experience, this complication was seen most commonly in those AVMs with long feeders, greater than 8cm when measured from the Circle of Willis. They demonstrated that these long feeding vessels had a greater pressure drop from systemic arterial blood pressure to the intravascular pressure measured immediately proximal to the AVM, with associated higher velocities. They sought to explain this by suggesting that these vessels gave rise to more branches prior to termination within the malformation, which would, by necessity, be maximally dilated to divert blood tending to pass preferentially into the lower resistance AVM. In order to prevent these dramatic changes in cerebral haemodynamics with AVM obliteration, Spetzler

recommended staging treatment with two or more procedures involving partial embolisation or resection.

Whilst there is general agreement that resection, in particular, of high-flow AVMs can be associated with intra- and postoperative complications of oedema and haemorrhage, the underlying mechanisms remain disputed. Hassler *et al.* (Hassler and Steinmetz, 1987) demonstrated normal vasomotor responses to changes in arterial partial pressure of carbon dioxide in all brain-supplying arteries immediately following AVM removal, suggesting that these vessels show preserved autoregulation. It was only the terminal feeding arteries and branches of transit arteries that directly supplied the AVM that showed an impaired response to hyper- and hypocapnia. Alternative hypotheses have therefore been proposed. Some suggest that perioperative hypoperfusion could lead to microinfarcts, with resultant oedema and haemorrhage post-operatively when the systemic blood pressure is returned to more normal levels (Morgan and Sundt, 1989). Alternatively, spontaneous thrombosis or inadvertent surgical ligation of a major draining vein distally may lead to occlusive hyperaemia (Wilson and Hieshima, 1993). The sudden drop of DVP to almost zero following excision of the AVM is likely to predispose to an increased risk of thrombotic occlusion. On the arterial side of the system, some authors have hypothesised that retrograde thrombosis of feeding vessels may have the same effect, supported by the fact that postoperative angiograms in affected individuals show stagnant or very slow arterial flow (al-Rodhan, 1993). Miyasaka *et al.* (Miyasaka, 1990) reported retrograde thrombosis of former feeders in five (6.6%) of 76 patients. The incidence increased to 14% when only medium-sized and large AVMs were considered.

Another mechanism that has been proposed is a derangement in the autonomic perivascular innervation, which can profoundly influence CBF and would be compatible with certain paradoxical CBF responses in AVM patients (Young, 1996). Batjer *et al.* (Batjer, 1988) argues that post-treatment hyperaemia is caused by a deranged vascular bed that actively participates in swelling. Local changes in

peptidergic activity in adjacent circulatory regions may somehow affect distant beds by collateral innervation. Such a mechanism might explain why there is a global increase in CBF after many cases of AVM resection, which cannot be explained by local changes in perfusion pressure. A final explanation that may result in such complications is that resection of the AVM may have been incomplete and that post-operative haemorrhage may be as a result of rupture of an underlying remnant.

2.5 Risk factors for haemorrhage

Prevention of spontaneous haemorrhage is the primary objective of AVM treatment, but the risks of treatment (especially for larger lesions) can be high. For this reason, identification of risk factors, particularly modifiable risk factors, is important in allowing a more targeted approach in cases where only partial treatment is possible. Many authors have hypothesised that there must exist a finite set of pathophysiological conditions, coupled with anatomic aberrations, that result in spontaneous ICH and that it ought to be possible to identify such factors (Kader, 1994).

2.5.1 Patient factors

2.5.1.1 Gender

Male patients appear to be at greater risk of a haemorrhage in the first year after presentation whilst females are at a greater risk in the first 10 years. The average annual risk for females is 3-4%, whilst males average 2% per year. However, at 20 years following diagnosis, males and females are equally affected (Graf, 1983).

There is considerable disagreement as to whether pregnancy is a risk factor for haemorrhage. In one series, one in four female patients aged 20 – 29 years were pregnant at the time of presentation with haemorrhage, suggesting that pregnancy may be a risk factor (Crawford, 1986a). Other series have found that pregnancy is

not a risk factor for haemorrhage, but most recommend that vaginal delivery should be avoided (Stein and Kader, 1992).

2.5.1.2 Age

The older the patient the greater the risk of haemorrhage (Graf, 1983; Crawford, 1986a). In those aged greater than 60 years, the nine year risk is 89% whilst in those aged 20-29 years, it is only 15% (Crawford, 1986a).

2.5.1.3 Presentation

In a series of 217 conservatively treated individuals (from a total population of 343 AVM patients), Crawford *et al.* (Crawford, 1986a) found that patients had a 42% 20 year and 30% 10 year overall chance of developing haemorrhagic complications. There was a slight increase in the risk of haemorrhage in the first two years after diagnosis but this settled to 2% per year. This risk varied depending on symptoms at diagnosis. In individuals presenting initially with haemorrhage, the risk of a further haemorrhage was higher (51% 20 year risk, 36% 10 year risk) than in those who had not bled (33% 20 year risk, 17% 10 year risk). In those whose presenting complaint was epilepsy, the risk of haemorrhage at 20 years was 30% (22% at 10 years), whilst those presenting with a neurological deficit had only an 8% risk of haemorrhage at 20 years (8% at 10 years). Of those AVMs found incidentally, no patient bled. Graf *et al.* (Graf, 1983) confirmed that patients presenting with convulsions were at a lower risk of haemorrhage of 30% at 10 years, whilst those not presenting with seizures had a 45% 10 year risk of haemorrhage.

2.5.2 AVM factors

2.5.2.1 Site of AVM

Deep AVMs, such as basal ganglia and posterior fossa lesions, more commonly present with haemorrhage whilst superficial lesions more commonly present with epilepsy (Crawford, 1986a; Turjman, 1995; Duong, 1998; Mansmann,

2000). This may however not be independent of the fact that these deep lesions are often associated with deep venous drainage. Temporal or occipital lesions have a higher risk of presenting with haemorrhage (67% and 52% at 20 years and 36% and 42% at 10 years respectively), whilst parietal AVMs are associated with a lower risk of subsequent haemorrhage (32% at 20 years and 23% at 10 years) (Crawford, 1986a). Many deep lesions are non-cortical and are therefore perhaps unlikely to cause seizures, the second most common presenting symptom, making them more likely to present with haemorrhage.

2.5.2.2 Size of AVM

Small AVMs more commonly present with haemorrhage whilst large AVMs more commonly present with epilepsy, although the risk of rehaemorrhage does not appear to be dependent upon size (Guidetti and Delitala, 1980; Graf, 1983; Crawford, 1986a; Albert, 1990; Spetzler, 1992; Kader, 1994; Duong, 1998; Mansmann, 2000). In their series of 110 patients, Albert *et al.* (Albert, 1990) found that of those patients presenting with haemorrhage, 12 had large AVMs, 45 had medium AVMs and 53 had small AVMs. In contrast, of the 40 patients whose presentation was non-haemorrhagic, only four had small AVMs. They pointed out however that this may not be independent of the fact that most small AVMs have a single draining vein.

An alternative explanation may exist for the fact that small AVMs present more commonly with haemorrhage than large AVMs. Small and large AVMs may have similar haemorrhage risks, but small AVMs may fail to become symptomatic in other ways, such as seizures or progressive neurological deficit, in the way that large AVMs do. However, if this were the case, it might be expected that large AVMs would come to medical attention at an earlier age than smaller AVMs, presenting with symptoms other than haemorrhage. Identical age at time of presentation in haemorrhage and non-haemorrhage groups supports the hypothesis that small AVMs do indeed have a higher risk of haemorrhage (Kader, 1994). Conversely, large and

small AVMs may bleed at similar rates, but haemorrhages from large AVMs may be less likely to be clinically evident. The size of the haematoma does appear to be inversely related to the size of the AVM, thought to be due to the higher FAP and higher perfusion pressures seen in smaller AVMs (Spetzler, 1992; Duong, 1998). As many as 10% of individuals have evidence of previous clinically silent haemorrhage at the time of surgery, although this has not been specifically related to AVM size (Stein and Wolpert, 1980).

2.5.3 Angiographic features

2.5.3.1 AVM nidus

AVMs with a diffuse nidus morphology have been shown to be at increased risk of presenting with haemorrhage (Pollock, 1996a).

2.5.3.2 Arterial supply

Small AVMs are at a higher risk of bleeding than larger lesions and many have hypothesised that this may be because they have a higher pressure in their feeding arteries (Spetzler, 1992; Fleischer, 1993). Spetzler *et al.* (Spetzler, 1992) demonstrated an inverse relationship between FAP and AVM size, regardless of presentation. This difference in FAP is readily explained by a difference in the resistance to flow of small and large AVMs. They also found that the average difference between mean arterial blood pressure and FAP was 6.5 mmHg in those who did not present with haemorrhage, but 40 mmHg in those whose AVM had ruptured (Spetzler, 1992). This has been confirmed by other authors (Miyasaka, 1993; Duong, 1998). Kader *et al.* measured mean FAP just proximal to the nidus with an intravascular microcatheter or intraoperatively by direct puncture using 26-gauge needle (Kader, 1994). Mean FAP was again found to be higher in patients with haemorrhage than those without, although was only weakly related to size of lesion. However it remains unclear whether the increase in FAP is an important

factor in the pathophysiology of AVM haemorrhage or is the haemodynamic sequelae of the AVM rupture (Pollock, 1996a).

There is concern that FAP increases with reduction of AVM size by partial embolisation, thus increasing the risk of haemorrhage immediately following the procedure (Spetzler, 1992). Sorimachi *et al.* (Sorimachi, 1995) found that FAP did increase with gradual obliteration of nidus with an associated increased risk of peri-procedure haemorrhage, particularly in those with low FAP initially and in those with the greatest changes in FAP before and after embolisation. Their overall complication rate was 28% and as a result they advocated staged embolisation (Sorimachi, 1995). If the resistance to flow in a large AVM increases following embolisation, then the FAP in the remaining lesion will be elevated. Assuming that the risk of haemorrhage is related to FAP then the usefulness of partial embolisation as a sole treatment for AVMs needs careful scrutiny. The goal of treatment for AVMs should be complete obliteration (Spetzler, 1992).

The pattern and distribution of feeding arteries is also important. The feeding arteries with transient branches (brain-nutrifying branches distal to nidus) have a higher resistance than an artery terminating in an AVM, resulting in a significantly higher pressure in these vessels (Sorimachi, 1995). The pressure in feeders with terminal divided branches also tend to be lower than in those with single branches although the differences are not statistically significant (Sorimachi, 1995). Perforator feeding vessels and vertebro-basilar supply have also been found to be predictive of a haemorrhagic presentation (Turjman, 1995).

2.5.3.3 Venous drainage

AVM haemorrhage is generally thought to be consistent with venous bleeding, and it is therefore not surprising that venous characteristics predominate amongst risk factors for AVM haemorrhage (Miyasaka, 1992). AVMs with deep venous drainage or a single draining vein are more likely to haemorrhage (Miyasaka, 1992; Kader, 1994; Turjman, 1995; Pollock, 1996a; Duong, 1998). Both of these

factors may have a profound effect on AVM haemodynamics by promoting an increased pressure gradient across the vasculature of the nidus (Miyasaka, 1992; Miyasaka, 1993).

Young *et al.* (Young, 1994) examined AVM physiology and discovered that there was a direct relationship between FAP and DVP. Despite this, the transnidal pressure gradient was lower in large AVMs, possibly explaining the lower incidence of haemorrhage in large AVMs (Spetzler, 1992; Young, 1994). However, DVP alone was neither predictive of AVM haemorrhage nor related to the presence or otherwise of deep venous drainage. This was confirmed by Kader *et al.* (Kader, 1994). Draining vein stenosis, occlusion and venous hypertension may also result in critical haemodynamic stresses that predispose to rupture of AVMs (Miyasaka, 1992; Murayama, 1998; Mansmann, 2000). It has been suggested that turbulent flow and elevated pressure in the deep venous system may compound the problem by promoting enhanced platelet aggregation and thrombosis sufficient to cause AVM haemorrhage (Duong, 1998).

2.5.3.4 Associated aneurysms

Turjman *et al.* (Turjman, 1995) found that both intranidal and multiple aneurysms increased the risk of haemorrhage. This has been confirmed by other authors (Dion and Mathis, 1994). However other studies have found that the presence of aneurysms did not independently predict haemorrhagic complications (Duong, 1998; Mansmann, 2000). Arterial stenoses, angioectasia and arteriovenous fistulae however appear to be protective against haemorrhage (Mansmann, 2000).

2.5.3.5 Combined risk factors

The risk of haemorrhage can be quantified by drawing together several of the known predictive factors. Pollock *et al.* (Pollock, 1996a) suggested such a system. Low risk AVMs consist of those which have not previously bled and have more than one draining vein and a compact nidus. They found the annual risk of haemorrhage

in this group of individuals to be 1.0%. An intermediate low risk group with an annual risk of 2.2% is made up of those with AVMs that again have not previously bled, but have a single draining vein, with or without a diffuse nidus. A third group of intermediate high risk (3.7%) consist of those individuals who have previously had an associated haemorrhage, have more than one draining vein and have a compact nidus. High risk individuals are those that have previously bled, have a single draining vein, with or without diffuse nidus morphology. Their annual risk of haemorrhage was 8.9%.

The management of AVM patients should be based not only on the morbidity of the proposed treatment but also on those factors that predispose individuals to either a low or high haemorrhagic risk. Such systems improve the accuracy of risk-benefit decisions regarding further management of these individuals.

2.6 Investigation

From a morphological point of view, neuroradiological studies should not only identify all feeding arteries and draining veins, but also evaluate the angioarchitecture and other characteristics of the nidus as well as the different manifestations of high flow angiopathy, the associated parenchymatous lesions or other incidental and clinically asymptomatic cerebral pathologies. From the haemodynamic point of view, flow velocities in the different vascular compartments and global modifications of the cerebral circulation should also be evaluated in detail.

2.6.1 Plain Xrays

Although not often used in the routine investigation of a suspected AVM, calcification can be seen on plain skull Xrays in up to 25% of affected individuals. Prominent tortuous vascular channels can also be sometimes identified.

2.6.2 CT scan

CT scans are most commonly used in the clinical setting of acute haemorrhage, where the haematoma is readily identifiable. Most commonly this occurs in the brain parenchyma adjacent to the AVM, with SAH or IVH observed less frequently.

In the absence of haemorrhage, AVMs usually appear as patchy mixed-density lesions on non-contrasted scans. The low density areas may represent areas of infarction or encephalomalacia from previous haemorrhage, whilst high-density areas may be caused by areas of small recent haemorrhage or calcification. In some large AVMs the feeding arteries, draining veins or tightly packed nidus may be visible on non-contrast scans as slightly hyperdense structures. Almost all AVMs will exhibit marked enhancement following contrast injection (Figures 2.1a and b). The nidus and large serpentine afferent and efferent pedicles can often be seen, although small AVMs may be missed.

As a rule, draining veins have a larger diameter than feeding arteries. Furthermore, draining veins may exhibit varicose or aneurysmal dilatations. Superficial draining veins are located on the surface of the brain immediately beneath dura and appear as round enhancing nodules when seen in cross section, that can be traced on higher sections to join the SSS. In contrast, superficial arteries feeding the AVM may be followed in the depths of a sulcus. They have a curvilinear appearance and usually are of a smaller size than the veins. Based on these criteria, it is usually possible to predict, by CT, the main arteries supplying the AVM and the venous system(s) involved in its drainage.

2.6.3 Digital subtraction angiography

DSA is still the 'gold standard' method for evaluating the angioarchitecture and haemodynamics of AVMs, prior to the consideration of treatment. DSA has almost entirely replaced conventional angiography. The recent introduction of biplanar DSA equipment is a technological advancement permitting reduction of

Figure 2.1: a) Pre- and b) post contrast CT scan of a left occipital AVM

a

b

radiation exposure, the amount of contrast material used and investigation time compared with monoplanar equipment. Iodinated non-ionic contrast materials are preferred because of their decreased neurotoxicity compared with ionic agents.

Evaluation of cerebral AVMs by selective angiography requires studies aimed at depicting both the AVM and the arterial and venous circulation of the brain (Figures 2.2a and b). Therefore four-vessel studies and additional external carotid studies are generally required depending on the location of the AVM. Complete angiographic evaluation usually involves two steps. Firstly the selective angiographic investigation of the AVM and cerebral vasculature and secondly, the superselective angiographic investigation of the AVM nidus.

Complete selective angiography of cerebral AVMs should provide the following information:

1. Arterial territory or territories involved in supplying the AVM
2. Individual feeding arteries
3. Assessment of changes secondary to high-flow angiopathy
    a. isolated or multiple stenoses
    b. arterial enlargement, ectatic vessels
    c. flow-related aneurysms
4. Gross assessment of the nidus (shape, size, presence of arteriovenous fistulae, large ectasias, flow conditions)
5. Venous territory or territories involved in the AVM drainage
6. Individual draining veins
7. Venous high-flow angiopathy
    a. dural sinus high-flow
    b. venous thrombosis
    c. venous enlargement, stenoses, varices
8. Venous drainage of the brain

Figure 2.2: a) Arterial and b) venous phases of an AVM on DSA

a

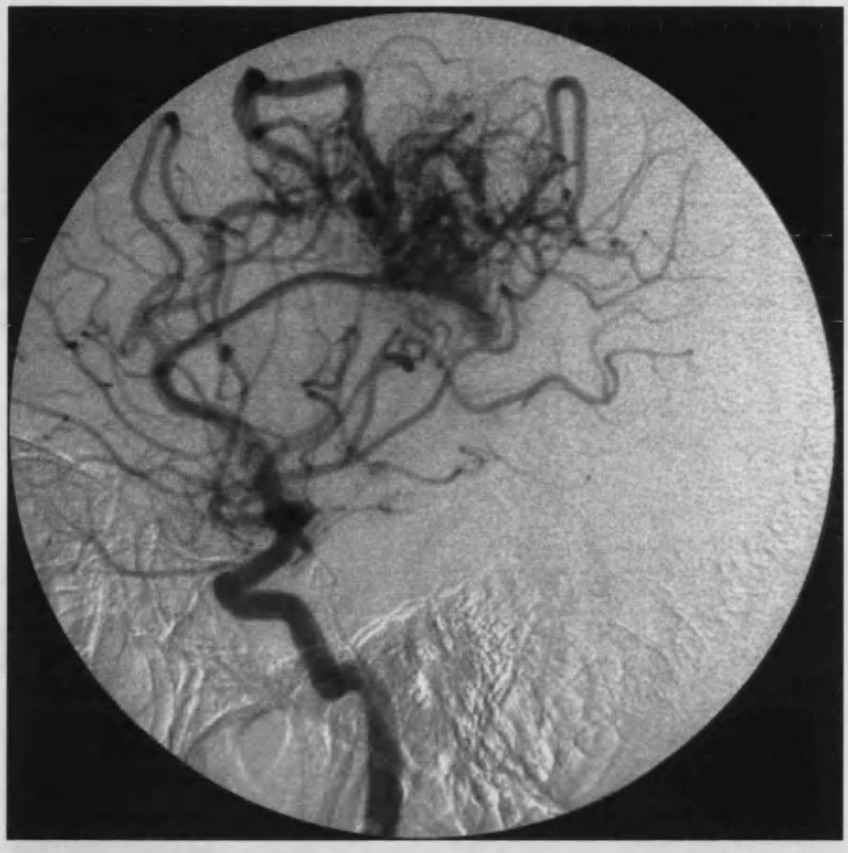

b

The low resistance AVM nidus means that by the time contrast is seen in normal brain capillaries it is already seen in the veins draining the AVM. Even using DSA, it can be difficult to see the arterial feeders at the fistulous site because of rapid recirculation of contrast material through the fistula, often exacerbated by wash-out by non-opacified blood (Konno, 1996). Alternatively, intranidal pathology such as aneurysms or direct arteriovenous fistulae, may remain undetected.

In certain situations, AVMs are not identified. This may mean that the AVM is occult, of slow flow or thrombosed. In the acute phase of parenchymal haemorrhage, the haematoma may compress the AVM nidus. Cerebral angiography performed early may therefore not demonstrate the entire AVM giving the incorrect impression of reduced flow through the AVM. Depending on the relative sizes of the haematoma and AVM, the nidus may be compressed by the haematoma in the early phase of haemorrhage and therefore undetectable by angiography. Exceptionally, nidus compression by an acute haematoma may lead to thrombosis and spontaneous obliteration of the AVM. Unless there is an indication for early surgical evacuation of the haematoma, cerebral angiography should be repeated, if not delayed until after haematoma resorption has taken place, to allow demonstration of the true size, extension and flow conditions of the AVM.

Angiography is not without complications. It is invasive and currently requires inpatient admission. In the Co-operative study from 1966, the complication rate was found to be 5.8% with an associated mortality of 0.82%. This risk was related to age and was found to be higher in those requiring a general anaesthetic for the procedure (Perret and Nishioka, 1966a). The accepted complication rate is currently 1-2% (Mani, 1978; Waugh and Sacharias, 1992). In a more recent study, Heiserman *et al.* (Heiserman, 1994) documented a 1% overall incidence of neurological deficit with a 0.5% incidence of permanent deficit following cerebral angiography. All complications occurred in patients presenting with a history of stroke, transient ischaemic attacks (TIAs) or carotid bruit, which they felt reflected

the difficulty of performing angiography in a population at risk of atherosclerotic changes. Patients suffering complications were older, had longer average procedure times and were given a greater volume of radiographic contrast than those unaffected. In a separate study, hyperintense lesions seen on diffusion-weighted MRI consistent with silent embolic events were seen in 23% (Bendszus, 1999). Risk factors included larger contrast medium volumes, longer fluoroscopy time, additional catheters and vessels more difficult to cannulate. Again, patients with vascular risk factors (including previous stroke, TIA, suspected vasculitis, intraparenchymal haemorrhage, excluding aneurysmal or AVM haemorrhage) had a 44% risk of hyperintense lesions compared with 13% in those with no vascular risk factors (Bendszus, 1999).

2.6.4 Magnetic Resonance Imaging

MRI provides useful information regarding the location and topography of the AVM, presence or absence of haemorrhage and associated parenchymal changes such as oedema, ischaemia, gliosis, atrophy or mass effect. This information is essential for planning the angiographic work-up and correlative analysis of the angiographic information.

AVMs are identified as flow-voids visualised on either T1 or T2 weighted sequences, often with associated foci of encephalomalacia (Figure 2.3). MRI has been shown to be better at establishing the size of AVMs than CT or DSA (Noorbehesht, 1987). This is thought to be due to the difficulty in separating out draining veins on CT and DSA. The size on MR is smaller than that determined from angiographic films, the discrepancy increasing with increasing size of AVM. MRI appears more accurate in defining the AVM nidus with implications as far as radiosurgical planning is concerned, when it is important to identify nidus accurately allowing treatment of the nidus only and not normal surrounding brain, thus reducing associated morbidity (Noorbehesht, 1987).

Figure 2.3: Axial T2 FSE image of a left occipital AVM with obvious flow voids

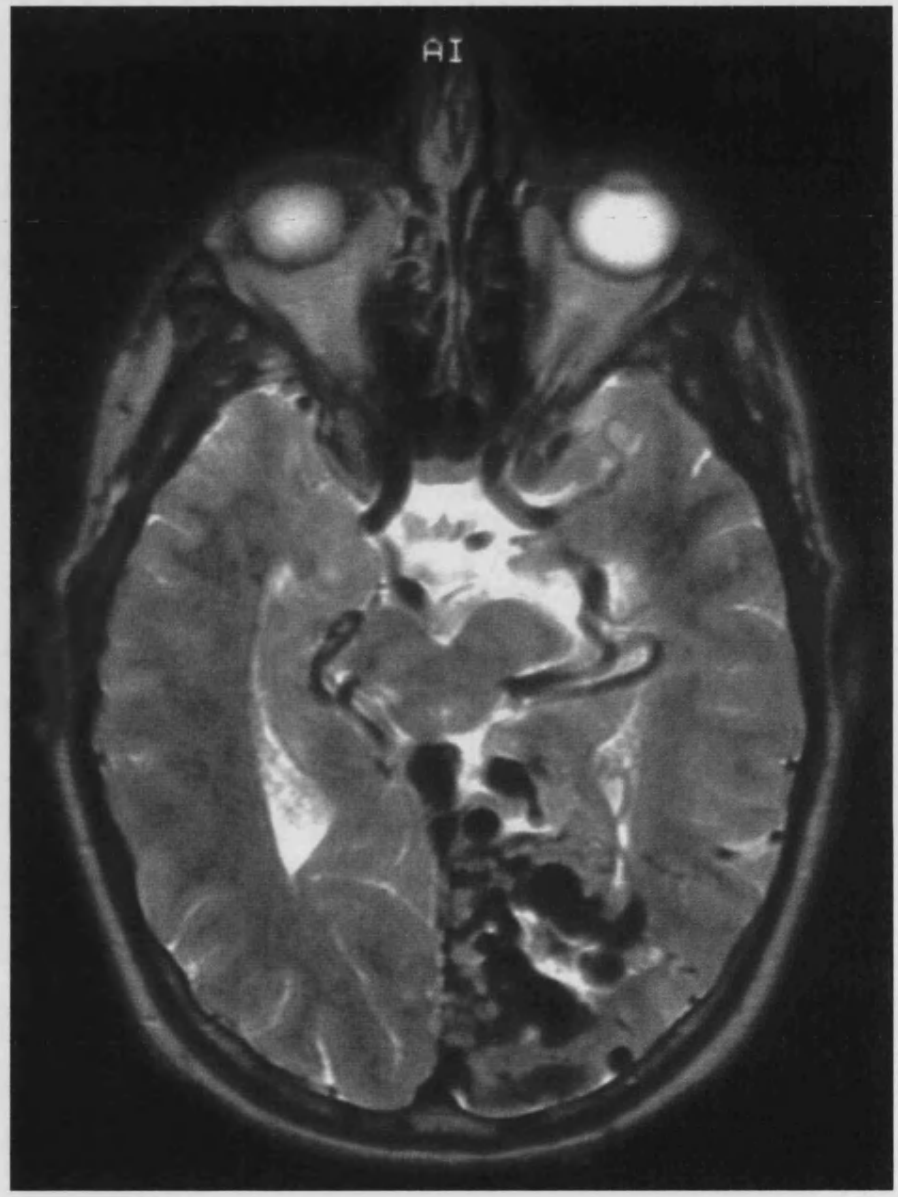

MRI also has its uses in follow-up imaging after treatment: endovascular embolisation, surgery or stereotactic radiosurgery. Pollock *et al.* (Pollock, 1996b) analysed MR images performed 2 years following radiosurgical treatment for an AVM. Only those patients who had AVMs visible on pre-treatment MR imaging were studied. They found that MRI had a sensitivity of 80%, specificity of 100%, a negative predictive value of 84% and positive predictive value of 100% with respect to predicting patency of AVMs at 2 years following treatment. A few false negatives went on to total obliteration at 3 years; it was felt likely that flow was so slow that it was not appreciated on MR images at 2 years in these cases (Pollock, 1996b). The authors advocated timing of DSA in relation to MRI changes in an effort to diminish the need for repeated DSA procedures (Pollock, 1996b). It is likely that, with routine use of MRI and MRA simultaneously, these figures could be improved upon still further.

2.6.4.1 MR Angiography

MRA is performed on a conventional MR scanner and does not normally require the injection of a contrast medium. If accurate, MRA offers several advantages over conventional angiography including its non-invasive nature and lack of need for contrast agents. There are in principle two different techniques of MRA: time of flight (TOF) and phase contrast (PC) angiography. In both techniques the contrast between blood vessel and stationary tissue is as a result of blood motion. Both are non-invasive, with a good safety profile and a spatial resolution that approaches that of DSA.

In 3D TOF MRA, a short TR, minimum TE, gradient recalled sequence (T1 weighted), stationery tissue is saturated by a repetitive radiofrequency pulse and 'fresh spins' from non-saturated in-flowing blood, which traverses the region of interest (ROI), give high signal. Substances that normally have very high T1 signal, such as fat or blood, may be incompletely saturated (T1 contamination artifact) and appear as high signal areas. This can interfere with the diagnostic interpretation

either by mimicking or by obscuring vascular structures (Rieger, 1996; Harrison, 1997).

The advantages of 3D TOF are excellent spatial resolution, a high sensitivity and specificity, efficient scan time yielding a favourable signal-to-noise ratio, reduced complex flow signal loss and clearly visible T1–weighted anatomy. It is well suited to demonstrating high velocity flow in the major feeding vessels and the nidus of AVMs. Contrast enhancement with gadolinium can be used to further increase contrast resolution with overall improvement in the delineation of small vessels. With rapid radiofrequency pulsing, the blood signal approaches a steady state saturation and blood/static tissue contrast can diminish over time. This loss of vascular contrast from the saturation effect, together with loss of signal from structures with slow flow are the primary limitation of TOF sequences (Harrison, 1997; Pernicone, 1997). Slower flow within compartments of the nidus and in draining veins may therefore remain undetected. In addition it has a limited acquisition volume, but the use of multiple overlapping thin slab acquisition can overcome this. 2D TOF acquisitions have a lower spatial resolution and are insensitive to complex flow, but are of more value in imaging larger lesions with slower flow.

Of the TOF techniques, 3D TOF angiography is used almost exclusively for the examination of intracranial vessels, whilst 2D TOF is more commonly used for neck vessels.

PC MRA is based on the detection of phase shifts generated by a flow-encoding gradient. The phase shift is proportional to the velocity of blood and indicates flow direction (Brant-Zawadzki and Heiserman, 1997). Care must be taken to chose an appropriate 'velocity window' depending on the area studied. Typical velocity parameters are 15 cm sec^{-1} for dural sinuses and 50 – 60 cm sec^{-1} for major cerebral arteries. This gives it a higher sensitivity to slower flow than 3D TOF, but it can be time-consuming, particularly if several sequences with different

velocity settings have to be performed to encompass the full velocity range of a vascular system.

PC sequences again can be either 2D or 3D but are generally less sensitive for small lesions than 3D TOF. Fast 2D PC assesses flow quickly, provides a projective view of the vasculature and allows determination of flow direction. 3D PC requires longer acquisition times, but a volumetric data set is acquired that is used to produce maximum intensity projections (MIPs). Background suppression in PC MRA, even in tissues with a short T1, is excellent. PC angiography often has advantages over 3D TOF sequences in high-flow large vascular lesions that are geometrically complicated. Especially with 3D PC, huge and complex volumes can be covered by one stack without risk of intravolume saturation and can therefore be useful in imaging large AVMs. However 3D PC MRA does require long acquisition times and can be degraded by eddy currents and susceptibility artifacts. Time-consuming 3D PC can be partially replaced by the much faster 2D technique without a substantial compromise in image quality in most cases. The 2D method can also provide a rapid semi-quantitative haemodynamic evaluation, consisting of several acquisitions of three or four single-slice images each of which has a different velocity-encoding velocity. Moreover the 2D PC technique is capable of providing direct quantification of both flow velocity and flow volume in principle arterial feeders and draining veins. All these features mean that a 2D PC study is often sufficient for the diagnosis and even the post-therapeutic follow-up of cerebral AVMs except when a 3D presentation is specifically required.

Contrast enhanced MRA (CEMRA) is a relatively new technique. Paramagnetic contrast agents strongly increase the MR signal due to enhanced T1 shortening. With contrast, blood regains its longitudinal magnetisation more rapidly giving a stronger signal intensity and therefore improving the signal-to-noise ratio between blood vessels and background and eliminating flow artifacts. The contrast can be increased still further by subtracting pre-contrast from post-contrast images provided the patient does not move. In 2D acquisitions, patient motion artifacts

may render one or many of the sequentially collected slices uninterpretable. Signal-to-noise ratios are better during 3D acquisitions and therefore these artifacts can be compensated for as long as they are not too numerable and do not occur in central k space measurements. Shorter TR and TE and thinner slices are possible with 3D data sets, allowing large volumes to be acquired within several seconds. Sequential imaging permits measurement of arterial, capillary and venous bolus passage. The primary limitation of 3D CEMRA is the k space acquisition speed and thus the achievable image resolution during the limited first pass of contrast media. The availability of high performance gradient sets on clinical scanners now allows speed-up to an extent where the fundamental signal-to-noise ratio limit becomes imminent. To maximise signal-to-noise ratio for a given spatial resolution, a contrast agent with maximal intravascular concentration should be chosen. Visualisation of vessels much less than 1 mm in diameter is now possible with a sufficient signal-to-noise ratio.

The advantage of MRI and MRA in combination is the ability to detect not only the nidus of the vascular malformation but also signs of past haemorrhage, which may influence management (Brant-Zawadzki and Heiserman, 1997). In addition, MRI is non-invasive, quicker, cheaper, more acceptable to patients and does not have the same potential for neurological complications (except in the presence of contra-indications to MRI scanning) compared with DSA (Pollock, 1996b).

2.7 Conclusion

Cerebral AVMs are congenital lesions with a prevalence of up to 0.5% in autopsy series. They are protean in their clinical manifestations, which include cerebral haemorrhage, epilepsy, progressive neurological deficit and headaches. Intracranial haemorrhage is the most common clinical presentation, seen in 60-70%

of individuals. It is an important cause of stroke in young people, each bleed being associated with a 10% mortality and 30% morbidity.

Treatment of these lesions by endovascular embolisation, microsurgery or radiosurgery carries a small but substantial risk and being able to predict the haemorrhagic risk in the individual patient would enable better clinical decision making. There have been a number of studies assessing the risk of haemorrhage from an AVM but the results are contradictory. Many questions, such as the relative importance of the AVM size or type of venous drainage, remain unresolved. Factors favouring presentation with epilepsy and influencing its control are even less well researched. It seems clear that morphological analysis of these lesions alone is not sufficient and that haemodynamic factors may play an important role.

Intra-arterial catheter angiography remains the 'gold standard' investigation in patients with cerebral AVMs. DSA allows a detailed analysis of angioarchitecture of these lesions providing information about feeding arteries, nidus structure and draining veins. These results have an influence on the choice of treatment and prognosis of individual AVMs. However, DSA is an invasive procedure which requires inpatient care and carries a risk of neurological complications in 0.5 - 2%. Complete cure can usually only be achieved for small AVMs and patients with larger AVMs may have to undergo several staged procedures and follow-up DSAs with their associated risks.

The investigation and understanding of both the angioarchitecture and the haemodynamic effects of AVMs clearly requires much work. Associated improvements may allow advances in their management, with a reduction in overall patient morbidity and mortality.

PART 2

STRUCTURAL IMAGING

Chapter 3

CT ANGIOGRAPHY

3.1 Introduction

CTA is a form of spiral CT scanning. Spiral CT is achieved by continuously acquiring CT data while the patient is moved through the gantry. Rapid acquisition enables an entire vascular territory to be imaged within 30 - 60 sec. Initially used for imaging larger vessels such as the aorta, renal and hepatic arteries (Rubin, 1994; Costello and Gaa, 1995; Kanematsu, 1996; Wicky, 1998), CTA is being increasingly used in the investigation of intracranial vascular disease.

3.1.1 Basic principles

During CTA, thin section axial images are acquired during the injection of an iodinated contrast medium bolus, while simultaneous rotation of the CT Xray tube and movement of the scanning table takes place. Detailed demonstration of vascular anatomy depends on the intravascular iodine concentration, threshold selection and voxel size. Collimator width and table speed have important consequences on the quality of the CTA. The ratio of table speed to collimator width multiplied by the gantry rotation period is defined as scan pitch (typical range 1.0 – 2.0). An increase in pitch will increase the spiral length and therefore volume coverage but at the expense of spatial resolution. Collimator width selection strongly affects spatial resolution and signal-to-noise ratio. For intracranial CTA, 1 mm collimation with submillimetre reconstruction intervals should be used (Rubin, 1995).

CTA, using a 512 x 512 matrix with a field of view of 14 cm, has a spatial resolution of 0.5 mm (in plane), which is approximately ten times worse than that

afforded by intra-arterial DSA (Rieger, 1996). This is primarily due to partial volume and noise effects. Furthermore, iodine concentration is considerably lower as it is given intravenously and peripherally. With a fixed threshold and voxel size in a 512 x 512 matrix, a decrease in iodine concentration results in an increase in partial volume effects, especially when the vascular luminal diameter becomes less that the section thickness (Rieger, 1996). If lumen diameters of less than 2 mm do not need to be visualised, CTA may be adequate. Resolution could be improved with introduction of higher heat capacity Xray tubes to allow for a higher current during spiral acquisition. As a result, the signal-to-noise ratio would improve, enabling collimation width reduction (Rubin, 1995). The recent introduction of multi-detector CT systems will improve volume coverage also leading to improvements in resolution (Rubin, 1999).

3.1.2 Post processing

Continuity of spiral CT data enables axial sections to be reconstructed on a computer workstation at any point along the spiral path and at arbitrary intervals. Thus overlapping sections can be generated that will result in smoother 3D renderings and diminished partial volume artifact, which leads to improved small vessel visualisation.

Threshold surface-shaded display (SSDs) renders volumes by generating images on the basis of a predefined threshold value. Contiguous pixels above the threshold are modelled as a single 3D structure by the computer. The computer then generates an imaginary source of illumination to depict surface reflections that are encoded in the image grey scale. SSDs can be made with multiple threshold levels and coloured displays can be used to enable segmentation of separate structures with varying attenuation (Figures 3.1 and 3.2). SSDs depict complex 3D relationships well, particularly in regions of overlapping structures, but much information regarding relative Xray attenuation is lost in the thresholding process.

Figure 3.1: Segmented SSD image showing vessels (pink), embolisation material (green) and ventriculo-peritoneal shunt (blue) using multiple threshold levels and a coloured display

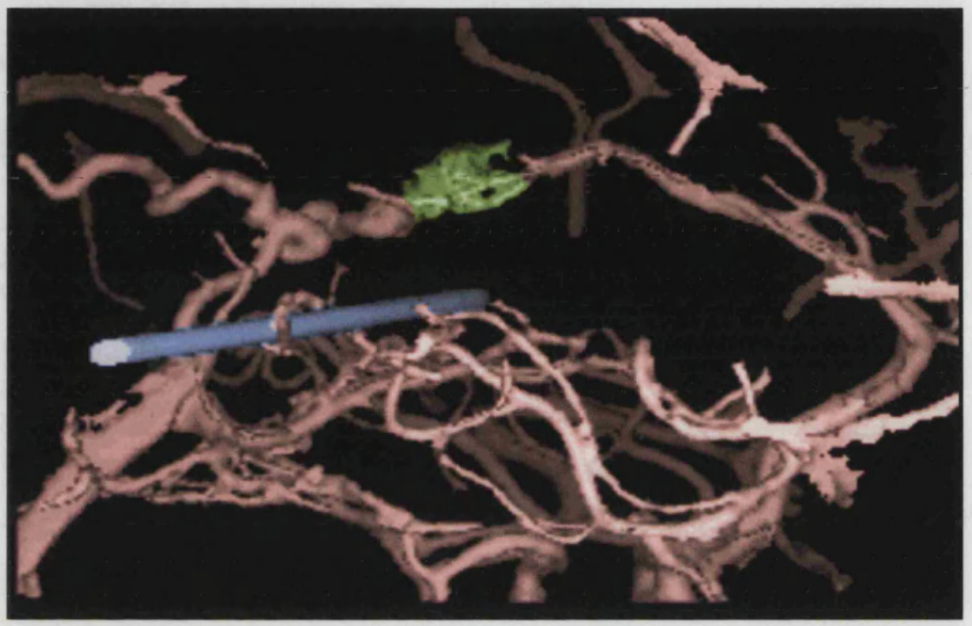

Figure 3.2: Segmented SSD image showing vessels (pink) and bone (grey) using multiple threshold levels and a coloured display

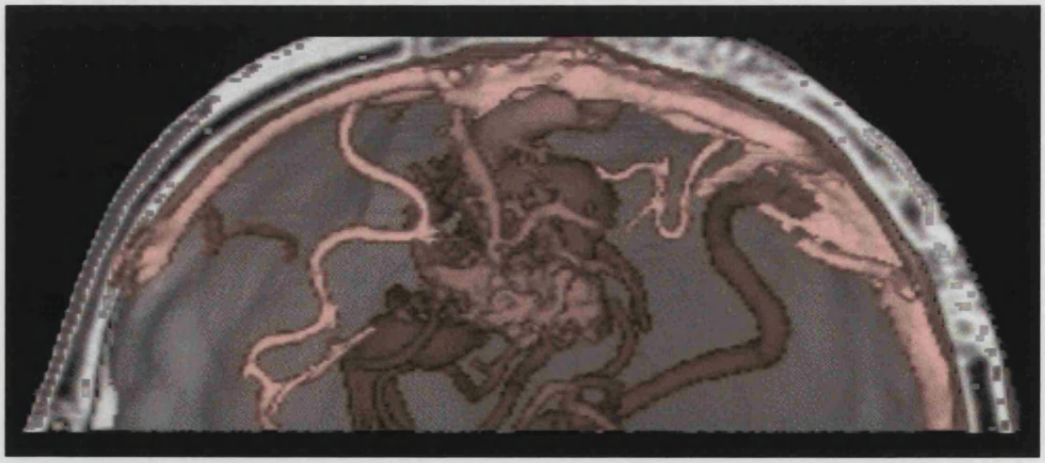

MIPs are reconstructed automatically such that pixels with greatest attenuation values in a given direction are extracted to give a projection image. Attenuation values in the final reconstructed image more accurately reflect those in the axial images; thus calcium is easily distinguished from intraluminal contrast (Schwartz, 1994). The absence of a thresholding step ensures that no information is lost and subtle variations in attenuation can be appreciated.

A disadvantage of MIPs is that a single projection image does not encode depth relationships. This shortcoming is countered by the generation of multiple MIPs at view angles around an axis of rotation with resultant images viewed as a cine loop to enable appreciation of spatial relationships. Highly attenuating structures such as bone, metallic implants or intensely enhancing parenchyma can mask target anatomy on MIPs and some SSDs. Because the MIP selects only the brightest pixel along each direction, a high attenuation structure anywhere along that path will dominate and thus mask a structure of lesser attenuation. MIP representations of intracranial CTAs are particularly difficult to post-process compared with other regions of the vascular tree, as the highly attenuating skull hides the majority of vasculature. For the Circle of Willis and other central vessels it is relatively simple to define a sub-volume of the data within the skull, and to produce a MIP of just that volume. However, where the vessels of interest lie close to bony structures, this can become very difficult and time-consuming. Surface renderings have the property of occlusivity, less attenuating structure will be visible if its attenuation falls above the selected threshold and it lies closer to the 'eye' than a more attenuating structure (Figures 3.3a - c).

Post-processing is operator-dependant and can be time-consuming, particularly if manual segmentation is required. Valuable information can be lost by exclusion of relevant anatomical structures.

Figure 3.3: a) MIP, b) left lateral SSD and c) right lateral SSD images of the same AVM

a

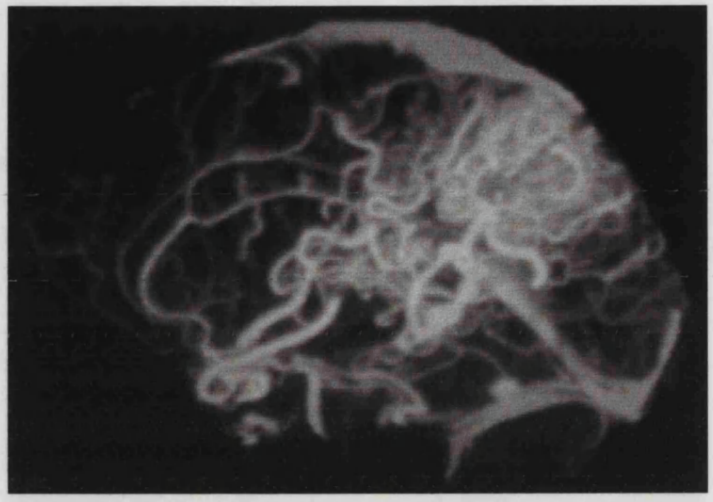

b

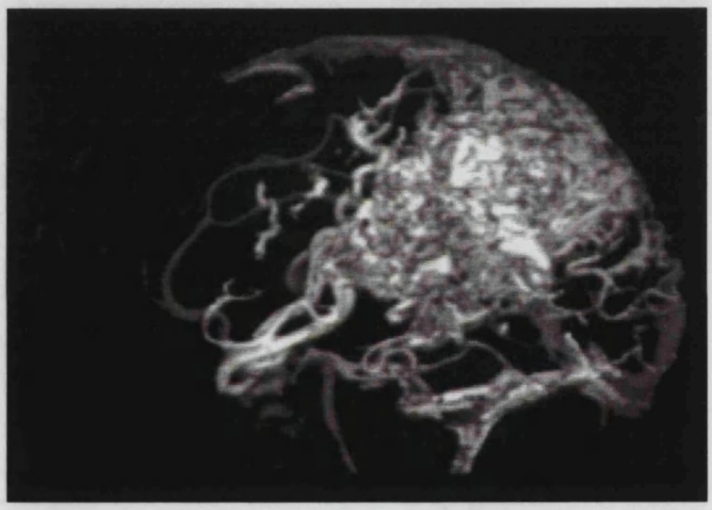

c

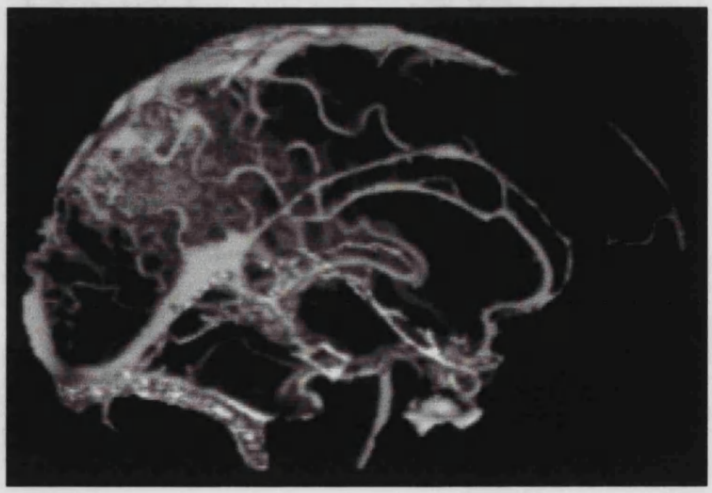

The left and right SSD lateral projections are different because of the property of occlusivity, whilst the left and right lateral MIP projections are the same.

3.1.3 Clinical applications

3.1.3.1 CTA of intracranial aneurysms

The most common indication for intracranial CTA is currently in the delineation of aneurysms. The processed 3D model permits multiple projections of the lesion to be visualised, allowing assessment of the 3D anatomy of the aneurysmal complex and reproduction of the surgical approach. Young *et al.* (Young, 1999) demonstrated an overall sensitivity for detecting aneurysms on CTA of 96%, although this was better in larger aneurysms (97% if lesion > 3 mm, but 87% if < 3 mm). Others have had similar findings (Schwartz, 1994). Visualisation of axial source images can be critical in the diagnosis of small or thrombosed aneurysms as they may fail to fill with intravascular contrast or be too small to be visualised on the 3D model (Young, 1999). CTA has also been used to demonstrate dissecting aneurysms (Lanzino, 1997).

CTA may be an alternative to DSA for early detection of aneurysms in patients with SAH. CTA can be performed immediately after conventional unenhanced CT has confirmed the diagnosis of SAH. Evaluation of the intracranial circulation can be undertaken non-invasively, giving the surgeon information regarding the site and configuration of any aneurysm present, which may prove invaluable should the patient require emergency evacuation of the haematoma. In addition, it can indicate whether endovascular treatment of the aneurysm might be possible prior to haematoma evacuation (Le Roux, 1993). Velthuis *et al.* (Velthuis, 1997) demonstrated CTA to have a sensitivity 92% and specificity 100%, with 88% true positives and 35% false negatives. They found MIPs to be superior to SSDs, although cavernous sinus and internal carotid artery (ICA) lesions were particularly difficult to identify because of the proximity of the skull base.

Metal artifacts can severely degrade the CTA image quality, limiting its utility in post-operative situations. However, post-operative lesions have been assessed with CTA, which can be concurrently used to demonstrate vasospasm and

patency of distal vessels (van Loon, 1997). Techniques to minimise the effects of beam-hardening artifact have been described where the AP digital scout image is used as a reference to tilt the patient's head. This allows projection of the aneurysm clip away from the remainder of the Circle of Willis on the axial slice and therefore reduces beam-hardening artifact in relevant areas (Brown, 1999; Young, 1999). Artifact can also be reduced by using very thin collimation (1mm) (Vieco, 1996). Some authors believe that in the post-operative situation beam-hardening artifact is always present, limiting image interpretation, such that CTA at present cannot replace DSA for evaluation of aneurysm clip placement (Vieco, 1996).

3.1.3.2 CTA of intracranial AVMs

The use of CTA in delineating AVMs has been limited. Several small studies have been performed comparing DSA with CTA in patients with AVMs, where CTA has provided definitive information about site and size of the nidus (Gorzer, 1994; Rieger, 1996). In the study of Tanaka *et al.* (Tanaka, 1997), 12 patients underwent CTA, MRA and DSA. They found that CTA demonstrated only 50% of arteries but 78% of veins and concluded that this may have been due to suboptimal contrast enhancement and suggested that a shorter scanning time with an increased pitch and larger concentration of iodine may have improved the findings (Tanaka, 1997). However demonstration and measurement of the nidus was possible in all 12 patients. In AVMs with well-developed draining veins, dense opacification of these superimposed on the nidus may make identification of the nidus difficult by DSA. The 3D data set of the CTA can, however, be manipulated to allow adequate visualisation of the nidus without overlying veins. Tanaka *et al.* (Tanaka, 1997) concluded that the use of both MIP and SSD images improved visualisation of the relevant vasculature, but SSDs best delineated vessels and nidus. Aoki *et al.* (Aoki, 1998) reported similar findings and found that CTA provided precise anatomical information on niduses and draining veins, but could not demonstrate fine feeders. They suggested that CTA may therefore have a role in

planning stereotactic radiosurgery where demonstration of the nidus is of utmost importance. Rieger *et al.* (Rieger, 1996) concluded that spiral CT seems to have the same potential as MRA for showing main feeding vessels, the angiomatous nidus and large draining veins, although these were not analysed quantitatively and were not compared with appearances on DSA.

In a single study of post-embolisation CTA in AVM, the remaining malformation was distinctly visualised since the hyperdense embolisation material could be erased by subtraction at the post-processing stage (Gorzer, 1994).

These studies show the potential uses of CTA in the delineation of AVMs, although systematic comparative studies of these newer techniques are still needed.

3.2 Methods

3.2.1 Patients

Patients were recruited from those seen by the neurovascular surgery or interventional neuroradiology services at The National Hospital for Neurology and Neurosurgery between February 1998 and January 1999. All patients were known to have AVMs and had undergone recent catheter angiography confirming the diagnosis. Those who were pregnant, had a history of allergy to iodine or were aged less than 16 years were excluded.

3.2.2 Imaging

CT scanning took place on a Somatom® Plus-4 scanner (Siemens Medical, Erlangen, Germany) at The National Hospital for Neurology and Neurosurgery. CTAs were acquired in spiral mode with a beam width 1 mm, table feed 2 mm (pitch 2.0), rotation time 0.75 sec, 140 kV, 111 mA, using a 512 x 512 matrix with a field of view of 16 - 22 cm depending on the size of the patient's head. A spiral length of 68 or 112 mm was acquired, depending on the size of the AVM, with a scan time of

27 or 43.5 sec respectively in a caudal to cranial direction. A reference slice was used to monitor a ROI in the cavernous sinus to detect the arrival of the contrast agent (1 mm beam width, 1.5 sec tube rotation, 140 kV, 111 mA, sample period 3.4 sec), automatically triggering the CTA acquisition when a pre-determined threshold of 25 Hounsfield units (HU) was reached (Figure 3.5). A sample threshold graph is shown in Figure 3.4. A fixed volume of either 100 or 150 ml (depending on the spiral length) of iodinated contrast agent (Xenetix® 350, Guerbet Laboratories, Aulnay-sur-Bois, France), regardless of patient weight, was injected at a rate of 3 ml sec^{-1} using a power injector (AS 200-CT, Medex, Annecy, France). The total effective dose equivalent to the patient was estimated to be 0.72 mSv.

Figure 3.4 : A sample threshold graph of CTA acquisition showing average Hounsfield unit values for ROI.

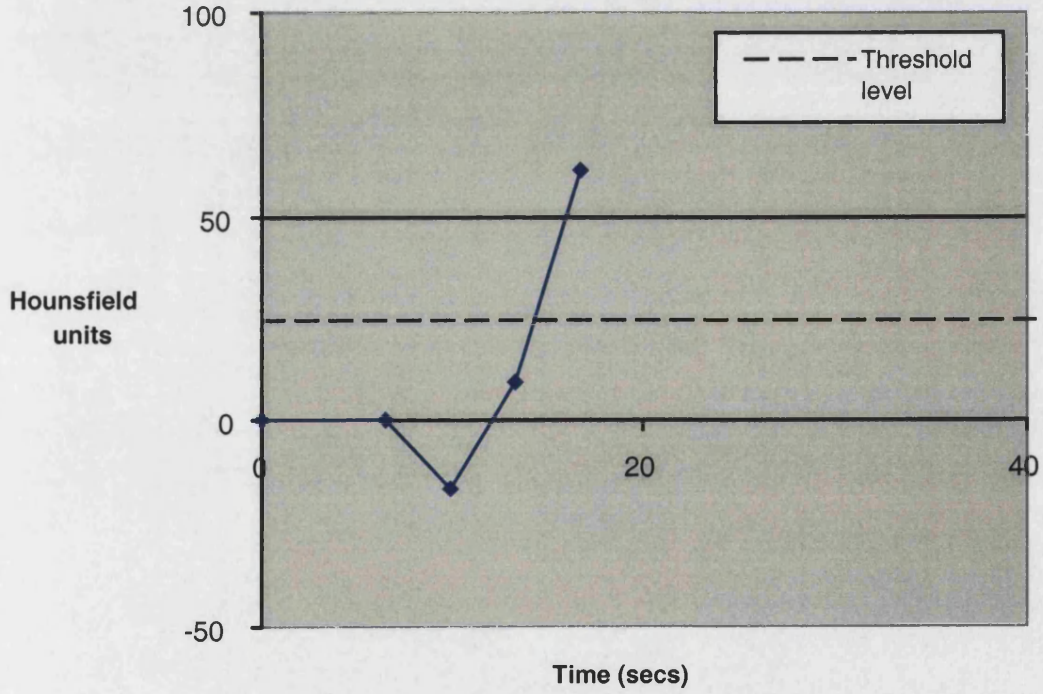

Figure 3.5: Reference slice showing ROI over cavernous sinus to detect arrival of contrast bolus

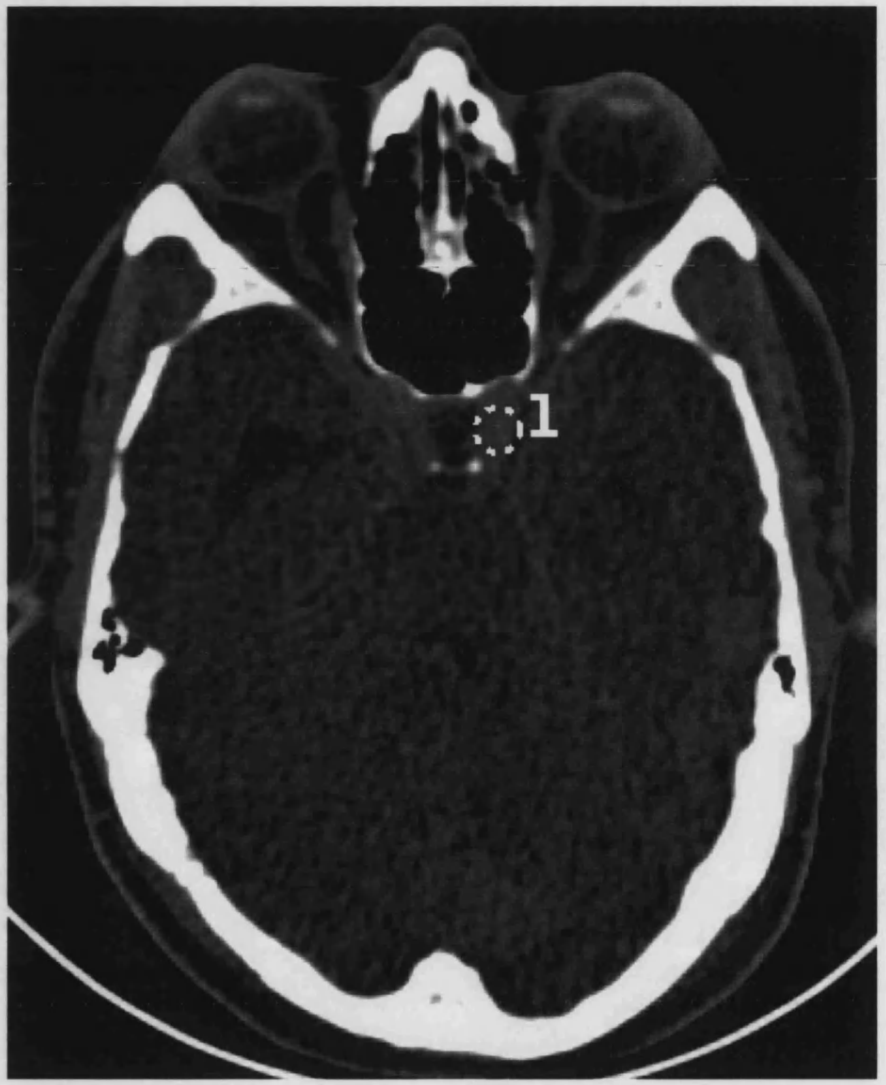

3.2.3 Processing

Both SSD and MIP images were generated for each patient and standardised views of the resulting CTAs were saved on film for review. All processing was carried out on a Sun® Ultra 5 workstation (Sun Microsystems, Berkley, USA) running Advantage Windows® (version 1.2) software (General Electric Medical Systems, Milwaukee, USA).

With this software, an 'object' is a 3D connected set of voxels whose HU values are within given thresholds, and objects can be selected for deletion or retention using a cursor. Up to four 'viewports' can be open, each working independently on the loaded volume. Images were reconstructed using an increment of 0.5 mm and 180 degree interpolation and collimation of 1 mm in all cases.

An initial 3D 'model' was built using thresholds of 0-1500 HU, which included all the contrast-enhanced vessels and bony tissues, as well as the head rest and immobilisation pads. The latter objects were deleted immediately. Segmentation of the bone from the model was achieved by applying a threshold of 250-1500 HU and then selecting only the skull as the object of interest. This object was then 'dilated' with 2-4 iterations using the supplied dilation tool. Each iteration dilated the object using a 3x3x3 kernel, adding only voxels which were part of the original 3D model.

When generating a SSD, in a third viewport, the original model was re-thresholded to leave the vessels and to remove as much bone as possible, with typical thresholds of 80-350 HU. The dilated skull object was then subtracted from the vessels object, thus creating a clear separation between the intracranial contents and the soft tissues of the face and scalp. Finally, the main vessels could be separated from other unwanted tissues by selection with the cursor over the AVM. At this stage final adjustments to the thresholds were made to leave a clear 3D render of the vessels, including removal of small groups of voxels ('floaters') of less than 25 mm^3. The vessels object can also be merged with the undilated skull object, allowing appreciation of vascular anatomy in relation to bony structures.

When generating MIPs, however, no further thresholding was required and the 'dilated' bony structures were simply removed. A MIP image was made from the remaining intracranial structures, all other subcutaneous soft tissue being lost by selection of the central structures as an 'object'.

3.2.4 Image analysis

3D SSDs and MIPs of the CTAs were analysed independently by two neuroradiologists according to a pre-determined proforma; this was drawn up by the radiologists on the basis of their previous experience in analysing imaging of AVM patients.

CTAs were analysed for the following information:

1. Size (according to Spetzler classification (Spetzler and Martin, 1986))
2. Topographical classification (according to Berenstein and Lasjaunias (Berenstein and Lasjaunias, 1992) as in section 1.3.1)
3. Arterial supply (anterior or posterior circulation or external carotid supply)
4. Number of arterial feeders (1, 2, 3 or greater than 3)
5. Presence of aneurysms (on Circle of Willis, on feeding artery or intranidal)
6. Venous drainage (superficial, deep or both)
7. Number of draining veins (1, 2, 3 or greater than 3)
8. Venous anatomy (the presence or otherwise of focal or diffuse varices, stenosis or thrombosis)
9. Nidus definition (good, average, poor)
10. Presence of calcification
11. Presence of angiogenesis
12. Presence of embolic material
13. Clinical goal of treatment
14. Morphological goal of treatment
15. Proposed treatment plan

Some details of presentation and symptomatology were given to allow an informed decision regarding future management plans for the patients to be made. The images were stratified according to AVM size and then randomised, using a table of randomised numbers, to whether the SSD or MIPs were analysed first (Altman, 1991).

The CTAs were first assessed from film and any uncertainties that arose were resolved using the interactive model on the workstation. Having assessed the images independently, any disagreements between the two neuroradiologists were reviewed and a consensus opinion reached for use in comparison with DSA. These results were compared with those reached in a similar way by a third neuroradiologist reviewing the DSAs.

3.2.5 Statistical analysis

Data were collated using Microsoft® Excel 98 and statistical analysis was performed using Stata™ 4.0 (Stata Corporation, Texas, USA), on an Apple Macintosh® iMac computer.

Kappa (κ), as described by Altman (Altman, 1991), was used as a measure of agreement. Kappa values were generated in order to assess the interobserver variability for SSD and MIP images and to compare SSD and DSA and MIP and DSA consensus findings. Kappa has a maximum value of 1.00 and can be used to assess how close an agreement there is between groups. Conventionally accepted levels are shown in Table 3.1. Weighted kappa, a further refinement of this test, can be used in the setting of ordinal variables (for example, in this study, the number of arteries or veins) where there may be degrees of agreement.

Table 3.1: Value of kappa and strength of agreement

Value of κ	Strength of agreement
< 0.20	Poor
0.21 – 0.40	Fair
0.41 – 0.60	Moderate
0.61 – 0.80	Good
0.81 – 1.00	Very good

from Altman (Altman, 1991)

A worked example for the calculation of an unweighted kappa value on the basis of interobserver variability for pattern of venous drainage on SSD images is shown below (Table 3.2):

Table 3.2: Pattern of venous drainage on SSD images reported by two radiologists

	Radiologist B			
Radiologist A	Superficial	Deep	Superficial and Deep	Total
Superficial	7	-	2	9
Deep	-	1	1	2
Superficial and Deep	1	1	7	9
Total	8	2	10	20

The expected frequency in a cell, calculated on the assumption of the null hypothesis of no association, is the product of the totals of the relevant row and column divided by the total number of observations.

The expected frequencies of agreement are therefore:

Superficial	9 x 8 / 20 = 3.6
Deep	2 x 2 / 20 = 0.2
Superficial and Deep	10 x 9 / 20 = 4.5
Total	8.3

Total observed agreements $7 + 1 + 7 = 15$

$$\kappa = (15 / 20 - 8.3 / 20) / (1 - 8.3 / 20)$$
$$= 0.57$$

3.3 Results

3.3.1 Patient baseline characteristics

Twenty patients, 11 male and nine female, known to have AVMs underwent CTA and DSA, separated by a median of one day, interquartile range 1 – 69 days. They had a median age of 42 years with an interquartile range of 35 – 46 years. Seven patients presented with seizures, six with haemorrhage (SAH, ICH or IVH), two with headaches and a homonymous hemianopia, two with a progressive neurological deficit, two with headaches alone and a single patient had an enlarging cosmetic deformity. Patient demographic data is summarised in Table 3.3.

3.3.2 CTA analysis

The radiologists' findings are summarised in Appendix 2. On DSA, eight patients had small, five had medium-sized and seven had large AVMs. The anatomical locations were cortical in nine, cortico-ventricular in seven, cortico-callosal in two and deep-seated in two. Arterial supply was from the anterior

Table 3.3 : Demographic data of all patients undergoing CTA

	Gender	Age	Presentation	AVM			*Time interval	Prior treatment	Planned treatment
				Site	Anatomy	Size			
1	F	35	Seizures	Left temporal	Cortical	Small	70	None	Embolisation
2	M	57	ICH	Right frontal	Cortical	Small	1	None	Stereotactic DXT
3	M	53	ICH SAH	Left callosal	Callosal	Small	1	None	Embolisation
4	M	44	Migraine Hemianopia	Left parieto-occipital	Cortico-ventricular	Large	1	None	Conservative
5	F	35	Migraine	Right parietal	Cortical	Small	1	Embolisation	Stereotactic DXT
6	M	56	Seizures	Right temporo-parietal	Cortical	Medium	2	Embolisation	Embolisation
7	M	21	Seizures	Left frontal	Cortico-ventricular	Large	1	None	Conservative

Table 3.3 (continued) Demographic data of all patients undergoing CTA

	Gender	Age	Presentation	AVM			*Time	Prior treatment	Planned treatment
				Site	Anatomy	Size	interval		
8	F	32	Haemorrhage	Left callosal	Cortico-callosal	Small	1	Embolisation	Conservative
9	M	43	Seizures	Left temporal	Cortical	Medium	1	Embolisation	Embolisation
10	F	46	Seizures	Left fronto-parietal	Cortico-ventricular	Medium	1	None	Conservative
11	M	41	Progressive hemiparesis	Right fronto-parietal	Cortico-ventricular	Large	130	None	Embolisation
12	M	48	Cosmetic	Left holo-hemispheric	Cortico-ventricular	Large	1	None	Conservative
13	F	36	SAH	Left callosal	Callosal	Medium	1	Stereotactic DXT	Embolisation
14	M	55	Seizures	Right temporal	Cortical	Medium	1	Embolisation	Conservative

Table 3.3 (continued) Demographic data of all patients undergoing CTA

	Gender	Age	Presentation	AVM			*Time interval	Prior treatment	Planned treatment
				Site	Anatomy	Size			
15	F	25	Progressive hemiparesis	Left thalamic	Deep	Large	74	None	Embolisation
16	F	40	SAH	Right thalamic	Deep	Small	69	None	Stereotactic DXT
17	M	38	Hemianopia Headaches	Right holo-hemispheric	Cortico-ventricular	Large	91	None	Conservative
18	M	46	Haemorrhage	Left temporo-parietal	Cortical	Small	11	None	Surgery
19	F	46	Headaches	Right frontal	Cortical	Small	1	Embolisation	Embolisation/ Stereotactic DXT
20	F	37	Seizures	Left fronto-parietal	Cortico-ventricular	Large	2	None	Embolisation

* time interval in days between CTA and DSA

circulation alone in nine, anterior and posterior in six, anterior, posterior and external in four and anterior and external carotid supply in one case. Venous drainage was superficial in 10, deep in three and both in seven cases. Seven of the 20 patients had undergone partial treatment of their AVM prior to undergoing CTA, of whom six had undergone partial embolisation whilst the seventh had undergone stereotactic radiosurgery.

3.3.3 Kappa Values

The kappa values calculated for both interobserver variability and comparison of imaging techniques are shown in Table 3.4. Kappa values were similarly generated, using the results from the patients with small AVMs only.

3.4 Discussion

CTA is a quick, cheap and simple procedure to perform which does not have the attendant risks of catheter angiography. Unlike MRI, it can be performed in patients with ferromagnetic devices and is possible in claustrophobic patients as well as being less susceptible to movement artifact. It is relatively insensitive to turbulent or slow flow because the patent lumen enhances regardless. It does, however, use ionising radiation and has the potential risk of anaphylactic reactions to the iodinated contrast medium. Post-processing of the images is operator dependent and can be time-consuming, particularly when separating out osseous structures in lesions close to the base of skull or lying on the inner table of the skull. The presence of an acute haematoma also makes post-processing difficult as it is difficult to threshold out haematoma and iodinated contrast separately. Volume coverage of the CTA can be limited, due to the need to maintain adequate spatial resolution. This can sometimes pose a problem in large AVMs. CTA has poor temporal resolution, such that arterial and venous phases are seen together.

Table 3.4: Kappa values for interobserver variability and comparison of imaging techniques for CTA images

	Interobserver variability		Comparison of imaging techniques for all AVMs		Comparison of imaging techniques for small AVMs only	
	SSD	MIP	SSD versus DSA	MIP versus DSA	SSD versus DSA	MIP versus DSA
Size*	0.84	0.83	0.84	0.62	1.00	1.00
Nidal definition*	0.53	0.20	0.17	0.12	0.00	0.00
Anatomical classification	0.61	0.55	0.55	0.63	0.50	0.76
Arterial supply	0.64	0.61	0.53	0.51	0.00	0.00
Number of arterial feeders*	0.69	0.68	0.93	0.79	1.00	0.75
Venous drainage	0.57	0.75	1.00	0.75	1.00	0.77
Number of draining veins*	0.63	0.65	0.86	0.76	0.75	0.14
Aneurysm on feeding arteries	-	0.00	0.00	0.00	-	-
Aneurysm on Circle of Willis	1.00	0.77	0.77	0.77	1.00	1.00
Intranidal aneurysm	0.00	-0.14	0.35	0.35	1.00	1.00
Presence of focal varix	0.35	0.38	0.59	0.12	0.50	0.25

Table 3.4 (continued): Kappa values for interobserver variability and comparison of imaging techniques for CTA images

	Interobserver variability		Comparison of imaging techniques for all AVMs		Comparison of imaging techniques for small AVMs only	
	SSD	MIP	SSD versus DSA	MIP versus DSA	SSD versus DSA	MIP versus DSA
Presence of diffuse varices	0.29	0.27	-0.17	0.53	-0.20	0.60
Presence of venous stenosis	0.00	-0.08	0.00	0.21	0.00	0.00
Presence of venous occlusion	0.00	0.00	0.32	0.46	-	-
Presence of embolisation material	0.00	0.88	0.00	0.88	0.00	1.00
Presence of calcification	0.00	0.66	-	0.00	-	0.00
Presence of angiogenesis	0.05	0.74	0.53	0.60	-	-
Clinical goal of treatment	0.64	0.61	0.59	0.58	0.00	0.00
Morphological goal of treatment	0.52	0.35	0.42	0.42	0.00	0.00
Mode of treatment	-0.05	-0.04	0.13	0.06	0.00	-0.21

* weighted kappa values

- spread of data insufficient to calculate kappa

CTA, however, has the advantage of producing a 3D volume. The 3D model processed permits multiple projections of the lesion to be visualised, allowing assessment of the 3D anatomy of the AVM complex (unavailable with catheter angiography) and it can be used to reproduce the surgical approach, with its unique capacity to display the relationship of vascular structures to bone. This can also be done retrospectively.

3.4.1 Interobserver variability

Both SSD and MIP images showed good agreement with regard to size, anatomical classification and identification of numbers of feeding arteries and draining veins and their origin / destination.

There was moderate agreement on nidal definition between the two radiologists on SSDs but extremely poor agreement on MIPs. This was a very subjective variable and it became clear that the two radiologists viewed nidus definition very differently. Another particular problem with nidus definition was the presence of overlying draining veins. The poor temporal resolution of CTA means that both arterial and venous phases of the angiogram are seen simultaneously, with overlying veins obscuring details of the nidus.

Specific arterial and venous features such as aneurysms, varices, venous stenosis and occlusion had low kappa values and therefore marked interobserver variability except in the case of aneurysms on the Circle of Willis (Figure 3.6). However kappa may not provide a good measure of agreement in situations with small numbers of patients and categories and poor spread across the cells. It may be better to examine the raw data in these situations (Appendix 2), where it can be seen that the two radiologists actually agreed in at least 70% of analyses.

There was very good agreement between observers as far as presence of embolisation material and calcification were concerned on MIP images (κ was 0.88 and 0.66 respectively). Both calcification and embolisation material can be easily appreciated on MIP images. Kappa values were 0.00 for the presence of

Figure 3.6: DSA with corresponding SSD images of an anterior communicating artery aneurysm and venous pouches associated with an AVM

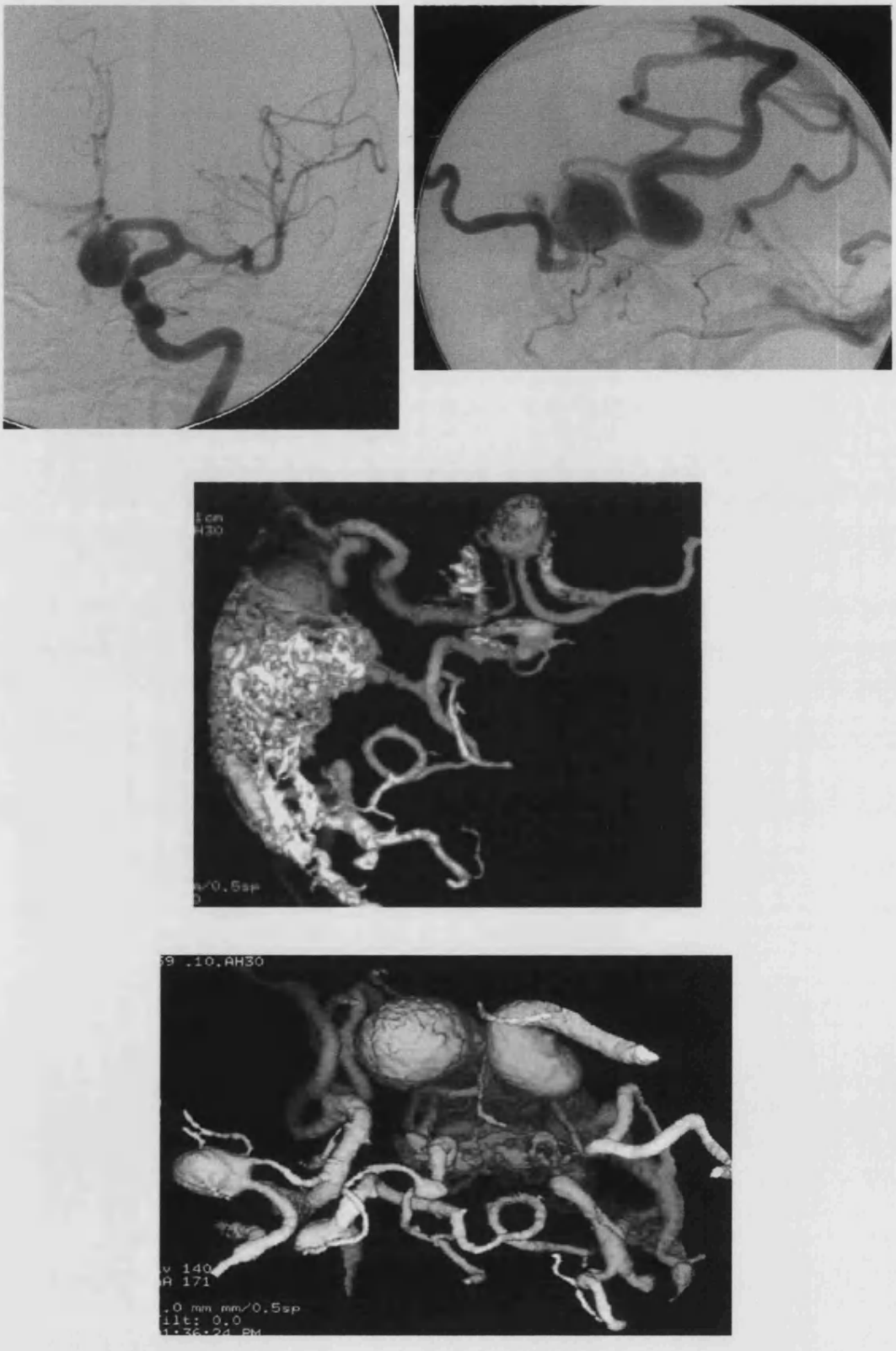

calcification and embolic material on SSDs, although observers agreed in 100% of cases. Review of the raw data revealed that neither observer was able to appreciate embolisation material or calcification on the SSD images. This is not surprising as the majority of information regarding relative Xray attenuation is lost in the thresholding process for SSDs. Examination of the axial source images during interactive viewing would allow visualisation of embolisation material, often with associated beam hardening artifact (Figures 3.7a - d). Calcification is often more subtle and of much smaller volume than embolisation material and therefore, in the case of SSDs, all axial source images or reformats must be viewed carefully to exclude the presence of calcification. This may involve many images and can therefore be a time-consuming process.

There was again good interobserver agreement in MIP images but poor agreement in SSD images for the presence of angiogenesis. Angiogenesis can also be subtle and is often found only within a tightly packed nidus.

SSDs have the property of occlusivity and any overlying structure, such as a large vein, can obscure the nidal structure from view. Appreciation of the nidus structure and identification of the presence of angiogenesis would again require careful evaluation of the axial source images and coronal or sagittal reformats with thin enough slices such that the fine intranidal structure is not lost.

Agreement was good for clinical goal of treatment on both SSD and MIP images, and moderate for morphological goal of treatment on SSD. However, agreement was poor between observers for morphological goal of treatment on MIPs and mode of treatment on both SSD and MIP images (κ was 0.35, -0.05 and –0.04 respectively). Examination of the raw data showed agreement between the reviewers of at least 75%. Certainly in the case of mode of treatment, this was partly related to the fact that this was a highly selected group of patients with at least 50% undergoing embolisation.

Figure 3.7: Embolisation material as seen on a) lateral DSA (black arrow), b) CT axial source data, c) inferior MIP and d) inferior SSD images of the same patient.

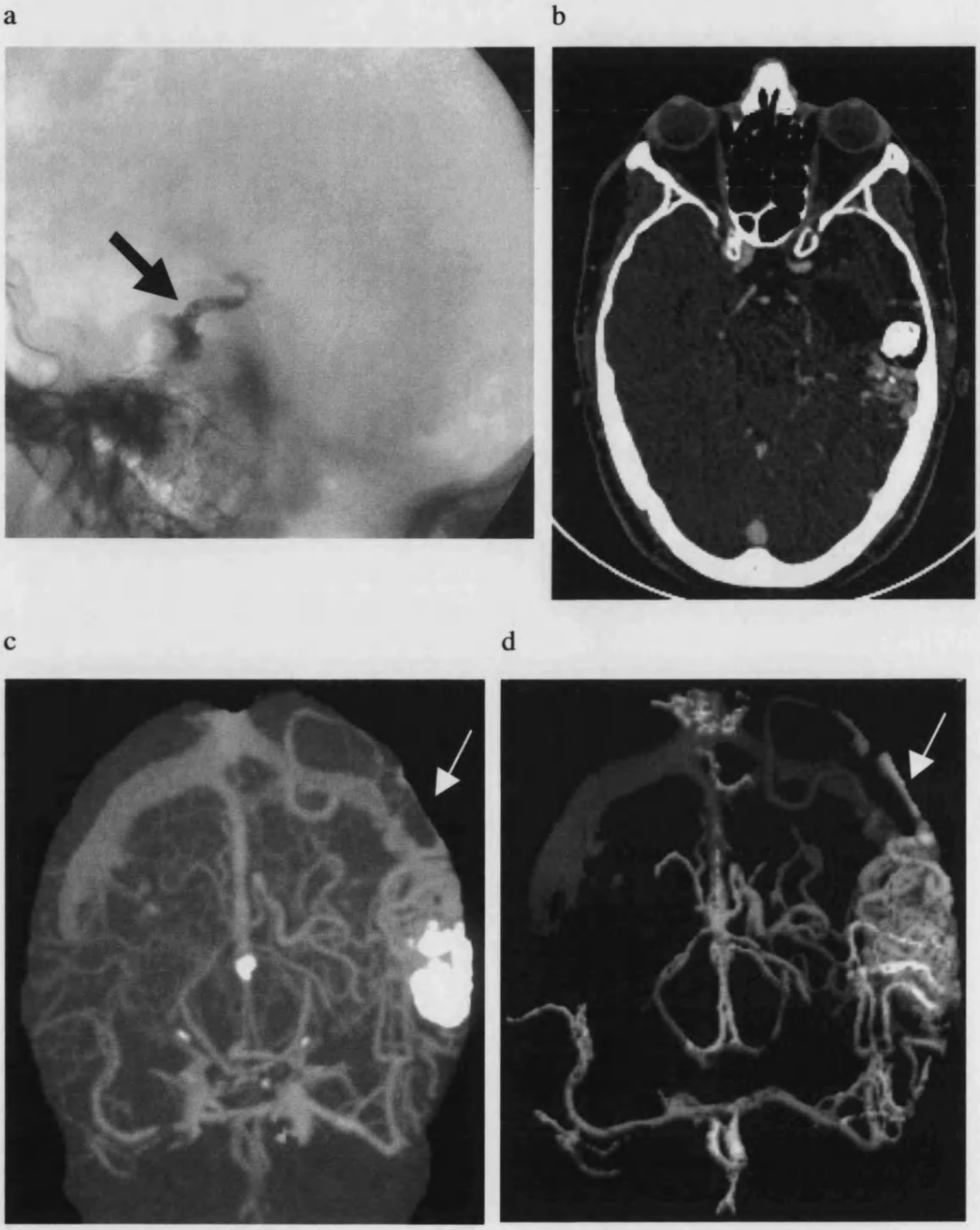

SSD has the property of occlusivity and therefore the glue cannot be visualised. These CTA images also show how draining veins lying just deep to the inner table of the skull can be partially lost with post-processing (white arrows)

3.4.2 Comparison of imaging techniques

3.4.2.1 CTA and DSA of all AVMs

SSD and MIP demonstrated well the size, pattern of venous drainage and numbers of arterial feeders and draining veins. MIP appeared to be marginally better than SSD at identifying the anatomical type of AVM present (κ 0.63 and 0.55 respectively) but the raw data showed that both types of images agreed with DSA in 75% of cases. They were both moderately good at identifying the origin of arterial feeders. One consistent difficulty with CTA and identification of the origin of arterial feeders was that any contribution from the external carotid was often removed with bone and therefore not appreciated by blinded observers. External carotid supply was present in five of the patients studied, but was not identified from any of the CTA (SSD or MIP) images. Nidal definition was extremely poorly demonstrated on both SSDs and MIPs (κ 0.17 and 0.12 respectively) when compared to DSA. Observers commented that this was often as a result of overlying draining veins (Figures 3.8a – c).

Kappa values for abnormal arterial and venous structures were in the main very poor for CTA images compared with DSA, with four exceptions: aneurysms arising from the Circle of Willis (κ 0.77 in both SSDs and MIPs); the presence of focal varices on SSDs (κ 0.59); and on MIPs, the demonstration of diffuse varices (κ 0.53) and venous occlusion (κ 0.46). However, in all cases of abnormal arterial anatomy and the presence of venous occlusion on SSDs, there was agreement between CTA and DSA in at least 75% of cases. MIPs were again particularly good at demonstrating the presence of embolisation material (κ 0.88). In SSDs, as previously mentioned, embolic material cannot be seen on the SSDs images themselves, resulting in poor agreement between SSDs and DSA (κ 0.00). Presence of calcification showed no agreement between SSD and MIP images and DSA. This is due to the fact that DSA images were subtracted images and therefore calcification was not seen. In this situation, it is likely that the MIP images in

Figure 3.8: a) Arterial and b) venous phases of an AVM on DSA with a corresponding c) MIP image

a

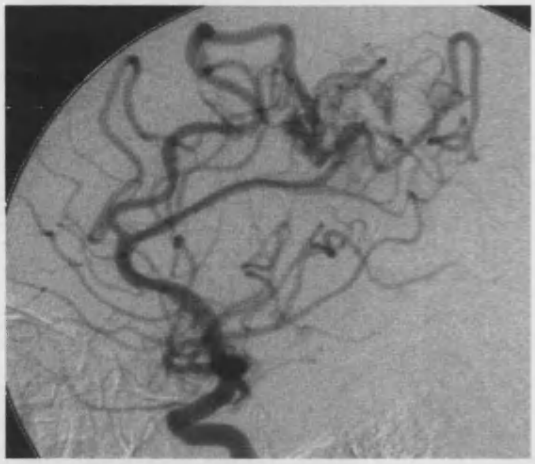

b

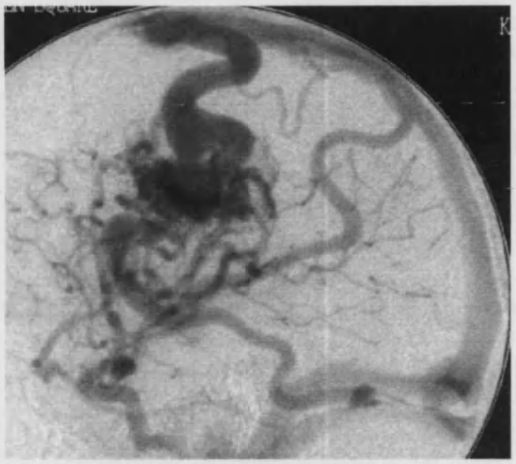

c

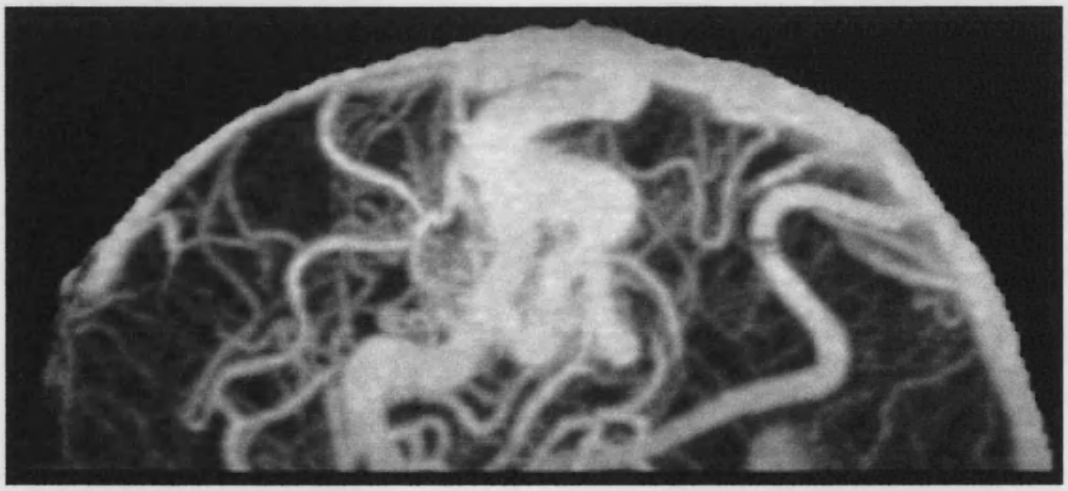

The combination of both arterial and venous phases on CTA images can prevent accurate analysis of the nidal structure which is frequently obscured by large draining veins

particular would demonstrate calcification well if compared to unsubtracted DSA films. Angiogenesis was moderately well demonstrated on CTA images with kappa values of 0.53 and 0.60 (SSD and MIP respectively).

Clinical and morphological goals of treatment from CTA agreed moderately well with DSA, but mode of treatment had kappa values of only 0.13 and 0.06 (SSD and MIP respectively). This was a highly selected group of patients, nearly half of whom underwent partial embolisation as their initial treatment. In addition, the neuroradiologists evaluating the CTAs were given only limited information about the patients to make a decision regarding treatment options, whilst the neuroradiologists evaluating the DSAs knew the patients well. Knowledge of symptomatology, as well as AVM anatomy, was clearly important in making an informed decision about the most appropriate form of treatment in these situations. If these CTAs had been evaluated prospectively by the neurovascular team that includes both interventional neuroradiologists and neurosurgeons, it is likely that decision-making using CTA would be improved.

3.4.2.2 CTA and DSA of small AVMs

The observers of the CTAs felt that analysis of small AVMs was much easier than that of large complicated lesions (Figures 3.9a and b). For this reason, the eight small AVMs were re-analysed separately. Analysis of the kappa values in this group was particularly difficult because of the small numbers involved.

There was very good agreement between DSA and SSD and MIP images of small AVMs in size, number of arterial feeders and venous drainage. MIP images showed better agreement with DSA, compared with SSD, with respect to anatomical classification (κ 0.76 and 0.50 respectively). Kappa values for the origin of arterial supply showed poor agreement between CTA images and DSA, however analysis of raw data showed agreement in over 60%. SSD was considerably better at identifying draining veins than MIP, when compared to DSA with respectively kappa values of 0.75 and 0.14. In an effort to reduce the radiation dose given to

Figure 3.9: MIP images of a) large and b) small sized AVMs

a

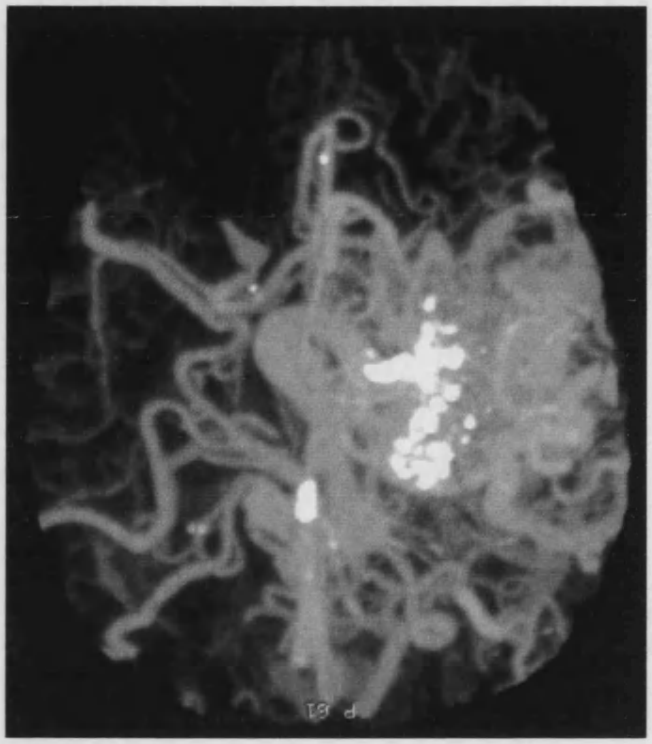

b

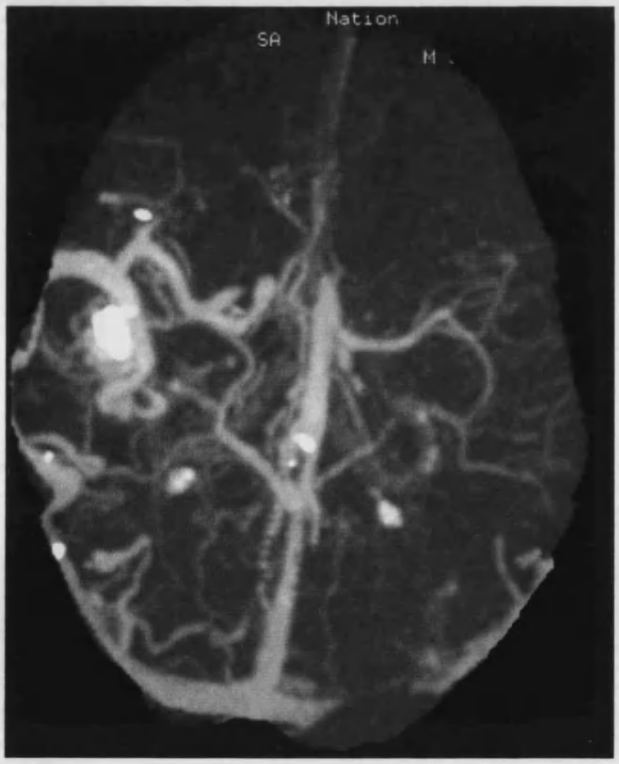

Analysis of the smaller lesion is clearly more straight-forward than that of the larger lesion

patients, the CTA volume acquired varied according to the size of the AVM. In some small cortical lesions lying close to the top of the skull this meant that the Circle of Willis was not included in the scanned volume. Observers of the CTAs found that this made distinction of arteries from veins more difficult and may have had some bearing on identification of the origin of arterial supply (both SSD and MIP) and numbers of draining veins on MIPs. Agreement on nidal definition was poor with kappa values of 0.00 in both cases, but evaluation of the raw data suggested that SSD showed better agreement than MIPs with DSA with agreement in 75% and 50% of cases respectively.

There was very good agreement between CTA images and DSA when identifying the presence or otherwise of arterial aneurysms. This was not reflected in the kappa values for aneurysms lying on the feeding arteries. There was perfect agreement between imaging modalities in this situation, but as there were no aneurysms identified, there was poor spread across the kappa frequency table and, as a result, too few categories to be able to calculate kappa.

This situation was also seen in identifying the presence of venous occlusion and angiogenesis. Although the kappa values for the presence of calcification was 0.00 using MIPs, there was agreement in 75% of cases. There was no agreement between SSD images and DSA in detecting calcification. There was, however, perfect agreement in the identification of embolic material between MIPs with DSA (κ 1.00), but poor agreement between SSDs and DSA (κ 0.00).

Identification of abnormal venous anatomy had generally poor kappa values, except SSDs identifying the presence of a focal varix (κ 0.50) and MIPs demonstrating diffuse varices (κ 0.60). Again, review of the raw results data showed there was perfect agreement of both SSDs and MIPs with DSA in the identification of venous occlusion.

Poor kappa values were seen between both CTA images and DSA for treatment options, reflecting the highly selected group and that the vast majority of these patients can be cured with obliteration of the nidus. Clinical goal and

morphological goals show kappa values of 0.00, but there was agreement in seven of the eight cases. This was not the case for mode of treatment kappa values (SSD and MIP, κ 0.00 and –0.21 respectively), where there was poor agreement between reviewers.

3.5 Conclusion

During evaluation of the CTAs, it became clear that observers' interpretation of certain characteristics was very different. Many features were objective, such as the number of feeders, site and presence or otherwise of aneurysms. Other features however, such as nidus definition and the distinction between focal and diffuse varices, were much more subjective. This was partly due to observer experience and therefore some of the kappa values have to be interpreted with this in mind.

The use of kappa as a measure of agreement does have limitations. Small numbers of observations with poor spread can result in there being too few categories to be able to calculate kappa. The analysis of a highly selected group of individuals will also mean poor scatter across the kappa frequency table. Both of these situations can lead to poor kappa values, and examination of the raw data may be of greater use in interpreting the level of agreement between observers. This was seen in several of the observations made in this study, in particular, the identification of aneurysms on feeding arteries and venous stenoses and occlusion and also in the comparison of imaging techniques when only small AVMs were considered. This was a limitation of the study. The methodology of the study could be improved by imaging a larger number of patients whose AVMs were managed by a wider variety of treatments.

CTA correctly identified main arterial feeders, associated arterial aneurysms, venous drainage patterns and venous varices in most cases, but was poor at identifying external carotid supply to the AVM. Small draining veins, particularly lying on the inner table of the skull, were also occasionally difficult to identify

Figure 3.10: Coronal reformat from axial source data allowing appreciation of intranidal structure and features

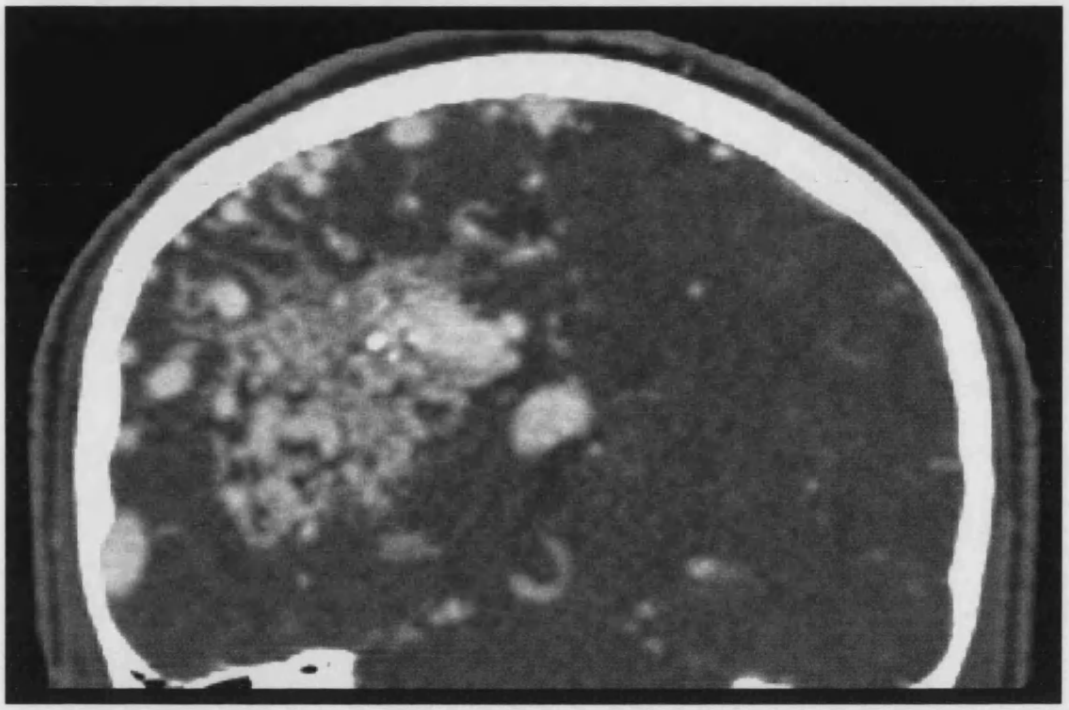

because they were frequently subtracted out with the 'bone' object. These problems could be rectified by modifying the post-processing protocol. In addition, observers of the CTAs found that in cases where the Circle of Willis had not been included in the imaged volume, distinction of arteries from veins and the identification of the origin of arterial supply were more difficult. The Circle of Willis should therefore always be included in the imaged volume. This often requires use of the larger of the two CTA acquisition protocols, allowing larger z-axis coverage and therefore easier and improved orientation and identification of feeding arteries for interpretation of the images. Although CTA was able to detect most important angio-architectural features in AVMs, it was not as accurate as DSA for making decisions regarding future management of patients, particularly because both temporal resolution and nidus definition were poor.

SSD CTAs were slightly superior to MIPs in most AVMs, particularly in those with a cortical location and superficial venous drainage. In addition, bone could be shown in SSDs as a separate differently-coloured object if required.

Isolated small feeding vessels were not always detected with CTA. This was more problematic on SSD than MIP images because of thresholding effects.

MIPs are easier and quicker to post-process. MIPs were better than SSDs at demonstrating intranidal glue or calcification but did not allow appreciation of bony relationships as bone was subtracted out during post-processing. However, access to the raw data axial slices prevented this from being a problem.

Interpretation of both SSD and MIP images was aided by the availability of the source data (Figure 3.10). SSD images in particular did not allow full appreciation of the internal structure of tightly packed niduses which prevented the observer from appreciating, for example, the presence of embolisation material or calcification. These features, however, are evident from source data. In reality, source data is always available for analysis and CTAs are not viewed in isolation, allowing appreciation of particular details from the source data alone, even if it is not identified on the CTA images themselves.

Chapter 4

MR ANGIOGRAPHY

4.1 Introduction

DSA is invasive and has associated risks, in particular that of stroke. MRA is a non-invasive vascular imaging method which in some situations has replaced DSA and has now become part of clinical routine (Pollock, 1996c). Carotid artery stenosis, for example, can be demonstrated on MRA, most commonly using a 2D TOF sequence. Avoidance of DSA in these patients is of great advantage as many have vascular risk factors and are therefore at greater risk of complications when undergoing DSA.

MRA can be performed using either 2D TOF, 3D TOF or PC sequences. TOF sequences are based on the inflow of magnetised blood into a saturated stationary tissue, whilst phase-contrast imaging uses a bipolar pulse sequence to detect shifts in the phase caused by blood flowing through a magnetic gradient. In all techniques, contrast between blood vessel and stationary tissue is as a result of blood motion. All of these methods can detect laminar flow above a certain velocity, but turbulent or slow flow or in-plane flow may remain undetected. In addition, associated T1 contamination artifact, caused by blood or fat, appears as high signal areas and can obscure vascular detail. In AVMs, these can be highly relevant issues, with poor demonstration of the complex angioarchitecture of the lesion or the slow-flowing draining veins, particularly in the context of acute haemorrhage.

The use of gadolinium-based contrast medium has been advocated to minimise some of these disadvantages. Gadolinium shortens the T1 relaxation time of blood, which increases intravascular signal, making it less dependent on laminar

flow and improving the signal-to-noise ratio. The resulting short T1 of blood permits sequences with very short TRs and thus short acquisition times. MRA images are therefore based on short T1 rather than flow-related enhancement and saturation effect problems are avoided (Pernicone, 1997). This has the potential for better visualisation of slow flow or flow running in the imaging plane (Parker, 1998). Intracranial contrast-enhanced MRA has, to date, mostly used a modified TOF sequence.

Few studies have prospectively assessed the accuracy and resolution of MRA in the assessment of AVM angioarchitecture when compared with DSA. Tanaka *et al.* (Tanaka, 1997) analysed the results of 12 unenhanced 3D TOF sequences with those acquired from both CTA and DSA. MRA detected 73% of arteries but only 32% of veins due to saturation effects. Huston *et al.* (Huston, 1991) performed a similar study comparing 3D TOF and PC MRA. Fifty two percent of arteries and 11% of veins were identified on 3D TOF sequences, whilst 44% of arteries and 54% of veins were identified on the PC MRA sequences.

Dynamic contrast-enhanced MRA uses a rapid sequence acquisition (gradient-echo slices) during the injection of a gadolinium bolus. This method is increasingly used for the investigation of the carotid artery but its application to the intracranial circulation has been limited (Bongartz, 1997). This is mainly because the rapid acquisition does not allow coverage of a large area. By investigating the use of contrast-enhanced MRA in small AVMs, large area coverage was not necessary.

4.2 Methods

4.2.1 Patients

Patients were recruited from those seen by the neurovascular surgery or interventional neuroradiology services at The National Hospital for Neurology and

Neurosurgery between March 1999 and January 2000. All patients were known to have AVMs measuring less than 3 cm in one dimension and had undergone recent catheter angiography. To allow adequate temporal and spatial resolution on the contrast-enhanced gradient-echo sequences, only 12 slices at a maximum thickness of 2.5 mm were acquired. This necessitated restriction of the size of AVM that could be imaged. Patients with the usual contra-indications to MRI scanning were excluded.

4.2.2 Imaging

Scanning took place on a 1.5T Signa® scanner (General Electric Medical systems®, Milwaukee, USA) at the Multiple Sclerosis NMR Research Group, Institute of Neurology. All patients underwent 3D TOF pre and post contrast and dynamic contrast-enhanced gradient-echo sequences.

4.2.2.1 3D TOF sequences

The 3D SPGR-TOF sequence was acquired axially with TR 52 msec, TE 6.9 msec, flip angle 30°, bandwidth 32kHz, 24 cm field of view, 0.9 mm slice thickness, 64 slices and 512 x 192 matrix. Acquisition took 8:03 min. This sequence was performed before and after administration of a 15 ml bolus of gadolinium-based contrast medium, Dotarem® (Guerbet Laboratories, Aulnay-sur-Bois, France), irrespective of body weight. Only one contrast bolus per patient was required for the study, the second 3D TOF sequence being performed after the dynamic contrast-enhanced gradient-echo sequence described below.

4.2.2.2 Contrast-enhanced gradient-echo sequences

A 3D SPGR sequence was acquired with scan parameters TR minimum, TE minimum, flip angle 30°, bandwidth 32kHz, 22cm field of view, slice thickness 1.5 – 3.0mm (depending on size of AVM), 12 slices per slab and 256 x 128 matrix. Each sequence took 13 sec. This sequence was performed 3 times in quick succession to allow subtraction of the second and third acquisitions from the first baseline

acquisition in an effort to produce 3D angiographic representation of arterial and venous phases separately. A 15 ml hand-bolus of gadolinium-based contrast medium, Dotarem® (Guerbet Laboratories, Aulnay-sur-Bois, France), was given over 5 - 7 sec at 3 sec into the first acquisition.

4.2.3 Post processing

All processing was carried out on a Sun® Ultra 5 workstation (Sun Microsystems, Berkley, USA) running Advantage Windows® (version 3.1) software (General Electric Medical Systems, Milwaukee, USA).

Pre- and post-contrast 3D TOF images were produced in the usual way and standardised views of the resulting MRAs were saved on film for review.

The first gradient-echo acquisition, prior to contrast bolus arrival, was used as a baseline and subtracted from the second acquisition in order to demonstrate the arterial phase of the angiogram. The second was then subtracted from the third acquisition in order to demonstrate the venous phase of the angiogram. As above, standardised views of the resulting MRAs were saved on film for review

4.2.4 Image analysis

Image analysis was performed as described in section 3.2.4. All pre-contrast TOF images were reviewed in one sitting, followed by the contrast-enhanced gradient-echo sequences at a second viewing and finally the post-contrast TOF images at a third sitting.

4.2.5 Statistical analysis

Data were collated using Microsoft® Excel 98 and statistical analysis was performed using Stata™ 4.0 (Stata corporation, Texas, USA) as described in section 3.2.5.

4.3 Results

4.3.1 Patient baseline characteristics

Ten patients, three male and seven female, known to have AVMs measuring less than 3cm in at least one dimension underwent MRA and DSA, separated by a median of 61 days, interquartile range 4 - 167 days. They had a median age of 40 years with an interquartile range of 23 - 48 years. Four patients presented with seizures, five with haemorrhage (SAH, ICH or IVH) and one was asymptomatic, having been identified following DSA for investigation of a remote haemorrhage. Patient demographic data is summarised in Table 4.1.

4.3.2 MRA analysis

The radiologists' findings are summarised in Appendix 3. From DSA, the anatomical locations were cortical in nine and deep-seated in one. Arterial supply was from the anterior circulation alone in four, posterior circulation in four and anterior and posterior in two. Venous drainage was superficial in eight and deep in two. Six of the 10 patients had undergone partial treatment of their AVM prior to undergoing MRA, five had undergone partial embolisation whilst the sixth had undergone both partial embolisation and stereotactic radiosurgery.

4.3.3 Kappa values

4.3.3.1 Pre- and post-contrast 3D TOF

The kappa values calculated for both interobserver variability and comparison of imaging techniques are shown in Table 4.2.

Table 4.1 : Demographic data of all patients undergoing pre- and post-contrast 3D TOF and contrast-enhanced gradient-echo MRA

Patient Number	Gender	Age	Presentation	AVM			Time interval*	Prior treatment	Planned treatment
				Site	Anatomy	Size			
1	F	27	Seizures	Right parietal	Cortical	Small	1	Embolisation	Stereotactic DXT
2	M	18	ICH	Right parietal	Cortical	Medium	36	None	Embolisation
3	F	61	Seizures	Right fronto-parietal	Cortical	Medium	1	Embolisation	Conservative
4	F	49	Asymptomatic	Left ambient cistern	Cortical	Small	269	None	Conservative
5	F	40	SAH	Right thalamic	Deep	Small	421	None	Stereotactic DXT
6	F	41	Seizures	Left temporal	Cortical	Small	60	Embolisation	Conservative
7	F	32	IVH	Left temporal	Cortical	Medium	63	Embolisation / Stereotactic DXT	Conservative
8	F	48	SAH	Left occipital	Cortical	Large	69	Embolisation	Embolisation
9	M	55	Seizures	Right temporal	Cortical	Medium	266	Embolisation	Conservative
10	M	19	IVH	Left cerebellar	Cortical	Small	8	None	Embolisation

* time interval in days between MRA and DSA

Table 4.2: Kappa values for interobserver variability and comparison of imaging techniques for MRA images

	Interobserver variability			Comparison of imaging techniques for all AVMs		
	Pre contrast TOF	CEMRA	Post contrast TOF	Pre contrast TOF versus DSA	CEMRA versus DSA	Post contrast TOF versus DSA
Size*	0.74	1.00	1.00	0.68	0.63	0.72
Nidal definition*	0.75	0.78	0.76	0.18	0.57	0.55
Anatomical classification	0.30	0.53	0.83	0.43	0.41	0.59
Arterial supply	0.36	0.40	0.69	0.19	0.00	0.69
Number of arterial feeders*	0.76	0.60	0.71	0.68	0.43	0.81
Venous drainage	0.31	0.39	0.17	- 0.02	0.58	0.57
Number of draining veins*	0.60	0.74	0.53	0.12	0.64	0.77
Aneurysm on feeding arteries	0.43	1.00	0.00	- 0.07	- 0.07	0.00
Aneurysm on Circle of Willis	0.62	1.00	0.00	0.00	0.00	0.00
Intranidal aneurysm	0.71	1.00	0.00	- 0.22	- 0.08	- 0.18
Presence of focal varix	0.67	0.17	- 0.19	0.08	0.25	0.09

Table 4.2 (continued): Kappa values for interobserver variability and comparison of imaging techniques for MRA images

	Interobserver variability			Comparison of imaging techniques for all AVMs		
	Pre contrast TOF	CEMRA	Post contrast TOF	Pre contrast TOF versus DSA	CEMRA versus DSA	Post contrast TOF versus DSA
Presence of diffuse varices	0.67	0.55	0.52	- 0.01	0.39	0.52
Presence of venous stenosis	0.67	0.41	0.00	- 0.14	0.19	- 0.43
Presence of venous occlusion	0.67	0.30	0.00	0.00	0.00	0.00
Clinical goal of treatment	0.31	0.74	0.57	0.15	0.41	0.12
Morphological goal of treatment	0.31	0.62	0.67	0.18	0.15	0.10
Mode of treatment	0.32	0.62	0.43	0.17	- 0.25	- 0.19

* weighted kappa values

4.3.3.2 'Arterial' phase contrast-enhanced gradient-echo MRAs

Although designed to show only the arterial phase of the angiogram, these images showed both arterial and venous phases due to the rapid arteriovenous shunting present in AVMs. The kappa values calculated for both interobserver variability and comparison of imaging techniques are shown in Table 4.2.

4.3.3.3 'Venous' phase contrast-enhanced gradient-echo MRAs

Subtracting the second acquisition images (actually showing both arterial and venous phases) from the third set of images left very little vasculature evident. As a result, all of these images were uninterpretable.

4.4 Discussion

MRI is non-invasive with a good safety profile. There are contra-indications to MR scanning which most importantly include those patients with ferromagnetic devices or implants. Although most intracranial implants now used are MR compatible, this has not always been the case.

3D TOF has a high spatial resolution. However, in high-flow vascular lesions, which are often geometrically complicated, 3D TOF does have disadvantages. 3D TOF sequences are less sensitive to turbulent or slow flow, which has particular implications in patients with AVMs. The use of gadolinium can contribute to an increase in contrast resolution with overall improvement in delineation of small vessels.

CEMRA, using a paramagnetic contrast agent, results in enhanced T1 shortening and therefore a more favourable signal-to-noise ratio, limiting signal loss. Stationary spins of the background tissue are saturated giving minimal signal whilst the unsaturated spins of moving blood giving a bright signal. Signal intensity increases with increasing blood velocity and TR and decreasing slice thickness. Blood regains its longitudinal magnetisation more rapidly giving stronger signal intensity and therefore increasing the difference in signal intensity between blood

vessels and the surrounding background tissue. Contrast can be increased still further by subtracting pre- from post-contrast images provided the patient does not move between sequences. Exclusive arterial enhancement can theoretically be achieved by imaging first pass of the contrast bolus only. Venous contrast passage can also be imaged with only one intravenous bolus of contrast. The primary limitation of 3D CEMRA is the k space acquisition speed and thus the achievable image resolution during the time limited first pass of contrast media. This was a problem seen in the patients imaged in this study and in particular limited the size of AVM that could be imaged to a maximum of 3 cm in one conventional plane (sagittal, coronal or axial). The availability of high performance gradient sets on clinical scanners now allows speed-up to an extent where the fundamental signal-to-noise ratio limit becomes imminent.

4.4.1 Interobserver variability

All three MR sequences showed good interobserver agreement with regard to size, nidal definition, and numbers of feeding arteries and draining veins (range κ 0.53 to 1.00). Anatomical classification was only fair on pre-contrast TOF sequences as in up to four cases this was not assessable by the observers (κ 0.3). This was partly a reflection of the fact that only small AVMs were studied. However there was moderate agreement on CEMRA and very good agreement on post contrast TOF sequences (κ 0.53 and 0.83 respectively). The origin of arterial feeders showed only fair agreement between observers on pre-contrast TOF and CEMRA sequences, again partly compounded by the fact that the AVM nidus could not be visualised in up to four individuals (κ 0.36 and 0.40 respectively). However, there was good agreement on post-contrast TOF sequences (κ 0.69). There was universally only poor to fair agreement on the pattern of venous drainage (range κ 0.17 to 0.39).

Identification of abnormal arterial and venous anatomy showed generally good or very good agreement on pre-contrast TOF and CEMRA sequences. There

were very low kappa values for post-contrast TOF sequences and the identification of focal varices and venous occlusion on CEMRA images. In all of these situations, looking at the raw data (Appendix 3), there was agreement in 50 – 90% of cases and the low kappa values reflect a poor spread of data amongst the cells of the tables.

Decisions regarding management of individual patients showed poor interobserver variability on pre-contrast TOF sequences although there was agreement in 50% of cases (range κ 0.31 to 0.32). Some of these options, however, were not assessable as the AVM was too poorly visualised. Interobserver variability was moderate or good on CEMRA and post-contrast TOF sequences (range κ 0.43 to 0.74), although only seven of the AVMs could be assessed on CEMRA, whilst decisions could be made about all patients on the basis of the post-contrast TOF sequences.

4.4.2 Comparison of imaging techniques

Post contrast TOF sequences were by far the best at demonstrating the size, nidal definition, anatomical classification and identification of numbers of feeding arteries and draining veins and their origin / destination (range κ 0.45 to 0.81). CEMRA sequences were the next best at identifying the above features, only showing no agreement with arterial supply. The main difficulty associated with the CEMRA sequences was the limited volume acquisition possible allowing reasonable spatial resolution. This meant that landmarks, in particular the Circle of Willis, were often not included in the scanned volume. As a result, in four individuals, the origin of feeding arteries could not be identified (κ 0.00). Pre-contrast TOF sequences were the worst at identifying several factors, in particular nidal definition (which is often a subjective issue anyway as demonstrated on CTA previously (section 3.4.1)) (κ 0.18), origin of feeding arteries (κ 0.19) and venous drainage (κ -0.02) and the number of draining veins (κ 0.12). In up to nine cases this was because vessels, in particular slow-flowing veins, were not visualised.

The kappa values when comparing visualisation of abnormal arterial and venous anatomy were low (range κ -0.43 to 0.19), suggesting poor agreement between DSA and all MR sequences, except in the identification of diffuse varices on CEMRA and post-contrast TOF (κ 0.39 and 0.52 respectively). However inspection of the post-contrast TOF raw data showed agreement in 60 – 100%. There was poor agreement of only 40 – 50% in identifying focal varices and venous stenosis when compared with DSA. Again kappa values were low because of few cells and poor spread across the tables in Appendix 3. CEMRA in general showed poorer agreement with DSA than post-contrast TOF sequences, whilst pre-contrast TOF showed still poorer agreement. However, even these two sequences were able to demonstrate at least 50% of all abnormal arterial and venous anatomy.

There was generally poor agreement of all MR sequences with DSA when assessing management options.

4.5 Conclusion

MRA was able to demonstrate salient angioarchitectural features of AVMs but was not able to provide an accurate enough assessment with regard to treatment options to replace DSA as an initial diagnostic procedure on which future management is planned.

Of the three sequences used here, post-contrast 3D TOF provided the most accurate data although was worst at predicting appropriate management on the basis of MRA alone (Figures 4.1a – d). Interobserver variability of post contrast 3D TOF sequences showed good kappa values, allowing for the limitations of the kappa statistic, suggesting that the assessment was reproducible. CEMRA was the next most accurate of sequences, followed finally by pre-contrast TOF sequences. This confirmed that the use of gadolinium-based contrast agents was able to improve signal-to-noise ratio and visualisation of slow and turbulent flow, particularly for nidus definition (Figures 4.2a and b) and draining veins (Figures 4.3a - d).

Figure 4.1: a) DSA, b) CEMRA and c) pre- d) and post-contrast 3D TOF images of a small parietal AVM

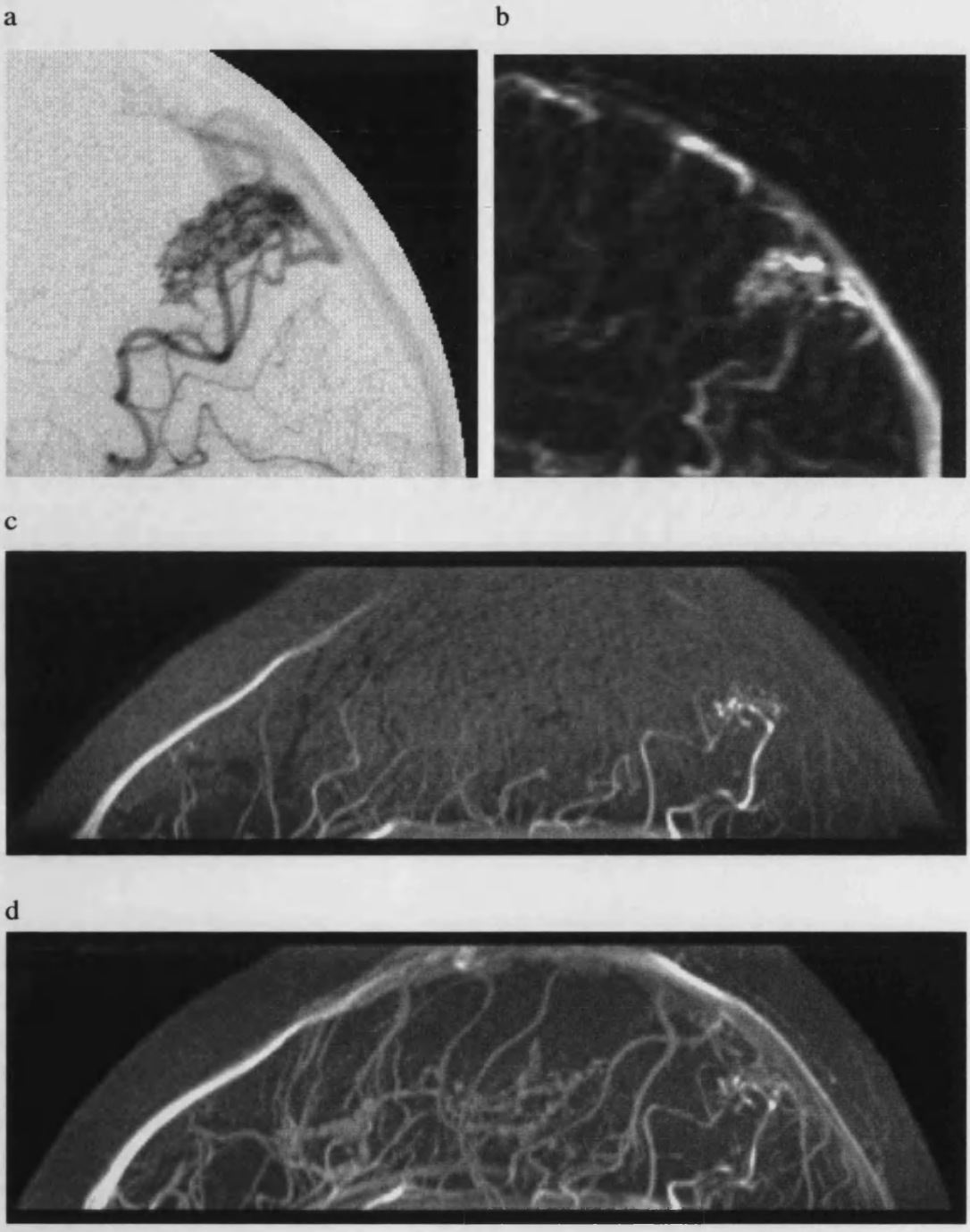

improved demonstration of slow flow is seen on the contrasted images, particularly in the superior sagittal sinus

Figure 4.2: a) Pre- and b) post-contrast 3D TOF images of an AVM only visualised well post-contrast because of slow flow in the draining veins (white arrow)

a

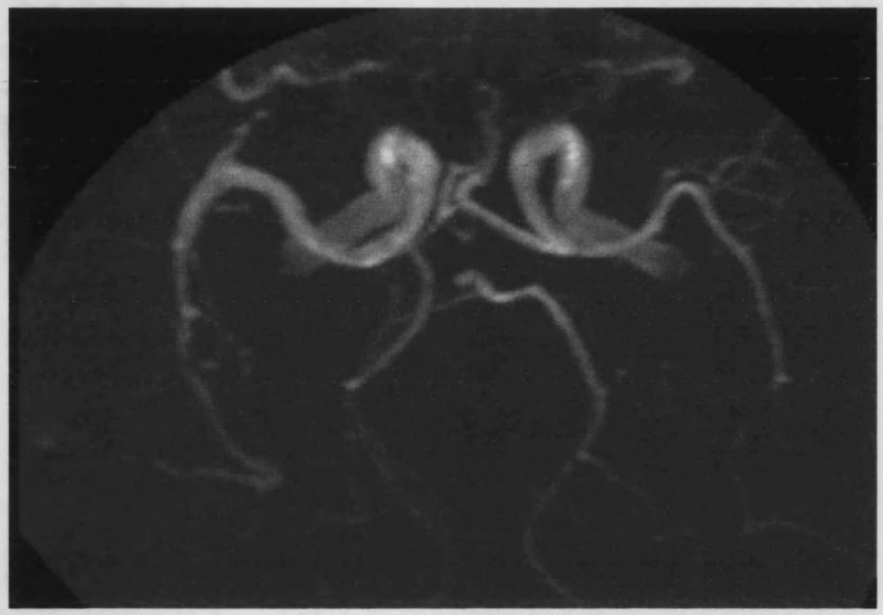

b

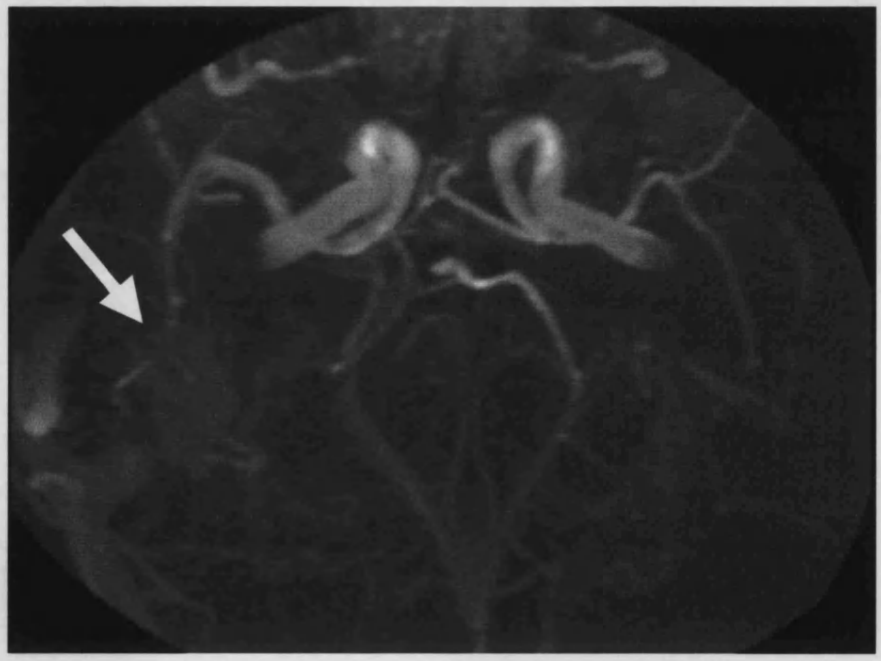

Figure 4.3: Visualisation of a draining vein

a DSA arterial phase

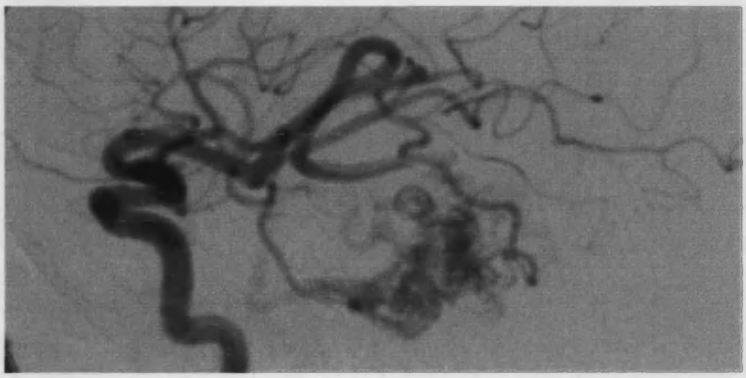

b DSA venous phase

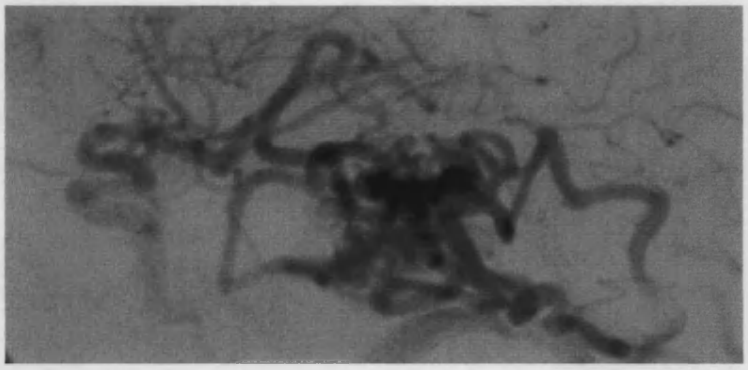

c Pre-contrast 3D TOF

d Post-contrast 3D TOF

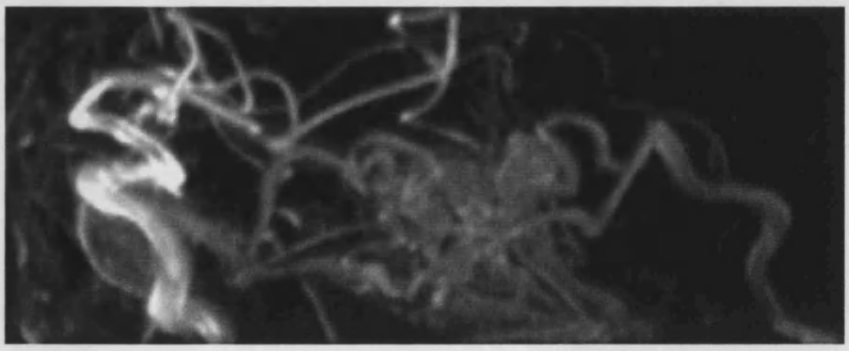

In this selected group of small AVMs, it allowed visualisation of the AVM itself in several cases where it could not be seen at all on pre-contrast images.

As with CTA images, temporal resolution of CEMRA was not good enough to allow a 3D representation of separate arterial and venous phases of the AVM without an unacceptable deterioration in spatial resolution. This clearly remains a major disadvantage over DSA. Since the completion of this study, a new technique of MRA DSA for the assessment of AVMs has emerged. 2D MR acquisitions with a temporal resolution of one image sec^{-1} can now be achieved, allowing separation of arterial and venous phases.

Chapter 5

VOLUMETRIC ANALYSIS OF AVM NIDUS USING MRI

5.1 Introduction

Accurate nidus measurement is important for predicting surgical outcome and assessing suitability for radiosurgery. It is an important component of the Spetzler grade of the lesion, which influences the mortality and morbidity associated with surgical treatment of AVMs (Spetzler and Martin, 1986; Heros, 1993). The results of stereotactic radiosurgery are also dependent upon the size and more importantly, the volume of AVM, being treated (Lunsford, 1991; Gallina, 1998). With increasing volume, the obliteration rate decreases with an associated increase in morbidity and side effects. Successful radiosurgical treatment requires accurate assessment of the AVM volume, precise delivery of radiation dose to the often irregular AVM margin and 3D imaging of the AVM nidus. Although biplane angiography is adequate to define the AVM shape in the vast majority of patients, MRI provides additional 3D anatomical information (Lunsford, 1991). Treatment of AVMs by radiosurgery currently involves stereotactic localisation of the AVM by DSA. MRI is used primarily to assess the precise location of the nidus and whether it involves eloquent areas of brain and hence the associated risks of stereotactic radiosurgery and possible side effects. However, some units are increasingly using stereotactic localisation from MRI, thus reducing the need for invasive DSA (Petereit, 1993; Kondziolka, 1994; Pollock, 1996c).

A commonly used measure of AVM size is the largest linear dimension, as in the Spetzler grading (Spetzler and Martin, 1986). Alternatively, an ellipsoid approximation is generated from three orthogonal measurements taken from conventional DSA. In a study by Noorbehesht *et al.* (Noorbehesht, 1987), AVM

size was determined from DSA, CT and MR by taking the largest orthogonal measurement from all three investigations. The size of the malformation measured on MR was found, in general, to be smaller than the size determined from angiographic films. This discrepancy increased as the size of the AVM increased. They concluded that MR by virtue of its ability to discriminate between draining veins and AVM nidus, and its ability to do this in three planes, provided a more accurate estimate of AVM size than that calculated from DSA.

This study was performed in order to examine the differences in AVM nidal volumes generated from three MR sequences (3D fast spin-echo (FSE) and pre- and post-contrast 3D TOF) and to compare these with the more commonly used ellipsoid approximation of the AVM nidal volume from DSA.

5.2 Methods

5.2.1 Patients

Patients were recruited from those seen by the neurovascular surgery or interventional neuroradiology services at The National Hospital for Neurology and Neurosurgery between January and October 1999. All patients were known to have AVM and had undergone recent catheter angiography confirming its presence, anatomy and size. Patients with the usual contra-indications to MRI scanning were excluded.

5.2.2 Imaging

Scanning was performed on a 1.5T Signa® scanner (General Electric Medical Systems, Milwaukee, USA) at the Multiple Sclerosis NMR Research Group, Institute of Neurology. All patients underwent 3D TOF pre- and post-gadolinium contrast and 3D FSE.

5.2.2.1 3D TOF sequences

A 3D TOF sequence (TR 30msec, TE 6.9msec, flip angle 30°, 0.9mm slice thickness, 21cm field of view, 512x128 matrix) was acquired in the axial plane, before and after administration of 15ml 0.1mM Gd-DOTA (Dotarem®, Guerbet Laboratories, Aulnay-sur-Bois, France), irrespective of body weight. The scan sequence took 7:10 min.

5.2.2.2 FSE sequences

T_2–weighted 3D FSE images (TR 3000msec, TE 84msec, 1.5mm slice thickness, 25cm field of view and 256x192 matrix) were acquired in the coronal plane. The sequence took 3:21 min.

5.2.3 Post processing

All three sequences were post-processed on a Sun® Ultra 5 workstation (Sun Microsystems, Berkley, USA) running Advantage Windows®, version 3.1, software (General Electric Medical Systems, Milwaukee, USA). The volumetric data sets were reformatted to produce contiguous slices of 1.5mm thickness in the sagittal, coronal or axial planes. Sagittal slices were defined as parallel to and coronal slices perpendicular to the interhemispheric fissure of the brain, whilst axial slices were defined as parallel to the line joining the anterior and posterior commisures of the corpus callosum. The choice of the reformatting plane depended upon the shape of the AVM and was perpendicular to the shortest axis of the nidus. This approach minimises errors due to partial volume effects in the end slices of the AVM, since the lesion has the smallest cross-sectional area in the reformatted plane.

5.2.4 Image analysis

5.2.4.1 MRI

The AVM nidus volume was estimated using Cavalieri's principle (McNulty, 2000):

$$\text{Volume} = \sum_i A_i \,.\, \Delta z$$

where Δz is the reformatted slice thickness and A is the area of nidus defined on each slice.

The boundaries of the nidus were defined independently by three neuroradiologists on the Sun® Ultra 5 workstation (Sun Microsystems, Berkley, USA) by drawing a freehand trace around the nidus on each reformatted slice. Hard copy films of the manual tracings were produced for future review. The area measurement of each ROI was multiplied by the slice thickness (1.5mm). The subvolumes derived by this method were summed for all slices giving the total AVM nidus volume in mm^3. The order of sequences on which the nidus was defined was randomised in order to minimise bias and no two sequences from the same patient were analysed consecutively.

5.2.4.2 DSA

Three orthogonal measurements of the AVM nidus were taken on the AP and lateral DSA projections by the same three observers (Figure 5.1). The AVM nidus volume was estimated using approximation to an ellipsoid, where:

$$\text{Volume} = \frac{4}{3}\pi\left(\frac{dx \,.\, dy \,.\, dz}{8}\right)$$

where x, y and z are the maximum dimensions of the AVM nidus in three orthogonal planes.

Figure 5.1: DSA of AVM showing three orthogonal measurements of nidus for use in ellipsoid approximation of nidal volume (white arrows)

a Lateral view

b AP view

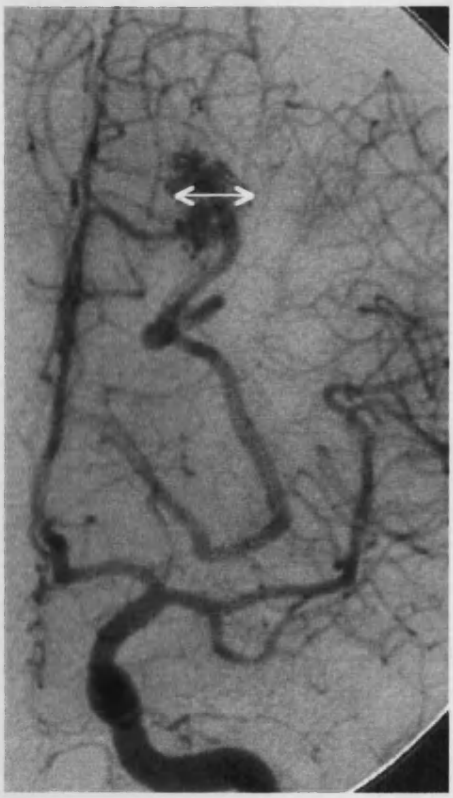

5.2.5 Statistical analysis

Data were collated using Microsoft® Excel 98 and statistical analysis was performed using Stata™ 4.0 (Stata Corporation, Texas, USA) as described in section 3.2.5.

5.3 Results

5.3.1 Patient baseline characteristics

Ten patients with AVMs were recruited to the study (Table 5.1). Three were male, seven female with a median age of 36 years (interquartile range of 22 – 46 years). Four patients had small AVMs, five medium sized and one, a large AVM. There was a median time of 31 days (interquartile range 1 – 69 days) between MRI and DSA in these patients. Five patients had presented with seizures and five with intracranial haemorrhage. Five individuals had undergone previous partial embolisation of their AVM, whilst one individual had previously been treated with stereotactic radiosurgery.

5.3.2 AVM nidus volumes

5.3.2.1 Intersequence variability

Comparison of the mean nidal volume of all observers for each patient and imaging method can be used to assess any systematic differences between sequences (Table 5.2). On inspection of this table, it appears that nidal volumes calculated from post-contrast TOF sequences are consistently larger than those calculated from DSA and both pre-contrast TOF and 3D FSE sequences.

To assess intersequence variability between DSA and MR more closely, the average nidal volume calculations of all three observers for DSA and MR sequences were compared. The average DSA volume for each patient was compared directly with the average volume for each MR sequence (Figure 5.2).

Table 5.1 : Demographic data of all patients undergoing MR volumetric studies

Patient Number	Gender	Age	Presentation	AVM			Time interval*	Prior treatment	Planned treatment
				Site	Anatomy	Size			
1	F	22	SAH	Left callosal	Callosal	Small	79	None	Embolisation
2	F	21	SAH	Right basal ganglia	Deep	Small	35	None	Stereotactic DXT
3	M	18	IVH	Left callosal	Callosal	Small	28	None	Embolisation
4	F	47	SAH	Left occipital	Cortical	Large	40	Embolisation	Embolisation
5	F	27	Seizures	Right parietal	Cortical	Small	1	Embolisation	Embolisation
6	M	36	Seizures	Left parietal	Cortico-ventricular	Medium	1	Embolisation	Conservative
7	M	43	Seizures	Left temporal	Cortical	Medium	69	Embolisation	Embolisation
8	F	46	Seizures	Left fronto-parietal	Cortico-ventricular	Medium	365	None	Conservative
9	F	36	SAH	Left callosal	Callosal	Medium	1	Stereotactic DXT	Embolisation
10	F	62	Seizures ICH	Left occipital	Cortico-ventricular	Medium	2	None	Embolisation

* time interval in days between MR studies and DSA

Table 5.2: Mean nidal volume for all investigations

	Sequence			
Patient	DSA	3D FSE	Pre-contrast TOF	Post-contrast TOF
1	1.37	0.84	1.28	3.79
2	0.59	0.89	1.02	1.16
3	4.27	3.59	3.10	3.81
4	23.04	20.85	21.17	27.97
5	1.78	1.98	1.59	1.97
6	29.21	49.37	48.19	64.90
7	10.25	7.06	8.83	11.76
8	23.88	16.21	23.08	24.71
9	22.88	16.99	21.84	30.44
10	34.78	26.21	27.27	37.11

Figure 5.2: Graph showing average DSA volumes against volumes by all three MR sequences, together with the line of identity.

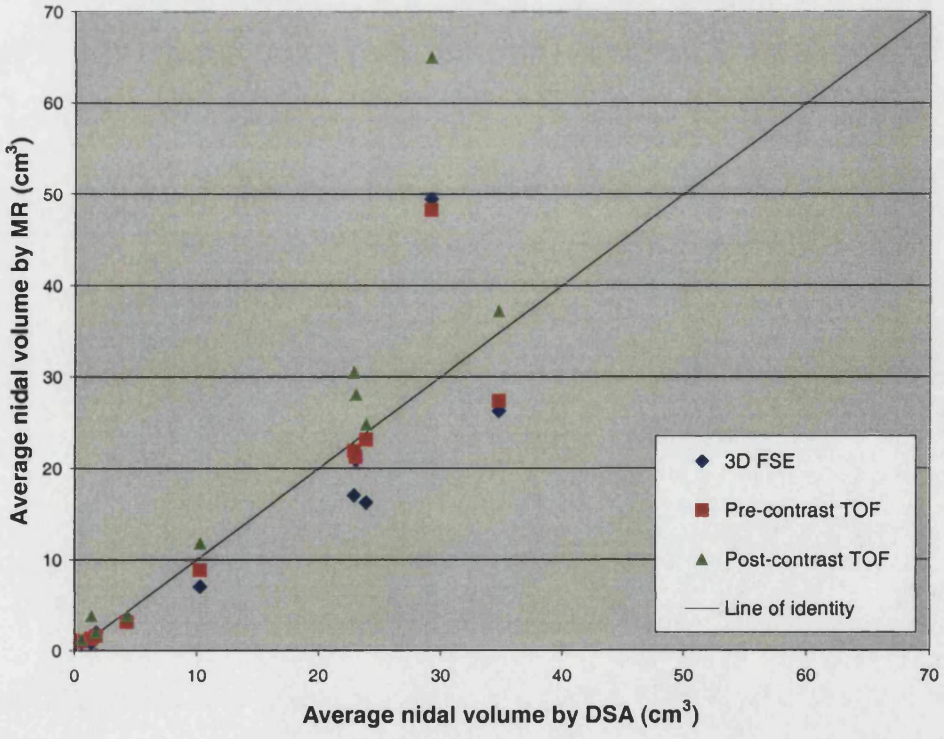

To assess the data further, the method described by Bland and Altman (Bland and Altman, 1986) for assessing agreement between two methods of clinical measurement was used. Initially the nidus volume by DSA and each MR sequence was averaged and compared with the difference between these two volumes. It can be seen that the differences between average nidal volume by DSA and MR increases with increasing nidal volumes (Figure 5.3).

Figure 5.3: Graph showing the average nidus volume by DSA and MR against the difference in nidus volume by the same two techniques

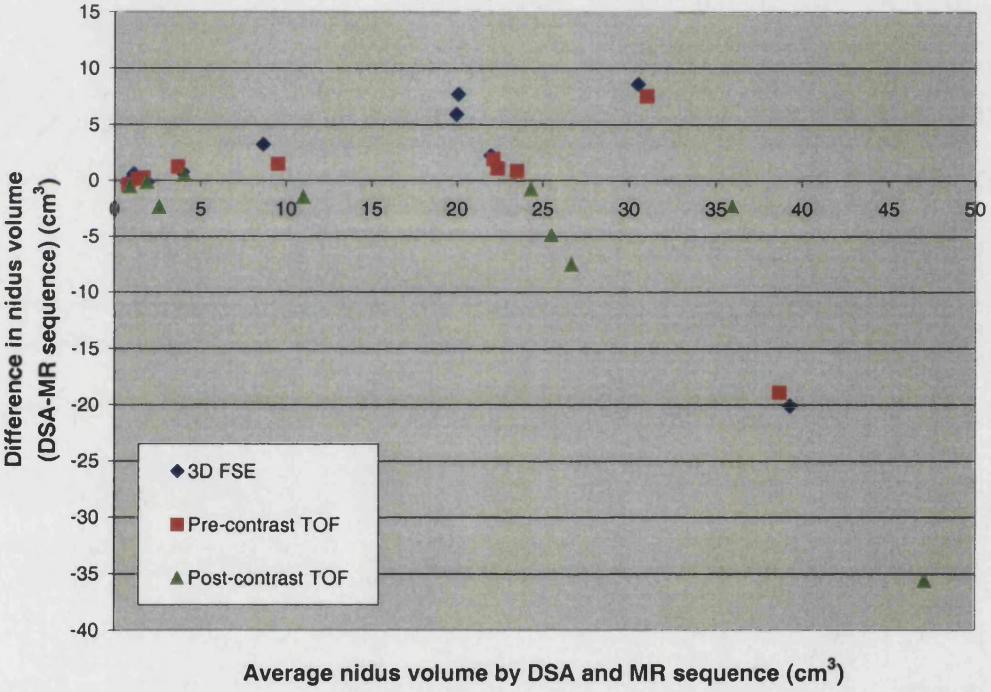

These differences did not have a Normal distribution (Shapiro-Francia W' test for Normal distribution for differences between DSA and MR sequence were p=0.00 for 3D FSE and pre- and post-contrast). For further statistical analysis, the original data was transformed using a logarithmic transformation. The log-transformed data is displayed in a similar way in Figure 5.4 where, although there were still differences across the values, the scatter was more evenly spread with increasing average nidal volume by DSA.

Figure 5.4: Graph showing the average log nidus volume by DSA and MR against the difference in log nidus volume by the same two techniques

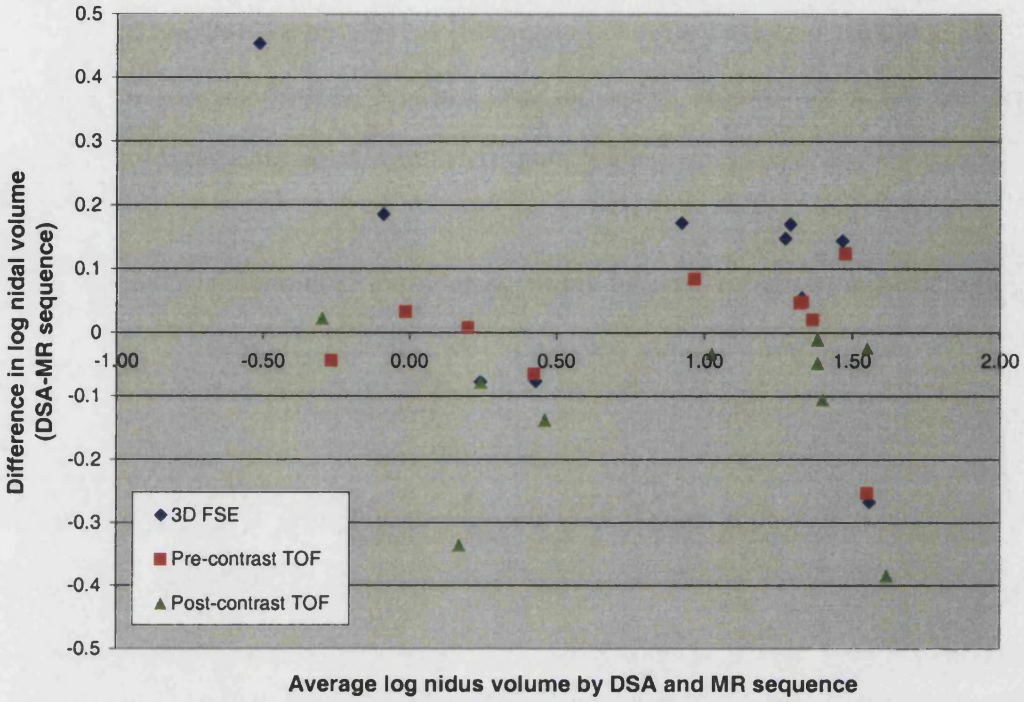

Using the log-transformed data, limits of agreement can be calculated:

mean difference ± 2 standard deviation

between which 95% of measurements would be expected to lie. These limits of agreement are shown in Table 5.3 and graphically in Figure 5.5.

Figure 5.5: Limits of agreement for 3D FSE, pre-contrast and post-contrast TOF

3D FSE

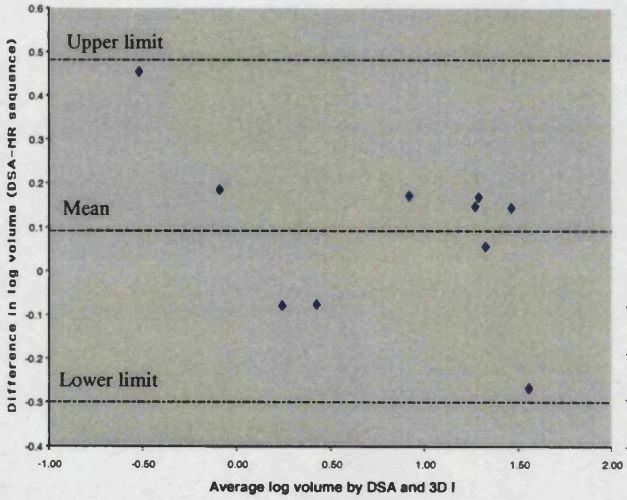

Pre-contrast TOF

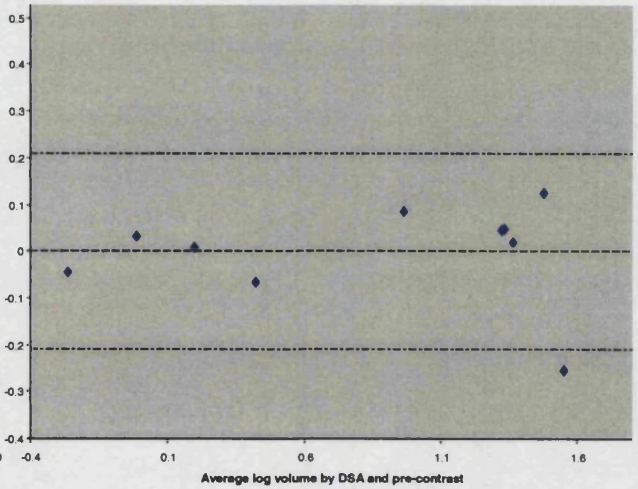

Post-contrast TOF

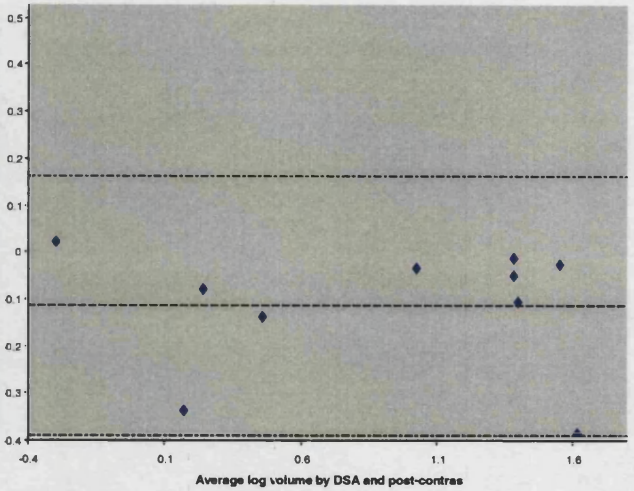

Table 5.3: Limits of agreement for all three MR sequences

Sequence	Mean Difference	Standard Deviation	Limits of agreement	Antilogs of limits of agreement
3D FSE	0.09	0.20	0.48 to –0.30	3.03 to 0.50
Pre-contrast TOF	0.00	0.11	0.21 to –0.21	1.62 to 0.62
Post-contrast TOF	-0.11	0.14	0.16 to –0.39	1.45 to 0.41

These limits of agreement are based upon log-transformed data and therefore need to be related to the original scale of measurement. The antilog of these limits is a dimensionless ratio. That is, in 95% of cases, the nidus volume by 3D FSE will be between 3.03 and 0.50 times the volume by DSA, the nidus volume by pre-contrast TOF will be between 1.62 and 0.62 times the volume by DSA and the nidus volume by post-contrast TOF will be 1.45 and 0.41 times the volume by DSA.

To compare the results obtained by DSA and each of the three MR sequences, the paired *t* test was used in the case of 3D FSE and the non-parametric equivalent of the paired *t* test, the Wilcoxon matched pairs signed rank sum test, was used in the cases of pre- and post-contrast TOF. This was performed on the transformed data because there were larger differences seen for larger AVM volumes as shown in Figure 5.3. The non-parametric equivalent was used in the cases of pre- and post-contrast TOF because the differences in transformed data were not Normally distributed (Shapiro-Francia W' test for Normal distribution of differences in transformed data were $p = 0.27$, $p = 0.04$ and $p = 0.03$ for 3D FSE and pre- and post-contrast TOF respectively).

Null hypothesis: Volume $_{DSA}$ = Volume $_{3D\ FSE}$

t = 1.46 with 9 degrees of freedom

p = 0.18

Null hypothesis: Volume $_{DSA}$ = Volume $_{pre\text{-}contrast\ TOF}$

Sum of Positive Ranks = 34

Sum of Negative Ranks = 21

z statistic = 0.66

p = 0.51

Null hypothesis: Volume $_{DSA}$ = Volume $_{post\text{-}contrast\ TOF}$

Sum of Positive Ranks = 2

Sum of Negative Ranks = 53

z statistic = -2.60

p < 0.01

For both 3D FSE and pre-contrast TOF, the null hypothesis cannot be rejected suggesting that the volumes calculated from DSA do not differ significantly from those calculated from these MR sequences. In the case of the post-contrast TOF sequence however, the null hypothesis is rejected suggesting that the volumes calculated from post-contrast TOF sequences differ significantly from those calculated from DSA. Examination of the raw data suggests that those calculated from post-contrast TOF sequences are greater than those calculated from DSA.

5.3.2.2 Interobserver variability

Comparison of the mean nidal volume of the ten patients for each observer across the imaging methods can be used to assess any systematic differences between observers (Table 5.4).

Table 5.4: Mean volumes for each observer

	Observer		
Patient	1	2	3
1	3.82	0.50	1.14
2	2.11	0.20	0.43
3	6.09	1.46	3.53
4	28.42	17.57	23.78
5	2.28	1.50	1.72
6	58.85	42.47	42.43
7	9.31	8.71	10.41
8	23.98	19.92	22.02
9	31.21	13.62	24.28
10	34.06	28.46	31.51

On inspection of this table, it appears that, observer 1 generally tended to overestimate nidus volumes compared with observers 2 and 3 and that, on occasions observer 2 tended to underestimate the nidus volumes when compared with observers 1 and 3.

The reproducibility of different observer measurements is relevant to the study of method comparison because the variability between two methods of measurement potentially limits the amount of agreement which is possible. If one method has poor repeatability, the agreement between the two methods is bound to be poor also. When the established method is the more variable one, even a new method that is perfect will not agree with it. If both methods have poor repeatability, the problem is compounded.

Two way analysis of variance (ANOVA) and its non-parametric equivalent, Friedman's two way ANOVA, allow a more accurate assessment of interobserver

variability or repeatability of volumes calculated from each type of investigation. The DSA residuals do not have a Normal distribution and hence Friedman's two way ANOVA was used (Shapiro-Francia W' test for Normal distribution of residuals was $p < 0.01$).

Null hypothesis: Differences in volume $_{DSA} = 0$

H statistic = 3.8

Degrees of freedom = 2

$0.2 > p > 0.1$

The null hypothesis cannot be rejected suggesting that there is no significant interobserver variability in the nidal volumes calculated from DSA.

Shapiro-Francia W' test for Normal distribution of residuals gave $p = 0.28$, $p = 0.90$ and $p = 0.77$ for 3D FSE and pre- and post-contrast TOF respectively. For all the MR sequences, two way ANOVA was therefore used to assess interobserver variability (Tables 5.5 - 7).

Table 5.5: Results of two way ANOVA for 3D FSE

Source of Variation	Degrees of freedom	Sums of Squares	Mean squares	*F* statistic	p value
Patients	9	6316.29	701.81	38.43	<0.01
Radiologists	2	164.53	82.26	4.50	0.03
Residual	18	328.71	18.26		
Total	29	6809.52			

Table 5.6: Results of two way ANOVA for pre-contrast 3D TOF

Source of Variation	Degrees of freedom	Sums of Squares	Mean squares	*F* statistic	p value
Patients	9	6419.61	713.29	26.15	< 0.01
Radiologists	2	257.13	128.57	4.71	0.02
Residual	18	490.92	27.27		
Total	29	7167.66			

Table 5.7: Results of two way ANOVA for post-contrast 3D TOF

Source of Variation	Degrees of freedom	Sums of Squares	Mean squares	*F* statistic	p value
Patients	9	11310.19	1256.69	41.90	< 0.01
Radiologists	2	571.25	285.63	9.52	< 0.01
Residual	18	539.94	30.00		
Total	29	12421.38			

When comparing the nidal volumes calculated by the three observers from 3D FSE and pre- and post-contrast TOF sequences using Friedman's two way ANOVA, the null hypothesis was rejected ($p = 0.03$, 0.02 and < 0.01 for 3D FSE, pre and post contrast TOF sequences respectively). This suggested that there was significant interobserver variability in the nidal volumes calculated from all three MR sequences.

5.4 Discussion

The basis of AVM grading according to size is currently the measurement of the largest diameter of the nidus on 2D projectional DSA images. A simple line measurement from a projected image is, however, inadequate to describe a complex three-dimensional shape. This can be improved by using three orthogonal measurements of the AVM nidus from DSA, from which a volume calculation can be derived based on an ellipsoid approximation.

5.4.1 Intersequence variability

Although the results of the Wilcoxon matched pairs test comparing mean results obtained from DSA and MR suggest that those obtained from DSA and 3D FSE and pre-contrast TOF sequences were not significantly different, there was a wide variability and standard deviation as shown by the limits of agreement between which 95% of future values calculated would be expected to lie. The nidus volume by 3D FSE could be between 3.03 and 0.50 times the volume by DSA, and that by pre contrast TOF between 1.62 and 0.62 times the volume by DSA. This variation is clearly unacceptable in clinical practice. Post-contrast TOF appears to give significantly higher values than DSA (Wilcoxon matched pairs test, $p < 0.01$) (or the other MR methods). Areas of slow and complex flow and small calibre vessels are not well visualised on the pre-contrast TOF and do not produce reliable flow voids on the 3D FSE sequence. These vessels, and in particular, draining veins are much better visualised on the contrast-enhanced 3D TOF, which explains the higher volume measurements on this sequence (Figures 5.6a - c). Enhancing draining veins can also interfere with a clear delineation of the nidus on the reformatted images of the contrast-enhanced 3D TOF and lead to an overestimation of the nidus size. Although draining veins frequently overlie the nidus on projectional images of DSA, these can be isolated by choosing an earlier time frame, which shows only the arterial phase, from which to measure nidal size. In a small number of cases there was enhancement of abnormal parenchyma with gadolinium around the nidus which

was falsely included in the nidus volume measurement, thus contributing to overestimation of the nidus size (Figures 5.7a - c).

This study has a small sample size, where there are limited observers, some of whom have had limited experience. The three observers had a varying degree of experience of neuroradiology and endovascular intervention. One of the observers was a consultant neuroradiologist with a major interest in vascular intervention, one was a specialist registrar in neuroradiology nearing the end of his training period and the third was a fellow just beginning his specialist training in neuroradiology. Much of the intersequence variability may be improved by repeating this study with a larger sample size and with a larger number of better trained observers.

5.4.2 Interobserver variability

There is significant variation between the volumes measured by the three observers on MR, although the two way ANOVA test does not indicate where the differences lie. Examination of the raw data suggests observer 1, who was the least experienced, generally tended to overestimate nidus volumes compared with observers 2 and 3 and that, on occasions observer 2 tended to underestimate the nidus volumes when compared with observers 1 and 3 (Figures 5.8a - c). This suggests that there is poor repeatability of nidal volumes calculated from MR. In contrast there is minimal difference and therefore good repeatability in those values obtained from DSA. This was also seen by Al-Shahi *et al.* (Al-Shahi, 2001) recently. This may be due to a difference in experience with MRI between observers and to the learning curve in applying the new method of nidus measurement. The presumed 'gold standard' of DSA has been used as a measure of nidal size and volume for many years; the use of MR in this way has not. There are often decisions to be made as to whether a draining vein or arterial supply should be included in the nidal volume and at what point these vessels do not make up part of the nidus (Figures 5.9a and b). In many AVMs, draining veins make up a relatively large associated volume and therefore difficulties or differences in opinion in this

regard will potentially result in a large interobserver variability. This was a difficulty that was particularly highlighted by the observers in this study. With experience, these decisions are likely to be become more routine and consistent amongst observers. In addition, appropriate DSA images can be used to define nidal volumes. Nidal views are often visualised best on the earlier frames of a DSA run, prior to the veins filling, during the arterial phase. This allows the nidus to be more easily appreciated without overlying veins. This temporal resolution is not a luxury afforded by MR currently.

Calculation of nidal volume from DSA requires one main decision – that is, which is the largest nidal diameter demonstrated. From this the other two orthogonal planes are obvious, although further decisions have to be made about where the nidal dimensions are maximal within that plane. Ultimately, six decisions are made regarding the size of the AVM nidus, from which a volume is generated. When generating volumes from MR, a large number of images have to be viewed, each of them requiring a decision on nidal boundaries. This means that they are vulnerable to many more subjective decisions and opinions. This may be compounded by performing high resolution slices. By reducing the number of slices imaged, fewer decisions would have to be made by each observer and the interobserver variability might thus be reduced. Eleven slices across the AVM were imaged in this study, based on previous volumetric work with MR, in this case measuring hippocampal volumes in epilepsy patients (Cook, 1992). Any increase in the number of slices does not increase the accuracy of the volume calculated (McNulty, 2000).

Again, this study has a small sample size and observers with varying experience. By increasing the numbers of patients examined and including only neuroradiologists with a dedicated interest and expertise in cerebral AVMs, the interobserver variability is likely to improve.

Figure 5.6: Observer 3 freehand traces demonstrating intersequence variability on a) T2 FSE, b) pre-contrast and c) post-contrast 3D TOF images

a

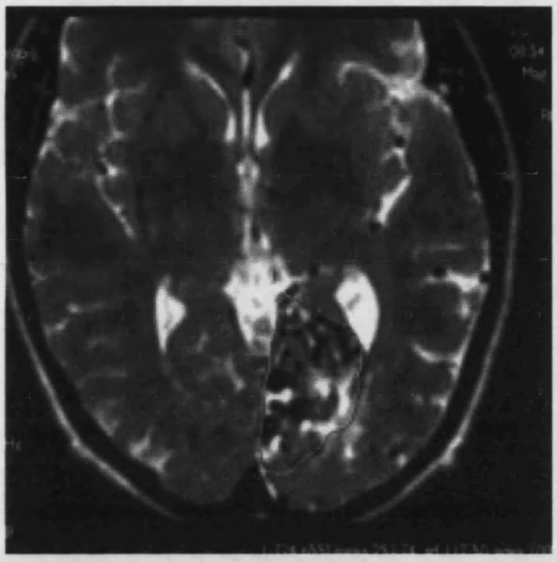

Total volume 22.8 ml

b

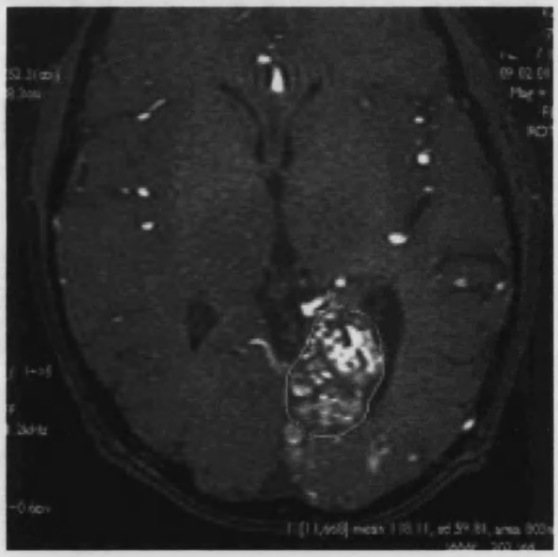

Total volume 19.0 ml

c

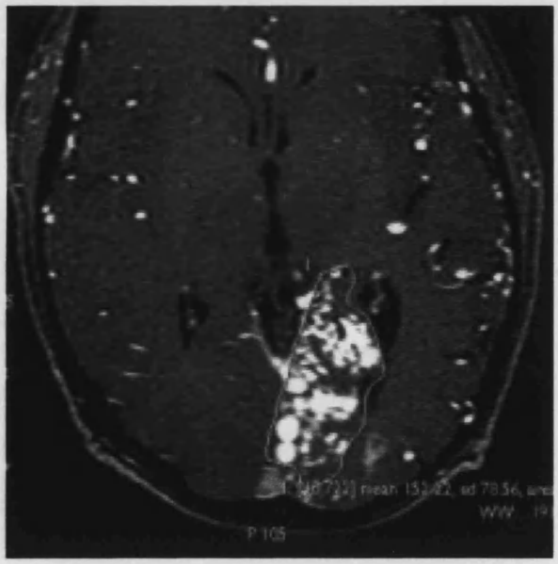

Total volume 33.5 ml

Figure 5.7: The problem with enhancing gliotic tissue

a T2 FSE

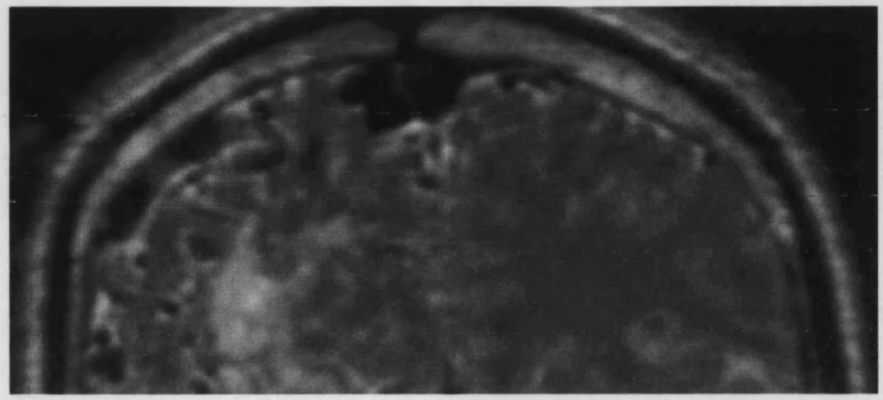

b Pre-contrast 3D TOF

c Post-contrast 3D TOF

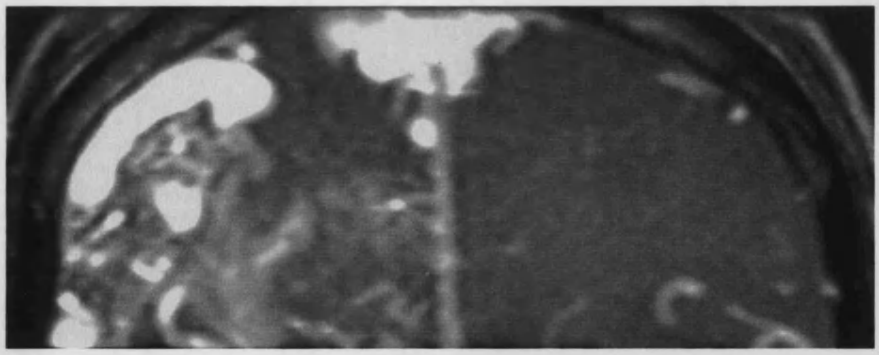

Figure 5.8: Freehand traces of observers 1 to 3 (a-c) demonstrating interobserver variability on post-contrast 3D TOF images

a

Observer 1

Total volume 44.5 ml

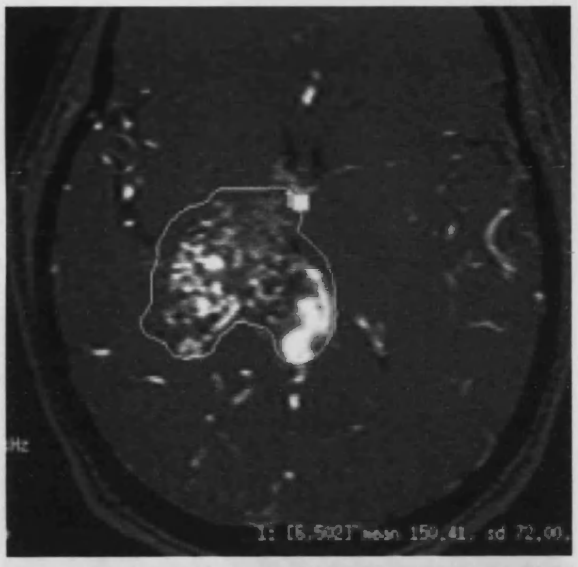

b

Observer 2

Total volume 17.9 ml

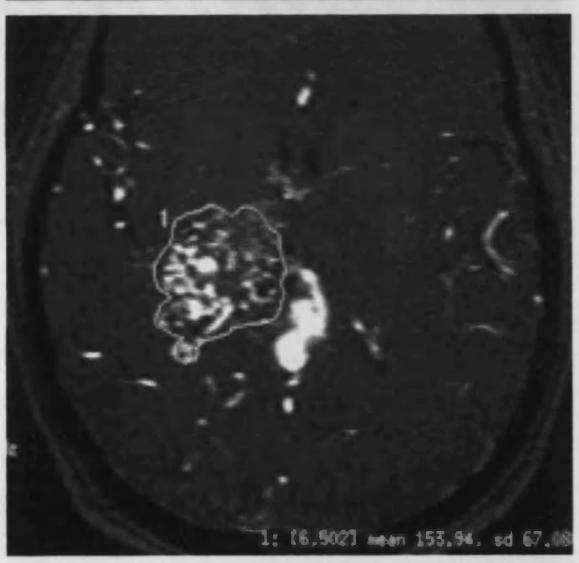

c

Observer 3

Total volume 28.9 ml

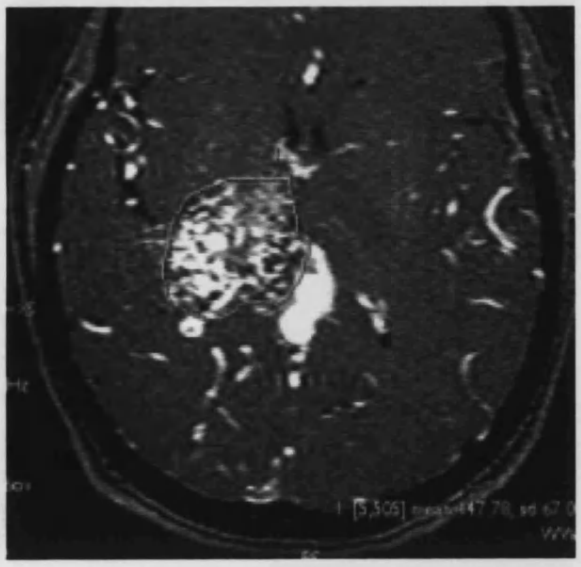

Figure 5.9: The difficulty with draining veins

a Observer 1 – total volume 74.8 ml

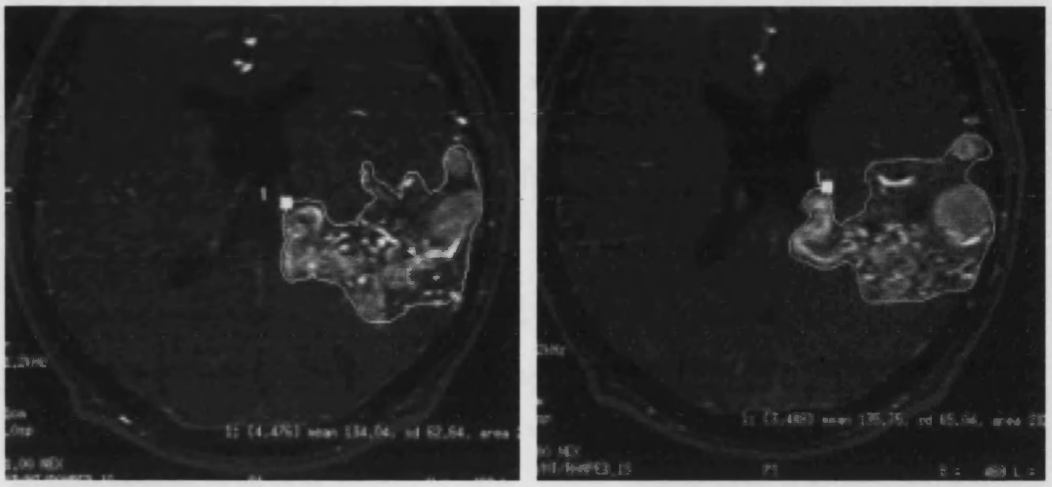

b Observer 2 – total volume 54.9 ml

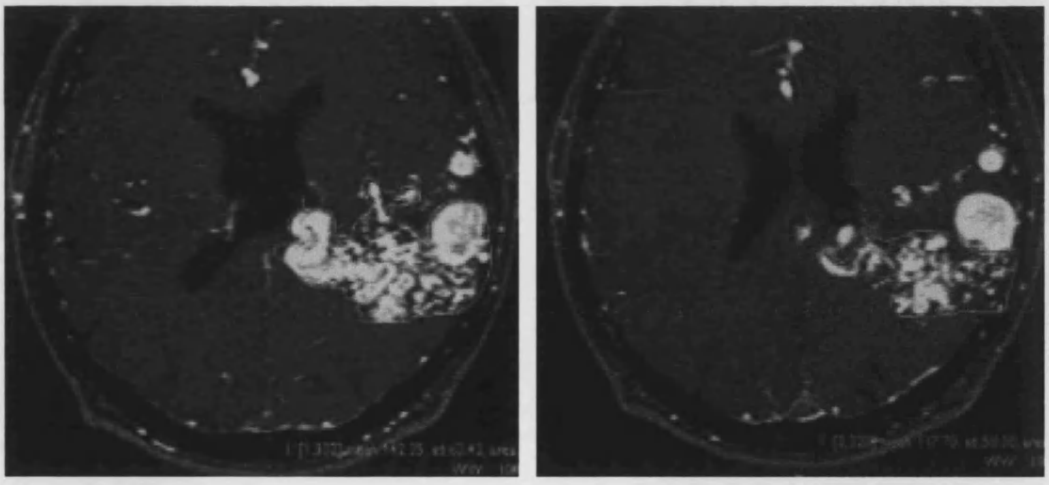

Differences in observer opinion about the point at which a draining vein has left the AVM nidus will result in significant differences in nidal volumes

5.5 Conclusion

There is currently no definitive and accurate technique for measuring AVM nidus volumes. The 'standard' measurement of AVM size by a linear distance on DSA images appears inadequate. With biplane DSA it is possible to calculate an ellipsoid volume based on orthogonal projections, which offers some improvement in accuracy. Although these are used as a standard measurement, the accuracy of these dimensions cannot be confirmed. MR images show considerable potential in this regard and are likely to be most accurate due to their cross-sectional nature, but are not easy to interpret due to the varied appearances of flowing blood on different sequences and therefore firm conclusions cannot be drawn about the absolute size of AVMs from any of the three MR sequences. This may be further complicated by enhancement of abnormal brain tissue with the administration of gadolinium. In addition, much of the current inaccuracies of measuring nidal volumes may be observer related and could become more consistent with greater experience in the new techniques.

PART 3

PERFUSION IMAGING

Chapter 6

PERFUSION IMAGING USING MRI

6.1 Introduction

Cerebral AVMs can affect the haemodynamics of the brain to a variable degree and in a variety of ways. The two main mechanisms are arterial 'steal' and venous hypertension. The relative importance of these mechanisms is subject to ongoing debate. Until recently there has been no readily accessible technique for quantifying cerebral perfusion. Perfusion imaging with MRI is theoretically suited to assess regional haemodynamic disturbances at a microvascular or tissue level. It is being increasingly used in acute cerebral ischaemia and to assess perfusion in organs such as the liver and kidneys (Kashitani, 1995; Kuo, 1995; Uematsu, 1998; Vallee, 2000).

6.1.1 Kety method for measuring cerebral blood flow

According to the Fick principle, the blood flow of any organ can be measured by determining the amount of a given substance (Q_x) removed from the bloodstream by the organ per unit time and dividing that value by the difference between the concentration of the substance in arterial blood and the concentration in the venous blood from the organ ($[A_x] - [V_x]$).

$$\text{Cerebral Blood Flow} = CBF = \frac{Qx}{[Ax]-[Vx]}$$

With the exception of a few cerebral disorders, rCBF is generally coupled or related to metabolism. Tracers are therefore trapped primarily by neurones in relationship to local CBF. This observation is the basis for cerebral perfusion

imaging, most indirect methods using Kety's application of the Fick principle to calculate CBF. The ideal brain perfusion tracer: is able to cross the intact blood brain barrier freely; undergoes complete first pass extraction from the blood into the brain; has a proportional distribution to CBF; has a long retention within the brain without redistribution and metabolism; is widely available for clinical use; and in the case of nuclear medicine techniques, gives a low radiation dose to patients.

6.1.2 Clinical methods of measuring cerebral blood flow

6.1.2.1 Xenon CT

Xenon is highly lipid soluble and freely crosses the blood brain barrier. Because stable xenon gas is radiodense, its concentration in the brain can be determined directly by the CT scanner, and the measurement of venous concentration is unnecessary. The concentration of xenon in the brain is related to its arterial concentration (which itself is time dependent), the CBF and the duration of exposure to xenon (because the equilibration of xenon between blood and brain is not instantaneous). These factors determine the total amount of xenon presented to the brain. Uptake is also determined by the affinity of the brain for xenon, which is measured by the brain-blood partition coefficient, λ. This reflects the relative solubility of xenon gas in the brain and blood or, more simply, the xenon concentration in the brain and blood in equilibrium.

Two baseline scans are obtained at two to eight different levels of the brain before xenon inhalation. Six enhanced scans per level are then obtained during a 4.5 minute xenon inhalation. The pairs of baseline scans are averaged and then subtracted from each of the enhancement images. End-tidal xenon concentration is measured by a thermoconductivity analyser. The image that results is a CBF map which uses a fixed colour scale with associated numeric flow values that can be extracted by placing ROIs of any shape or size on this CBF map. When larger

regions are measured, both grey and white matter are usually included in the ROI, and the flow measurement will reflect the average of these two compartments.

The main advantages of stable Xe/CT is that it noninvasively provides rapid access to high-resolution, quantitative, local CBF information coupled to CT anatomy. Xenon-based CBF methodologies are rapidly repeatable and therefore capable of defining brain regions with compromised cerebrovascular reserve by examining the CBF response to a vasodilatory challenge. The disadvantages are the radiation dose of the CT scan, the pharmacological effects of xenon gas, and the limitations of the study. Xenon is a potent anaesthetic agent at high concentrations. Patients need to be co-operative as alteration of the patient's sensorium by xenon gas can contribute to movement artefact. Limiting the inhaled concentration of xenon can reduce the potential side-effects but still allow adequate signal-to-noise. The other concern is the degree of flow activation that occurs with xenon inhalation and its effects on the accuracy of the measurements. This is thought to be minimal because the significant xenon-induced flow activation is delayed for about 2 minutes.

6.1.2.2 Cerebral blood flow ^{133}Xenon

Intra-arterial injection of ^{133}Xenon (^{133}Xe), a radioactive isotope, into the internal carotid artery with extracranial monitoring of the clearance curve using highly collimated scintillation detectors can be used to measure CBF. The clearance curves obtained from the washout of ^{133}Xe can be analysed by one of several methods of curve analysis to calculate the value of CBF: the stochastic method or CBF 'height over area' method; the initial slope index; and the two-compartmental analysis. The latter gives both grey and white CBF values and provides the values of the relative weights for the two tissue compartments.

This method suffers from poor resolution when compared with tomographic methods secondary to scatter, tissue overlap and blood flow in extracranial soft tissue. Information is therefore limited to the superficial cortex.

6.1.2.3 Nuclear Medicine

Conventional gamma cameras acquire planar images of the brain, imaging the presence of radiopharmaceuticals emitting either single photons (SPECT) or positrons (PET). To generate tomographic images, the gamma camera obtains a series of images of the brain from a number of different angles as it is rotated about the brain. Typically 60 to 120 planar images of the brain are acquired over a 360° rotation of the gamma camera.

The primary advantage of SPECT and PET is that of any tomographic technique, the ability to view activity in a region of the body without the confounding effects of superposition of activity from overlying or adjacent regions. The resolution of the final tomographic images depend on a number of factors, the primary ones being the intrinsic resolution of the gamma camera and the resolution of the gamma camera collimator. In clinical studies, an additional factor, patient movement, may often be the limiting factor in determining overall image resolution. Conventional gamma cameras have intrinsic resolutions of approximately 2.5 – 4 mm. The collimator, however, has considerably poorer resolution. A standard high-resolution collimator gives a resolution of 8 to 10mm in air at a distance of 10cm.

^{133}Xe is the original radiotracer flow marker for the measurement of rCBF in the brain using SPECT. This agent can be administered by intraarterial, intravenous or inhalation routes. It is an inert gas that does not undergo any chemical transformation in the brain. It allows the assessment of absolute quantitative data, however the spatial resoultion when using ^{133}Xe is less than with other agents. In addition, the rapid transit of ^{133}Xe (with the resultant short half-life in the brain) requires the use of high-sensitivity detector devices that are capable of acquiring rapidly changing image data in short time frames. Newer gamma-emitting radiopharmaceuticals used in SPECT to measure CBF include ^{123}I-IMP (I-d, I-N-isopropyl-p-iodoamphetamine hydrochloride); ^{99m}Tc-HMPAO (Hexamethylpropyleneamine oxime); and ^{99m}Tc-ECD (ethyl cysteinate dimer).

SPECT relative CBV (rCBV) measurements require a compound that will stay within the vascular compartment during acquisition. ^{99m}Tc-labelled red blood cells are the most readily prepared, although ^{99m}Tc-labelled albumin and ^{111}In or ^{113}In-labelled transferrin have also been used.

Data from SPECT are at best semi-quantitative and often expressed as a ratio of the abnormal area to similar normal brain. An obvious limitation to the widely used left:right ratio is the assumption that one side is normal.

PET utilises positron-emitting isotopes, bound to compounds of biological interest. Positron-emitting isotopes depend on a cyclotron for production and their half-life is short. Each decaying positron results in the release of two photons in diametric opposition; these activate two coincidental detectors. Multiple pairs of detectors and computer processing techniques enable quantitative determination of local radioactivity (and density of the labelled compound) for each voxel within the imaged field.

The most widely employed PET technique is the oxygen-15 steady-state technique which uses tracer doses of the ^{15}O-labelled gases carbon dioxide, oxygen and carbon monoxide to obtain quantitative tomographic maps of CBF, CBV, the cerebral metabolic rate of oxygen ($CMRO_2$), the cerebral oxygen extraction fraction (OEF) and mean transit time (MTT). Other non steady-state techniques also mostly employ ^{15}O, notably as labelled water, to measure CBF. To estimate the cerebral glucose utilisation, the most widely used technique employs the D–glucose analogue ^{18}F-fluoro-2-deoxy-D-glucose (^{18}FDG). However PET has not gained routine clinical usage because of its complexity and limited availability.

6.1.3 MR perfusion

There are two methods of assessing brain perfusion using MR, contrast bolus tracking (CBT) and arterial spin tagging. In this study, CBT was used as it is more widely available clinically and offers the possibility of measuring rCBV and MTT,

as well as rCBF. CBT was evaluated to see whether it could be used to demonstrate the effects of intracranial AVMs on cerebral haemodynamics.

A rapid injection of high-concentration contrast agent is given, and the MRI signal observed as the bolus passes through the brain. This method exploits the magnetic susceptibility (T2*) effect of the first pass of an intravascular contrast medium which causes a loss of signal intensity in the tissues that are perfused. This loss of signal intensity is proportional to the amount of contrast medium present in the voxel and is therefore proportional to tissue perfusion. Ischaemic or non-perfused regions remain relatively hyperintense. This has been demonstrated in animal models with experimentally induced MCA ischaemia (Moseley, 1990; Kucharczyk, 1993). Kucharczyk *et al.* (Kucharczyk, 1993) found that within 10 sec of injection of the contrast bolus there was 45% - 95% dose-dependent signal intensity decrease below baseline in normally perfused brain. They also found that contrast agent transit times were sufficiently different in occluded and reperfused cerebral tissue to allow distinction on perfusion sensitive images (Kucharczyk, 1993). These changes were seen within minutes of the ischaemic insult and correlated well spatially with hyperintense lesions seen on diffusion-weighted images, whilst initially T2-weighted images remained normal.

6.1.3.1 Determination of regional cerebral blood flow

The concentration of the contrast agent (measured by changes in T2 or T2*) in a ROI can be expressed as (Figure 6.1) (Calamante, 1999):

$$C(t) = \frac{\rho}{H_f}.CBF.[C_a(t) \otimes \Re(t)] = \frac{\rho}{H_f}.CBF.\int_0^t C_a(\tau)\Re(t-\tau)d\tau$$

where $\Re(t)$ is the residue function (the fraction of contrast agent in ROI at time t following an ideal instantaneous bolus injected at t=0); $C_a(t)$ is the arterial input function (AIF) (the concentration of contrast entering the ROI at time t); $\otimes$ indicates

the convolution operation; ρ the density of brain tissue; and H_f a haematocrit factor that accounts for the difference in haematocrits between capillaries and large vessels since only the plasma is accessible to tracer. The convolution operation accounts for the fact that, for a non-ideal bolus, part of the spread in the concentration-time curve is due to a finite length of the actual bolus. It is generally believed that deconvolution of the above curve provides an accurate measurement of CBF.

Figure 6.1: Tracer kinetics

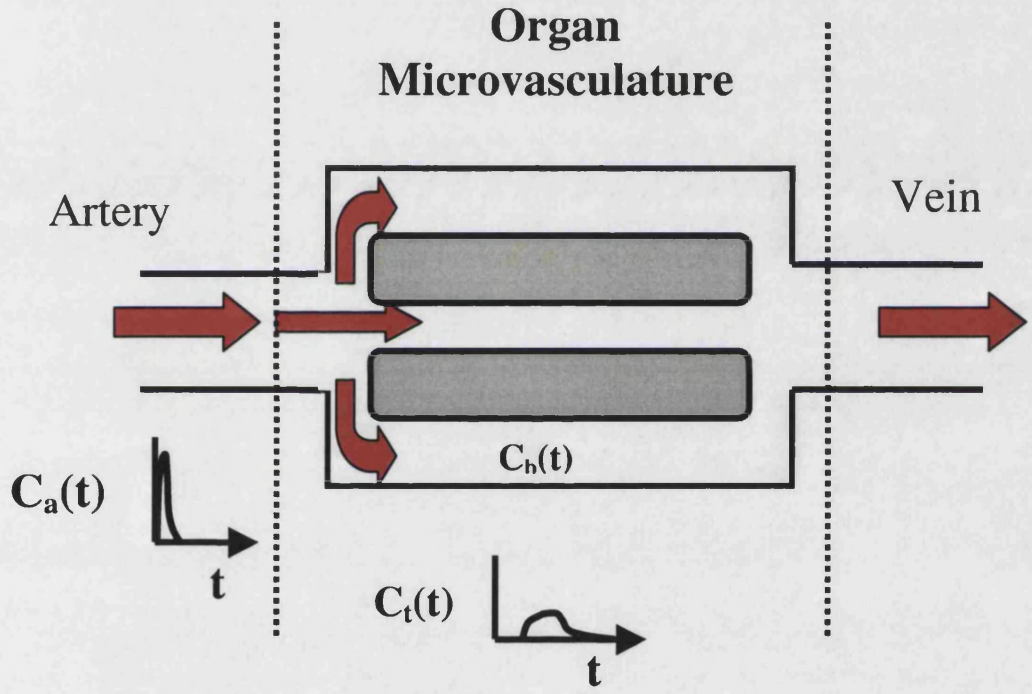

The time dependence of the tracer concentration entering the brain is described by the arterial input, $C_a(t)$. The tracer is then distributed through the microcirculation where the tracer concentration in the post arterial blood is given by $C_b(t)$ and the net concentration in the whole tissue is given by $C_t(t)$.

6.1.3.2 Determination of regional cerebral blood volume

In addition to the measurement of CBF, tracer methods can also be used to determine the vascular distribution of the agent. For an intravascular tracer, this volume is the tissue blood plasma volume. The rCBV can be determined from the bolus tracking study by integrating the tissue concentration-time curve and normalising the data to the integrated AIF (Calamante, 1999):

$$rCBV = \frac{H_f}{\rho} \frac{\int_0^\infty C_t(t)dt}{\int_0^\infty C_a(t)dt}$$

The integral in the numerator reflects the total amount of tracer that passes through the voxel, while the denominator gives the total amount of tracer in the blood which enters the brain, thus the ratio gives the fraction of blood in the brain or region of brain.

6.1.3.3 Determination of mean transit time

The third physiological parameter, MTT, is the average time required for any given particle of tracer to pass through the tissue given an ideal bolus injection. MTT of the bolus can then be determined from the ratio of the blood volume and blood flow maps as:

$$MTT = \frac{CBV}{rCBF}$$

6.2 Methods

6.2.1 Patients

Patients were recruited from those seen by the neurovascular surgery or interventional neuroradiology services at The National Hospital for Neurology and Neurosurgery between January and October 1999. All patients were known to have AVMs and had undergone recent catheter angiography confirming its presence. Patients were excluded with the usual contra-indications to MRI scanning.

6.2.2 Imaging

All patients underwent a series of T2* weighted gradient-echo EPI images (TR 1200 msec, TE 44 msec, 0.75 NEX, flip angle 90°, matrix size 128 x 128). One

hundred volumes each of 5 contiguous slices (slice thickness 5mm) were acquired over 2 min. At 15 sec into the acquisition, a 15ml hand bolus of 0.1mM Gd-DOTA (Dotarem®, Guerbet Laboratories, Aulnay-sur-Bois, France) was given over 3 - 5 sec.

6.2.3 Post processing

Images were transferred to the Sun® Ultra 5 workstation (Sun Microsystems, Berkley, USA) running Advantage Windows®, version 3.1, software (General Electric Medical Systems, Milwaukee, USA). Using proprietary software (Functool®, General Electric Medical Systems, Milwaukee, USA), ROIs were placed over an artery (most commonly the MCA or distal branch of the MCA) and vein (most commonly the SSS) distant to the AVM. Time-signal intensity curves were generated from these ROIs (Figure 6.2). Following determination of baseline image numbers, pre- and post- contrast bolus passage, and threshold values, Functool® was used to create colour maps of CBF, CBV, MTT and time to minimum contrast concentration (TTM) for each of the five slices. Deconvolution of the arterial time-intensity curve was used to correct for differences in bolus shape.

One shortcoming of Functool® is the inclusion of zero-level pixels in 'uncomputable' regions of the colour maps which interfere with the quantification of haemodynamic parameters in the ROI. To overcome this problem, maps were transferred to an independent workstation for further analysis, using Analyze® AVW 3.0 (Mayo Foundation, Minnesota, USA), which allows exclusion of zero value pixels. ROIs were defined for nidus and perinidus by freehand trace. The perinidus region was defined as the area immediately adjacent to the AVM nidus but excluding any large draining veins. This region was divided into three 'onionskin' regions with increasing distance from the nidus using the automated division of regions tool of Analyze® AVW 3.0 (Mayo Foundation, Minnesota, USA). A corresponding region to the nidal ROI was defined in the contralateral hemisphere as the 'contralateral nidus equivalent region'. Ipsilateral and contralateral white and

Figure 6.2: A sample arterial time–signal intensity curve

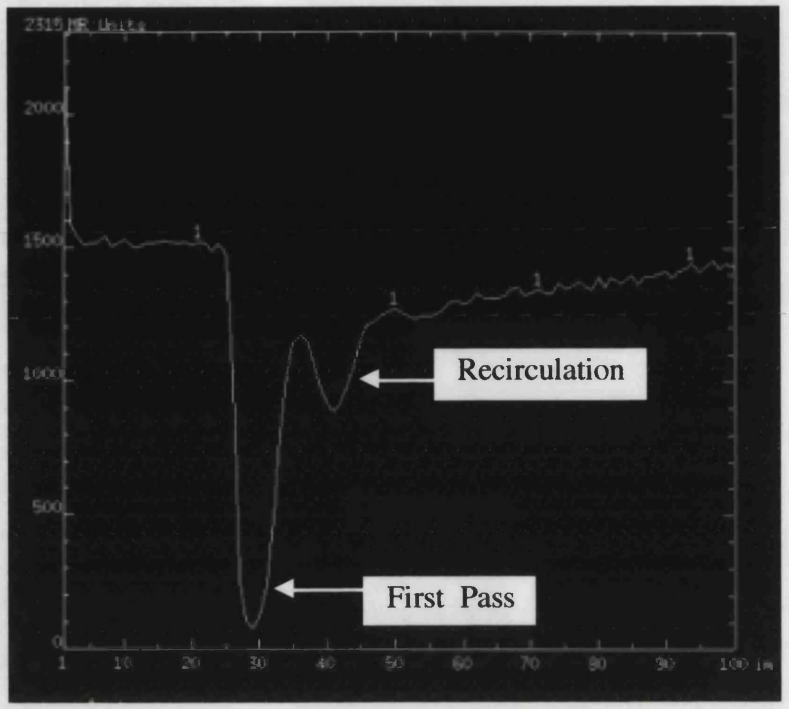

Figure 6.3: Regions of interest defined for each slice for each patient

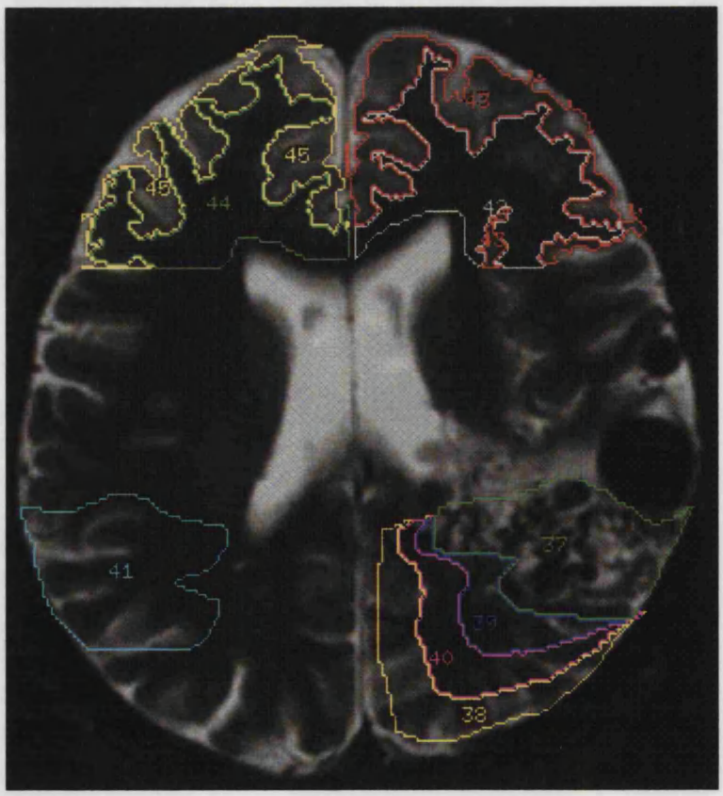

37 nidus, 38-40 perinidal onionskin rings, 41 contralateral nidus equivalent, 42 ipsilateral white matter, 43 ipsilateral grey matter, 44 contralateral white matter, 45 contralateral grey matter

grey matter regions were defined using the thresholding tool in an area distant to the AVM nidus, in most cases in the frontal lobes. These ROIs were generated on all five slices using the baseline T2* images and saved as 'object maps' (Figure 6.3).

These object maps were superimposed on all four colour maps: CBF, CBV, MTT and TTM. Size (in mm^3), number of voxels, mean and standard deviation voxel values were generated for each region on every slice for all four colour maps. Only those voxels with values greater than zero were included.

6.2.4 Statistical analysis

Data were collated using Microsoft® Excel 98 and statistical analysis was performed using Stata™ 4.0 (Stata corporation, Texas, USA) as described in section 3.2.5.

6.3 Results

6.3.1 Patient baseline characteristics

Fifteen patients with AVMs were recruited to the study (Table 6.1). Six were male, nine female with a median age of 36 years (interquartile range of 25 – 43 years). Six patients had originally presented with seizures, six with intracranial haemorrhage, two with a progressive neurological deficit and one with headaches and a homonymous hemianopia. Five individuals had undergone previous partial embolisation of their AVM, whilst one individual had previously been treated with stereotactic radiosurgery. The remaining nine individuals had had no previous treatment.

6.3.2 Haemodynamic parameters

The values from all five slices for each of the haemodynamic parameters were averaged. Only those values with a standard deviation of greater than zero

Table 6.1 : Demographic data of all patients undergoing MR perfusion studies

Patient Number	Gender	Age	Presentation	AVM			Prior treatment	Planned treatment
				Site	Anatomy	Size		
1	M	49	SAH	Right temporo-parietal	Cortico-ventricular	Large	Embolisation	Embolisation
2	F	22	SAH	Left callosal	Callosal	Small	None	Embolisation
3	F	21	SAH	Right basal ganglia	Deep	Small	None	Stereotactic DXT
4	M	18	IVH	Left callosal	Callosal	Small	None	Embolisation
5	F	47	SAH	Left occipital	Cortical	Large	Embolisation	Embolisation
6	F	27	Seizures	Right parietal	Cortical	Small	Embolisation	Embolisation
7	F	36	SAH	Left callosal	Callosal	Medium	Stereotactic DXT	Embolisation
8	F	62	Seizures ICH	Left occipital	Cortico-ventricular	Medium	None	Embolisation

Table 6.1 (continued) Demographic data of all patients undergoing MR perfusion studies

Patient Number	Gender	Age	Presentation	AVM			Prior treatment	Planned treatment
				Site	Anatomy	Size		
9	M	36	Seizures	Left parietal	Cortico-ventricular	Medium	Embolisation	Conservative
10	M	43	Seizures	Left temporal	Cortical	Medium	Embolisation	Embolisation
11	F	46	Seizures	Left fronto-parietal	Cortico-ventricular	Medium	None	Conservative
12	M	41	Progressive hemiparesis	Right fronto-parietal	Cortico-ventricular	Large	None	Embolisation
13	F	25	Progressive hemiparesis	Left thalamic	Deep	Large	None	Embolisation
14	M	38	Hemianopia Headaches	Right holo-hemispheric	Cortico-ventricular	Large	None	Conservative
15	F	37	Seizures	Left fronto-parietal	Cortico-ventricular	Large	None	Embolisation

were included. Those values with a standard deviation of zero were assumed to lie outside the range that this technique could meaningfully post-process. The results for CBF, CBV, MTT and TTM across the nidus, perinidal regions and normal parenchyma are shown in Figures 6.4 – 7 respectively.

The scale of the y axis has been adjusted to demonstrate the data as clearly as possible, which has meant exclusion of several data points (there is a single data point missing in Figure 6.4 for patient 8 as the standard deviation for the average nidus CBF was zero). All data are shown in Appendix 4. The ipsilateral white and grey matter were compared with the corresponding contralateral regions and the white matter and grey matter were compared with each other both ipsilaterally and contralaterally. The values for nidus were compared with those from the contralateral nidus equivalent ROI. The perinidal onion skin regions were compared for within subject differences, to see if there was a trend of values across the regions with increasing or decreasing distance from the nidus.

All differences were tested to see if they represented a Normal distribution using the Shapiro-Francia W' test for Normal distribution. If the values did not represent a Normal distribution, they were log transformed. In those parameters where the data, either as raw data or log transformed data, represented a Normal distribution, a paired *t* test was performed to assess the differences between parameters. In those which did not represent a Normal distribution, a Wilcoxon signed rank test was performed to assess the significance of differences (Table 6.2).

Trend was assessed across the three perinidal 'onionskin' rings and 'normal' parenchyma (contralateral nidus equivalent ROI). Initially, the residuals were generated. These were not Normally distributed in all parameters (Shapiro-Francia W' test for Normal distribution for CBF was $p < 0.02$ and for CBV, MTT and TTM was $p < 0.00$). Trend was therefore assessed using the non-parametric equivalent of a two way ANOVA, a Friedman's two way ANOVA (Table 6.2).

Figure 6.4: Cerebral blood flow in all 15 patients

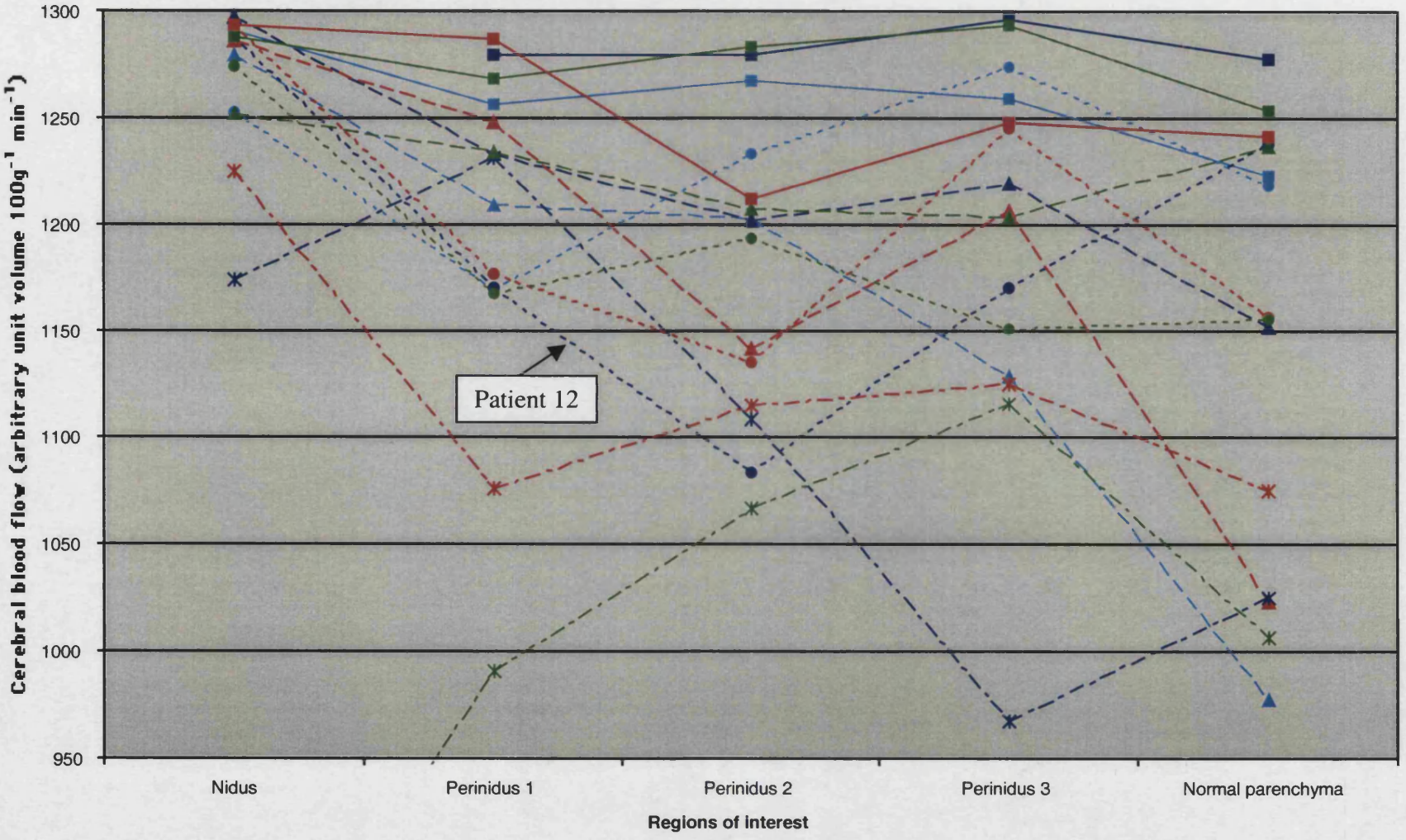

Figure 6.5: Cerebral blood volume in all 15 patients

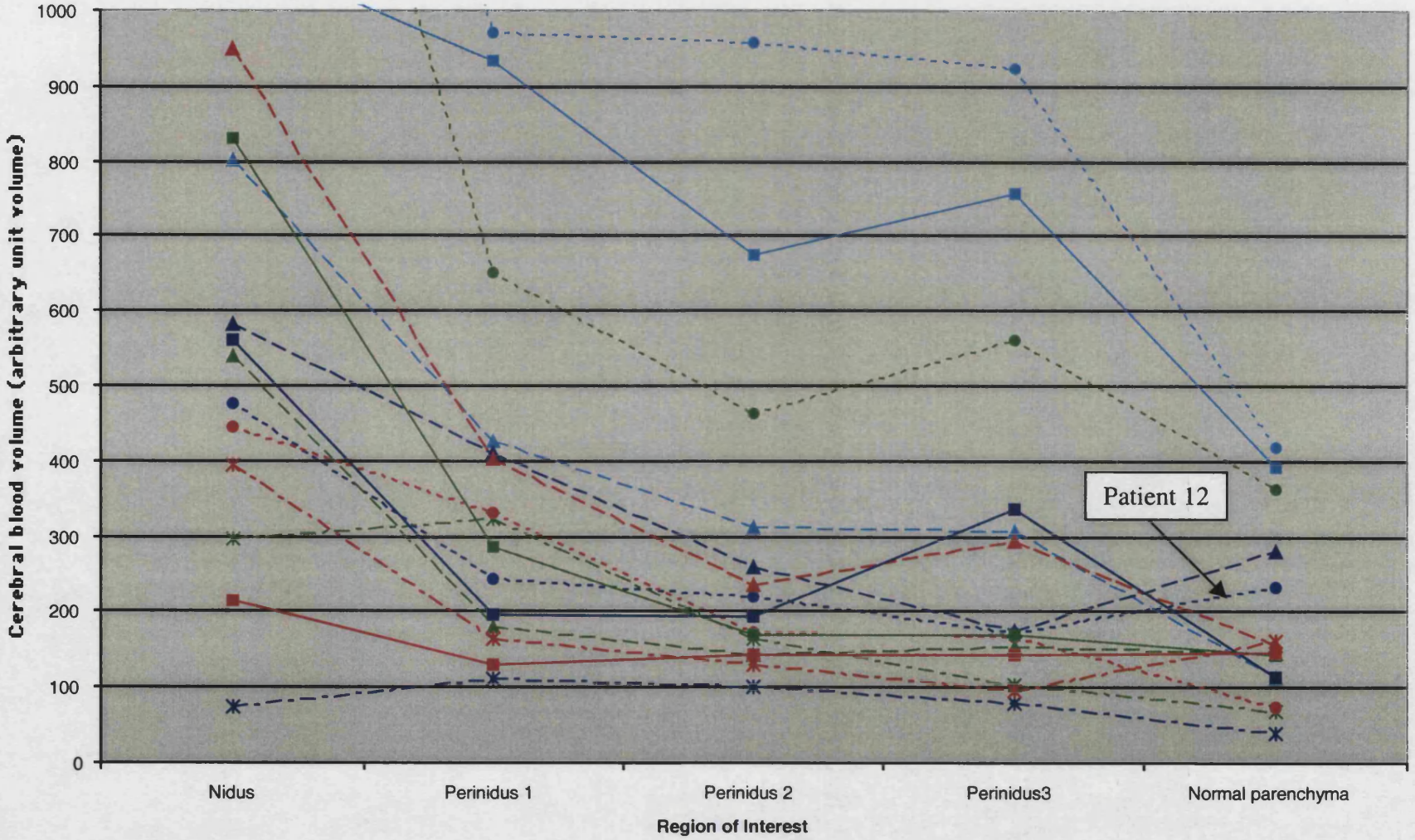

Figure 6.6: Mean transit time in all 15 patients

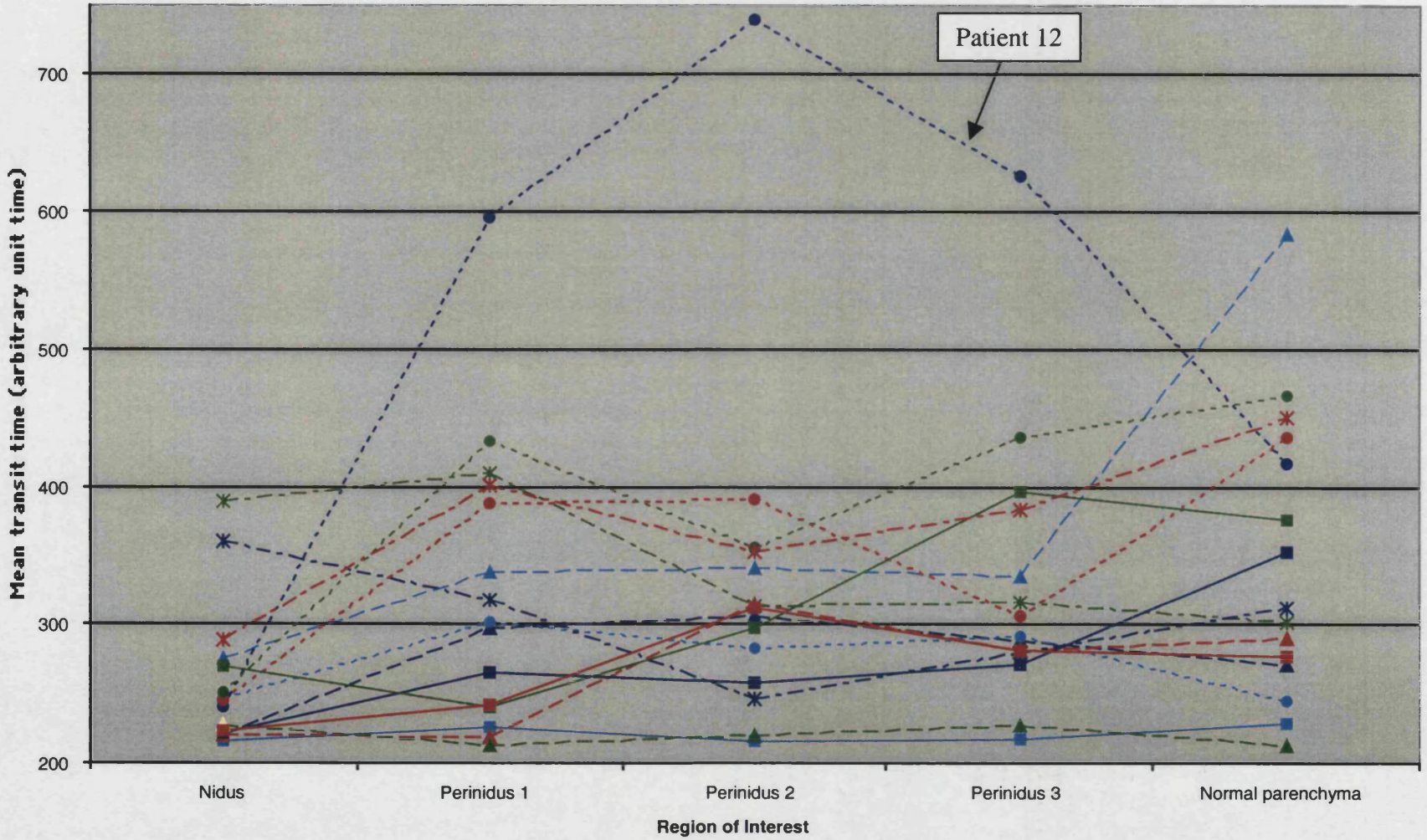

Figure 6.7: Time to minimum signal intensity in all 15 patients

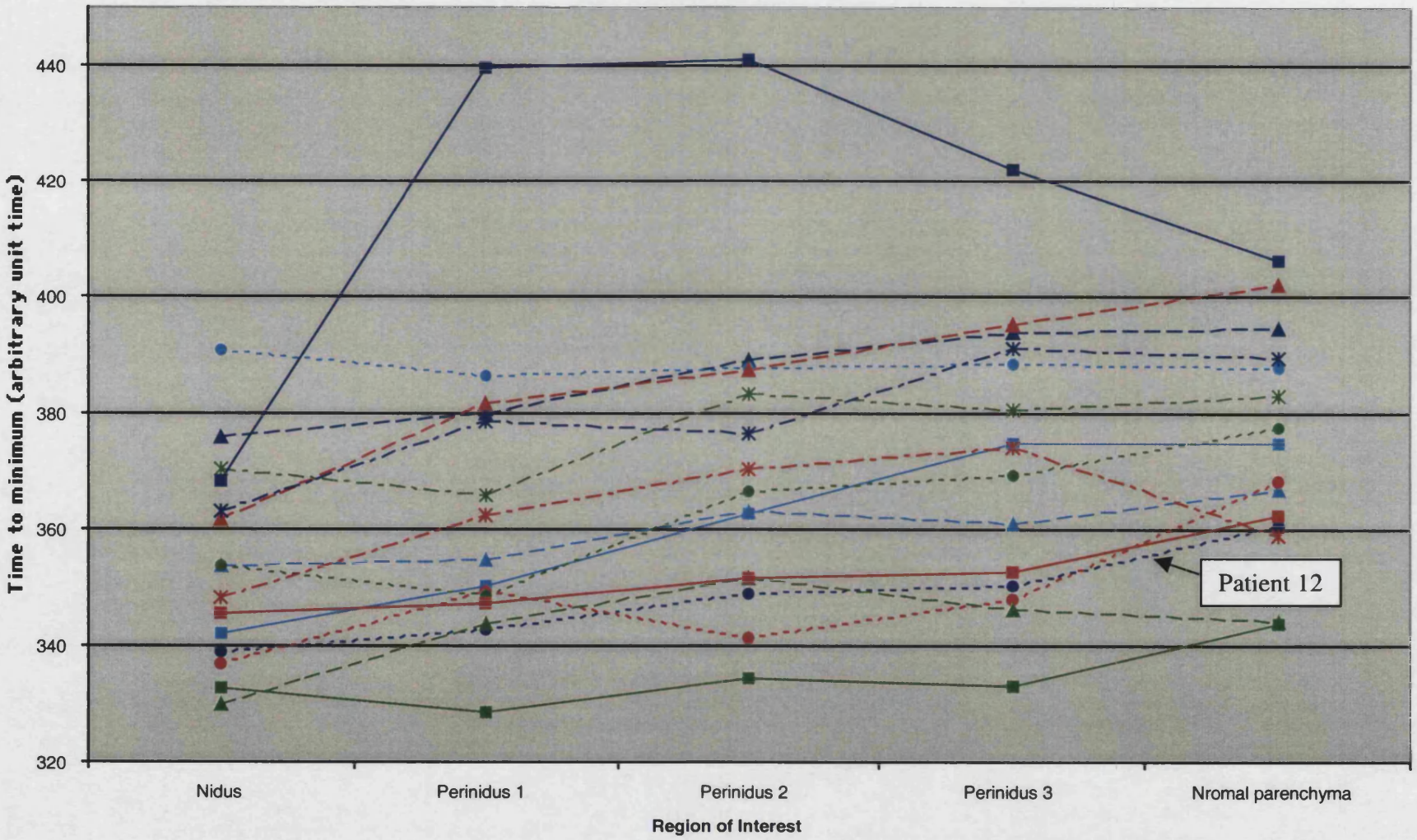

Table 6.2: Results of haemodynamic parameter comparisons

	CBF	CBV	MTT	TTM
Ipsilateral white versus grey matter	$p < 0.01$	$p < 0.01$	$p = 0.78$	$p = 0.20$*
Contralateral white versus grey matter	$p < 0.01$	$p < 0.01$	$p = 0.08$†	$p = 0.64$
Ipsilateral versus contralateral white matter	$p = 0.91$†	$p = 0.83$	$p = 0.24$	$p = 0.57$
Ipsilateral versus contralateral grey matter	$p = 0.46$†	$p = 0.96$	$p = 0.31$†	$p = 0.20$*
Nidus versus contralateral nidus	$p = 0.01$	$p < 0.01$*	$p < 0.01$	$p < 0.01$
Trend across perinidus	$p = 0.06$	$p < 0.01$	$p > 0.20$	$p < 0.01$

* *t* test performed on log transformed data
† Wilcoxon signed rank test

6.3.2.1 White and grey matter

Both ipsilateral and contralateral measurements showed that there was a significant difference between CBF and CBV between white and grey matter. Examination of the raw data revealed the values for CBF and CBV for grey matter were higher than those for white matter. Previous studies have shown this to be the case with average white matter CBF of 17 - 49 ml $100ml^{-1}$ min^{-1} and that of grey matter 43 - 90 ml $100ml^{-1}$ min^{-1} (Leenders, 1990; Schreiber, 1998; Vonken, 1999). CBV values are more difficult to obtain, but those calculated from dynamic susceptibility MRI and PET again show significantly higher values for grey matter compared with white matter. CBV in white matter is normally 2.1 – 4.7 ml $100g^{-1}$ and that of grey matter 3.8 – 7.8 ml $100g^{-1}$ (Leenders, 1990; Vonken, 1999).

However, white and grey matter do not appear to have significantly different MTT and TTM values. Values from PET studies suggest there are no significant differences in MTT values between grey and white matter with values of 4.6 – 9.2 sec in white matter and 4.6 – 8.2 sec in grey matter, whilst those of time to arterial bolus peak values, similar to TTM, were 1.5 – 4.5 sec and 1.0 – 3.8 sec for white and grey matter respectively (Vonken, 1999). Although there was no statistically significant difference in TTM between white and grey matter, in 19 out of 30 measurements TTM was higher in white matter than grey. This suggests that the technique was able to demonstrate appropriate differences in CBF, CBV, MTT and TTM between areas of normal brain, albeit semi-quantitatively.

When ipsilateral and contralateral values for white and grey matter were compared, there were no significant differences.

6.3.2.2 Nidus versus contralateral nidus equivalent

All haemodynamic parameters showed a significant difference between the nidal ROI and the corresponding contralateral region.

6.3.2.3 Perinidal region

There appeared to be no significant difference across the perinidal regions when examining MTT. However there was a significant difference across the four ROIs for CBV and TTM. The differences in CBF almost reached significance. Examination of the raw data showed that there was a gradual decrease in CBF and CBV with increasing distance from the nidus, with a gradual increase in TTM with increasing distance from the nidus.

6.4 Discussion

6.4.1 Limitations of Contrast Bolus Tracking MRI

The maps generated using this technique can be misleading in some circumstances, with important clinical implications. Although deconvolution of the concentration-time course could in theory provide accurate quantification, there are several assumptions in the tracer kinetic model used in the quantification of perfusion, and many of these assumptions may be invalid in some situations, particularly ischaemia (Calamante, 2002).

One of the main assumptions is about AIF. The calculation of CBF requires knowledge of the AIF, which in practice is estimated from a major artery (for example, MCA or ICA) with the assumption that this represents the exact input to the tissue. Any delays and dispersion of the bolus that are introduced during its passage from the site of AIF estimation to the tissue of interest will therefore introduce an error in quantification of CBF, and this error could well vary from one region to another. In addition to these difficulties, absolute CBF quantification requires an absolute measurement of the AIF. The accuracy of this may be compromised as a result of partial volume effects. These are not uncommon in the relatively low spatial resolution images used in CBT.

Secondly, the tissue characteristics can influence the proportionality constants involved in the quantification of CBF in two ways. The concentration of contrast agent (in both the tissue and AIF) is assumed to be linearly proportional to the change in relaxation time T2 or T2*. This proportionality constant has been shown to be tissue dependent and is therefore likely to vary with pathology. In addition, to obtain absolute CBF, values for the density of tissue, and a uniform value for the capillary haematocrit are usually assumed. Although the density of tissue may not be expected to vary substantially during the acute stages of ischaemia, that is not necessarily true for the haematocrit levels in the tissue.

Instead of assuming values for the proportionality constants, an alternative approach for measuring absolute CBF involve cross calibration with other techniques. Thus an empirical scaling to absolute units can be obtained. However similar to the problems of fixing values for the proportionality constants, this scaling constant should be used with caution because it is likely to vary with pathology.

Quantification of CBV is generally believed to provide a robust measure. However, since CBV is proportional to the area under the peak, its measurement can be insensitive to bolus delay and dispersion. In addition, any changes in the proportionality constants as mentioned before (for example, haematocrit levels) or errors in the quantification of the area under the AIF (for example, partial volume effects) will also introduce error in the quantification of absolute CBV.

Figure 6.8: Schematic demonstration of haemodynamic parameters from the signal intensity – time curve

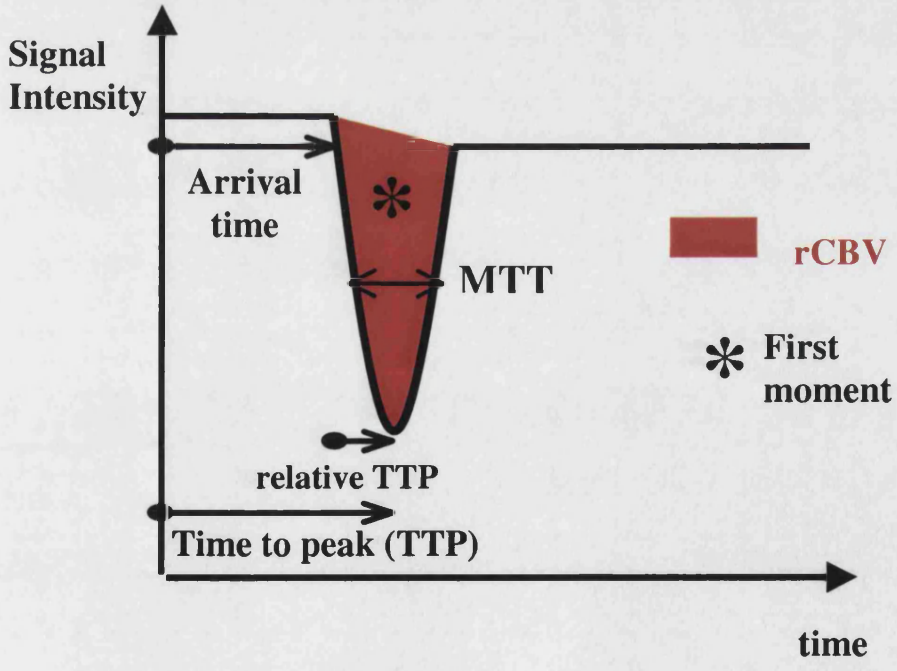

With appropriate knowledge of the AIF and careful analysis, it is therefore possible to generate high-resolution parametric maps of CBF, CBV and MTT from the time course of the MRI signal changes by applying kinetic analysis. However in the typical clinical setting, MRI-based maps of tracer kinetics are qualitative in

nature because arterial input in not well characterised and the relaxivity is unknown. Relative measurements in the same subject are thought to be reasonably reliable and have therefore been used to analyse the data in this study, with no absolute quantification of the units used. Absolute quantification of MTT is less subject to model assumptions and therefore more robust.

6.4.2 White and grey matter

Grey matter was shown to have significantly higher CBF and CBV compared with white matter using this technique. This is supported by previous studies. The AVMs did not, however, appear to have a generalised effect on haemodynamics throughout the ipsilateral hemisphere as demonstrated by the lack of difference in white and grey matter values for ipsilateral and contralateral sides. This may be due to the relatively small series, in which four lesions were small and four were medium sized. These may have not been of a sufficient size to cause such effects. In addition, some of the AVMs were fed by supplied both anterior and posterior circulations and therefore sampling frontal white and grey matter (as was done in the majority of cases) may not have been a representative sample of what might be regarded as 'normal' white and grey matter within the supplying vascular territory.

6.4.3 Nidus

CBV and CBF were increased in the AVM nidus compared with a corresponding contralateral region, whilst MTT and TTM were decreased. Previous PET and SPECT studies have also shown this to be the case (Takeuchi, 1987; Fink, 1992; Prohovnik, 1993). This is consistent with an increase in vascular density and arteriovenous shunting which are known key features of cerebral AVMs. However, the CBT technique is only semi-quantitative and reproducibility studies have not been performed.

6.4.4 Perinidus

The gradual decrease in CBF and CBV and increase in TTM seen with increasing distance from the nidus could all be explained by the presence of draining veins within the innermost of these 'onionskin' rings as they exit the AVM nidus. Most radiologists do not regard draining veins as part of the nidus and therefore, where possible, they have been excluded from the nidus ROI. In practice, using this technique, this is extremely difficult to do and the freehand trace is too crude a tool. This effect becomes less apparent with increasing distance from the nidus, with CBF, CBV and TTM approaching more normal parenchymal values.

In addition, macroscopic susceptibility effects interfere with the assessment of cerebral microcirculation in the immediate vicinity of the AVM as the total amount of gadolinium within the nidus is very high. This creates a 'blooming' effect beyond the limits of the intranidal vessels. If this was wholly responsible for the progressive changes in CBF, CBV and TTM values across the perinidal region, then MTT should also be affected when it is clearly also decreased in the nidus compared with the contralateral nidus equivalent ROI. It may be that there is a less obvious increase in true MTT values across the perinidus than the other three parameters.

In the case of cerebral AVMs, CBT may have methodological limitations in distinguishing and separating out the often conflicting effects of 'steal' against draining veins and the 'blooming' effect beyond the limits of the nidus of high concentrations of gadolinium. The 'blooming' effect may be reduced by using a spin-echo EPI sequence instead of a gradient-echo EPI sequence, as the susceptibility effect from large vessels is less pronounced with the former.

Closer examination of both Figures 6.4 – 7 and the colour maps (Figure 6.9), suggest that Patient 12, who had a large AVM and presented with a progressive hemiparesis, may not follow this pattern. There was some evidence of a low CBF in the innermost regions of the perinidus adjacent to the AVM nidus, with an increasing trend across the perinidus. This was accompanied by a higher MTT in the

Figure 6.9: a) Mean transit time colour map for patient 12 with b) corresponding EPI image

a

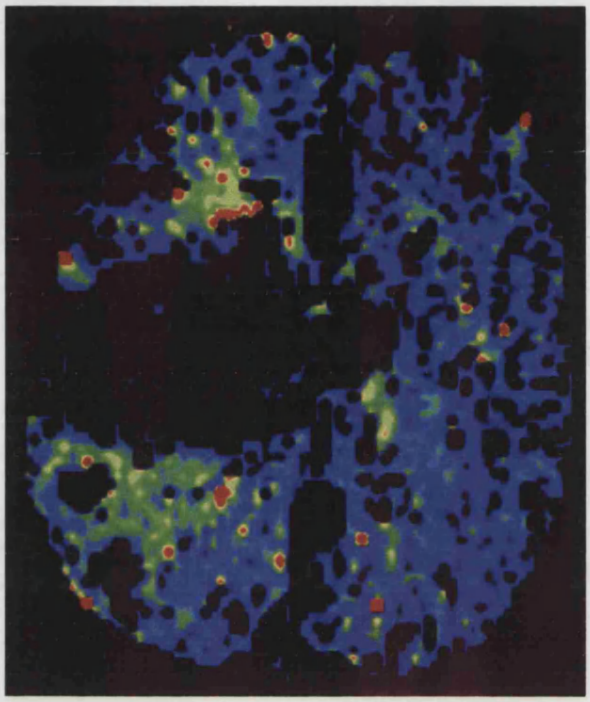

b

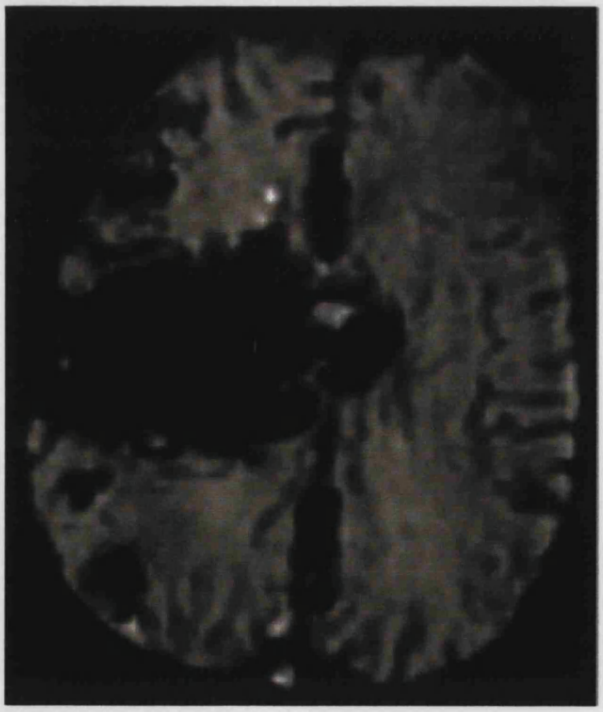

the areas of increased MTT (corresponding to the yellow, green and red regions on the colour map seen anterior and posterior to the central black region within the right hemisphere (this black region demonstrates uncomputable pixels corresponding to the AVM nidus)) can be seen to extend beyond the nidal region seen on the EPI image (area of signal intensity loss)

innermost regions of the perinidus, with a decreasing trend towards normal parenchymal values. There appeared to be little change in the CBV and TTM values across the perinidus. The data from the innermost perinidal 'onionskin' ring may have been contaminated by draining veins exiting from the nidus and these effects were more obviously seen if the innermost 'onionskin' ring was ignored. Low CBF and prolongation of MTT in the innermost perinidal regions could be related to a decreased arterial feeding pressure or increased venous pressure.

Most studies demonstrate a reduction in pressure within AVM feeding vessels, the fall in pressure being proportional to the number and length of feeding arteries (Nornes and Grip, 1980; Handa, 1993; Kader and Young, 1996). This may in part be related to AVM size since FAP is also inversely proportional to AVM size (Nornes and Grip, 1980; Spetzler, 1992). The pressure within draining veins, however, is increased compared with normal cerebral veins (Nornes and Grip, 1980; Young, 1994). Transnidal pressure drop or net CPP gradient is therefore inversely correlated with AVM size, suggesting that relative arterial hypotension or venous hypertension may be a compounding factor in large AVMs and may be a cause of the demonstrated haemodynamic effects seen in Patient 12 (Young, 1994). Sugita *et al.* (Sugita, 1993) reported on a single case demonstrating improvement in CBF, on the basis of SPECT, and clinical symptoms associated with the treatment of a large AVM. Venous hypertension was implicated as the cause of this patient's neurological symptoms on the basis of angiographic cortical vein reflux.

6.5 Conclusion

CBT was able to demonstrate appropriate relative differences in haemodynamic parameters when compared with previous studies. The evaluation of the haemodynamic effects of AVMs was complicated by the draining veins that are commonly extremely large and lie in the perinidal region as they exit the AVM nidus. This meant that the effects of the AVM on haemodynamic parameters,

particularly in the innermost region of the perinidus, were over-shadowed by the intravascular contrast bolus flowing through the draining veins. In addition, high concentrations of intravascular contrast caused a 'blooming' effect beyond the limits of both the nidus and large feeding or draining vessels, which again contaminated the results derived from the perinidal regions. In small or medium-sized AVMs, which are unlikely to have a far-reaching effect on cerebral haemodynamics, any subtle changes may well be lost.

PART 4

HAEMODYNAMIC IMAGING

Chapter 7

DIGITAL SUBTRACTION ANGIOGRAPHY

7.1 Introduction

The natural history of cerebral AVMs is not fully understood and structural analysis of the AVM angioarchitecture alone does not provide sufficient haemodynamic information. A small number of studies have examined the influence of FAP and DVP and have suggested that raised arterial or venous pressures within an AVM may be associated with an increased risk of haemorrhage (Kader, 1994; Young, 1994; Duong, 1998). These pressures were measured invasively, either by superselective arterial catheterisation requiring sophisticated calibration methods or intra-operatively by *in situ* cannulation which is more invasive but allows measurement of venous pressures. Measuring blood flow velocities at various points may provide valuable information about the resistance, pressure gradients and shunting within an AVM. By correlating these results with patients' presentation and symptoms, this may help to identify features such as high flow fistulae and intranidal aneurysms that carry a risk of haemorrhage and help to target treatment. Velocities could be correlated with presentation, quantification of the haemodynamic effects of partial or complete treatment by embolisation or radiosurgery may be possible or disease progression assessed.

Conventional angiographic techniques to measure flow require the measurement of the time difference between the passage of a bolus of contrast material between two sites, a known distance apart along the vessel. Diagnostic intra-arterial angiography is normally performed using a rate of 2 – 4 images sec^{-1} in the arterial phase, or in the case of AVMs at 6 images sec^{-1}. Acquisition of up to 30 images sec^{-1} however produces a large number of time-resolved images of the

contrast medium bolus as it passes through the vasculature. A variety of post-processing techniques can then be used in order to derive haemodynamic parameters.

Time-density curves can be created for several sites along a blood vessel. Blood velocity is then calculated from the plots by determining the transport time for the passage of a bolus of contrast between sites (bolus transport time) (Silverman and Rosen, 1977; Forbes, 1984). Distinct points on the curve, such as the peak or the leading edge, are usually identified. The transport time is taken as the time difference between the two identical points on the curve at the two sites under study. The blood flow is then calculated as the product of the average cross-sectional area of the vessel and the distance between the two sites, divided by the transport time. This method has been used to determine MTT, peak density time (time to peak opacification) (PDT) and time to half peak opacification (T1/2) of cerebral aneurysms (Tenjin, 1998). Cerebral AVMs have a more complex angioarchitecture and are therefore even more challenging.

Alternatively, Swanson *et al.* (Swanson, 1986) suggested a technique for determining the velocity by tracking the position of a fixed length of vessel which contains the same mass of contrast material in time sequences of radiographic images. The integrated radiographic density of all pixels along a defined length of artery is determined on the first angiographic image. The integrated radiographic densities of the identical length of vessel in the next frame are then similarly calculated. These integrated radiographic densities are then shifted relative to each other. For each shift the density in the first frame is subtracted from that in the second frame. The shift for which the absolute difference in integrated radiographic density was a minimum was then determined. The length between this point and the original starting point provides a measurement of the distance moved by the blood during a known time period (tracking of bolus mass).

A final method was that proposed by Seifalian *et al.* (Seifalian, 1989) using density-distance curves rather than time-density curves. This technique matches the amplitude of the plot of contrast medium concentration (density) versus distance in

adjacent images in a time sequence of radiographic images (matching of contrast concentration profiles). Adjacent concentration-distance profiles in the parametric image of iodine concentration versus distance are shifted along a vessel axis until a match occurs. A match is defined as the point where the sum of squares of the difference between the two profiles is a minimum. The distance of translation per time frame is equal to the bolus velocity. This allows the pulsatile velocity waveform throughout the complete cardiac cycle to be computed.

The aim of this study was to assess whether bolus transport time could be used to evaluate the haemodynamic effects of the AVM on feeding artery velocity and flow values.

7.2 Phantom studies

7.2.1 Method

A vascular phantom was designed and built to validate measurements of velocity and blood flow using RFRDSA (Figure 7.1). This phantom consisted of a length of radiolucent tubing (the packaging sheath of a GDC® - 10 (Boston Scientific, Cedex, France)), with two radio-opaque markers (fuse wire) at a distance of 10cm from each other, secured alongside a radio-opaque ruler. This was connected to a power injector (MedRad® mark V power injector, Wolverson Xray, Willenhall, UK) and the whole system primed with water. This power injector allowed predetermined values for flow rate to be programmed into the machine, but at the end of the run reported the actual flow rate of the injection in ml sec^{-1} or ml min^{-1}. The actual flow rate varied from run to run by up to 2% from the nominal required flow rate in accordance with the manufacturer's specifications. An air bubble of approximately 0.5ml was introduced through a three-way tap situated between the power injector and phantom. The injector was primed and injection of water triggered after the 'mask' had been acquired at the beginning of the

Figure 7.1: Unsubtracted DSA image of the vascular phantom

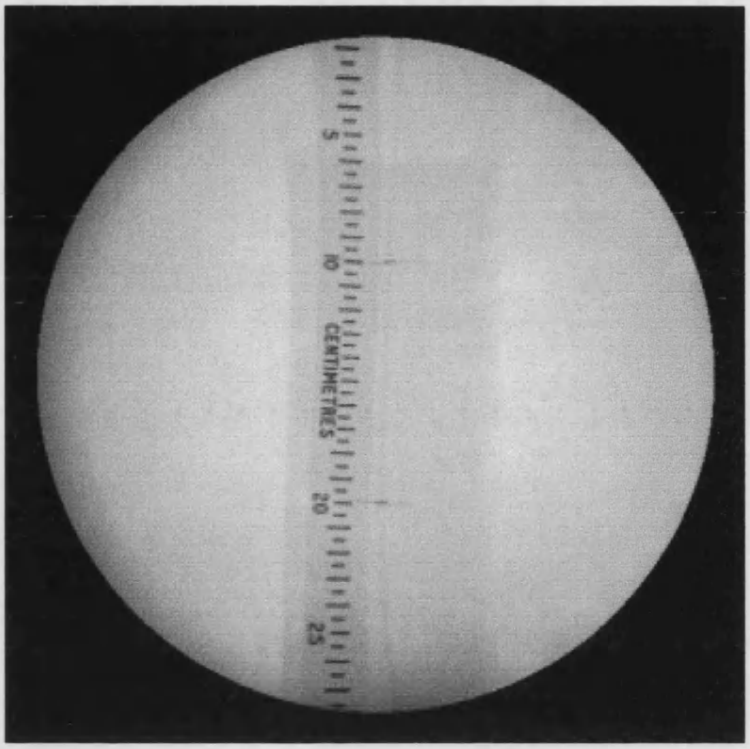

Figure 7.2: Subtracted DSA image of vascular phantom demonstrating air bubble (black arrow)

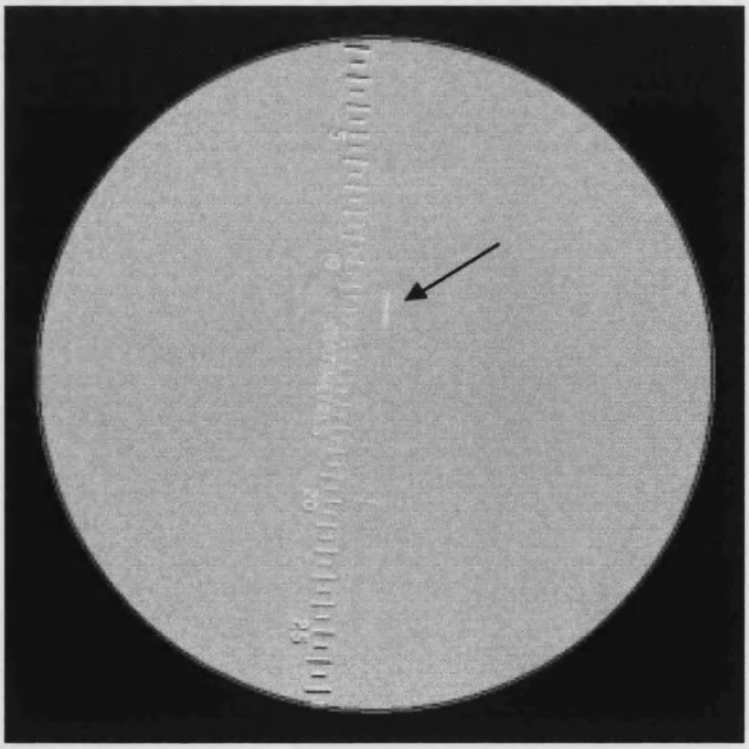

angiographic sequence. Angiography was performed on a biplane Toshiba digital fluorography system DFP 2000A® (Toshiba, Tochigi-Ken, Japan), using a frontal projection only. The angiographic sequence used consisted of an initial 'mask' sequence (0.8 sec at 7.5 frame sec^{-1}) followed by the true angiographic acquisition.

The six frames of the 'mask' acquisition were automatically averaged and were then subtracted from the subsequent images, allowing visualisation of only data or objects that had changed between images (i.e. the air bubble) (Figure 7.2).

A series of experiments was performed to assess the accuracy of flow measurements calculated by RFRDSA, compared with those reported by the power injector. Reproducibility of the system and the effects of varying injection rate, frame rate, field of view, table height, source-image distance and patient-source distance were assessed (Appendix 5).

DSA produces a 2-D projectional image of a vessel. To allow calculation of velocities from these images, an accurate measurement of the distance between two

Figure 7.3: Diagram showing arrangement of phantom as the angle from the horizontal is increased

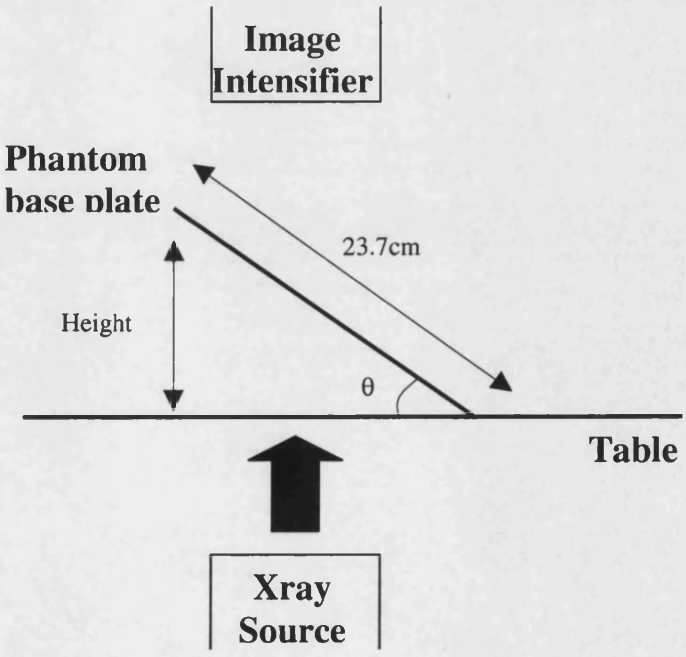

ROIs on the vessel is needed. Unless the vessel concerned lies exactly within the plane of the DSA image (which is exceedingly unusual), the distance between two points is foreshortened. To assess the effect of the angle of the vessel in relation to the plane of the DSA image on calculated velocities, a series of experiments was performed using a frontal projection, increasing the angle of the phantom from the horizontal (Figure 7.3) (Appendix 5).

7.2.1.1 Post processing

Using the ROI function on angiography system, two ROIs of approximately 10 x 10 pixels were positioned over the path of the air bubble. A time-density curve was produced, transferred to Toshiba 230CX® laptop (Toshiba, Tochigi-Ken, Japan) and imported into Microsoft® Excel 5.0/95. From this Excel graph, start and end frame numbers for the pre- and post-bolus baselines were identified. The pre-bolus baseline was defined as that prior to the first dip (created as the air bubble traversed the proximal ROI) and the post-bolus baseline as that after the second dip (created at the distal ROI) (Figure 7.4).

Inputting these frame numbers, total number of frames taken in the run and diameter of the 'vessel' into a home-written fitting programme, flow was calculated. Software was developed in-house to read the time-density curves and automatically detect the minimum intensity which represented the passing of the air bubble. Having found these peaks, the software then fitted the time-density curves to a Gaussian function and used fitting parameters to calculate more accurately the time between the two points. This value was then used with the acquisition frame rate and the diameter of the tubing (or blood vessel) to calculate velocity and flow rates.

In each series of experiments, measured flow was compared with flow reported by the pump injector.

Figure 7.4: Time density curve from DSA showing two dips as the air bubble passes the proximal and distal ROIs

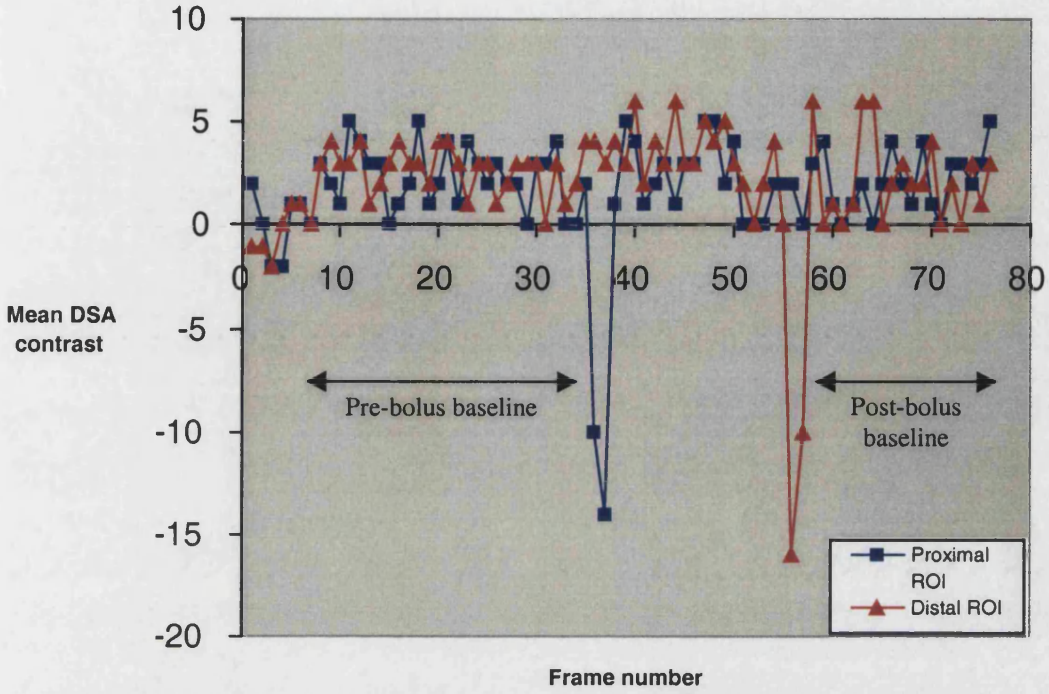

7.2.1.2 Statistical analysis

Graphs, with their corresponding regression lines and equations, were produced using Microsoft® Excel 98 and statistical analysis was performed using Stata™ 4.0 (Stata corporation, Texas, USA), on an Apple Macintosh® iMac computer.

7.2.2 Results

7.2.2.1 Terminology

Throughout this chapter, specific terminology has been used. Flow and velocity are represented by f and v respectively. If these values had been calibrated or adjusted for the model, this was shown by an apostrophe (′). All subscriptions refer to the origin of the values. In the phantom, t was the true reported value from the pump injector, m was the measured value (calculated from DSA) and p was the

predicted value. In the patient experiments, TCD represents the values measured by TCD, and DSA those calculated from RFRDSA.

7.2.2.2 Calibration of the model

Flow rates were measured from 10 separate runs for each of three nominal flow rates, 1, 5 and 10 ml sec^{-1}. The model can be calibrated by regressing measured flow rate on true reported flow rate (Figure 7.5). True flow rate was plotted along the x axis as this was the independent variable.

Figure 7.5: Graph showing the relationship between true reported and measured flow rates from DSA at 30 frames sec^{-1}

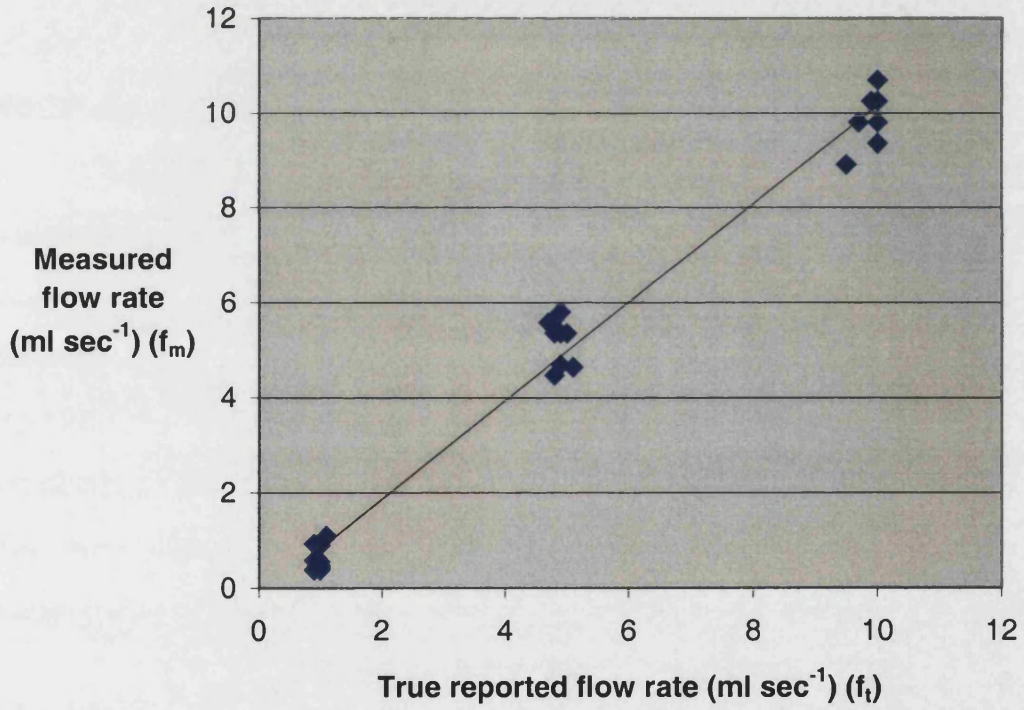

The regression equation was:

$f_m = 1.04f_t - 0.21$

Residual standard deviation = 0.50

$R^2 = 0.98$

True flow rates can be predicted from measured flow rates by reversing this regression equation. This equation is:

$$f_t = (f_m + 0.21) / 1.04$$

This demonstrated the systematic error within the system. In using regression analysis, three statistical assumptions were made. Firstly, the values of measured flow rate should have a Normal distribution for each value of the predictor variable pump reported flow rate; secondly that the variability of measured flow rates should be the same for each value of reported flow rate; and thirdly that the relationship between the two variables should be linear. If the three above assumptions hold then the residuals should have a Normal distribution which they did (Shapiro-Francia W' test for Normal distribution, $p = 0.56$).

Residual standard deviation indicates the variation not explained by the regression line so it is a measure of the 'goodness-of-fit' of the line in units of measurement i.e. ml sec^{-1} (Altman, 1991). Similarly the high R^2 value shows that the majority of variability in measured flow rate is explained by variation in the true reported flow rate. R^2 values can be reported as a percentage i.e. 98% of the variability in measured flow rate is explained by the variation in the true reported flow rate. These results suggested that the model for calculating flow rates from pump-reported flow rates was accurate at 30 frames sec^{-1}.

7.2.2.3 Reproducibility of the model

In order to assess the reproducibility or random error of the calibration model, this same series of measurements was used. The measured flow rates (f_m) were adjusted for the model using the above regression equation. These values were plotted against the true reported values, together with their confidence and prediction intervals (Figure 7.6).

Figure 7.6: Graph showing the 95% confidence and prediction intervals for reported and measured flow rates at 30 frames sec^{-1}

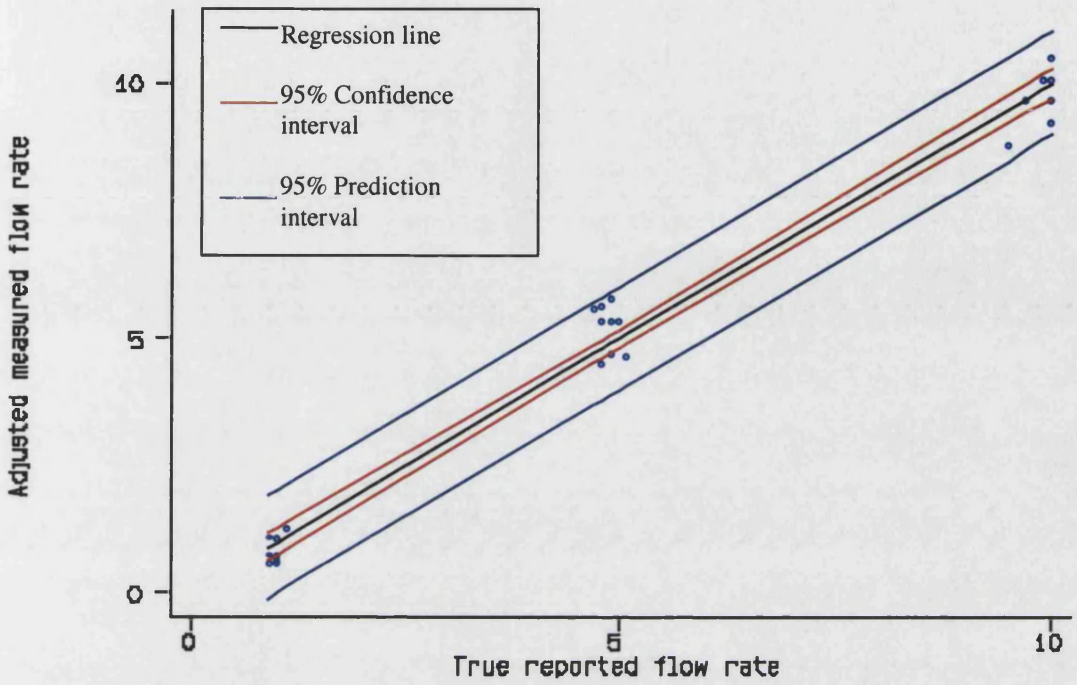

The true reported flow rates (f_t) and adjusted measured flow rates (f'_m) were compared using the paired *t* test as the differences between flow rates had a Normal distribution using the Shapiro-Francia W' test for Normal distribution (p = 0.55).

Null hypothesis: f_t = Adjusted f_m = f'_m

t = 0.00 with 29 degrees of freedom

p = 0.99

The null hypothesis could not be rejected, suggesting that the reported flow rates and adjusted measured flow rate did not differ significantly. In addition, the confidence and prediction intervals were narrow, again suggesting that true reported and measured flow rates had good reproducibility.

7.2.2.4 Angle from the horizontal

Again, the measured flow rates (f_m) were adjusted using the regression equation from section 7.2.2.2. This equation is:

$$f_t = (f_m + 0.21) / 1.04$$

This adjusted measured flow rate, f'_m, when plotted against angle from the horizontal, showed a cosine drop-off (Figure 7.7).

Figure 7.7: Graph showing effect of angle from the horizontal on adjusted measured flow rate

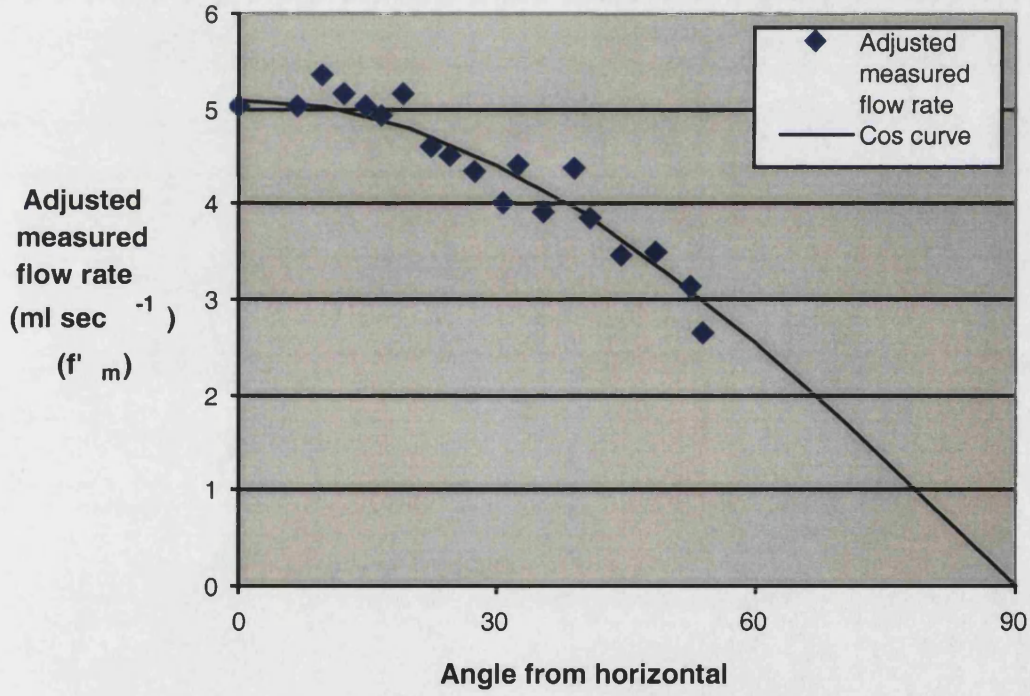

To test this model, adjusted measured flow rate was compared with predicted flow rate (f_p), where:

$$f_p = f_t \cos \theta$$
$$= f_t \cos (\sin^{-1}(\text{height}/23.7))$$

The predicted flow rates (f_p) and adjusted measured flow rates (f'_m) were compared using the Wilcoxon matched pairs signed rank sum test as the differences between flow rates did not have a Normal distribution, both before and after transformation of the data (Shapiro-Francia W' test for Normal distribution, p = 0.03).

Null hypothesis: $f_p = f'_m$

Sum of Positive Ranks = 120

Sum of Negative Ranks = 70

z statistic = 1.01

p = 0.31

The null hypothesis could not be rejected, suggesting that the predicted flow rate and adjusted measured flow rate do not differ significantly.

7.2.2.5 Frame rate, injection rate, field of view, table height, source-image distance and patient-source distance

Varying frame rate, field of view, table height, source-image distance and patient-source distance was found to have no effect on the measured flow rates. Injection rates up to 10 ml sec^{-1} at 15 and 30 frames sec^{-1} showed linear agreement between reported flow rate and measured flow rate.

7.2.2.6 Reproducibility and accuracy of angiography machine

The angiography system automatically reported the source-image distance, table height and C-arm height. The accuracy of the reported figures was tested and each found to be within 1 cm of the true measurements. This was of particular importance in the calculation of magnification of images and hence distances travelled by the air bubble, where:

$$\text{Magnification} = \frac{\text{Source-image distance}}{\text{Source-patient distance}}$$

$$= \frac{\text{Source-image distance}}{\text{Source-image distance} - \text{Patient-image distance}}$$

Allowing for the potential 1 cm error reported by the system of these measurements, the error in magnification factor was a maximum of 2.6%.

7.2.3 Conclusion

Using this phantom, it was possible to calculate true flow rates from measured flow rates at 30 frames sec^{-1} accurately and reproducibly using the calibration equation of:

$$f_t = (f_m + 0.21) / 1.04$$

These values have narrow 95% confidence and predictive intervals as seen in Figure 7.6. The measured flow rates show a cosine relationship to reported flow rates when the 'vessel' of interest does not lie in the horizontal plane as expected. The error in reported measurements from the angiography system result in a maximum of 2.6% error in magnification ratios.

7.3 Patient studies

Having validated the model, a similar technique was used to examine flow and velocity rates in patients with AVMs.

7.3.1 Methods

7.3.1.1 Patients

Patients with known AVMs were recruited from those due to undergo DSA as a planned procedure as part of their management, immediately prior to an embolisation procedure, between October 1999 and January 2000. Those who were pregnant, had a history of allergy to iodine or were aged less than 16 years were excluded.

7.3.1.2 Imaging

Prior to the procedure, patients underwent TCD of the intracranial circulation to act as a control measurement of velocity within individual vessels. This was performed bilaterally immediately prior to the procedure, when the patient was lying supine on the angiogram table and under general anaesthesia. The TCD machine used was the Pioneer™ Transcranial Doppler System (Nicolet Biomedical, Wisconsin, USA).

TCD uses ultrasound to measure blood velocity within the brain. Advantage is taken of the relatively thin temporal bone to image the ICA and MCA and the technique relies on knowledge of both the depths of these arteries from the temporal bone and the velocity and direction of blood flow in these vessels. Using occipital and orbital windows, most intracranial vessels can be imaged by an experienced operator. Signals can be obtained in about 95% of individuals.

Angiographic studies were performed on a biplane Toshiba digital fluorography system DFP 2000A® (Toshiba, Tochigi-Ken, Japan). Femoral puncture and insertion of the femoral sheath and angiographic catheter were performed in a routine fashion. The catheters used varied according to the nature of the planned procedure and therefore prior to insertion, the dead space of the catheter was determined. Measurement of the catheter dead space allowed injection of a precise 1ml contrast bolus into the patient. After catheterisation of the proximal

ICA, a routine angiographic run was acquired. Having confirmed the correct positioning of the catheter and an adequate angiographic acquisition, RFRDSA was performed from this same position. Using a frontal projection, a similar 'mask' was acquired (0.8 sec at 7.5 frames sec^{-1}) followed by a run up to 8 sec at 30 frames sec^{-1}, but acquisition was stopped as soon as the contrast bolus had passed through the arterial side of the circulation. A contrast bolus of Omnipaque® 300 (Nycomed Amersham, Little Chalfont, UK) was given as a hand bolus immediately after the 'mask' acquisition. A total volume equal to 1ml plus the dead space of the catheter was injected, such that the intravascular contrast bolus given was 1ml. All RFRDSA angiographic injections were performed on the side of the AVM.

The procedure was completed in a routine fashion. The mean effective radiation dose equivalent of a standard four vessel cerebral angiogram was 0.5 – 0.7mSv. RFRDSA delivered an additional 0.25mSv. Many of these patients underwent repeated DSA and embolisation procedures which further increased the radiation dose. In this context the additional radiation dose related to RFRDSA was considered acceptable.

7.3.1.3 Post processing

Two ROIs of approximately 10 x 10 pixels were this time placed on both the ICA and MCA (Figure 7.8). The average diameter of the ICA and MCA and the distance between the two ROIs on each vessel were measured. Time-density curves were produced, transferred to the Toshiba 230CX® laptop (Toshiba, Tochigi-Ken, Japan) and imported into Microsoft® Excel 5.0/95. Software was developed in-house to read the time-density curves and automatically detect the maximum intensity, representing the leading edge of the contrast bolus. Having found these peaks, the software then fitted the time-density curves to a gamma variate function and used fitting parameters to calculate more accurately the time between the two points. This value was then used with the acquisition frame rate and the diameter of

Figure 7.8: Magnified example of a DSA image with placement of ROIs for generation of time-density curve

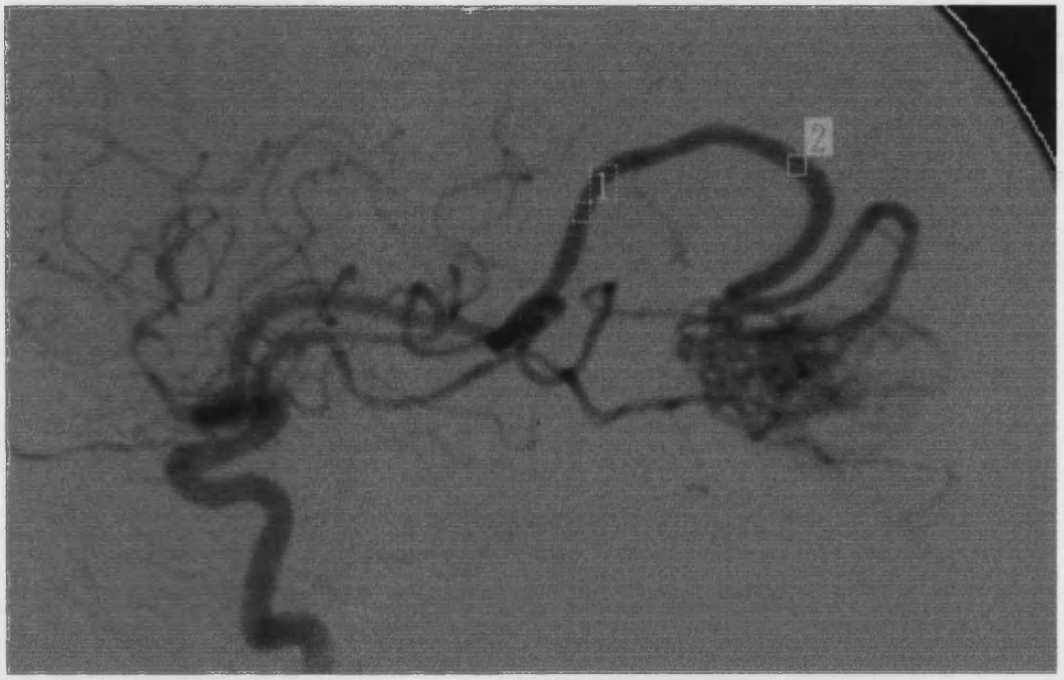

the blood vessel to calculate speed and flow rates. Curves were fitted using a gamma variate function, which better described an in-vitro bolus than a Gaussian function. Velocities and flow rates were calculated as before.

7.3.1.4 Statistical analysis

Statistical analysis was performed as described in section 7.2.1.2.

7.3.2 Results

7.3.2.1 Patient baseline characteristics

Five patients, three male and two female, underwent RFRDSA (Table 7.1). They had a median age of 44 years with an interquartile range of 31 - 46 years. All patients underwent RFRDSA as part of a planned embolisation procedure and were therefore under general anaesthesia at the time.

Three patients had initially presented with haemorrhage, one with seizures and the final patient with a cosmetic deformity with associated visual deterioration. Two patients had undergone previous partial embolisations.

7.3.2.2 Transcranial Doppler findings

All patients underwent successful TCD measurement of bilateral MCA and ICA velocities. Mean, systolic and diastolic velocities are shown in Table 7.2. The values shown are the mean values taken from three TCD measurements taken immediately before the angiographic procedure, whilst under general anaesthesia, with their 95% confidence intervals (CIs).

Table 7.1 : Demographic data of patients undergoing RFRDSA

Patient Number	Gender	Age	Presentation	AVM			Prior treatment	Planned treatment
				Site	Anatomy	Size		
1	M	44	Seizures	Left temporal	Cortical	Medium	Embolisation	Embolisation
2	F	45	Cosmetic Visual deterioration	Right orbital	Orbital	Medium	None	Embolisation
3	M	20	ICH	Right parietal	Cortical	Large	None	Embolisation
4	M	19	ICH IVH	Right parietal	Cortical	Small	None	Embolisation
5	F	48	SAH	Left occipital	Cortical	Large	Embolisation	Embolisation

Table 7.2 : Velocities determined by transcranial doppler of all five patients undergoing RFRDSA

Patient no.	Laterality of AVM	Velocity (cm sec^{-1})	R MCA (95% CI)	R ICA (95% CI)	L MCA (95% CI)	L ICA (95% CI)
1	Left	Mean	79	55	73	64
			(63 – 96)	(40 – 70)	(67 – 79)	(52 – 75)
		Systolic	118	80	104	91
			(98 – 138)	(61 – 99)	(99 – 110)	(76 – 106)
		Diastolic	55	39	54	47
			(43 – 66)	(28 – 50)	(49 – 59)	(39 – 55)
2	Right	Mean	56	46	62	37
			(50 – 63)	(21 – 71)	(52 – 71)	(30 – 44)
		Systolic	82	68	93	56
			(75 – 89)	(34 – 103)	(83 – 103)	(46 – 67)
		Diastolic	39	31	41	24
			(35 – 44)	(13 – 49)	(34 – 48)	(18 – 30)
3	Right	Mean	125	114	84	66
			(118 – 131)	(107 – 120)	(80 – 88)	(59 – 72)
		Systolic	157	160	115	84
			(145 – 169)	(153 – 166)	(109 – 121)	(77 – 90)
		Diastolic	96	89	65	48
			(86 – 106)	(82 – 95)	(60 – 69)	(41 – 54)
4	Right	Mean	60	45	50	43
			(53 – 68)	(38 – 53)	(46 – 54)	(41 – 45)
		Systolic	93	78	84	70
			(75 – 111)	(60 – 95)	(78 – 92)	(64 – 76)
		Diastolic	41	34	40	30
			(36 – 46)	(29 – 39)	(38 – 42)	(25 – 35)
5	Left	Mean	50	44	69	62
			(38 – 49)	(38 – 49)	(64 – 75)	(47 – 77)
		Systolic	74	64	97	89
			(71 – 78)	(58 – 70)	(90 – 103)	(72 – 106)
		Diastolic	34	30	51	47
			(31 – 37)	(26 – 35)	(47 – 56)	(33 – 61)

7.3.2.3 Time-density curves and calculated velocities

Time-density curves were created for the ICA and MCA on the side of injection for each patient as shown in Figure 7.9.

Figure 7.9 : Time-density curve of the right ICA injection of patient 2

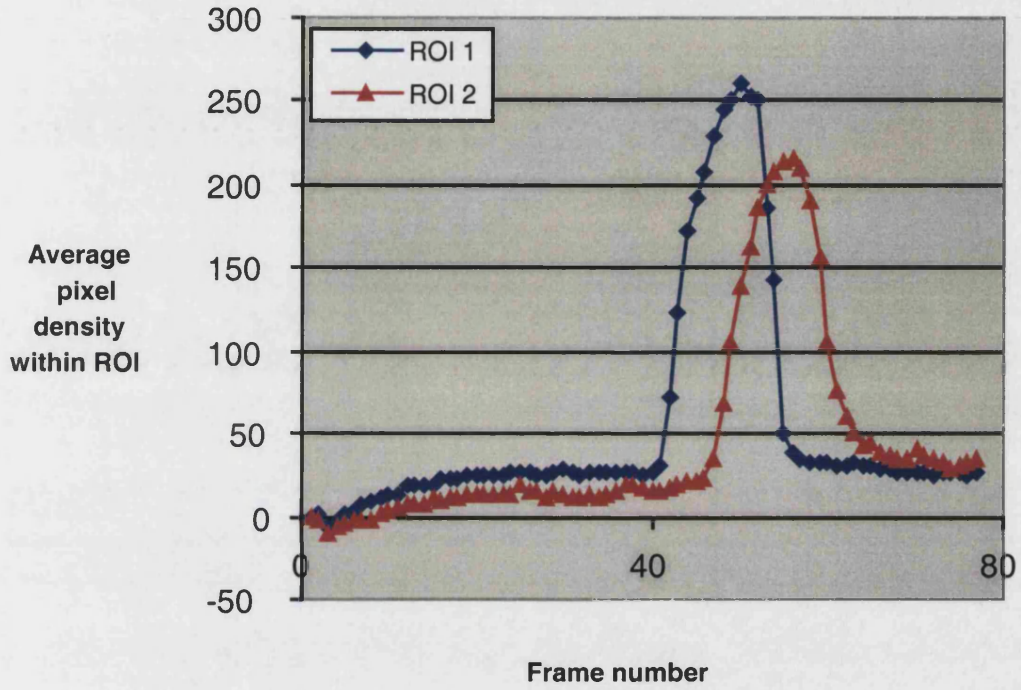

In two of the five patients, time-density curves showed a poor bolus injection with a double peak as shown in Figure 7.10. In these situations, velocities were not calculated by fitting to a gamma curve, but were calculated from the raw data. The relevant peaks were identified visually and the number of frames taken for the bolus to travel between the two ROIs calculated. This number of frames was divided by the frame rate (i.e. 30) giving the time in seconds for the bolus taken to travel the distance between the two ROIs. The distance between the two ROIs was then divided by this figure giving velocity. Flows were calculated similarly, using the diameter of the relevant vessel to calculate the cross-sectional area.

Calculated velocities and flows are shown in Table 7.3.

Figure 7.10 : Time-density curve of left MCA injection of patient 5 showing a poor bolus injection

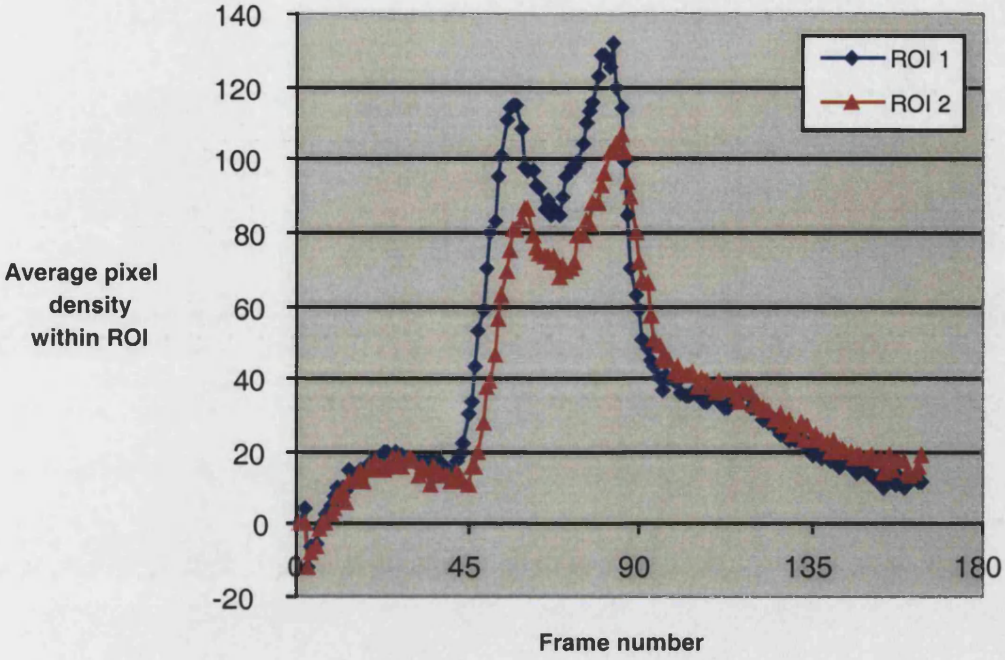

Table 7.3 : MCA and ICA velocities and flows in all patients calculated from RFRDSA

Patient no.	Laterality of AVM	MCA velocity (cm sec^{-1})	MCA flow (ml sec^{-1})	ICA velocity (cm sec^{-1})	ICA flow (ml sec^{-1})
1	Left	30	1.5	22	3
2	Right	31	1	30	3
3	Right	52*	5*	39*	10*
4	Right	18	0.5	22	3
5	Left	28*	2*	23*	2.5*

*calculated using raw data and without gamma fitting

7.3.2.4 Comparison of Transcranial Doppler measurements and measured velocities from time-density curves

MCA and ICA velocities calculated from RFRDSA (v_{DSA}) were adjusted for the model using the regression equation from section 7.2.2.2 (v'_{DSA}). These values were then compared with the mean MCA and ICA velocities measured by TCD (v_{TCD}) as seen in Figure 7.11. Their accompanying regression lines are also shown.

Figure 7.11 : Graph showing comparison of MCA and ICA velocities measured by TCD with those calculated from RFRDSA and their accompanying regression lines

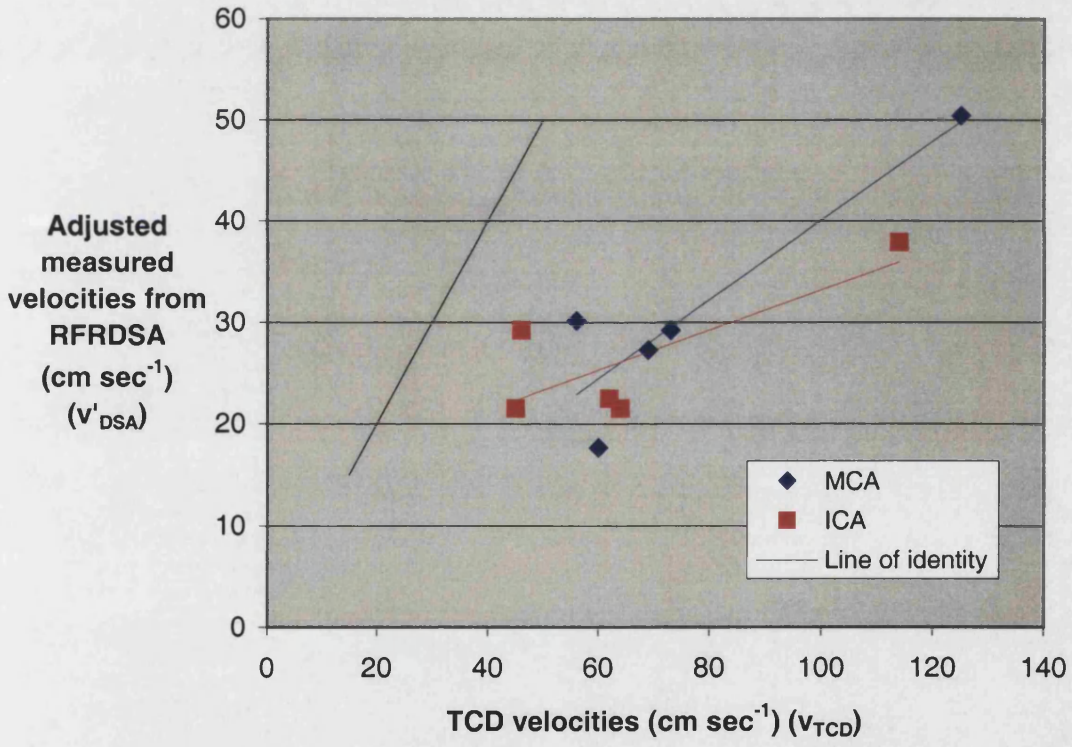

The regression line for MCA velocities has the equation of:

$v'_{DSA} = 0.39\ v_{TCD} + 1.00$

Residual standard deviation = 5.79

$R^2 = 0.83$

Shapiro-Francia W' test for Normal distribution of residuals, p = 0.42

The ICA regression line has the equation of:

$v'_{DSA} = 0.20\ v_{TCD} + 13.39$

Residual standard deviation = 5.18

$R^2 = 0.60$

Shapiro-Francia W' test for Normal distribution of residuals, $p = 0.74$

Comparison of the adjusted MCA velocities calculated from RFRDSA (v'_{DSA}) and those measured on TCD (v_{TCD}) using paired *t* test showed the measurements to be significantly different.

Null hypothesis: $v'_{DSA} = v_{TCD}$

$t = 5.76$ with 4 degrees of freedom

$p < 0.01$

Shapiro-Francia W' test for Normal distribution, $p = 0.13$

Comparison of the adjusted ICA velocities calculated from RFRDSA (v'_{DSA}) and those measured on TCD (v_{TCD}) using paired *t* test also showed the measurements to be significantly different.

Null hypothesis: $v'_{DSA} = v_{TCD}$

$t = 3.86$ with 4 degrees of freedom

$p = 0.02$

Shapiro-Francia W' test for Normal distribution, $p = 0.42$

7.3.3 Discussion

Generally accepted values for MCA and ICA velocities are 55 ± 12 and 39 ± 9 cm sec^{-1} respectively, whilst the average CBF in young adults is 54 ml $100g^{-1}$ min^{-1}. The average adult brain weighs about 1400g, which means that the total

cerebral flow is about 756 ml min^{-1}. These values vary with age, generally reducing with increasing years. AVMs are often high flow lesions, resulting in considerably higher velocities and flows in feeding vessels than normal. Arteries supplying an AVM can have a flow ranging from 3 to 550 ml min^{-1} with an average of 180 ml min^{-1}. Total AVM flow ranges from 50 to 900 ml min^{-1} with an average of 490 ml min^{-1} (Nornes and Grip, 1980). Velocity appears to be related to size of vessel, reaching 70cm sec^{-1} (Nornes and Grip, 1980).

Although the measured velocities and adjusted measured velocities from RFRDSA grossly underestimated the true velocity shown on TCD, it consistently demonstrated a lower velocity but higher flow in the ICA when compared to the MCA. This suggests that there was a systematic error in the RFRDSA measurements. This was confirmed by the relatively high R^2 values for both regression lines comparing MCA and ICA velocities measured using TCD with those calculated from RFRDSA (0.82 and 0.60 respectively). However, both regression lines did have relatively high residual standard deviations (cm sec^{-1}), suggesting that the 'goodness-of-fit' of the line could be improved.

7.3.3.1 Sources of error

Blood velocity within vessels varies depending upon the precise point of the cardiac cycle at which measurements are taken. This is seen on TCD, with values varying dramatically between diastolic and systolic values (Table 7.2). TCD values usually quoted in the literature are systolic values and therefore the highest velocities seen within a single cardiac cycle. The RFRDSA values determined may represent velocities at any point during the cardiac cycle, including the lowest velocities seen at diastole. The ability to calculate instantaneous blood velocity and therefore flow measurements at any point in the cardiac cycle, as in the matching of contrast concentration profiles technique proposed by Seifalian *et al.* (Seifalian, 1989), may improve accuracy. Mean flow rates can also be determined using the same technique (Hoffman, 1991). Systolic, mean and diastolic values could then be

compared in a much more meaningful way to those obtained from TCD. However the RFRDSA values obtained were generally lower than even diastolic TCD velocities, so other errors must have been present.

During phantom validation, the air bubble flows and velocities were measured through a straight, in-plane 'vessel' over a length in the order of 10 cm. The distances travelled by the contrast bolus in most patients were very much shorter, in the order of 2 – 6 cm. The irregular winding course of the vessel must be measured accurately and in it's entirety to obtain the true distance travelled by the contrast medium. This was seldom achieved by a single straight line but was closely approximated by summing multiple, short segments that paralleled the axis of the curving vessel. In order to calculate the flow rates from velocity figures, an accurate measurement of the vessel diameter is required. This is subject to considerable greater error because of the smaller size relative to the number of pixels. In addition, these vessels were often not completely in-plane, making the measured distances travelled by the contrast bolus increasingly inaccurate. As shown using the phantom at increasing angles from the horizontal, flow rates measured showed a cosine drop-off from the true flow rate values so non-parallel vessels will show reduced velocities. Biplanar imaging could improve the accuracy in measuring the distance travelled by the contrast bolus by allowing a three-dimensional image of the course travelled by the vessel concerned. This would in turn improve the accuracy of calculated RFRDSA velocities. This was not possible due to hardware and software limitations in the system used. A single injection and a single projection only were used in an effort to minimise radiation dose to the patient and because time-density curves could be created from only a single plane on the angiogram machine used. The frontal projection was chosen because the MCA has as near in-plane course as possible on this view. Hawkes *et al.* (Hawkes, 1994) describe a technique that allows the measurement of the three-dimensional path length of vascular segments with a minimal error of between 1.3 – 1.6%. This uses a rapid frame rate of 25 frames sec^{-1} in one plane but a standard frame rate of only 2

frames sec^{-1} in an orthogonal plane. The use of this technique would limit the radiation dose to patients to an acceptable level but would allow a more accurate measurement of the distance travelled by the contrast bolus.

There is a trade-off between maximum measurable blood velocity, vessel path length and frame rate. To be able to measure velocity using RFRDSA, the contrast bolus must be visible on the imaging screen on two consecutive frames. At 30 frames sec^{-1} using a magnification factor of 1, the maximum measurable velocity is therefore equal to the image diameter divided by the frame period. With an image diameter of 25cm, this gives a maximum measurable velocity of 750 cm sec^{-1}. In the phantom experiments, using a 'vessel' of 2.75mm diameter, this velocity equates to a maximum measurable flow of 44 ml sec^{-1}. To avoid pincushion effects, the distance measured should be limited to the middle third of the image, giving a maximum flow of 15 ml sec^{-1} or velocity of 250 cm sec^{-1}. Accurate measurement of velocities of this magnitude would appear to be adequate for most AVMs. In the AVMs studied, the maximum velocity measured by TCD was 160 cm sec^{-1} (Patient 3, R ICA).

Seifalian *et al.* (Seifalian, 1989) compared true mean and measured mean velocities calculated from bolus mass tracking and matching contrast concentration profiles methods. The first method showed fair agreement between the true and measured mean values at low velocities up to 15 cm sec^{-1} but it underestimated higher velocities (up to 35 cm sec^{-1}). This was felt to be due to the fact that a finite maximal length of blood vessel is visible within an image at any one particular magnification. This limits the maximum velocity, or distance travelled by the bolus, which can be measured at a specific frame rate. They suggested that if the window were reduced in size to detect higher velocities, then the statistical error in the calculated velocities would increase significantly. The second method did not show this same underestimate of measured velocity when compared with true velocity at higher values. They were able to measure instantaneous velocities of 1 m sec^{-1} using only an 80 mm length of vessel at 25 frames sec^{-1} (Hawkes, 1994). Using this

method of analysis, a frame-to-frame overlap of only approximately 50% is needed to provide adequate data to match distance concentration functions. At extremely high velocities however, similar limitations to this technique are seen. Despite using the contrast concentration profile method, Seifalian *et al.* (Seifalian, 1991) demonstrated a systematic fall in the measured velocities as the length of 'vessel' analysed was reduced. When peak flow along a vessel was greater than about half of the length of the vessel segment analysed per frame interval, then the tracking algorithm failed. Even at velocities of only 30 cm sec^{-1}, the accuracy of the measured values decreased as the length of 'vessel' analysed was reduced from 200 to 20mm. The RFRDSA used in this study showed similar limitations which were compounded in the clinical situation by considerably shorter lengths of vessels. In the best situation of ICA measurements in patient 4 with a vessel length of 75mm and an average diameter of 4mm, the maximum measurable velocity were 250 cm sec^{-1} and 31 ml sec^{-1} respectively. Whilst in the worst situation of MCA measurements in patient 4 with a vessel length of 12mm and an average diameter of 1.7mm, the maximum measurable velocity and flow were 36 cm sec^{-1} and 1 ml sec^{-1} respectively. These values are clearly not adequate to evaluate accurately the majority of patients in this study.

In addition to these limitations, there are further inaccuracies due to the smearing effect of a finite pulse width of Xray acquisitions. This means that the leading edge of the contrast bolus with respect to time and distance travelled is difficult to define accurately. This effect increases with higher velocities.

7.3.4 Conclusion

RFRDSA, using the described methods, is currently not able to provide accurate absolute flow and velocity values for intracranial vessels. It is likely as a result of the above difficulties that the inaccuracies in measuring velocity in this manner with RFRDSA will increase to a maximum measurable velocity. There are several errors which cause reduction in the measured velocity compared with the

true velocity. Although the results obtained were extremely inaccurate, they were consistent with what is known about the errors involved. Analysis of similar data using the matching of contrast concentration profiles as advocated by Seifalian *et al.* (Seifalian, 1989) and Hoffman *et al.* (Hoffman, 1991) may yield increasingly accurate velocity and flow rates. However, it is unlikely that, at 30 frames sec^{-1}, this will improve significantly as the frame rate resolution appears to be one of the main limiting factors, particularly at high flows and velocities over the short distances and with the narrow vessels involved in the cerebral vasculature. With further work, determination of relative values comparing different vessels may be of use within individual patients and may allow targeting of specific high flow feeders in individuals being treated by endovascular methods.

PART 5

CONCLUSIONS

Chapter 8

CONCLUSIONS AND FUTURE STUDIES

8.1 Structural Imaging

8.1.1 CT and MR angiography

CTA has enormous potential value in the investigation of AVMs, since it is non-invasive and quick to acquire. CTA can be useful in a first level diagnosis, excluding or confirming the presence of an AVM in a suggestive clinical context. When compared with MRA, CTA has advantages in that calcium is easily visualised, bony relationships can be appreciated, there are no flow-related artifacts and it is fast and less costly. However, its disadvantages include the post processing time, the limited volume that can be acquired (important for large AVMs) and that arterial and venous phases are seen together.

At a higher diagnostic level, involving the pre-therapeutic decision–making process, CTA cannot yet replace conventional angiography, but could be used in conjunction with conventional MR and CT images to obtain a 3D volume-rendered display of both the malformation and surrounding normal brain. It could therefore be particularly useful in planning surgical approaches as bone and vessels can be segmented out separately but viewed together. Precise 3D localisation would be helpful for both pre-surgical and pre-radiosurgical evaluation.

3D information about the nidus of AVMs and surrounding structures could have a potentially significant impact on evaluation of the effects of treatment. Based on true volumetric data allowing 3D reconstructions, CTA may have a future role in providing more accurate volume calculations to assess the effects of treatment or as a non-invasive alternative for planning of radiosurgery. For treatment with

radiotherapy, the site of interest must be precisely localised by means of cerebral angiography and meticulous attention given to location and shape of nidus. Definition of the AVM nidus on CTA may decrease the volume of irradiation. In addition, embolisation material is hyperdense on CTA and it may therefore be possible to quantify the volume of AVM treated by endovascular means. As an outpatient procedure it is ideal for monitoring the response of the lesion to surgery or radiotherapy, involving a small radiation dose (less than 1 mSv) compared with DSA (3–4 mSv for a typical four vessel cerebral angiogram). Ultimately CTA may be able to take the place of conventional follow-up angiography with its associated benefits, although further evaluation of CTA in these clinical situations is required (Aoki, 1998).

MR techniques are also non-invasive, have a good safety profile and have the advantage over CT of not involving ionising radiation.

The use of 3D TOF in the evaluation of AVMs is well established, because it has excellent spatial resolution, a high sensitivity and specificity, efficient scan time yielding a favourable signal-to-noise ratio, reduced complex flow signal loss and clearly visible T1–weighted anatomy. It is often performed at the same time as MRI, necessary because it provides useful information regarding the location and topography of the AVM, presence or absence of haemorrhage and associated parenchymal changes such as oedema, ischaemia, gliosis, atrophy or mass effect. This information is essential for planning the angiographic work-up and correlative analysis of the angiographic information. The use of gadolinium-based contrast agents is being increasingly used to improve signal-to-noise ratio and to limit the effects that slow or turbulent flow have on the visualisation of AVMs, as demonstrated in this study (Runge, 1993).

The primary limitation of 3D CEMRA is the k space acquisition speed and thus the achievable image resolution during the time limited first pass of contrast media. In this study, temporal resolution was not sufficient to allow a 3D representation of separate arterial and venous phases of AVM flow, but the use of

gadolinium meant that AVM angio-architecture was better visualised than on pre-contrast 3D TOF images.

DSA is currently assumed to be the 'gold standard' investigation in AVM patients. However, there may be considerable interobserver variability in the assessment of DSAs which was not addressed in these studies and should be investigated. These study designs could be improved further by having a second radiologist review the DSA films and a second consensus opinion reached.

Both studies considered a relatively small group of patients which were highly selected. In particular, many of the patients investigated had been or were due to be treated by endovascular methods. This meant that the kappa statistic had its limitations and did not always accurately reflect the degree of agreement between images. This could be improved by studying a larger group of patients who are due to be treated in a variety of ways.

One of the particular problems encountered in both the CTA and MRA studies was the lack of temporal resolution afforded by these imaging techniques. CTA currently has heat loading limitations (Brant-Zawadzki and Heiserman, 1997). As a result protocols presently in use for CTA require data acquisition times in the order of 30-60 sec to provide adequate z-axis coverage. This leads to the inclusion of both arterial and venous structures in the data, which can be problematic in accurate interpretation of these studies. However the advent of multi-slice CT will allow faster CT scans and better temporal resolution when several volumes may be acquired during a single contrast injection, the volume acquisitions being timed to coincide with arterial or venous phases as in conventional angiography (Rubin, 1999). Further improvements in MR hardware and software will certainly improve the quality of dynamic MRA studies using intravenous contrast injections and will allow the study of large AVMs. There will however always be a trade off between area coverage, spatial resolution and temporal resolution. It remains to be seen whether 2D techniques with a high temporal resolution approaching that of DSA or

3D techniques just able to resolve arterial and venous phases will be the future of MRA use in AVMs. All of these methods will require careful scrutiny.

8.1.2 MR nidal volumes

MRI appears to allow an improvement on the quantification of AVM nidal volume over the currently acceptable methods of the largest orthogonal measurement or an ellipsoid approximation from DSA. It would be expected that MR images are likely to be more accurate than these alternative methods due to their cross-sectional nature. Of the three MR sequences analysed, it was the pre-contrast TOF images that agreed most closely with those volumes calculated from DSA. However, the use of MR in this way may be limited by the large discrepancy in the volumes generated from MR and DSA.

In addition, there was a large interobserver variability in volumes generated from the MR sequences, but not from DSA. Further experience needs to be gained by observers in calculating AVM nidal volumes from MRI. It can be expected that with experience the variation in nidal volumes calculated by different observers would become more consistent decreasing the interobserver variability. The use of only experienced observers in generating AVM nidal volumes from MR may prevent this from being a major limitation and may improve interobserver variability significantly. At this stage, with few radiosurgical follow-up studies based on MR localisation, the need to include certain vascular aspects, such as draining veins or feeding arteries, in the irradiated field is unknown.

Although AVM nidal volumes generated from DSA are regarded as the 'gold standard', it is difficult to know how precise these volumes actually are. Further phantom work using DSA and MR may allow a more accurate assessment of the limitations of both DSA and MR as techniques to quantify volumes. This may also allow the optimum MR sequence for assessing AVM nidal volume to be determined. With the advent of 3D DSA, accuracy may be improved still further, although a high

temporal resolution, which is one of the advantages of 2D DSA, is lost with 3D DSA and this may represent a limiting factor.

8.2 Perfusion imaging

The use of CBT to evaluate the haemodynamic effects of AVMs shows potential. Further work is required to evaluate the technique fully, but this study showed useful preliminary findings. It appears able to demonstrate relative differences in the haemodynamic parameters, CBF, CBV, MTT and TTM. In particular, it was able to demonstrate appropriate differences in distant grey and white matter as well as those effects seen within the nidus itself. The 'blooming' effect caused by the high CBV in the nidus is a major drawback in the current study, and future work using smaller doses of gadolinium may reduce these effects. AVMs have specific problems with their associated large draining veins, which may mask haemodynamic effects in the innermost perinidal regions. The post-processing techniques require further work in order to eliminate some of these effects.

Gradient-echo EPI was used in this study as the signal-to-noise ratio is better and imaging is faster, however spin-echo EPI could have been used as an alternative. The 'blooming' effect may be reduced by using a spin-echo EPI sequence instead of a gradient-echo EPI sequence, as the susceptibility effect from large vessels is less pronounced with the former. Spin-echo EPI tends to remove the effects of larger vessels and may therefore be more effective at looking at the effect AVMs have haemodynamically at capillary level.

The results of this study do not show any immutable evidence for 'steal', diaschisis or venous hypertension, but in selected individuals there is a suggestion that CBT may be useful in confirming or refuting these diagnoses. Further examination with CBT of a selected group of patients with progressive neurological symptoms may allow firmer conclusions to be drawn. A combined study using

CBT and PET studies of CBF, CBV and regional cerebral metabolic rates in these patients may also improve our understanding of the haemodynamic effects of AVMs.

Currently CBT has the major disadvantage of being only semi-quantitative and is a relatively crude tool when used to examine the haemodynamic effects of cerebral AVMs. The reproducibility of the technique needs to be evaluated further with repeated examinations within one individual. If the technique were reproducible, comparison of repeated examinations in one individual would allow an assessment of the effects of intervention, such as endovascular embolisation, on cerebral haemodynamics. With further refinement of quantification, it would be valuable to assess how different nidal features, such as the presence of direct intranidal fistulae, influence these haemodynamic parameters.

8.3 Haemodynamic imaging

Further geometric studies are needed to investigate the effect on velocity and flow of 2D imaging of oblique vessels not lying in plane. It is possible, with slight modifications to the hardware, to have synchronous ECG monitoring which is projected on to the RFRDSA images. This would allow some idea of the point in the cardiac cycle at which the bolus passes through the intracranial vessels, allowing a more meaningful correlation with velocities determined by TCD.

The ability to use higher frame rates would also increase accuracy although this is at the expense of increasing radiation dose to patients. The hardware described in these experiments is unable to image at higher frame rates and this would therefore not possible with the current set-up. In addition the reduction in signal-to-noise ratio at the high frame rates may introduce other errors.

The low resistance of the AVM nidus clearly results in increased velocity within the feeding vessels as demonstrated by TCD. These values however cannot be replicated with RFRDSA using the described methods. Many of the sources of

error are inherent in the technique. Even with a concerted effort at reducing the many inaccuracies present, it is unlikely that this method will ever provide accurate absolute flow and velocity values for intracranial vessels in the clinical setting of AVMs. It seems that a completely different approach to measuring velocity is required.

8.4 Conclusion

Much work remains to be done, but currently the temporal resolution afforded by these newer structural and haemodynamic imaging techniques is not adequate for accurate evaluation of high flow lesions such as AVMs. Improvements in hardware such as stronger gradients in MRI and multi-slice CT scanners may allow further progress to be made.

BIBLIOGRAPHY

al-Rodhan NR, Sundt TM, Jr., Piepgras DG, Nichols DA, Rufenacht D, Stevens LN. Occlusive hyperemia: a theory for the hemodynamic complications following resection of intracerebral arteriovenous malformations. *J Neurosurg* 1993; 78(2): 167-75.

Al-Shahi R, Pal N, Bhattacharya J, Clifton A, Gholkar A, Halpin S, Lewis S, Millar J, Molyneux A, Sellar R. Do neuroradiologists agree about the angioarchitecture of arteriovenous malformations of the brain? An inter- and intraobserver variability study of angiogram interpretation. British Society of Neuroradiologists, Harrogate, 2001.

Albert P, Salgado H, Polaina M, Trujillo F, Ponce de Leon A, Durand F. A study on the venous drainage of 150 cerebral arteriovenous malformations as related to haemorrhagic risks and size of the lesion. *Acta Neurochir* 1990; 103(1-2): 30-4.

Altman DG. Practical Statistics for Medical Research (1 ed). London: Chapman and Hall, 1991.

Aoki S, Sasaki Y, Machida T, Hayashi N, Shirouzu I, Ohkubo T, Terahara A, Sasaki Y, Kawamoto S, Araki T, Maehara T. 3D-CT angiography of cerebral arteriovenous malformations. *Radiat Med* 1998; 16(4): 263-71.

Barnett GH, Little JR, Ebrahim ZY, Jones SC, Friel HT. Cerebral circulation during arteriovenous malformation operation. *Neurosurgery* 1987; 20(6): 836-42.

Batjer HH, Devous MD, Sr., Meyer YJ, Purdy PD, Samson DS. Cerebrovascular hemodynamics in arteriovenous malformation complicated by normal perfusion pressure breakthrough. *Neurosurgery* 1988; 22(3): 503-9.

Beltramello A. Motor cortex activation in a patient with arteriovenous angioma in the left region. *Int Neuroradiol* 1996; 2: 155-6.

Bendszus M, Koltzenburg M, Burger R, Warmuth-Metz M, Hofmann E, Solymosi L. Silent embolism in diagnostic cerebral angiography and neurointerventional procedures: a propsective study. *Lancet* 1999; 354: 1594-7.

Berenstein A, Lasjaunias P. Classification of Brain Arteriovenous Malformations. In: Berenstein A, Lasjaunias P, eds. Endovascular treatment of cerebral lesions. Surgical Neuroangiography; vol 4 (1 ed). Berlin: Springer-Verlag, 1992: 1-88.

Bland JM, Altman DG. Statistical methods for assessing agreement between two methods of clinical measurement. *Lancet* 1986; 1(8476): 307-10.

Bongartz GM, Boos M, Winter K, Ott H, Scheffler K, Steinbrich W. Clinical utility of contrast-enhanced MR angiography. *Eur Radiol* 1997; 7(Suppl 5): 178-86.

Brant-Zawadzki M, Heiserman JE. The roles of MR angiography, CT angiography, and sonography in vascular imaging of the head and neck. *AJNR* 1997; 18(10): 1820-5.

Brown JH, Lustrup ES, Ley MH, Ogilvy CS, Taveras JM. Reduction of aneurysm clip artifacts on CT angiograms: A technical note. *AJNR* 1999; 20: 694-6.
Brown RD, Jr., Wiebers DO, Forbes G, O'Fallon WM, Piepgras DG, Marsh WR, Maciunas RJ. The natural history of unruptured intracranial arteriovenous malformations. *J Neurosurg* 1988; 68(3): 352-7.

Brown RD, Jr., Wiebers DO, Torner JC, O'Fallon WM. Frequency of intracranial hemorrhage as a presenting symptom and subtype analysis: a population-based study of intracranial vascular malformations in Olmsted Country, Minnesota. *J Neurosurg* 1996; 85(1): 29-32.

Calamante F, Thomas DL, Pell GS, Wiersma J, Turner R. Measuring cerebral blood flow using magnetic resonance imaging techniques. *J Cereb Blood Flow Metab* 1999; 19: 701-35.

Calamante F, Gadian DG, Connelly A. Quantification of perfusion using bolus tracking magnetic resonance imaging in stroke. *Stroke* 2002; 33: 1146-51.

Cook MJ, Fish DR, Shorvon SD, Straughan K, Stevens JM. Hippocampal volumetric and morphometric studies in frontal and temporal lobe epilepsy. *Brain* 1992; 115: 1001-15.

Costello P, Gaa J. Spiral CT angiography of abdominal aortic aneurysms. *Radiographics* 1995; 15(2): 397-406.

Crawford PM, West CR, Chadwick DW, Shaw MD. Arteriovenous malformations of the brain: natural history in unoperated patients. *J Neurol Neurosurg Psych* 1986a; 49(1): 1-10.

Crawford PM, West CR, Shaw MD, Chadwick DW. Cerebral arteriovenous malformations and epilepsy: factors in the development of epilepsy. *Epilepsia* 1986b; 27(3): 270-5.

Crowell RM. Aneurysms and arteriovenous malformations. *Neurol Clin* 1985; 3(2): 291-312.

Cunha e Sa MJ, Stein BM, Solomon RA, McCormick PC. The treatment of associated intracranial aneurysms and arteriovenous malformations. *J Neurosurg* 1992; 77(6): 853-9.

Dandy W. Venous abnormalities and angiomas of the brain. *Arch Surg* 1928; 17: 715-93.

Dembo M. Arteriovenous malformations of the brain: a review of the literature since 1960. *Arch Phys Med Rehabil* 1982; 63(11): 565-8.

Deruty R, Pelissou-Guyotat I, Amat D, Mottolese C, Bascoulergue Y, Turjman F, Gerard JP. Complications after multidisciplinary treatment of cerebral arteriovenous malformations. *Acta Neurochir* 1996; 138(2): 119-31.

Deshpande DH, Vidyasagar C. Histology of the persistent embryonic veins in arteriovenous malformations of brain. *Acta Neurochir* 1980; 53(3-4): 227-36.

Deutsch G. Blood flow changes in arteriovenous malformations during behavioural activation. *Ann Neurol* 1983; 13: 38-43.

Dion JE, Mathis JM. Cranial arteriovenous malformations. The role of embolization and stereotactic surgery. *Neurosurg Clin N Am* 1994; 5(3): 459-74.
Drake CG. Cerebral arteriovenous malformations: considerations for and experience with surgical treatment in 166 cases. *Clin Neurosurg* 1979; 26: 145-208.

Duong DH, Young WL, Vang MC, Sciacca RR, Mast H, Koennecke HC, Hartmann A, Joshi S, Mohr JP, Pile-Spellman J. Feeding artery pressure and venous drainage pattern are primary determinants of hemorrhage from cerebral arteriovenous malformations. *Stroke* 1998; 29(6): 1167-76.

Feindel W, Yamamoto YL, Hodge CP. Red cerebral veins and the cerebral steal syndrome. Evidence from fluorescein angiography and microregional blood flow by radioisotopes during excision of an angioma. *J Neurosurg* 1971; 35(2): 167-79.

Fink GR. Effects of cerebral angiomas on perifocal and remote tissue: a multivariate positron emission tomography study. *Stroke* 1992; 23(8): 1099-105.

Fleischer LH, Young WL, Pile-Spellman J, terPenning B, Kader A, Stein BM, Mohr JP. Relationship of transcranial doppler flow velocities and arteriovenous malformation feeding artery pressures. *Stroke* 1993; 24(12): 1897-902.

Forbes G, Gray JE, Felmlee JP. Phantom testing of peripheral artery absolute blood flow measurement with digital arteriography. *Invest Radiol* 1985; 20(2): 186-92.

Gallina P, Merienne L, Meder JF, Schlienger M, Lefkopoulos D, Merland JJ. Failure in radiosurgery treatment of cerebral arteriovenous malformations. *Neurosurgery* 1998; 42(5): 996-1002; discussion 2-4.

Gorzer H, Heimberger K, Schindler E. Spiral CT angiography with digital subtraction of extra- and intracranial vessels. *J Comput Assist Tomogr* 1994; 18(5): 839-41.

Graf CJ, Perret GE, Torner JC. Bleeding from cerebral arteriovenous malformations as part of their natural history. *J Neurosurg* 1983; 58(3): 331-7.

Guidetti B, Delitala A. Intracranial arteriovenous malformations. Conservative and surgical treatment. *J Neurosurg* 1980; 53(2): 149-52.

Guterman LR, Standard SC, Ahuja A, Hopkins LN. Vascular and endovascular neurosurgery. *Curr Opin Neurol* 1993; 6(6): 854-9.

Hacein-Bey L, Nour R, Pile-Spellman J, Van Heertum R, Esser PD, Young WL. Adaptive changes of autoregulation in chronic cerebral hypotension with arteriovenous malformations: an acetazolamide-enhanced single-photon emission CT study. *AJNR* 1995; 16(9): 1865-74.

Handa T, Negoro M, Miyachi S, Sugita K. Evaluation of pressure changes in feeding arteries during embolization of intracerebral arteriovenous malformations. *J Neurosurg* 1993; 79(3): 383-9.

Harrison MJ, Johnson BA, Gardner GM, Welling BG. Preliminary results on the management of unruptured intracranial aneurysms with magnetic resonance angiography and computed tomographic angiography. *Neurosurgery* 1997; 40(5): 947-55; discussion 5-7.

Hartmann A, Mast H, Mohr JP, Koennecke HC, Osipov A, Pile-Spellman J, Duong DH, Young WL. Morbidity of intracranial hemorrhage in patients with cerebral arteriovenous malformation. *Stroke* 1998; 29(5): 931-4.

Hassler W, Steinmetz H. Cerebral hemodynamics in angioma patients: an intraoperative study. *J Neurosurg* 1987; 67(6): 822-31.

Hawkes DJ, Seifalian AM, Colchester ACF, Iqbal N, Hardingham CR, Bladin CF, Hobbs KEF. Validation of volume blood flow measurements using three-dimensional distance-concentration functions derived from digital x-ray angiograms. *Invest Radiol* 1994; 29(4): 434-42.

Heiserman JE, Dean BL, Hodak JA, Flom RA, Bird CR, Drayer BP, Fram EK. Neurologic complications of cerebral angiography. *AJNR* 1994; 15(8): 1401-7; discussion 8-11.

Heros RC, Morcos J, Korosue K. Arteriovenous malformations of the brain. Surgical management. *Clin Neurosurg* 1993; 40: 139-73.

Hoffman KR, Doi K, Fencil LE. Determination of instantaneous and average blood flow rates from digital angiograms of vessel phantoms using distance-density curves. *Invest Radiol* 1991; 26: 207-12.

Homan RW, Devous MD, Sr., Stokely EM, Bonte FJ. Quantification of intracerebral steal in patients with arteriovenous malformation. *Arch Neurol* 1986; 43(8): 779-85.

Huston JD, Rufenacht DA, Ehman RL, Wiebers DO. Intracranial aneurysms and vascular malformations: comparison of time-of-flight and phase-contrast MR angiography. *Radiology* 1991; 181(3): 721-30.

Iizuka H, Sakatani K, Young W. Neural damage in the rat thalamus after cortical infarcts. *Stroke* 1990; 21(5): 790-4.

Itoyama Y, Uemura S, Ushio Y, Kuratsu J, Nonaka N, Wada H, Sano Y, Fukumura A, Yoshida K, Yano T. Natural course of unoperated intracranial arteriovenous malformations: study of 50 cases. *J Neurosurg* 1989; 71(6): 805-9.

Kader A, Young WL. The effects of intracranial arteriovenous malformations on cerebral hemodynamics. *Neurosurg Clin N Am* 1996; 7(4): 767-81.

Kader A, Young WL, Pile-Spellman J, Mast H, Sciacca RR, Mohr JP, Stein BM. The influence of hemodynamic and anatomic factors on hemorrhage from cerebral arteriovenous malformations. *Neurosurgery* 1994; 34(5): 801-7; discussion 7-8.

Kalimo H, Kaste M, Hatia M. Vascular diseases. In: Graham DL, Lantos PL, eds. Greenfield's Neuropathology, vol 1 (6 ed). New York: Oxford University Press, 1997: 313-95

Kanematsu M, Imaeda T, Mizuno S, Yamawaki Y, Sone Y, Iida T, Kato M, Yokoyama R. Value of three-dimensional spiral CT hepatic angiography. *AJR* 1996; 166(3): 585-91.

Kashitani N, Kimoto S, Tsunoda M, Ito T, Tsuji T, Ono A, Hiraki Y. Portal blood flow in the presence or absence of diffuse liver disease: measurement by phase contrast MR imaging. *Abdom Imaging* 1995; 20(3): 197-200.

Kondziolka D, Lunsford LD, Kanal E, Talagala L. Stereotactic magnetic resonance angiography for targeting in arteriovenous malformation radiosurgery. *Neurosurgery* 1994; 35(4): 585-90; discussion 90-1.

Konno S, Numaguchi Y, Shrier DA, Qian J, Sinkin RA. Unusual manifestation of a vein of Galen malformation: value of CT angiography. *AJNR* 1996; 17(8): 1423-6.

Kucharczyk J, Vexler ZS, Roberts TP, Asgari HS, Mintorovitch J, Derugin N, Watson AD, Moseley ME. Echo-planar perfusion-sensitive MR imaging of acute cerebral ischemia. *Radiology* 1993; 188(3): 711-7.

Kuo PC, Li K, Alfrey EJ, Jeffrey RB, Garcia G, Dafoe DC. Magnetic resonance imaging and hepatic hemodynamics: correlation with metabolic function in liver transplantation candidates. *Surgery* 1995; 117(4): 373-9.

Lanzino G, Kaptain G, Kallmes DF, Dix JE, Kassell NF. Intracranial dissecting aneurysm causing subarachnoid hemorrhage: the role of computerized tomographic angiography and magnetic resonance angiography. *Surg Neurol* 1997; 48(5): 477-81.

Lasjaunias P, Piske R, Terbrugge K, Willinsky R. Cerebral arteriovenous malformations (C. AVM) and associated arterial aneurysms (AA). Analysis of 101 C. AVM cases, with 37 AA in 23 patients. *Acta Neurochir* 1988; 91(1-2): 29-36.

Le Roux PD, Dailey AT, Newell DW, Grady MS, Winn HR. Emergent aneurysm clipping without angiography in the moribund patient with intracerebral hemorrhage: the use of infusion computed tomography scans. *Neurosurgery* 1993; 33(2): 189-97; discussion 97.

Leblanc R, Little JR. Hemodynamics of arteriovenous malformations. *Clin Neurosurg* 1990; 36: 299-317.

Leenders KL, Perani D, Lammertsma AA, Heather JD, Buckingham P, Healy MJ, Gibbs JM, Wise RJ, Hatazawa J, Herold S. Cerebral blood flow, blood volume and oxygen utilization. Normal values and effect of age. *Brain* 1990; 113(Pt 1): 27-47.

Luessenhop AJ, Rosa L. Cerebral arteriovenous malformations. Indications for and results of surgery, and the role of intravascular techniques. *J Neurosurg* 1984; 60(1): 14-22.

Lunsford LD, Kondziolka D, Flickinger JC, Bissonette DJ, Jungreis CA, Maitz AH, Horton JA, Coffey RJ. Stereotactic radiosurgery for arteriovenous malformations of the brain. *J Neurosurg* 1991; 75(4): 512-24.

Mani RL, Eisenberg RL, McDonald EJ, Jr., Pollock JA, Mani JR. Complications of catheter cerebral arteriography: analysis of 5,000 procedures. I. Criteria and incidence. *AJR* 1978; 131(5): 861-5.

Mansmann U, Meisel J, Brock M, Rodesch G, Alvarez H, Lasjaunias P. Factors associated with intracranial hemorrhage in cases of cerebral arteriovenous malformation. *Neurosurgery* 2000; 46(2): 272-9; discussion 79-81.

Mast H, Mohr JP, Osipov A, Pile-Spellman J, Marshall RS, Lazar RM, Stein BM, Young WL. 'Steal' is an unestablished mechanism for the clinical presentation of cerebral arteriovenous malformations. *Stroke* 1995; 26(7): 1215-20.

McCormick WF. The pathology of vascular ("arteriovenous") malformations. *J Neurosurg* 1966; 24(4): 807-16.

McNulty V, Cruz-Orive LM, Roberts N, Holmes CJ, Gual-Arnau X. Estimation of brain compartment volume from MR Cavalieri slices. *J Comput Assist Tomogr* 2000; 24(3): 466-77.

Meyer JS. Does diaschisis have clinical correlates? *Mayo Clin Proc* 1991; 66: 430-2.
Michelson WJ. Natural history and pathophysiology of arteriovenous malformations. *Clin Neurosurg* 1979; 26: 307-131.

Miyasaka K, Wolpert SM, Prager RJ. The association of cerebral aneurysms, infundibula, and intracranial arteriovenous malformations. *Stroke* 1982; 13(2): 196-203.

Miyasaka Y, Yada K, Kurata A, Tokiwa K, Irikura K, Tanaka R, Ohwada T, Kitahara T. Correlation between intravascular pressure and risk of hemorrhage due to arteriovenous malformations. *Surg Neurol* 1993; 39(5): 370-3.

Miyasaka Y, Yada K, Ohwada T, Kitahara T, Endoh M, Saito M, Kurata A, Ohtaka H. Retrograde thrombosis of fedding arteries after removal of arteriovenous malformations. *J Neurosurg* 1990; 72: 540-5.

Miyasaka Y, Yada K, Ohwada T, Kitahara T, Kurata A, Irikura K. An analysis of the venous drainage system as a factor in hemorrhage from arteriovenous malformations. *J Neurosurg* 1992; 76(2): 239-43.

Moniz E. L'Angiographie Cérébrale. Masson, 1934.

Morgan MK, Johnston IH, Hallinan JM, Weber NC. Complications of surgery for arteriovenous malformations of the brain. *J Neurosurg* 1993; 78(2): 176-82.

Morgan MK, Sundt TM, Jr. The case against staged operative resection of cerebral arteriovenous malformations. *Neurosurgery* 1989; 25(3): 429-35; discussion 35-6.

Moseley ME, Mintorovitch J, Cohen Y, Asgari HS, Derugin N, Norman D, Kucharczyk J. Early detection of ischemic injury: comparison of spectroscopy, diffusion-, T2-, and magnetic susceptibility-weighted MRI in cats. *Acta Neurochir Suppl* 1990; 51: 207-9.

Mullan S, Mojtahedi S, Johnson DL, Macdonald RL. Embryological basis of some aspects of cerebral vascular fistulas and malformations. *J Neurosurg* 1996; 85(1): 1-8.

Murayama Y, Massoud TF, Vinuela F. Hemodynamic changes in arterial feeders and draining veins during embolotherapy of arteriovenous malformations: an experimental study in a swine model. *Neurosurgery* 1998; 43(1): 96-104; discussion 4-6.

Noorbehesht B, Fabrikant JI, Enzmann DR. Size determination of supratentorial arteriovenous malformations by MR, CT and angio. *Neuroradiology* 1987; 29(6): 512-8.

Norlen G. Arteriovenous malformations of the brain: report of ten cases of total removal of the lesion. *J Neurosurg* 1949; 6: 475-94.

Nornes H, Grip A. Hemodynamic aspects of cerebral arteriovenous malformations. *J Neurosurg* 1980; 53(4): 456-64.

Nussbaum ES, Heros RC, Madison MT, Awasthi D, Truwit CL. The pathogenesis of arteriovenous malformations: insights provided by a case of multiple arteriovenous malformations developing in relation to a developmental venous anomaly. *Neurosurgery* 1998; 43(2): 347-51; discussion 51-2.

Okabe T, Meyer JS, Okayasu H, Harper R, Rose J, Grossman RG, Centeno R, Tachibana H, Lee YY. Xenon-enhanced CT CBF measurements in cerebral AVM's before and after excision. Contribution to pathogenesis and treatment. *J Neurosurg* 1983; 59(1): 21-31.

Ondra SL, Troupp H, George ED, Schwab K. The natural history of symptomatic arteriovenous malformations of the brain: a 24-year follow-up assessment. *J Neurosurg* 1990; 73(3): 387-91.

Parker DL, Tsuruda JS, Goodrich KC, Alexander AL, Buswell HR. Contrast-enhanced magnetic resonance angiography of cerebral arteries. A review. *Invest Radiol* 1998; 33(9): 560-72.

Parkinson D, Bachers G. Arteriovenous malformations. Summary of 100 consecutive supratentorial cases. *J Neurosurg* 1980; 53(3): 285-99.

Pernicone JR, Siebert JE, Cooper TG, Potchen MJ. Magnetic resonance angiography. In: Grainger RG, Allison DJ, eds. Diagnostic Imaging in Radiology, vol 3 (3 ed). New York: Churchill Livingstone, 1997: 2410-23.

Perret G, Nishioka H. Report on the cooperative study of intracranial aneurysms and subarachnoid hemorrhage. IV. Cerebral angiography. An analysis of the diagnostic value and complications of carotid and vertebral angiography in 5,484 patients. *J Neurosurg* 1966a; 25(1): 98-114.

Perret G, Nishioka H. Report on the cooperative study of intracranial aneurysms and subarachnoid hemorrhage. Section VI. Arteriovenous malformations. An analysis of 545 cases of cranio-cerebral arteriovenous malformations and fistulae reported to the cooperative study. *J Neurosurg* 1966b; 25(4): 467-90.

Petereit D, Mehta M, Turski P, Levin A, Strother C, Mistretta C, Mackie R, Gehring M, Kubsad S, Kinsella T. Treatment of arteriovenous malformations with stereotactic radiosurgery employing both magnetic resonance angiography and standard angiography as a database. *Int J Radiat Oncol Biol Phys* 1993; 25(2): 309-13.

Pollock BE, Flickinger JC, Lunsford LD, Bissonette DJ, Kondziolka D. Factors that predict the bleeding risk of cerebral arteriovenous malformations. *Stroke* 1996a; 27(1): 1-6.

Pollock BE, Kondziolka D, Flickinger JC, Patel AK, Bissonette DJ, Lunsford LD. Magnetic resonance imaging: an accurate method to evaluate arteriovenous malformations after stereotactic radiosurgery. *J Neurosurg* 1996b; 85(6): 1044-9.

Pollock BE, Kondziolka D, Lunsford LD, Bissonette D, Flickinger JC. Repeat stereotactic radiosurgery of arteriovenous malformations: factors associated with incomplete obliteration. *Neurosurgery* 1996c; 38(2): 318-24.

Pott M, Huber M, Assheuer J, Bewermeyer H. Comparison of MRI, CT and angiography in cerebral arteriovenous malformations. *Bildgebung* 1992; 59(2): 98-102.

Prohovnik I, Huang J, Young WL, Stein B, Stoddart HA. Simultaneous SPECT CBF/CBV imaging with imperfect energy resolution. *J Cereb Blood Flow Metab* 1993; 13(Suppl 1): S321.

Rieger J, Hosten N, Neumann K, Langer R, Molsen P, Lanksch WR, Pfeifer KJ, Felix R. Initial clinical experience with spiral CT and 3D arterial reconstruction in intracranial aneurysms and arteriovenous malformations. *Neuroradiology* 1996; 38(3): 245-51.

Rubin GD, Dake MD, Napel S, Jeffrey RB, Jr., McDonnell CH, Sommer FG, Wexler L, Williams DM. Spiral CT of renal artery stenosis: comparison of three-dimensional rendering techniques. *Radiology* 1994; 190(1): 181-9.

Rubin GD, Dake MD, Semba CP. Current status of three-dimensional spiral CT scanning for imaging the vasculature. *Radiol Clin North Am* 1995; 33(1): 51-70.

Rubin GD, Shiau MC, Schmidt AJ, Fleischmann D, Logan L, Leung AN, Jeffrey RB, Napel S. Computed tomographic angiography: Historical perspective and new state-of-the-art using multi detector-row helical computed tomography. *J Comput Assist Tomogr* 1999; 23 (Suppl 1): S83-90.

Runge VM, Kirsch JE, Lee C. Contrast-enhanced MR angiography. *J Magn Reson Imaging* 1993; 3(1): 233-9.

Schlosser MJ, McCarthy G, Fulbright RK, Gore JC, Awad IA. Cerebral vascular malformations adjacent to sensorimotor and visual cortex. Functional magnetic resonance imaging studies before and after therapeutic intervention. *Stroke* 1997; 28(6): 1130-7.

Schreiber WG, Guckel F, Stritzke P, Schmiedek P, Schwartz A, Brix G. Cerebral blood flow and cerebrovascular reserve capacity: estimation by dynamic magnetic resonance imaging. *J Cereb Blood Flow Metab* 1998; 18(10): 1143-56.

Schwartz RB. Neuroradiological applications of spiral CT. *Semin Ultrasound CT MR* 1994; 15(2): 139-47.

Seifalian AM, Hawkes DJ, Colchester ACF, Hobbs KEF. A new algorithm for deriving pulsatile blood flow waveforms tested using simulated dynamic angiographic data. *Neuroradiology* 1989; 31: 263-9.

Seifalian AM, Hawkes DJ, Hardingham CR, Colchester AC, Reidy JF. Validation of a quantitative radiographic technique to estimate pulsatile blood flow waveforms using digital subtraction angiographic data. *J Biomed Eng* 1991; 13(3): 225-33.

Silverman NR and Rosen L. Arterial blood flow measurement: Assessment of velocity estimation methods. *Invest Radiol* 1977; 12(4): 319-24.

Sorimachi T, Takeuchi S, Koike T, Minakawa T, Abe H, Tanaka R. Blood pressure monitoring in feeding arteries of cerebral arteriovenous malformations during embolization: a preventive role in hemodynamic complications. *Neurosurgery* 1995; 37(6): 1041-7; discussion 7-8.

Spetzler RF, Hargraves RW, McCormick PW, Zabramski JM, Flom RA, Zimmerman RS. Relationship of perfusion pressure and size to risk of hemorrhage from arteriovenous malformations. *J Neurosurg* 1992; 76(6): 918-23.

Spetzler RF, Martin NA. A proposed grading system for arteriovenous malformations. *J Neurosurg* 1986; 65(4): 476-83.

Spetzler RF, Wilson CB, Weinstein P, Mehdorn M, Townsend J, Telles D. Normal perfusion pressure breakthrough theory. *Clin Neurosurg* 1978; 25: 651-72.

Stein BM, Kader A. Intracranial arteriovenous malformations. *Clin Neurosurg* 1992; 39: 76-113.

Stein BM, Wolpert SM. Arteriovenous malformations of the brain. I: Current concepts and treatment. *Arch Neurol* 1980; 37(1): 1-5.

Steinheil SO. Über einen Fall von Varix aneurysmaticus im Bereit der Gehirngefäße. Diss, Würzburg 1895. Cited in Dandy W: Venous abnormalities and angiomas of the brain. *Arch Surg* 1928; 17: 715-93.

Sugita M, Takahashi A, Ogawa A, Yoshimoto T. Improvement of cerebral blood flow and clinical symptoms associated with embolization of a large arteriovenous malformation: case report. *Neurosurgery* 1993; 33(4): 748-51; discussion 52.

Swanson DK, Myerowitz PD, Hegge JO, Watson KM. Arterial blood-flow waveform measurements in intact animals: New digital radiographic technique. *Radiology* 1986; 161: 323-8.

Takeuchi S, Kikuchi H, Karasawa J, Naruo Y, Hashimoto K, Nishimura T, Kozuka T, Hayashi M. Cerebral hemodynamics in arteriovenous malformations: evaluation by single-photon emission CT. *AJNR* 1987; 8(2): 193-7.

Tanaka H, Numaguchi Y, Konno S, Shrier DA, Shibata DK, Patel U. Initial experience with helical CT and 3D reconstruction in therapeutic planning of cerebral AVMs: comparison with 3D time-of-flight MRA and digital subtraction angiography. *J Comput Assist Tomogr* 1997; 21(5): 811-7.

Tanaka K, Yonekawa Y, Kaku Y, Kazekawa K. Arteriovenous malformation and diaschisis. *Acta Neurochir* 1993; 120(1-2): 26-32.

Tarr RW, Johnson DW, Rutigliano M, Hecht ST, Pentheny S, Jungreis CA, Horton JA, Yonas H. Use of acetazolamide-challenge xenon CT in the assessment of cerebral blood flow dynamics in patients with arteriovenous malformations. *AJNR* 1990; 11(3): 441-8.

Tenjin H, Asakura F, Nakahara Y, Matsumoto K, Matsuo T, Urano F, Ueda S. Evaluation of intraaneurysmal blood velocity by time-density curve analysis and digital subtraction angiography. *AJNR* 1998; 19(7): 1303-7.

Turjman F, Massoud TF, Vinuela F, Sayre JW, Guglielmi G, Duckwiler G. Correlation of the angioarchitectural features of cerebral arteriovenous malformations with clinical presentation of hemorrhage. *Neurosurgery* 1995; 37(5): 856-60; discussion 60-2.

Tyler JL, Leblanc R, Meyer E, Dagher A, Yamamoto YL, Diksic M, Hakim A. Hemodynamic and metabolic effects of cerebral arteriovenous malformations studied by positron emission tomography. *Stroke* 1989; 20(7): 890-8.

Uematsu H, Yamada H, Sadato N, Muramoto S, Inoue H, Hayashi K, Yonekura Y, Kimura H, Sakuma H, Matsuda T, Hayashi N, Yamamoto K, Ishii Y. Assessment of hepatic portal perfusion using T2 measurements of Gd-DTPA. *J Magn Reson Imaging* 1998; 8(3): 650-4.

Valavanis A. The role of angiography in the evaluation of cerebral vascular malformations. *Neuroimag Clin North Am* 1996; 6(3): 679-704.

Vallee JP, Lazeyras F, Khan HG, Terrier F. Absolute renal blood flow quantification by dynamic MRI and Gd-DTPA. *Eur Radiol* 2000; 10(8): 1245-52.

van Loon JJ, Yousry TA, Fink U, Seelos KC, Reulen HJ, Steiger HJ. Postoperative spiral computed tomography and magnetic resonance angiography after aneurysm clipping with titanium clips. *Neurosurgery* 1997; 41(4): 851-6; discussion 6-7.

Velthuis BK, van Leeuwen MS, Witkamp TD, Boomstra S, Ramos LM, Rinkel GJ. CT angiography: source images and postprocessing techniques in the detection of cerebral aneurysms. *AJR* 1997; 169(5): 1411-7.

Vieco PT, Morin Ed, Gross CE. CT angiography in the examination of patients with aneurysm clips. *AJNR* 1996; 17(3): 455-7.

Viñuela F, Nombela L, Roach MR, Fox AL, Pelz DM. Stenotic and occlusive disease of the venous drainage system of deep brain AVM's. *J Neurosurg* 1985; 63: 180-4.

Virchow R. Die krankhaften Geschwülste. 1863; III: 306-496. Cited in Dandy W: Venous abnormalities and angiomas of the brain. *Arch Surg* 1928; 17: 715-93.

Vonken EJ, van Osch MJ, Bakker CJ, Viergever MA. Measurement of cerebral perfusion with dual-echo multi-slice quantitative dynamic susceptibility contrast MRI. *J Magn Reson Imaging* 1999; 10(2): 109-17.

Wakabayashi S, Ohno K, Shishido T, Tamaki M, Matsushima Y, Hirakawa K. Marked growth of a cerebral arteriovenous malformation: case report and review of the literature. *Neurosurgery* 1991; 29(6): 920-3.

Waugh JR, Sacharias N. Arteriographic complications in the DSA era. *Radiology* 1992; 182(1): 243-6.

Wicky S, Capasso P, Meuli R, Fischer A, von Segesser L, Schnyder P. Spiral CT aortography: an efficient technique for the diagnosis of traumatic aortic injury. *Eur Radiol* 1998; 8(5): 828-33.

Wilkins RH. Natural history of intracranial vascular malformations: a review. *Neurosurgery* 1985; 16(3): 421-30.

Wilson CB, Hieshima G. Occlusive hyperemia: a new way to think about an old problem. *J Neurosurg* 1993; 78(2): 165-6.

Yamada H, Koshimoto Y, Sadato N, Kawashima Y, Tanaka M, Tsuchida C, Maeda M, Yonekura Y, Ishii Y. Crossed cerebellar diaschisis: assessment with dynamic susceptibility contrast MR imaging. *Radiology* 1999; 210(2): 558-62.

Yasargil MG. AVM of the brain, history, embryology, pathological considerations, hemodynamics, diagnostic studies, microsurgical anatomy. In: Yasargil MG, ed. Microneurosurgery; vol IIIA (1 ed). Stuttgart: Georg Thieme Verlag, 1987.

Young N, Dorsch NW, Kingston RJ. Pitfalls in the use of spiral CT for identification of intracranial aneurysms. *Neuroradiology* 1999; 41(2): 93-9.

Young WL, Kader A, Ornstein E, Baker KZ, Ostapkovich N, Pile-Spellman J, Fogarty-Mack P, Stein BM. Cerebral hyperemia after arteriovenous malformation resection is related to "breakthrough" complications but not to feeding artery pressure. The Columbia University arteriovenous malformation study project. *Neurosurgery* 1996; 38(6): 1085-93; discussion 93-5.

Young WL, Kader A, Pile-Spellman J, Ornstein E, Stein BM. Arteriovenous malformation draining vein physiology and determinants of transnidal pressure gradients. The Columbia University AVM study project. *Neurosurgery* 1994; 35(3): 389-95; discussion 95-6.

APPENDICES

APPENDIX 1

A1.1 Statement of originality

This work was carried out between February 1998 and January 2000, during an appointment as a Clinical Research Fellow at The National Hospital for Neurology and Neurosurgery, London, under the supervision of Dr H. Rolf Jäger (Reader in Neuroradiology and Consultant Neuroradiologist, Lysholm Radiological Department) and Mr Neil Kitchen (Consultant Neurosurgeon, Department of Surgical Neurology). All the work described is original and was conducted by myself, except where specifically stated below. No parts of this dissertation have been submitted for a degree or diploma at any other university.

A1.2 Collaboration and assistance

Chapter 3 – CT angiography

The CT Angiograms were analysed by Drs Mike Bynevelt and H. Rolf Jäger. The DSAs were analysed by Dr Wendy Taylor.

Chapter 4 – MR angiography

The MR Angiograms were analysed by Drs H. Rolf Jäger and Phil Rich. The DSAs were analysed by Dr Wendy Taylor.

Chapter 5 – Volumetric analysis of AVM nidus using MRI

The boundaries of the AVM nidus were defined by Drs H. Rolf Jäger, Panos Nikolopoulos and Adam Waldman. The nidal volumes from MR were calculated by Liz Moore.

Chapter 7 – Digital Subtraction Angiography

The home-written fitting programme was written by Liz Moore.

A 1.3 Ethical considerations

The protocols for the studies described in Chapters 3, 4, 5, 6 and 7 were approved by the National Hospital for Neurology and Neurosurgery Research Ethics Committee. The studies were performed with the understanding and written consent of each patient.

A 1.4 Publication

Part of the material in Chapters 3 and 4 has been published in the following articles:

Editorial: Advances in non invasive imaging of intracranial vascular disease.
H.R.Jäger and J.P.Grieve.
Annals of the Royal College of Surgeons of England 2000; 82(1): 1-5.

Robust processing of intracranial CT Angiograms for 3D volume rendering.
E.A.Moore, J.P.Grieve and H.R.Jäger.
European Radiology 2001; 11: 137-141.

APPENDIX 2

Data for Chapter 3 – CT Angiography

Interobserver variability for SSD

Nidus size

	Radiologist B		
Radiologist A	Small	Medium	Large
Small	9	-	-
Medium	-	3	2
Large	-	1	5

Nidus definition

	Radiologist B		
Radiologist A	Good	Intermediate	Poor
Good	5	1	1
Intermediate	-	2	2
Poor	2	-	7

Anatomical classification of AVM

	Radiologist B				
Radiologist A	Cortical	Cortico-ventricular	Deep-seated	Cortico-callosal	Choroid plexus
Cortical	9	-	-	-	-
Cortico-ventricular	1	5	-	-	-
Deep-seated	-	-	-	-	1
Cortico-callosal	-	-	-	1	1
Choroid plexus	1	-	-	-	-

Arterial supply

	Radiologist B				
Radiologist A	Ant	Post	Ant and post	Ant, post and ext	Ant and ext
Ant	9	1	-	-	-
Post	-	-	-	-	-
Ant and post	2	1	7	-	-
Ant, post and ext	-	-	-	-	-
Ant and ext	-	-	-	-	-

Ant – anterior circulation, Post – posterior circulation, Ext – external carotid supply

Presence of venous drainage

	Radiologist B		
Radiologist A	Superficial	Deep	Superficial and deep
Superficial	7	-	2
Deep	-	1	1
Superficial and Deep	1	1	7

Number of arterial feeders

	Radiologist B			
Radiologist A	1	2	3	>3
1	6	-	1	-
2	1	-	-	1
3	-	-	-	-
>3	-	1	2	8

Number of veins

	Radiologist B			
Radiologist A	1	2	3	>3
1	2	4	-	-
2	-	3	-	1
3	1	1	-	1
>3	-	-	-	7

Presence of aneurysm on feeding artery

	Radiologist B	
Radiologist A	Yes	No
Yes	-	-
No	-	20

Presence of Circle of Willis aneurysm

	Radiologist B	
Radiologist A	Yes	No
Yes	2	-
No	-	18

Presence of intranidal aneurysm

	Radiologist B	
Radiologist A	Yes	No
Yes	-	-
No	2	18

Presence of focal varix

	Radiologist B	
Radiologist A	Yes	No
Yes	10	4
No	2	4

Presence of diffuse varix

	Radiologist B	
Radiologist A	Yes	No
Yes	2	-
No	6	12

Presence of venous stenosis

	Radiologist B	
Radiologist A	Yes	No
Yes	-	1
No	-	19

Presence of venous occlusion

	Radiologist B	
Radiologist A	Yes	No
Yes	-	1
No	-	19

Presence of embolic material

	Radiologist B	
Radiologist A	Yes	No
Yes	-	-
No	-	20

Presence of angiogenesis

	Radiologist B	
Radiologist A	Yes	No
Yes	2	4
No	4	10

Presence of calcification

	Radiologist B	
Radiologist A	Yes	No
Yes	-	-
No	-	20

Clinical goal of treatment

	Radiologist B				
Radiologist A	Cure	Diminish risk of haemorrhage	Palliate	Adjunct to 2nd treatment	None
Cure	7	-	1	-	-
Diminish risk of haemorrhage	-	2	-	-	-
Palliate	-	1	6	-	-
Adjunct to 2nd treatment	-	-	-	-	-
None	-	2	1	-	-

Morphological goal of treatment

	Radiologist B				
Radiologist A	Eliminate high risk component	Decrease nidus size	Obliterate nidus	Eliminate specific feeders	No treatment
Eliminate high risk component	2	-	-	-	-
Decrease nidus size	-	1	-	-	-
Obliterate nidus	2	1	7	4	-
Eliminate specific feeders	1	-	-	2	-
No treatment	-	-	-	-	-

Proposed treatment

	Radiologist B				
Radiologist A	Conservative	Medical	Embolisation	DXT	Surgery
Conservative	-	-	3	-	-
Medical	-	-	-	-	-
Embolisation	-	-	15	-	1
DXT	-	-	-	-	-
Surgery	-	-	1	-	-

Interobserver variability for MIP

Nidus size

	Radiologist B		
Radiologist A	Small	Medium	Large
Small	9	1	-
Medium	-	4	-
Large	-	2	4

Nidus definition

	Radiologist B		
Radiologist A	Good	Intermediate	Poor
Good	-	1	1
Intermediate	5	2	4
Poor	-	1	6

Anatomical classification of AVM

	Radiologist B				
Radiologist A	Cortical	Cortico-ventricular	Deep-seated	Cortico-callosal	Choroid plexus
Cortical	7	1	-	-	-
Cortico-ventricular	2	4	-	-	-
Deep-seated	-	2	1	-	-
Cortico-callosal	1	-	-	2	-
Choroid plexus	-	-	-	-	-

Arterial supply

	Radiologist B				
Radiologist A	Ant	Post	Ant and post	Ant, post and ext	Ant and ext
Ant	10	-	2	-	-
Post	-	-	-	-	-
Ant and post	1	1	6	-	-
Ant, post and ext	-	-	-	-	-
Ant and ext	-	-	-	-	-

Ant – anterior circulation, Post – posterior circulation, Ext – external carotid supply

Pattern of venous drainage

	Radiologist B		
Radiologist A	Superficial	Deep	Superficial and deep
Superficial	8	-	1
Deep	-	1	-
Superficial and Deep	-	2	8

Number of arterial feeders

	Radiologist B			
Radiologist A	1	2	3	>3
1	4	2	-	-
2	2	1	-	-
3	-	1	1	2
>3	-	1	-	6

Number of veins

	Radiologist B			
Radiologist A	1	2	3	>3
1	7	-	1	-
2	1	1	-	-
3	1	1	-	4
>3	-	-	-	4

Presence of aneurysm on feeding artery

	Radiologist B	
Radiologist A	Yes	No
Yes	-	-
No	1	19

Presence of Circle of Willis aneurysm

	Radiologist B	
Radiologist A	Yes	No
Yes	2	-
No	1	17

Presence of intranidal aneurysm

	Radiologist B	
Radiologist A	Yes	No
Yes	-	2
No	3	15

Presence of focal varix

	Radiologist B	
Radiologist A	Yes	No
Yes	9	3
No	3	5

Presence of diffuse varix

	Radiologist B	
Radiologist A	Yes	No
Yes	1	-
No	4	15

Presence of venous stenosis

	Radiologist B	
Radiologist A	Yes	No
Yes	-	3
No	1	16

Presence of venous occlusion

	Radiologist B	
Radiologist A	Yes	No
Yes	-	-
No	1	19

Presence of embolic material

	Radiologist B	
Radiologist A	Yes	No
Yes	6	-
No	1	13

Presence of angiogenesis

	Radiologist B	
Radiologist A	Yes	No
Yes	4	-
No	2	14

Presence of calcification

	Radiologist B	
Radiologist A	Yes	No
Yes	5	2
No	1	12

Clinical goal of treatment

	Radiologist B				
Radiologist A	Cure	Diminish risk of haemorrhage	Palliate	Adjunct to 2nd treatment	None
Cure	8	-	1	-	-
Diminish risk of haemorrhage	-	2	2	-	-
Palliate	1	-	5	-	-
Adjunct to 2nd treatment	-	-	-	-	-
None	-	-	1	-	-

Morphological goal of treatment

	Radiologist B				
Radiologist A	Eliminate high risk component	Decrease nidus size	Obliterate nidus	Eliminate specific feeders	No treatment
Eliminate high risk component	-	-	-	2	-
Decrease nidus size	1	1	-	2	-
Obliterate nidus	-	1	8	-	-
Eliminate specific feeders	-	1	1	2	-
No treatment	-	-	-	1	-

Proposed treatment

	Radiologist B				
Radiologist A	Conservative	Medical	Embolisation	DXT	Surgery
Conservative	-	-	1	-	-
Medical	-	-	-	-	-
Embolisation	-	-	16	3	-
DXT	-	-	-	-	-
Surgery	-	-	-	-	-

Comparison of imaging techniques for all AVMs – SSD versus DSA

Nidus size

	DSA		
SSD	Small	Medium	Large
Small	8	1	-
Medium	-	4	2
Large	-	-	5

Nidus definition

	DSA		
SSD	Good	Intermediate	Poor
Good	8	-	-
Intermediate	3	-	-
Poor	6	2	1

Anatomical classification of AVM

	DSA				
SSD	Cortical	Cortico-ventricular	Deep-seated	Cortico-callosal	Choroid plexus
Cortical	8	2	1	-	-
Cortico-ventricular	-	5	1	-	-
Deep-seated	-	-	-	1	-
Cortico-callosal	-	-	-	2	-
Choroid plexus	-	-	-	-	-

Arterial supply

	DSA				
SSD	Ant	Post	Ant and post	Ant, post and ext	Ant and ext
Ant	9	-	1	-	1
Post	-	-	-	1	-
Ant and post	-	-	5	3	-
Ant, post and ext	-	-	-	-	-
Ant and ext	-	-	-	-	-

Ant – anterior circulation, Post – posterior circulation, Ext – external carotid supply

Pattern of venous drainage

	DSA		
SSD	Superficial	Deep	Superficial and deep
Superficial	10	-	-
Deep	-	3	-
Superficial and Deep	-	-	7

Number of arterial feeders

	DSA			
SSD	1	2	3	>3
1	6	-	-	-
2	1	1	-	-
3	-	-	-	1
>3	-	-	-	11

Number of veins

	DSA			
SSD	1	2	3	>3
1	5	-	-	-
2	1	4	-	1
3	-	-	1	1
>3	-	-	-	7

Presence of aneurysm on feeding artery

	DSA	
SSD	Yes	No
Yes	-	-
No	5	15

Presence of Circle of Willis aneurysm

	DSA	
SSD	Yes	No
Yes	2	-
No	1	17

Presence of intranidal aneurysm

	DSA	
SSD	Yes	No
Yes	1	-
No	3	16

Presence of focal varix

	DSA	
SSD	Yes	No
Yes	10	1
No	3	6

Presence of diffuse varix

	DSA	
SSD	Yes	No
Yes	2	6
No	5	7

Presence of venous stenosis

	DSA	
SSD	Yes	No
Yes	-	-
No	12	8

Presence of venous occlusion

	DSA	
SSD	Yes	No
Yes	1	1
No	2	16

Presence of embolic material

	DSA	
SSD	Yes	No
Yes	-	-
No	5	15

Presence of angiogenesis

	DSA	
SSD	Yes	No
Yes	4	3
No	1	12

Presence of calcification

	DSA	
SSD	Yes	No
Yes	-	-
No	-	20

Clinical goal of treatment

	DSA				
SSD	Cure	Diminish risk of haemorrhage	Palliate	Adjunct to 2nd treatment	None
Cure	7	-	-	-	-
Diminish risk of haemorrhage	-	2	-	-	1
Palliate	1	2	4	-	2
Adjunct to 2nd treatment	-	-	-	-	-
None	-	-	-	-	1

Morphological goal of treatment

	DSA				
SSD	Eliminate high risk component	Decrease nidus size	Obliterate nidus	Eliminate specific feeders	No treatment
Eliminate high risk component	2	-	-	-	2
Decrease nidus size	-	-	1	1	1
Obliterate nidus	-	-	7	-	-
Eliminate specific feeders	2	-	-	2	1
No treatment	-	-	-	-	1

Proposed treatment

	DSA				
SSD	Conservative	Medical	Embolisation	DXT	Surgery
Conservative	1	-	-	-	-
Medical	-	-	-	-	-
Embolisation	3	2	10	3	1
DXT	-	-	-	-	-
Surgery	-	-	-	-	-

Comparison of imaging techniques for all AVMs – MIP versus DSA

Nidus size

	DSA		
MIP	Small	Medium	Large
Small	8	2	-
Medium	-	2	4
Large	-	1	3

Nidus definition

	DSA		
MIP	Good	Intermediate	Poor
Good	5	-	-
Intermediate	7	-	-
Poor	5	2	1

Anatomical classification of AVM

	DSA				
MIP	Cortical	Cortico-ventricular	Deep-seated	Cortico-callosal	Choroid plexus
Cortical	7	2	-	-	-
Cortico-ventricular	1	5	-	-	-
Deep-seated	-	-	1	1	-
Cortico-callosal	-	-	1	2	-
Choroid plexus	-	-	-	-	-

Arterial supply

	DSA				
MIP	Ant	Post	Ant and post	Ant, post and ext	Ant and ext
Ant	9	-	1	-	1
Post	-	-	-	-	-
Ant and post	-	-	5	4	-
Ant, post and ext	-	-	-	-	-
Ant and ext	-	-	-	-	-

Ant – anterior circulation, Post – posterior circulation, Ext – external carotid supply

Pattern of venous drainage

	DSA		
MIP	Superficial	Deep	Superficial and deep
Superficial	9	-	-
Deep	-	1	-
Superficial and Deep	1	2	7

Number of arterial feeders

	DSA			
MIP	1	2	3	>3
1	6	-	-	-
2	1	1	-	1
3	-	-	-	3
>3	-	-	-	8

Number of veins

	DSA			
MIP	1	2	3	>3
1	5	2	-	-
2	3	2	-	-
3	-	-	1	3
>3	-	-	-	6

Presence of aneurysm on feeding artery

	DSA	
MIP	Yes	No
Yes	-	-
No	5	15

Presence of Circle of Willis aneurysm

	DSA	
MIP	Yes	No
Yes	2	-
No	1	17

Presence of intranidal aneurysm

	DSA	
MIP	Yes	No
Yes	1	-
No	3	16

Presence of focal varix

	DSA	
MIP	Yes	No
Yes	9	4
No	4	3

Presence of diffuse varix

	DSA	
MIP	Yes	No
Yes	4	1
No	3	12

Presence of venous stenosis

	DSA	
MIP	Yes	No
Yes	3	-
No	9	8

Presence of venous occlusion

	DSA	
MIP	Yes	No
Yes	1	-
No	2	17

Presence of embolic material

	DSA	
MIP	Yes	No
Yes	5	1
No	-	14

Presence of angiogenesis

	DSA	
MIP	Yes	No
Yes	4	--
No	1	15

Presence of calcification

	DSA	
MIP	Yes	No
Yes	-	7
No	-	13

Clinical goal of treatment

	DSA				
MIP	Cure	Diminish risk of haemorrhage	Palliate	Adjunct to 2nd treatment	None
Cure	7	-	1	-	-
Diminish risk of haemorrhage	-	3	-	-	1
Palliate	1	1	3	-	2
Adjunct to 2nd treatment	-	-	-	-	-
None	-	-	-	-	1

Morphological goal of treatment

	DSA				
MIP	Eliminate high risk component	Decrease nidus size	Obliterate nidus	Eliminate specific feeders	No treatment
Eliminate high risk component	2	0	0	1	-
Decrease nidus size	-	-	1	2	-
Obliterate nidus	-	-	7	1	-
Eliminate specific feeders	2	1	1	1	-
No treatment	-	-	-	-	1

Proposed treatment

	DSA				
MIP	Conservative	Medical	Embolisation	DXT	Surgery
Conservative	1	-	-	-	-
Medical	-	-	-	-	-
Embolisation	3	2	9	3	1
DXT	-	-	1	-	-
Surgery	-	-	-	-	-

Comparison of imaging techniques for small AVMs – SSD versus DSA

Nidus size

	DSA		
SSD	Small	Medium	Large
Small	8	-	-
Medium	-	-	-
Large	-	-	-

Nidus definition

	DSA		
SSD	Good	Intermediate	Poor
Good	7	-	-
Intermediate	1	-	-
Poor	-	-	-

Anatomical classification of AVM

	DSA				
SSD	Cortical	Cortico-ventricular	Deep-seated	Cortico-callosal	Choroid plexus
Cortical	5	-	1	-	-
Cortico-ventricular	-	-	-	-	-
Deep-seated	-	-	-	-	-
Cortico-callosal	-	-	-	1	-
Choroid plexus	-	-	-	1	-

Arterial supply

	DSA				
SSD	Ant	Post	Ant and post	Ant, post and ext	Ant and ext
Ant	7	-	1	-	-
Post	-	-	-	-	-
Ant and post	-	-	-	-	-
Ant, post and ext	-	-	-	-	-
Ant and ext	-	-	-	-	-

Ant – anterior circulation, Post – posterior circulation, Ext – external carotid supply

Pattern of venous drainage

	DSA		
SSD	Superficial	Deep	Superficial and deep
Superficial	5	-	-
Deep	-	2	-
Superficial and Deep	-	-	1

Number of arterial feeders

	DSA			
SSD	1	2	3	>3
1	6	-	-	-
2	-	1	-	-
3	-	-	-	-
>3	-	-	-	1

Number of veins

	DSA			
SSD	1	2	3	>3
1	4	-	-	-
2	1	3	-	-
3	-	-	-	-
>3	-	-	-	-

Presence of aneurysm on feeding artery

	DSA	
SSD	Yes	No
Yes	-	-
No	-	8

Presence of Circle of Willis aneurysm

	DSA	
SSD	Yes	No
Yes	1	-
No	-	7

Presence of intranidal aneurysm

	DSA	
SSD	Yes	No
Yes	1	-
No	-	7

Presence of focal varix

	DSA	
SSD	Yes	No
Yes	2	-
No	2	4

Presence of diffuse varix

	DSA	
SSD	Yes	No
Yes	-	2
No	1	5

Presence of venous stenosis

	DSA	
SSD	Yes	No
Yes	-	-
No	4	4

Presence of venous occlusion

	DSA	
SSD	Yes	No
Yes	-	-
No	-	8

Presence of embolic material

	DSA	
SSD	Yes	No
Yes	-	-
No	2	6

Presence of angiogenesis

	DSA	
SSD	Yes	No
Yes	-	-
No	-	8

Presence of calcification

	DSA	
SSD	Yes	No
Yes	-	-
No	8	-

Clinical goal of treatment

	DSA				
SSD	Cure	Diminish risk of haemorrhage	Palliate	Adjunct to 2nd treatment	None
Cure	7	-	-	-	-
Diminish risk of haemorrhage	-	-	-	-	-
Palliate	1	-	-	-	-
Adjunct to 2nd treatment	-	-	-	-	-
None	-	-	-	-	-

Morphological goal of treatment

	DSA				
SSD	Eliminate high risk component	Decrease nidus size	Obliterate nidus	Eliminate specific feeders	No treatment
Eliminate high risk component	-	-	-	-	-
Decrease nidus size	-	-	1	-	-
Obliterate nidus	-	-	7	-	-
Eliminate specific feeders	-	-	-	-	-
No treatment	-	-	-	-	-

Proposed treatment

	DSA				
SSD	Conservative	Medical	Embolisation	DXT	Surgery
Conservative	-	-	-	-	-
Medical	-	-	-	-	-
Embolisation	-	-	4	5	1
DXT	-	-	-	-	-
Surgery	-	-	-	-	-

Comparison of imaging techniques for small AVMs – MIP versus DSA

Nidus size

	DSA		
MIP	Small	Medium	Large
Small	8	-	-
Medium	-	-	-
Large	-	-	-

Nidus definition

	DSA		
MIP	Good	Intermediate	Poor
Good	4	-	-
Intermediate	4	-	-
Poor	-	-	-

Anatomical classification of AVM

	DSA				
MIP	Cortical	Cortico-ventricular	Deep-seated	Cortico-callosal	Choroid plexus
Cortical	5	-	-	-	-
Cortico-ventricular	-	-	-	-	-
Deep-seated	-	-	-	-	-
Cortico-callosal	-	-	1	2	-
Choroid plexus	-	-	-	-	-

Arterial supply

	DSA				
MIP	Ant	Post	Ant and post	Ant, post and ext	Ant and ext
Ant	7	-	1	-	-
Post	-	-	-	-	-
Ant and post	-	-	-	-	-
Ant, post and ext	-	-	-	-	-
Ant and ext	-	-	-	-	-

Ant – anterior circulation, Post – posterior circulation, Ext – external carotid supply

Pattern of venous drainage

	DSA		
MIP	Superficial	Deep	Superficial and deep
Superficial	5	-	-
Deep	-	1	-
Superficial and Deep	-	1	1

Number of arterial feeders

	DSA			
MIP	1	2	3	>3
1	6	-	-	-
2	-	1	-	1
3	-	-	-	-
>3	-	-	-	-

Number of veins

	DSA			
MIP	1	2	3	>3
1	4	2	-	-
2	1	1	-	-
3	-	-	-	-
>3	-	-	-	-

Presence of aneurysm on feeding artery

	DSA	
MIP	Yes	No
Yes	-	-
No	-	8

Presence of Circle of Willis aneurysm

	DSA	
MIP	Yes	No
Yes	1	-
No	-	7

Presence of intranidal aneurysm

	DSA	
MIP	Yes	No
Yes	1	-
No	-	7

Presence of focal varix

	DSA	
MIP	Yes	No
Yes	2	1
No	2	3

Presence of diffuse varix

	DSA	
MIP	Yes	No
Yes	1	1
No	-	6

Presence of venous stenosis

	DSA	
MIP	Yes	No
Yes	-	-
No	4	4

Presence of venous occlusion

	DSA	
MIP	Yes	No
Yes	-	-
No	-	8

Presence of embolic material

	DSA	
MIP	Yes	No
Yes	2	-
No	-	6

Presence of angiogenesis

	DSA	
MIP	Yes	No
Yes	-	-
No	-	8

Presence of calcification

	DSA	
MIP	Yes	No
Yes	-	2
No	-	6

Clinical goal of treatment

	DSA				
MIP	Cure	Diminish risk of haemorrhage	Palliate	Adjunct to 2nd treatment	None
Cure	7	-	-	-	-
Diminish risk of haemorrhage	-	-	-	-	-
Palliate	1	-	-	-	-
Adjunct to 2nd treatment	-	-	-	-	-
None	-	-	-	-	-

Morphological goal of treatment

	DSA				
MIP	Eliminate high risk component	Decrease nidus size	Obliterate nidus	Eliminate specific feeders	No treatment
Eliminate high risk component	-	-	-	-	-
Decrease nidus size	-	-	-	-	-
Obliterate nidus	-	-	7	-	-
Eliminate specific feeders	-	-	1	-	-
No treatment	-	-	-	-	-

Proposed treatment

	DSA				
MIP	Conservative	Medical	Embolisation	DXT	Surgery
Conservative	-	-	-	-	-
Medical	-	-	-	-	-
Embolisation	-	-	3	3	1
DXT	-	-	1	-	-
Surgery	-	-	-	-	-

APPENDIX 3

Data for Chapter 4 – MR Angiography

Interobserver variability for pre contrast TOF sequences

Nidus size

	Radiologist B			
Radiologist A	Small	Medium	Large	Not assessable
Small	5	2	-	1
Medium	-	1	-	-
Large	-	-	-	-
Not assessable	-	-	-	1

Nidus definition

	Radiologist B			
Radiologist A	Good	Intermediate	Poor	Not assessable
Good	-	1	-	-
Intermediate	2	1	1	-
Poor	-	1	2	1
Not assessable	-	-	-	1

Anatomical classification of AVM

	Radiologist B						
Radiologist A	Cortical	Cortico-ventricular	Deep-seated	Cortico-callosal	Choroid plexus	Posterior fossa	Not assessable
Cortical	3	1	1	-	-	-	3
Cortico-ventricular	-	-	-	-	-	-	-
Deep-seated	-	-	-	-	-	-	-
Cortico-callosal	-	-	-	-	-	-	-
Choroid plexus	-	-	-	-	-	-	-
Posterior fossa	-	-	-	-	-	1	-
Not assessable	-	-	-	-	-	-	1

Arterial supply

Radiologist A	*Radiologist B*					
	Ant	Post	Ant and post	Ant, post and ext	Ant and Ext	Not assessable
Ant	-	-	-	-	-	1
Post	2	3	-	-	-	-
Ant and post	-	-	-	1	-	-
Ant, post and ext	-	-	-	1	-	-
Ant and ext	1	-	-	-	-	-
Not assessable	-	-	-	-	-	1

Ant – anterior circulation, Post – posterior circulation, Ext – external carotid supply

Pattern of venous drainage

Radiologist A	*Radiologist B*			
	Superficial	Deep	Superficial and deep	Not assessable
Superficial	-	-	-	-
Deep	-	1	-	-
Superficial and Deep	-	-	-	-
Not assessable	3	1	-	5

Number of arterial feeders

Radiologist A	*Radiologist B*				
	1	2	3	>3	Not assess
1	2	2	-	-	-
2	-	1	1	-	-
3	-	1	-	-	-
>3	-	-	-	1	-
Not assess	-	-	-	-	2

Number of veins

Radiologist A	*Radiologist B*				
	1	2	3	>3	Not assess
1	1	-	-	-	-
2	-	-	-	-	-
3	-	-	-	-	-
>3	-	-	-	-	-
Not assess	2	-	-	-	7

Presence of aneurysm on feeding artery

Radiologist A	*Radiologist B*		
	Yes	No	Not assess
Yes	-	-	-
No	1	7	1
Not assess	-	-	1

Presence of Circle of Willis aneurysm

Radiologist A	*Radiologist B*		
	Yes	No	Not assess
Yes	-	-	-
No	-	8	1
Not assess	-	-	1

Presence of intranidal aneurysm

	Radiologist B		
Radiologist A	Yes	No	Not assess
Yes	-	-	1
No	-	8	-
Not assess	-	-	1

Presence of focal varix

	Radiologist B		
Radiologist A	Yes	No	Not assess
Yes	-	-	-
No	-	3	-
Not assess	-	2	5

Presence of diffuse varix

	Radiologist B		
Radiologist A	Yes	No	Not assess
Yes	-	-	-
No	-	3	-
Not assess	-	2	5

Presence of venous stenosis

	Radiologist B		
Radiologist A	Yes	No	Not assess
Yes	-	-	-
No	-	3	-
Not assess	-	2	5

Presence of venous occlusion

	Radiologist B		
Radiologist A	Yes	No	Not assess
Yes	-	-	-
No	-	3	-
Not assess	-	2	5

Clinical goal of treatment

	Radiologist B					
Radiologist A	Cure	Diminish risk of haemorrhage	Palliate	Adjunct to 2nd treatment	None	Not assessable
Cure	3	-	1	-	-	-
Diminish risk of haemorrhage	-	1	1	-	-	-
Palliate	1	1	-	-	-	-
Adjunct to 2nd treatment	-	-	-	-	-	-
None	-	-	-	-	-	-
Not assessable	-	-	1	-	-	1

Morphological goal of treatment

	Radiologist B					
Radiologist A	Eliminate high risk component	Decrease nidus size	Obliterate nidus	Eliminate specific feeders	No treatment	Not assessable
Eliminate high risk component	1	-	-	1	-	-
Decrease nidus size	-	-	-	-	-	-
Obliterate nidus	-	-	3	1	-	-
Eliminate specific feeders	1	-	1	-	-	-
No treatment	-	-	-	-	-	-
Not assessable	-	-	-	1	-	1

Proposed treatment

	Radiologist B					
Radiologist A	Conservative	Medical	Embolisation	DXT	Surgery	Not assessable
Conservative	-	-	-	-	-	-
Medical	-	-	-	-	-	-
Embolisation	-	-	6	-	-	-
DXT	-	-	2	-	-	-
Surgery	-	-	-	-	-	-
Not assessable	-	-	1	-	-	1

Interobserver variability for CEMRA

Nidus size

	Radiologist B			
Radiologist A	Small	Medium	Large	Not assessable
Small	8	-	-	-
Medium	-	1	-	-
Large	-	-	-	-
Not assessable	-	-	-	1

Nidus definition

	Radiologist B			
Radiologist A	Good	Intermediate	Poor	Not assessable
Good	-	-	-	-
Intermediate	3	3	1	-
Poor	-	1	1	-
Not assessable	-	-	-	1

Anatomical classification of AVM

	Radiologist B						
Radiologist A	Cortical	Cortico-ventricular	Deep-seated	Cortico-callosal	Choroid plexus	Posterior fossa	Not assess
Cortical	5	1	-	-	-	-	-
Cortico-ventricular	1	-	-	-	-	-	-
Deep-seated	-	-	-	-	-	-	-
Cortico-callosal	-	-	-	-	-	-	-
Choroid plexus	-	-	-	1	-	-	-
Posterior fossa	-	-	-	-	-	1	-
Not assessable	-	-	-	-	-	-	1

Arterial supply

	Radiologist B					
Radiologist A	Ant	Post	Ant and post	Ant, post and ext	Ant and Ext	Not assessable
Ant	2	-	-	-	-	-
Post	-	1	-	-	1	-
Ant and post	-	1	1	-	-	-
Ant, post and ext	-	-	-	-	-	-
Ant and ext	-	-	-	-	-	-
Not assessable	2	1	-	-	-	1

Ant – anterior circulation, Post – posterior circulation, Ext – external carotid supply

Pattern of venous drainage

	Radiologist B			
Radiologist A	Superficial	Deep	Superficial and deep	Not assessable
Superficial	4	-	1	1
Deep	-	1	-	1
Superficial and Deep	1	-	-	-
Not assessable	-	-	-	1

Number of arterial feeders

	Radiologist B				
Radiologist A	1	2	3	>3	Not assess
1	3	-	-	-	-
2	-	1	2	-	-
3	-	-	-	-	-
>3	-	-	-	-	-
Not assess	3	-	-	-	1

Number of veins

	Radiologist B				
Radiologist A	1	2	3	>3	Not assess
1	4	-	-	-	2
2	1	2	-	-	-
3	-	-	-	-	-
>3	-	-	-	-	-
Not assess	-	-	-	-	1

Presence of aneurysm on feeding artery

	Radiologist B		
Radiologist A	Yes	No	Not assess
Yes	-	-	-
No	-	9	-
Not assess	-	-	1

Presence of intranidal aneurysm

	Radiologist B		
Radiologist A	Yes	No	Not assess
Yes	-	-	-
No	-	9	-
Not assess	-	-	1

Presence of Circle of Willis aneurysm

	Radiologist B		
Radiologist A	Yes	No	Not assess
Yes	-	-	-
No	-	9	-
Not assess	-	-	1

Presence of focal varix

	Radiologist B		
Radiologist A	Yes	No	Not assess
Yes	-	2	-
No	-	5	2
Not assess	-	-	1

Presence of diffuse varix

	Radiologist B		
Radiologist A	Yes	No	Not assess
Yes	3	-	-
No	1	3	2
Not assess	-	-	1

Presence of venous stenosis

	Radiologist B		
Radiologist A	Yes	No	Not assess
Yes	-	-	-
No	-	7	2
Not assess	-	-	1

Presence of venous occlusion

	Radiologist B		
Radiologist A	Yes	No	Not assess
Yes	-	-	-
No	1	6	2
Not assess	-	-	1

Clinical goal of treatment

	Radiologist B					
Radiologist A	Cure	Diminish risk of haemorrhage	Palliate	Adjunct to 2nd treatment	None	Not assessable
Cure	2	-	-	-	-	-
Diminish risk of haemorrhage	-	1	-	-	-	-
Palliate	-	-	2	-	-	-
Adjunct to 2nd treatment	-	-	-	-	-	-
None	-	1	-	-	-	-
Not assessable	1	-	-	-	-	3

Morphological goal of treatment

	Radiologist B					
Radiologist A	Eliminate high risk component	Decrease nidus size	Obliterate nidus	Eliminate specific feeders	No treatment	Not assessable
Eliminate high risk component	1	-	-	-	-	-
Decrease nidus size	-	-	-	1	-	-
Obliterate nidus	-	-	2	-	-	-
Eliminate specific feeders	-	-	-	1	-	-
No treatment	-	-	-	1	-	-
Not assessable	-	-	1	-	-	3

Proposed treatment

	Radiologist B					
Radiologist A	Conservative	Medical	Embolisation	DXT	Surgery	Not assessable
Conservative	-	-	1	-	-	-
Medical	-	-	-	-	-	-
Embolisation	-	-	5	-	-	-
DXT	-	-	-	-	-	-
Surgery	-	-	-	-	-	-
Not assessable	-	-	1	-	-	3

Interobserver variability for post contrast TOF sequences

Nidus size

	Radiologist B			
Radiologist A	Small	Medium	Large	Not assessable
Small	2	-	-	-
Medium	-	8	-	-
Large	-	-	-	-
Not assessable	-	-	-	-

Nidus definition

	Radiologist B			
Radiologist A	Good	Intermediate	Poor	Not assessable
Good	-	-	-	-
Intermediate	1	3	1	-
Poor	1	1	3	-
Not assessable	-	-	-	-

Anatomical classification of AVM

	Radiologist B						
Radiologist A	Cortical	Cortico-ventricular	Deep-seated	Cortico-callosal	Choroid plexus	Posterior fossa	Not assess
Cortical	6	-	-	-	-	-	-
Cortico-ventricular	-	1	-	-	-	-	-
Deep-seated	-	-	1	1	-	-	-
Cortico-callosal	-	-	-	-	-	-	-
Choroid plexus	-	-	-	-	-	-	-
Posterior fossa	-	-	-	-	-	1	-
Not assessable	-	-	-	-	-	-	-

Arterial supply

	Radiologist B					
Radiologist A	Ant	Post	Ant and post	Ant, post and ext	Ant and Ext	Not assessable
Ant	4	-	-	-	-	-
Post	-	4	1	-	-	-
Ant and post	-	-	-	-	-	-
Ant, post and ext	-	-	1	-	-	-
Ant and ext	-	-	-	-	-	-
Not assessable	-	-	-	-	-	-

Ant – anterior circulation, Post – posterior circulation, Ext – external carotid supply

Pattern of venous drainage

	Radiologist B			
Radiologist A	Superficial	Deep	Superficial and deep	Not assessable
Superficial	4	-	1	1
Deep	-	1	1	1
Superficial and Deep	1	-	-	-
Not assessable	-	-	-	-

Number of arterial feeders

	Radiologist B				
Radiologist A	1	2	3	>3	Not assess
1	4	-	-	1	1
2	-	2	1	-	-
3	-	-	-	1	-
>3	-	-	-	-	-
Not assess	-	-	-	-	-

Number of veins

	Radiologist B				
Radiologist A	1	2	3	>3	Not assess
1	4	1	-	-	3
2	1	1	-	-	-
3	-	-	-	-	-
>3	-	-	-	-	-
Not assess	-	-	-	-	-

Presence of aneurysm on feeding artery

	Radiologist B		
Radiologist A	Yes	No	Not assess
Yes	-	-	-
No	1	9	-
Not assess	-	-	-

Presence of intranidal aneurysm

	Radiologist B		
Radiologist A	Yes	No	Not assess
Yes	-	-	-
No	1	9	-
Not assess	-	-	-

Presence of Circle of Willis aneurysm

	Radiologist B		
Radiologist A	Yes	No	Not assess
Yes	-	-	-
No	1	9	-
Not assess	-	-	-

Presence of focal varix

	Radiologist B		
Radiologist A	Yes	No	Not assess
Yes	-	4	-
No	1	5	-
Not assess	-	-	-

Presence of diffuse varix

	Radiologist B		
Radiologist A	Yes	No	Not assess
Yes	2	1	-
No	1	6	-
Not assess	-	-	-

Presence of venous stenosis

	Radiologist B		
Radiologist A	Yes	No	Not assess
Yes	-	3	-
No	-	7	-
Not assess	-	-	-

Presence of venous occlusion

	Radiologist B		
Radiologist A	Yes	No	Not assess
Yes	-	3	-
No	-	7	-
Not assess	-	-	-

Clinical goal of treatment

	Radiologist B					
Radiologist A	Cure	Diminish risk of haemorrhage	Palliate	Adjunct to 2nd treatment	None	Not assessable
Cure	4	-	-	-	-	-
Diminish risk of haemorrhage	1	-	1	-	-	-
Palliate	-	-	2	-	-	-
Adjunct to 2nd treatment	-	-	-	-	-	-
None	-	-	1	-	1	-
Not assessable	-	-	-	-	-	-

Morphological goal of treatment

	Radiologist B					
Radiologist A	Eliminate high risk component	Decrease nidus size	Obliterate nidus	Eliminate specific feeders	No treatment	Not assessable
Eliminate high risk component	-	-	1	1	-	-
Decrease nidus size	-	-	-	-	-	-
Obliterate nidus	-	-	4	-	-	-
Eliminate specific feeders	-	-	-	2	-	-
No treatment	-	-	-	1	1	-
Not assessable	-	-	-	-	-	-

Proposed treatment

	Radiologist B					
Radiologist A	Conservative	Medical	Embolisation	DXT	Surgery	Not assessable
Conservative	1	-	1	-	-	-
Medical	-	-	-	-	-	-
Embolisation	-	-	7	-	-	-
DXT	-	-	1	-	-	-
Surgery	-	-	-	-	-	-
Not assessable	-	-	-	-	-	-

Variability for DSA and pre contrast TOF sequences

Nidus size

	DSA			
Pre contrast	Small	Medium	Large	Not assessable
Small	5	3	-	-
Medium	-	-	1	-
Large	-	-	-	-
Not assessable	-	1	-	-

Nidus definition

	DSA			
Pre contrast	Good	Intermediate	Poor	Not assessable
Good	1	-	-	-
Intermediate	3	1	-	-
Poor	2	2	-	-
Not assessable	1	-	-	-

Anatomical classification of AVM

	DSA						
Pre contrast TOF	Cortical	Cortico-ventricular	Deep-seated	Cortico-callosal	Choroid plexus	Posterior fossa	Not assess
Cortical	7	-	1	-	-	-	-
Cortico-ventricular	-	-	-	-	-	-	-
Deep-seated	-	-	-	-	-	-	-
Cortico-callosal	-	-	-	-	-	-	-
Choroid plexus	-	-	-	-	-	-	-
Posterior fossa	-	-	-	-	-	1	-
Not assessable	1	-	-	-	-	-	-

Arterial supply

Pre contrast TOF	DSA					
	Ant	Post	Ant and post	Ant, post and ext	Ant and Ext	Not assessable
Ant	1	-	-	-	-	-
Post	1	3	1	-	-	-
Ant and post	-	1	-	-	-	-
Ant, post and ext	-	-	1	-	-	-
Ant and ext	1	-	-	-	-	-
Not assessable	1	-	-	-	-	-

Ant – anterior circulation, Post – posterior circulation, Ext – external carotid supply

Pattern of venous drainage

Pre contrast TOF	DSA			
	Superficial	Deep	Superficial and deep	Not assessable
Superficial	-	-	-	-
Deep	1	-	-	-
Superficial and Deep	-	-	-	-
Not assessable	7	2	-	-

Number of arterial feeders

Pre contrast	DSA				
	1	2	3	>3	Not assess
1	3	1	-	-	-
2	-	-	-	-	-
3	-	2	1	-	-
>3	-	-	-	1	-
Not assess	2	-	-	-	-

Number of veins

Pre contrast	DSA				
	1	2	3	>3	Not assess
1	1	-	-	-	-
2	-	-	-	-	-
3	-	-	-	-	-
>3	-	-	-	-	-
Not assess	8	1	-	-	-

Presence of aneurysm on feeding artery

Pre contrast	DSA		
	Yes	No	Not assess
Yes	-	-	-
No	2	7	-
Not assess	-	1	-

Presence of Circle of Willis aneurysm

Pre contrast	DSA		
	Yes	No	Not assess
Yes	-	-	-
No	-	9	-
Not assess	-	1	-

Presence of intranidal aneurysm

	DSA		
Pre contrast	Yes	No	Not assess
Yes	-	1	-
No	3	5	-
Not assess	-	1	-

Presence of focal varix

	DSA		
Pre contrast	Yes	No	Not assess
Yes	-	-	-
No	-	3	-
Not assess	2	5	-

Presence of diffuse varix

	DSA		
Pre contrast	Yes	No	Not assess
Yes	-	-	-
No	1	2	-
Not assess	2	5	-

Presence of venous stenosis

	DSA		
Pre contrast	Yes	No	Not assess
Yes	-	-	-
No	2	1	-
Not assess	1	6	-

Presence of venous occlusion

	DSA		
Pre contrast	Yes	No	Not assess
Yes	-	-	-
No	-	3	-
Not assess	-	7	-

Clinical goal of treatment

	DSA					
Pre contrast TOF	Cure	Diminish risk of haemorrhage	Palliate	Adjunct to 2nd treatment	None	Not assessable
Cure	2	-	-	-	-	-
Diminish risk of haemorrhage	1	-	-	-	-	-
Palliate	-	1	1	-	-	-
Adjunct to 2nd treatment	-	-	-	-	-	-
None	1	-	-	-	-	-
Not assessable	2	1	1	-	-	-

Morphological goal of treatment

	DSA					
Pre contrast TOF	Eliminate high risk component	Decrease nidus size	Obliterate nidus	Eliminate specific feeders	No treatment	Not assessable
Eliminate high risk component	-	-	1	-	-	-
Decrease nidus size	-	1	-	-	-	-
Obliterate nidus	-	-	2	-	-	-
Eliminate specific feeders	-	1	-	-	-	-
No treatment	-	1	-	-	-	-
Not assessable	1	1	2	-	-	-

Proposed treatment

	DSA					
Pre contrast TOF	Conservative	Medical	Embolisation	DXT	Surgery	Not assessable
Conservative	-	-	1	-	-	-
Medical	-	-	-	-	-	-
Embolisation	-	-	5	-	-	-
DXT	-	-	-	-	-	-
Surgery	-	-	-	-	-	-
Not assessable	-	-	2	2	-	-

Variability for DSA and CEMRA

Nidus size

	DSA			
CEMRA	Small	Medium	Large	Not assessable
Small	4	4	-	-
Medium	-	-	1	-
Large	-	-	-	-
Not assessable	1	-	-	-

Nidus definition

	DSA			
CEMRA	Good	Intermediate	Poor	Not assessable
Good	-	-	-	-
Intermediate	5	2	-	-
Poor	1	1	-	-
Not assessable	1	-	-	-

Anatomical classification of AVM

	DSA						
CEMRA	Cortical	Cortico-ventricular	Deep-seated	Cortico-callosal	Choroid plexus	Posterior fossa	Not assess
Cortical	6	-	-	-	-	-	-
Cortico-ventricular	1	-	-	-	-	-	-
Deep-seated	-	-	-	-	-	-	-
Cortico-callosal	-	-	-	-	-	-	-
Choroid plexus	-	-	1	-	-	-	-
Posterior fossa	-	-	-	-	-	1	-
Not assessable	1	-	-	-	-	-	-

Arterial supply

	DSA					
CEMRA	Ant	Post	Ant and post	Ant, post and ext	Ant and Ext	Not assessable
Ant	2	-	-	-	-	-
Post	-	-	2	-	-	-
Ant and post	-	2	-	-	-	-
Ant, post and ext	-	-	-	-	-	-
Ant and ext	-	-	-	-	-	-
Not assessable	2	2	-	-	-	-

Ant – anterior circulation, Post – posterior circulation, Ext – external carotid supply

Pattern of venous drainage

	DSA			
CEMRA	Superficial	Deep	Superficial and deep	Not assessable
Superficial	6	-	-	-
Deep	-	2	-	-
Superficial and Deep	1	-	-	-
Not assessable	1	-	-	-

Number of arterial feeders

	DSA				
CEMRA	1	2	3	>3	Not assess
1	1	1	1	-	-
2	1	1	-	1	-
3	-	-	-	-	-
>3	-	-	-	-	-
Not assess	3	1	-	-	-

Number of veins

	DSA				
CEMRA	1	2	3	>3	Not assess
1	6	1	-	-	-
2	2	-	-	-	-
3	-	-	-	-	-
>3	-	-	-	-	-
Not assess	1	-	-	-	-

Presence of aneurysm on feeding artery

	DSA		
CEMRA	Yes	No	Not assess
Yes	-	-	-
No	2	7	-
Not assess	-	1	-

Presence of intranidal aneurysm

	DSA		
CEMRA	Yes	No	Not assess
Yes	-	-	-
No	3	6	-
Not assess	-	1	-

Presence of Circle of Willis aneurysm

	DSA		
CEMRA	Yes	No	Not assess
Yes	-	-	-
No	-	9	-
Not assess	-	1	-

Presence of focal varix

	DSA		
CEMRA	Yes	No	Not assess
Yes	1	1	-
No	1	6	-
Not assess	-	1	-

Presence of diffuse varix

	DSA		
CEMRA	Yes	No	Not assess
Yes	2	1	-
No	1	5	-
Not assess	-	1	-

Presence of venous stenosis

	DSA		
CEMRA	Yes	No	Not assess
Yes	-	-	-
No	2	7	-
Not assess	1	-	-

Presence of venous occlusion

	DSA		
CEMRA	Yes	No	Not assess
Yes	-	-	-
No	-	9	-
Not assess	-	1	-

Clinical goal of treatment

	DSA					
CEMRA	Cure	Diminish risk of haemorrhage	Palliate	Adjunct to 2nd treatment	None	Not assessable
Cure	3	1	-	-	-	-
Diminish risk of haemorrhage	1	1	-	-	-	-
Palliate	-	-	2	-	-	-
Adjunct to 2nd treatment	-	-	-	-	-	-
None	-	-	-	-	-	-
Not assessable	2	-	-	-	-	-

Morphological goal of treatment

	DSA					
CEMRA	Eliminate high risk component	Decrease nidus size	Obliterate nidus	Eliminate specific feeders	No treatment	Not assessable
Eliminate high risk component	-	1	1	-	-	-
Decrease nidus size	-	-	-	-	-	-
Obliterate nidus	1	-	3	-	-	-
Eliminate specific feeders	-	2	-	-	-	-
No treatment	-	-	-	-	-	-
Not assessable	-	1	1	-	-	-

Proposed treatment

	DSA					
CEMRA	Conservative	Medical	Embolisation	DXT	Surgery	Not assessable
Conservative	-	-	-	-	-	-
Medical	-	-	-	-	-	-
Embolisation	-	-	4	2	-	-
DXT	-	-	2	-	-	-
Surgery	-	-	-	-	-	-
Not assessable	-	-	2	-	-	-

Variability for DSA and post contrast TOF sequences

Nidus size

	DSA			
Post contrast TOF	Small	Medium	Large	Not assessable
Small	5	4	-	-
Medium	-	-	1	-
Large	-	-	-	-
Not assessable	-	-	-	-

Nidus definition

	DSA			
Post contrast TOF	Good	Intermediate	Poor	Not assessable
Good	-	-	-	-
Intermediate	3	2	-	-
Poor	4	1	-	-
Not assessable	-	-	-	-

Anatomical classification of AVM

	DSA						
Post contrast TOF	Cortical	Cortico-ventricular	Deep-seated	Cortico-callosal	Choroid plexus	Posterior fossa	Not assess
Cortical	6	-	-	-	-	-	-
Cortico-ventricular	1	-	-	-	-	-	-
Deep-seated	1	-	1	-	-	-	-
Cortico-callosal	-	-	-	-	-	-	-
Choroid plexus	-	-	-	-	-	-	-
Posterior fossa	-	-	-	-	-	1	-
Not assessable	-	-	-	-	-	-	-

Arterial supply

	DSA					
Post contrast TOF	Ant	Post	Ant and post	Ant, post and ext	Ant and Ext	Not assessable
Ant	4	-	-	-	-	-
Post	-	4	1	-	-	-
Ant and post	-	-	-	-	-	-
Ant, post and ext	-	-	1	-	-	-
Ant and ext	-	-	-	-	-	-
Not assessable	-	-	-	-	-	-

Ant – anterior circulation, Post – posterior circulation, Ext – external carotid supply

Pattern of venous drainage

	DSA			
Post contrast TOF	Superficial	Deep	Superficial and deep	Not assessable
Superficial	6	-	-	-
Deep	1	2	-	-
Superficial and Deep	1	-	-	-
Not assessable	-	-	-	-

Number of arterial feeders

	DSA				
Post contrast	1	2	3	>3	Not assess
1	4	2	-	-	-
2	1	1	1	-	-
3	-	-	-	1	-
>3	-	-	-	-	-
Not assess	-	-	-	-	-

Number of veins

	DSA				
Post contrast	1	2	3	>3	Not assess
1	7	1	-	-	-
2	2	-	-	-	-
3	-	-	-	-	-
>3	-	-	-	-	-
Not assess	-	-	-	-	-

Presence of aneurysm on feeding artery

	DSA		
Post contrast	Yes	No	Not assess
Yes	-	-	-
No	2	8	-
Not assess	-	-	-

Presence of intranidal aneurysm

	DSA		
Post contrast	Yes	No	Not assess
Yes	-	1	-
No	3	6	-
Not assess	-	-	-

Presence of Circle of Willis aneurysm

	DSA		
Post contrast	Yes	No	Not assess
Yes	-	-	-
No	-	10	-
Not assess	-	-	-

Presence of focal varix

	DSA		
Post contrast	Yes	No	Not assess
Yes	1	3	-
No	1	5	-
Not assess	-	-	-

Presence of diffuse varix

	DSA		
Post contrast	Yes	No	Not assess
Yes	2	1	-
No	1	6	-
Not assess	-	-	-

Presence of venous stenosis

	DSA		
Post contrast	Yes	No	Not assess
Yes	-	3	-
No	3	4	-
Not assess	-	-	-

Presence of venous occlusion

	DSA		
Post contrast	Yes	No	Not assess
Yes	-	3	-
No	-	7	-
Not assess	-	-	-

Clinical goal of treatment

	DSA					
Post contrast TOF	Cure	Diminish risk of haemorrhage	Palliate	Adjunct to 2nd treatment	None	Not assessable
Cure	3	1	-	-	-	-
Diminish risk of haemorrhage	1	-	1	-	-	-
Palliate	-	1	1	-	-	-
Adjunct to 2nd treatment	-	-	-	-	-	-
None	2	-	-	-	-	-
Not assessable	-	-	-	-	-	-

Morphological goal of treatment

	DSA					
Post contrast TOF	Eliminate high risk component	Decrease nidus size	Obliterate nidus	Eliminate specific feeders	No treatment	Not assessable
Eliminate high risk component	-	1	1	-	-	-
Decrease nidus size	-	-	-	-	-	-
Obliterate nidus	-	1	3	-	-	-
Eliminate specific feeders	1	1	-	-	-	-
No treatment	-	1	1	-	-	-
Not assessable	-	-	-	-	-	-

Proposed treatment

	DSA					
Post contrast TOF	Conservative	Medical	Embolisation	DXT	Surgery	Not assessable
Conservative	-	-	-	-	-	-
Medical	-	-	-	-	-	-
Embolisation	-	-	5	2	-	-
DXT	-	-	1	-	-	-
Surgery	-	-	2	-	-	-
Not assessable	-	-	-	-	-	-

APPENDIX 4

Data for Chapter 6 – MR perfusion

Cerebral blood flow (in arbitrary unit volume $100g^{-1}$ min^{-1})

Region	Nidus	Perinidus 1	Perinidus 2	Perinidus 3	Normal
Patient					parenchyma
1	1290.51	1274.71	1286.51	1295.17	1253.25
2	1293.12	1239.54	1202.51	1128.99	977.69
3	812.44	1052.53	1066.26	1115.82	1006.92
4	1255.17	1165.43	1151.49	1124.98	1165.14
5	1297.31	1201.72	1135.60	1245.48	1156.36
6	1261.29	1234.24	1207.38	1203.27	1237.25
7	1296.29	1256.81	1267.88	1259.66	1223.01
8	-	1287.63	1287.81	1298.65	1277.77
9	1299.44	1233.18	1201.76	1219.47	1152.10
10	1174.15	1272.42	1108.63	967.74	1024.54
11	1297.23	1279.30	1173.60	1206.18	1023.00
12	1288.42	1170.06	1083.48	1170.30	1238.38
13	1271.54	1169.14	1232.94	1273.94	1218.87
14	1273.75	1140.76	1193.63	1151.29	1155.25
15	1297.34	1289.58	1229.93	1258.54	1241.83

- standard deviation for the average nidus CBF was zero therefore presumed to be 'uncomputable'

Cerebral blood volume (in arbitrary unit volume)

Region / *Patient*	Nidus	Perinidus 1	Perinidus 2	Perinidus 3	Normal parenchyma
1	1078.98	932.56	674.34	756.86	390.34
2	395.18	164.78	130.41	94.07	162.69
3	74.33	111.62	101.47	80.57	39.40
4	582.74	408.76	258.26	174.65	279.42
5	950.69	401.75	235.99	292.58	155.25
6	214.48	128.98	143.31	143.36	145.02
7	540.87	180.33	142.21	153.12	146.37
8	2139.01	971.75	958.22	923.52	418.91
9	831.95	286.82	169.34	168.19	142.86
10	296.91	323.56	163.92	102.88	70.03
11	445.50	331.30	171.90	166.93	74.97
12	1826.25	649.65	462.72	559.70	363.23
13	561.56	194.69	192.35	335.24	113.71
14	476.86	244.27	218.69	171.91	231.78
15	801.29	425.24	313.09	305.71	113.45

Mean transit time (in arbitrary unit time)

Region / *Patient*	Nidus	Perinidus 1	Perinidus 2	Perinidus 3	Normal parenchyma
1	270.34	240.82	296.77	396.77	375.80
2	275.26	337.82	341.73	334.70	584.41
3	389.83	410.03	312.94	316.80	301.80
4	288.59	401.49	353.46	383.62	449.68
5	244.61	387.02	390.32	306.40	435.52
6	227.25	212.6	220.02	228.25	212.83
7	216.18	226.32	215.54	217.32	229.60
8	222.32	265.55	258.27	270.59	352.88
9	219.81	297.94	305.82	288.46	270.58
10	360.18	318.37	246.37	280.52	311.58
11	220.68	219.61	315.58	281.12	289.60
12	240.14	595.69	739.99	625.97	417.50
13	246.73	301.29	283.49	290.97	245.10
14	250.86	433.32	355.53	435.70	466.11
15	222.65	241.49	312.28	282.21	277.44

Time to minimum signal intensity (in arbitrary unit time)

Region / *Patient*	Nidus	Perinidus 1	Perinidus 2	Perinidus 3	Normal parenchyma
1	342.11	350.31	362.71	374.61	374.78
2	345.38	347.30	351.66	352.76	362.45
3	336.90	349.38	341.34	347.89	368.18
4	375.69	379.85	389.277	394.05	394.52
5	370.10	365.57	383.19	380.64	382.82
6	390.78	386.34	387.88	388.43	387.76
7	332.83	328.55	334.46	332.95	343.71
8	338.92	342.54	348.79	350.10	360.65
9	348.34	362.29	370.37	374.03	358.83
10	363.04	378.65	376.24	391.26	389.50
11	353.64	348.59	366.54	369.03	377.33
12	368.02	439.84	440.95	422.11	406.30
13	329.87	343.80	351.75	346.02	344.03
14	361.50	381.48	387.26	395.40	402.06
15	353.64	354.69	362.83	360.80	366.68

APPENDIX 5

Data for Chapter 7 – Digital Subtraction Angiography

	Variables						
No.	Frame rate (fr sec^{-1})	Injection rate (ml sec^{-1})	SID (cm)	PSD (cm)	FOV (inches)	Table Height (cm)	Angle from horizontal
Calibration model							
1	30	1.0	100	87	12	87	0
2	30	1.0	100	87	12	87	0
3	30	1.0	100	87	12	87	0
4	30	1.0	100	87	12	87	0
5	30	1.0	100	87	12	87	0
6	30	1.0	100	87	12	87	0
7	30	1.0	100	87	12	87	0
8	30	1.0	100	87	12	87	0
9	30	1.0	100	87	12	87	0
10	30	1.0	100	87	12	87	0
11	30	5.0	100	87	12	87	0
12	30	5.0	100	87	12	87	0
13	30	5.0	100	87	12	87	0
14	30	5.0	100	87	12	87	0
15	30	5.0	100	87	12	87	0
16	30	5.0	100	87	12	87	0
17	30	5.0	100	87	12	87	0
18	30	5.0	100	87	12	87	0
19	30	5.0	100	87	12	87	0
20	30	5.0	100	87	12	87	0
21	30	10.0	100	87	12	87	0
22	30	10.0	100	87	12	87	0
23	30	10.0	100	87	12	87	0

	Variables						
No.	Frame rate (fr sec^{-1})	Injection rate (ml sec^{-1})	SID (cm)	PSD (cm)	FOV (inches)	Table Height (cm)	Angle from horizontal
24	30	10.0	100	87	12	87	0
25	30	10.0	100	87	12	87	0
26	30	10.0	100	87	12	87	0
27	30	10.0	100	87	12	87	0
28	30	10.0	100	87	12	87	0
29	30	10.0	100	87	12	87	0
30	30	10.0	100	87	12	87	0
Angle from horizontal							
31	30	5	100	87	12	87	0
32	30	5	100	87	12	87	6.78
33	30	5	100	87	12	87	9.72
34	30	5	100	87	12	87	12.18
35	30	5	100	87	12	87	14.66
36	30	5	100	87	12	87	16.67
37	30	5	100	87	12	87	19.22
38	30	5	100	87	12	87	22.32
39	30	5	100	87	12	87	24.69
40	30	5	100	87	12	87	27.38
41	30	5	100	87	12	87	30.7
42	30	5	100	87	12	87	32.4
43	30	5	100	87	12	87	35.31
44	30	5	100	87	12	87	38.95
45	30	5	100	87	12	87	40.84
46	30	5	100	87	12	87	44.46
47	30	5	100	87	12	87	48.32
48	30	5	100	87	12	87	52.49
49	30	5	100	87	12	87	53.69

	Variables						
No.	Frame rate (fr sec^{-1})	Injection rate (ml sec^{-1})	SID (cm)	PSD (cm)	FOV (inches)	Table Height (cm)	Angle from horizontal
Frame rates							
50	6	0.5	100	83	12	117	0
51	6	1.0	100	83	12	117	0
52	6	2.0	100	83	12	117	0
53	6	4.0	100	83	12	117	0
54	6	6.0	100	83	12	117	0
55	7.5	0.5	100	83	12	117	0
56	7.5	1.0	100	83	12	117	0
57	7.5	2.0	100	83	12	117	0
58	7.5	4.0	100	83	12	117	0
59	7.5	6.0	100	83	12	117	0
60	10	0.5	100	83	12	117	0
61	10	1.0	100	83	12	117	0
62	10	2.0	100	83	12	117	0
63	10	4.0	100	83	12	117	0
64	10	6.0	100	83	12	117	0
65	10	8.0	100	83	12	117	0
66	15	0.5	100	83	12	117	0
67	15	1.0	100	83	12	117	0
68	15	2.0	100	83	12	117	0
69	15	4.0	100	83	12	117	0
70	15	6.0	100	83	12	117	0
71	15	8.0	100	83	12	117	0
72	15	10.0	100	83	12	117	0
73	30	0.5	100	83	12	117	0
74	30	1.0	100	83	12	117	0
75	30	2.0	100	83	12	117	0
76	30	4.0	100	83	12	117	0

No.	Variables						
	Frame rate (fr sec^{-1})	Injection rate (ml sec^{-1})	SID (cm)	PSD (cm)	FOV (inches)	Table Height (cm)	Angle from horizontal
77	30	6.0	100	83	12	117	0
78	30	8.0	100	83	12	117	0
79	30	10.0	100	83	12	117	0
Field of view							
80	15	0.5	100	80	12	114	0
81	15	0.5	100	80	9	114	0
82	15	0.5	100	80	7	114	0
83	15	0.5	100	80	5	114	0
Table height							
84	15	0.5	100	48	12	82	0
85	15	0.5	100	53	12	87	0
86	15	0.5	100	58	12	92	0
87	15	0.5	100	63	12	97	0
88	15	0.5	100	68	12	102	0
89	15	0.5	100	73	12	107	0
90	15	0.5	100	78	12	112	0
91	15	0.5	100	83	12	117	0
Source-image distance (SID)							
92	15	0.5	110	68	12	102	0
93	15	0.5	105	68	12	102	0
94	15	0.5	100	68	12	102	0
95	15	0.5	95	68	12	102	0
96	15	0.5	90	68	12	102	0
97	15	0.5	85	68	12	102	0
Patient-source distance (PSD)							
98	15	0.5	100	83	12	117	0
99	15	0.5	95	78	12	117	0
100	15	0.5	90	73	12	117	0
101	15	0.5	85	68	12	117	0